Vrije Universiteit Brussel
Faculteit Toegepaste Wetenschappen
Vakgroep Toegepaste Natuurkunde en Fotonica
Pleinlaan 2, B-1050 Brussel, Belgium

European Synchrotron Radiation Facility
Topography Group
BP 220, F-38043 Grenoble,France

Contribution to Phase Contrast Imaging, Reconstruction and Tomography with Hard Synchrotron Radiation

Principles, Implementation and Applications

Peter Cloetens
March 1999

Promotor :	Prof. Dr. A. Hermanne
Co-promotor :	Prof. Dr. J. Van Landuyt
Mentoren:	Prof. Dr. M. Schlenker Dr. J. Baruchel

Proefschrift ingediend tot het behalen van de titel van doctor in de Toegepaste Wetenschappen

Acknowledgements

This work was prepared at the European Synchrotron Radiation Facility (ESRF) in the Topography Group directed by Dr. José Baruchel. Je remercie José pour l'accueil chaleureux dans son groupe et pour toutes les idées qu'il a apportées à ce travail.

Ik dank mijn promotoren Dr. A. Hermanne en Dr. J. Van Landuyt. Laatstgenoemde heeft steeds op efficiënte wijze de band weten te leggen tussen de X-stralen en elektronen wereld.

Je remercie tout particulièrement Dr. Michel Schlenker du Laboratoire Louis Néel qui m'a suivi du début jusqu'à la fin de cette thèse, des premiers essais "d'absorbeurs liquides" jusqu'aux corrections des conclusions (ouf!). Ces idées astucieuses et son amour pour l'imagerie directe ont clairement contribué à l'accomplissement de cette thèse.

I am honoured that Professors I. Veretennicoff, J. Cornelis, J. Schoukens, F. Poortmans, D. Van Dyck, H. Terryn, A. Cardon are willing to judge this work.

Prof. Roger Van Geen had accepted to be the initial supervisor of this work. I hope that he would have appreciated this work.

Les discussions avec Dr. Jean-Pierre Guigay ont toujours été d'une grande utilité. L'originalité de son approche théorique a souvent permis de débloquer la situation aux passages difficiles. Ce fut un plaisir de pouvoir réaliser ensemble quelques idées développées par Jean-Pierre sur les objets périodiques il y a bien longtemps, dans l'année de ma naissance.

De inbreng van Dr. Dirk Van Dyck en Dr. Marc Op de Beeck van EMAT was onmisbaar voor het fase reconstructie probleem. Dirk's enthousiasme en ideeën maakten het mogelijk om vrij snel tot quantitatieve beelvorming te komen.

C'est bien beau d'avoir des idées et beaucoup de photons, encore faut-il réaliser ces idées farfelues de physiciens. L'apport de René Chagnon était indispensable pour tous les problèmes techniques. Je le remercie pour ses solutions astucieuses, rapides et efficaces et son travail à la conception d'éléments importants du dispositif expérimental. Jacques Borrel a également conçu divers dispositifs experimentaux, ce fut un plaisir de collaborer pour la conception mécanique des détecteurs. Je remercie Denis Gambetti, José Sendra et Dominique Rolhion pour la réalisation de multiples pièces, ... avec nos excuses pour les délais impossibles.

More generally, I wish to thank all the people of the different supporting groups at ESRF. Without their support in the field of informatics, detectors, mechanics, electronics the ESRF could not operate. Je remercie particulièrement les membres de l'ex-BLPO François Thurel, Philippe et Gilles Retout et Ange Draperi pour leurs soins apportés au bon fonctionnement de la ligne de lumière ID19. L'équipe FReLoN, Jean-Claude Labiche et collaborateurs, a donné aux chercheurs une caméra dont les possibilités dépassent largement nos compétences, mais, ma foi, nous avons essayé d'en faire la meilleure utilisation possible. The work and ideas of Andréas Koch and Jean-Pierre Moy made the realisation of the high resolution detector possible. J'ai eu la chance de faire des mesures de métrologie avec Miguel Nicola et Hans-Peter Van Der Kleij. C'est appréciable de trouver au sein d'un monde agité et impatient tel que l'ESRF quelques gens qui prennent le temps nécessaire pour faire des mesures précises. J'ai également apprecié la patience de Jean-Pierre Vassalli et André Paul pour polir et repolir maintes fois les cristaux du monochromateur afin d'éviter toute rayure de surface.

Les surfaces des miroirs et multi-couches ne sont pas encore parfaites (ce n'est pas facile l'angström). Le travail sur ce sujet avec Olivier Hignette (merci pour les discussions), Eric Ziegler et Christian Morawe reste en cours et commence à compenser le manque, très relatif, de photons disponibles dans un synchrotron de troisième génération.

Parmi les collaborateurs les plus sympas figurent les gens de l'INSA de Lyon, Jean-Yves Buffière, Gilles Peix et Eric Maire pour les études d'endommagement de matériaux composites. Qu'est-ce qu'on en a fait des 'etirements' de materiaux! Je n'oublierai pas les courses gigantesques, la guitare et le sac de couchage derrière les armoires électriques pour passer une autre séance nocturne de tomographie. On finirait par regretter le raccourcissement du temps d'acquisition qui ne permet même plus de faire un petit somme entre deux échantillons.

Ce fut un grand plaisir de collaborer avec Joseph Gastaldi et Eric Reinier sur l'imagerie de quasicristaux et avec Murielle Salomé et Françoise Peyrin sur la micro-tomographie de matière osseuse. It was also a pleasure to work with Alessia Cedola, Stephano Lagomarsino, Silvia Di Fonzo, Werner Jark and Gérard Souillié on magnification using X-ray waveguides.

This work could not have been realised without A. Snigirev showing us the title and the list of authors of his initial publication on phase sensitive imaging.
I do not thank Microsoft for producing extremely irritating, stupid, heavy and unreliable software.

Bien sûr un grand merci véritable à tous les membres ou sympathisants du Groupe Topographie. En particulier la célèbre Lucia Mancini, Petra (vive le tennis) et Etienne (vive les barbecues) Pernot, Eetu Prieur (vive les X-ray films), Michael Ohler (j'ai fini par l'avoir l'ordinateur), Carlos Medrano de Sanchez ... (vive le ski), Ray Barrett et José Espeso (merci pour le boulot), Murielle Salomé (pour les premiers scans tomo assurés à la paire de ciseaux), Concetta de Martino (scusi dove la via per andare a sincrotrone?), Jürgen Härtwig (vive la théorie dynamique), Tilo Baumbach (merci pour la bonne humeur et la clarinette), Elodie Boller (chef du bureau d'observatoire) et finally but not least Wolfgang Ludwig (le Chef, au boulot et au ski).

Ik dank mijn familie voor hun steun en geduld. Sans oublier ma Sophieke: le rire est dans le coeur, le mot dans le regard, le coeur est voyageur et l'avenir est au hasard (le grand Jacques).

This work was realised with the financial support of the Fonds voor Wetenscappelijk Onderzoek – Vlaanderen.

L'incohérent prend sa retraite
en se mariant
ou en attrapant un rhumatisme!

Alphonse Allais

CONTENTS

1 Introduction

Imaging is performed with a variety of probes, including light and electrons, but also NMR-frequency electromagnetic waves, ultra-sound, neutrons and X-rays. All these techniques have developed because each probe has its merits in terms either of resolution or of the scale of the samples it can handle, and provides original information related to the physical quantities to which it is sensitive. Volume observations are of particular interest when they allow to visualise features (cracks, defects, tumours, ...) without significantly damaging the sample or altering the observed phenomena. Ideally an information carrier, some kind of wave, would suffer negligible attenuation in the object, but would be altered significantly in a different, more subtle way such as a change in its direction, polarisation or phase. In the absence of absorption no energy is deposited in the sample and the carrier can cross thick samples. For optically transparent materials the oldest of all microscopies, light microscopy, is doing an excellent job. Perfect, diffraction limited lenses exist and it includes several phase contrast possibilities. However truly three dimensional imaging remains difficult and many materials or tissues do not transmit visible light. X-rays were discovered more than 100 years ago and immediately used to make an image through the material, a radio-graph, of a normally opaque sample with inner structures. Right from the beginning Röntgen noticed that it was difficult to stop this particular radiation, but also to deviate or reflect it, hence that all interaction with matter was weak. Absorption radiography, based on inhomogeneous transmission of the beam, was the first and remains up to now the major form of X-ray imaging. It is extremely wide-spread both in industrial non-destructive testing and in medicine, and includes sophisticated variants such as computed tomography for three-dimensional imaging.

X-ray Bragg diffraction appeared few years (1912) after the discovery of X-rays. The diffraction pattern produced by the coherently scattered radiation is determined by the underlying atomic structure. In X-ray crystallography this is used to ‘image’ with sub-angstrom resolution the atomic structure of periodically repeated crystal units. Inhomogeneities in Bragg diffraction reflectivity make it possible to image defects in this periodic repetition. X-ray Bragg diffraction imaging, the second form of conventional X-ray imaging, developed into practical use about forty years ago. The possibility to easily visualise crystal defects allowed to improve the growth processes, making it possible to produce large, ‘perfect’ crystals. This paved the way to micro-electronics.

Conventional absorption radiography is not an ideal imaging technique as it is still based on the inhomogeneous stopping of the information carrier, hence results in the deposition of some dose. Furthermore, due to the weak interaction with matter, it can be expected that contrast will disappear when the thickness of the traversed features becomes too small. If one selects for example an X-ray energy of 25 keV to be able to cross a thick aluminium sample, a hole in this metal should have a diameter of at least 20 μm to produce 1 % contrast. Therefore it is of interest to apply a more sensitive contrast mechanism that does not imply deposition of dose. Especially light materials may change the *phase* of a transmitted wave much more significantly than its amplitude. Fig 1.1 shows for example the ratio of the effect on the phase and the amplitude as a function of the X-ray energy for the element aluminium. The large energy range includes soft X-rays and hard X-rays. In the soft X-ray range, more precisely in the 'water window' where soft X-ray microscopes usually operate, a gain exists but it is relatively modest. On the other hand in the hard X-ray range (energies above 6 keV) this ratio increases with energy to huge values (up to 1000). Thus, using the effect on the phase, the minimum detectable aluminium hole is reduced to about 0.05 µm at 25 keV. X-rays are adapted for imaging of thick samples thanks to their low absorption at high energies. If it is possible to visualise the phase of the transmitted wave, the sensitivity and spatial resolution remain good.

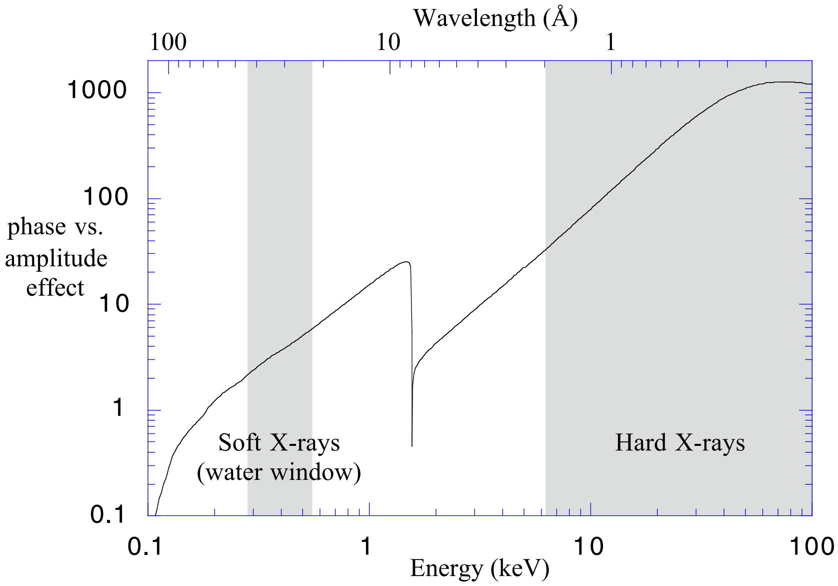

Fig 1.1 Ratio of the effect on the *phase* and the *amplitude* of a transmitted wave as a function of the X-ray energy for the element aluminium.

The earliest successful experimental evidence of refraction phenomena with X-rays were reported in 1926 by Davis and Slack [Dav26] who showed that it was possible to deviate an X-ray beam by a very small amount with a prism. This confirmed that the refractive index for X-rays is not exactly unity, but slightly smaller, by an amount about 10^5 times smaller than the usual index variations for visible light. All angular deviations (in the absence of Bragg diffraction) are consequently tiny. However, the optical wavelength of X-rays is 10^4 times smaller than its visible counterpart. Therefore the effect on the phase integrated along the path of the X-rays in matter may still be appreciable and huge compared to the corresponding effect on the amplitude. Realising X-ray lenses is a difficult task and elaborated forms of phase imaging such as Zernike type contrast or off-axis holography are therefore ruled out. Two conventional methods exist to visualise the phase with hard X-rays, but they are not trivial from an experimental point of view and involve rather sophisticated set-ups. An X-ray interferometer consisting of several slices of perfect crystal silicon carved out of a monolithic single-crystal block was developed and used for imaging. In this case differences in optical path for the beam transmitted through an object are directly converted, after interference with the reference beam, into inhomogeneous intensity, hence contrast. The second principle uses Bragg diffraction by crystals in order to amplify the small angular deviations of X-rays and to distinguish them from non deviated portions of the beam. These conventional methods have their merits but the complexity of the set-ups and the limited achievable spatial resolution hindered their development.

Free space propagation can also transform the phase modulation of the incident beam into an amplitude modulation. This is the basis for a trivial form of phase sensitive imaging that recently developed into practical use with the advent of third generation synchrotrons. These synchrotrons are characterised among others by the small size of the electron beam that acts as the source and large distances between this source and the sample. This results in a relatively high degree of spatial coherence at the level of the specimen. This kind of source, delivering also a flux orders of magnitudes larger than conventional laboratory sources, is therefore a priori well suited to coherent imaging. ‘Propagation images’ appeared first as a by-product in two quite different fields: hard X-ray focusing using diffractive optics [Har94, Sni95] and X-ray Bragg diffraction imaging [Kam65, Clo95]. We first encountered this effect during X-ray topographic work at the ESRF in the form of spurious images, obviously not related to the crystals under investigation. While based on the coherence properties of X-ray beams from a highly sophisticated third-generation synchrotron source, and in contrast to the other methods, this method is extremely simple and involves almost no instrumentation. The set-up is identical to that of conventional attenuation radiography except in the sample-detector distance. It corresponds to Gabor in-line holography in classical optics and to the defocusing mode in electron microscopy.

Our work contributes to three aspects of the novel technique of hard X-ray phase sensitive imaging using simple propagation of a coherent beam: the methodology, the instrumentation and first applications.

The *methodological aspect* involves a ‘correct’ recognition of the observed phenomena and the selection of an adapted theoretical framework, viz. Fresnel diffraction, to describe them. Some image features can qualitatively be understood as due to angular deviations of the X-ray beam, but a much more complete and quantitative description is found in a wave-optical approach. It is mandatory although the wavelength of interest is small and the spatial resolution is modest because the lateral displacements of the wavefronts are tiny due to the small refractive index variations. Different image regimes can be distinguished as a function of the propagation distance and several experimental results will show the possibility of using Fresnel imaging as a *direct imaging* technique in the ‘edge detection regime’. In this case rapid variations of the phase occurring at edges show up in the Fresnel diffraction patterns as localised interference fringes acting as signatures of these edges. *Quantitative imaging* allows to extract more information from the images and involves some numerical image processing. The latter will systematically be based on the physics underlying the image formation process. The purpose of the phase determination is 1) to obtain an image that can be directly interpreted with optimum spatial resolution 2) to obtain quantitative information on the sample, a prerequisite for three-dimensional imaging. A phase map has in the X-ray case (nearly always) a straightforward interpretation as the projection along the X-ray path of the electron density in the sample. These phase maps constitute therefore the correct input for a tomographic reconstruction. The relationship with work performed in the field of electron microscopy was crucial in the problem of retrieving the phase from the recorded images. In electron microscopy the equivalent of this X-ray method is the well-known technique of defocusing, the simplest technique of phase sensitive imaging. More specifically in the field of high resolution electron microscopy it is a way to obtain information with atomic resolution on the wave exiting the investigated crystal. Recently a method based on focus variation to solve the phase problem was improved and practically implemented in the electron case [Coe92]. This approach enabled us to solve in practical cases the inverse problem and reconstruct the phase from recorded images. Combined with a tomographic technique, the holographic reconstruction results in the determination of the refractive index distribution.

The *instrumental aspect* includes the development of an adapted set-up for phase sensitive imaging and tomography. Every object in the X-ray path can act as a phase object. Spurious images from ill-adapted optical elements (windows, monochromators, ...) can degrade the homogeneity and coherence of the beam. We will discuss the problems encountered and the measures taken to solve them. In the absence of significant X-ray magnification, the detector is a major element of the set-up and determines the achievable spatial resolution. We constructed a detector based on X-ray to visible light conversion and a state-of-the-art CCD camera with a spatial resolution approaching that of a usual optical microscope.

The *applications* illustrate the possibilities of coherent hard X-ray imaging as a useful recent member of the large family of microscopy techniques. In situ three-dimensional observations of damage progression in a particle reinforced composite show unique microstructural and fracture information. It helps understanding and modelling the damage mechanisms in such composites. Quasicrystals are investigated by a combination of phase sensitive and Bragg diffraction imaging. This yields new clues for the understanding of the structural defects of quasicrystals. Phase sensitive radiography shows microstructural features such as holes and precipitates whereas Bragg diffraction imaging reveales essentially the strain fields. The combination of both techniques is particularly interesting when the crystal behaves as an inhomogeneous phase object only when set to Bragg diffract. We will visualise ferroelectric domains in lithium niobate crystals using simultaneously Bragg and Fresnel diffraction and will extract quantitative information about atom displacements at the microscopic level.

The outline of this manuscript is the following.

In section 2, denoted ‘Principles’, three techniques for phase sensitive imaging with hard X-rays are compared (§ 2.1): the interferometric, the Schlieren and the propagation technique. We describe their principle and discuss the advantages and drawbacks of each regarding the accessible phase information, the complexity of the set-up, the requirements on the beam or the covered spatial frequency range. The technique further used in this work, simple propagation, is modelled with some detail in § 2.2. We treat the *direct problem* that consists in determining the defocused image of a known object under known experimental conditions. The transmission function of the object, a usual concept in the absence of Bragg diffraction, is introduced. The case of perfect and partial coherence are considered and an adapted description for the real synchrotron sources is proposed. The simulations of the Fresnel diffraction patterns are efficiently implemented using Fourier transformations. Tomography, which allows to retrieve an unknown three-dimensional distribution from a large number of projections corresponding to different directions, is described in § 2.3.

In section 3, denoted ‘Implementation’ the instrumentation used for phase sensitive radiography and tomography is described. The various devices used to produce synchrotron radiation are considered and special attention is paid to the coherence of the beam they deliver at the level of the sample (§ 3.1). In order to avoid parasitic images and to preserve the coherence, all optical elements in the beam are subject to stringent quality requirements. The problems identified and the way they were solved during the commissioning of the beam-line are described in § 3.2. The simple set-up we implemented is described in § 3.3, with emphasis on the alignment procedures of the rotation and the translation stage for the tomographic and the holographic scan respectively. We describe in § 3.4 the on-line detector based on an X-ray → visible light converter, coupled to a cooled CCD with a lens system. The sensitivity, noise characteristics and spatial resolution of the different detector systems are presented. We describe how their transfer function is determined and taken into account in a deconvolution procedure.

Section 4, denoted ‘Methods’ deals with quantitative aspects of coherent X-ray imaging. The most important ones are the determination of the degree of coherence and the treatment of the *inverse problem*. The special case of Fresnel diffraction on a periodic object leads to the spectacular effect of self-imaging known as the Talbot effect. A method to determine the spatial degree of coherence is deduced and implemented in § 4.2. The determination of the phase in the case of an arbitrary object, not necessarily periodic or weak, is the purpose of the holographic reconstruction in § 4.3. We use the method of focus variation which was successfully applied in high resolution electron microscopy. It consists in recording at different sample detector distances a series of images which are combined through a suitable algorithm to reconstruct the wave exiting the sample. The methods, linear and non-linear least squares optimisations, are presented and adapted to the X-ray case. Special attention is given to physically meaningful constraints. We present retrieved phase maps of an actual sample using this technique. In combination with a tomographic technique (§ 4.4), i.e. after repeating the holographic reconstruction for a large number of angular positions of the sample, the three dimensional distribution of the refractive index decrement in a polymer foam sample is mapped. The possibility of overcoming the detector resolution limit through magnification by projection is demonstrated in § 4.5. The divergent but coherent beam exiting an X-ray waveguide is shown to be effective, at least in one direction, for this purpose.

In section 5 we present useful applications of phase sensitive imaging eventually combined with other techniques such as electron microscopy or X-ray Bragg diffraction imaging. Phase sensitive radiography and tomography is applied to the study of damage mechanisms in composite materials in § 5.2. It is shown that Fresnel fringes enhance strongly the otherwise weak contrast between matrix and reinforcement. Fresnel fringes signal the presence and the position of cracks with an opening small compared to the spatial resolution. In-situ volume observations of the microstructure and damage in strained composites are presented and discussed. This work results from a collaboration with the following laboratories: GEMPPM, INSA, Lyon, France; CNDRI, INSA, Lyon, France and CREATIS, INSA, Lyon, France. Microstructural information similarly obtained on quasicrystals is presented in § 5.3. Investigating AlPdMn icosahedral single quasicrystals through phase sensitive imaging we observed in the bulk crystalline precipitates and several families of holes with a shape (dodecahedra) featuring the point symmetry of the material. The corresponding Bragg diffraction images show the strain field around the holes and precipitates. Both types of images can be obtained simultaneously. The information about the microstructure and the structural defects they provide is summarised. Several people from ESRF; CRMC2-CNRS, Marseille, France and Lab. Louis Néel, Grenoble, France contributed to the investigation of quasicrystals. Bragg diffraction and Fresnel diffraction are combined in § 5.4 to image ferroelectric domains in periodically poled lithium niobate crystals. We show that the phase difference in the structure factor of adjacent domains is the main origin of the contrast. The value of this phase difference is retrieved through simulation of the image contrast as a function of the defocusing distance. This study of materials for applications in the field of non-linear optics involves people from ESRF and LPCML, Université Claude Bernard, Lyon, France.

2 Principles

2.1 Sensing the phase of hard X-rays

An X-ray beam transmitted by an object acquires shifts in its phase due to the interaction with the electron shells of the atoms in the material. Using these phase shifts for imaging was pioneered in the early seventies by Ando et al [And72] who obtained images of bone tissues and of a slice of granite using a Bonse-Hart type interferometer [Bon65]. Since, this technique developed into a quantitative three-dimensional imaging technique and other techniques with many variants arose. This work is dedicated to the most recent development based on the oldest principle: free space propagation or Fresnel diffraction. The co-existence of the different methods shows that they all have their advantages and disadvantages with respect to the accessible phase-information, the complexity of the set-up, the requirements on the beam or the covered spatial frequency range. Therefore each technique has and will find specific applications in medical, industrial or scientific imaging where it is the most adapted one. Because of the limited quality of available lenses, elaborate forms of phase contrast imaging such as Zernike phase-contrast [Zer35] or off-axis holography [Lei62] are presently ruled out for hard X-rays.

2.1.1 The interferometric technique

Here the contrast is due to the interference of the beam transmitted through the object with a reference beam. If both beams are mutually coherent, the intensity will be directly affected by the local phase shift between both beams. The two beams are obtained by splitting the amplitude of the incident beam and this type of interferometry can be classified in the broad class of two-beam interferometry by division of amplitude [Bor80]. Bragg-diffraction by perfect crystals replaces the reflection by half-mirrors in the case of light optics. A possible configuration is shown in Fig 2.1 [Har75]. It consists in an interferometer of L-L-L type - L means the Laue or transmission geometry - cut out from a large, almost perfect monolithic silicon crystal. The first crystal slice or splitter acts as a coherent beam splitter, the second slice or mirror deviates the beams and allows for recombination in the third slice or analyser. The sample is inserted in one of both arms, normally between the mirror and the analyser. The interference fringes can be recorded in either of the outgoing beams using a large beam and a two-dimensional detector or a pointlike beam and scanning procedure. A phase shifter, inserted in one arm, can be varied in effective thickness through rotation. This external phase shift is used to compensate for imperfections of the interferometer and to reconstruct the phase modulation introduced by the object through the fringe scanning method.

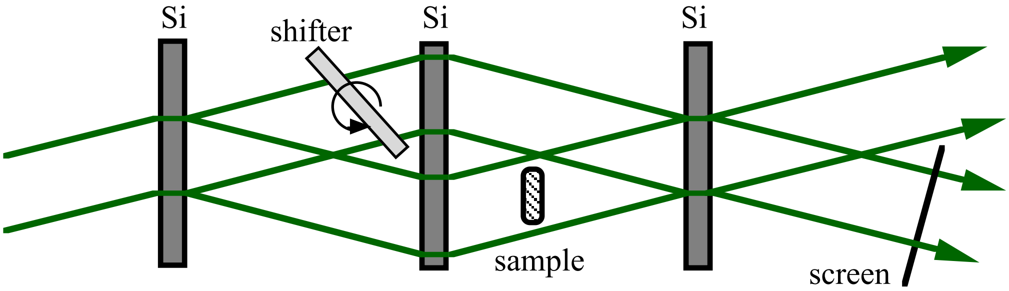

Fig 2.1 Principle of interferometric phase imaging.

The recorded interference patterns can not be exploited as they are because the interference fringes can not be directly linked to a projection of the object and because an intrinsic fringe pattern is always present. These intrinsic fringes exist without any object in the beam due to a static phase pattern introduced by the interferometer itself or the sample environment. The image treatment to reconstruct quantitatively the phase modulation introduced by the sample is however rather straightforward. Several images must be recorded to reconstruct a single phase-map in order to avoid ambiguity on the sign of the phase, to eliminate the incoherent contributions to the intensity and to compensate for static phase patterns. The fringe scanning method consists in recording a set of interference patterns where the external phase shift is changed step by step. During this scan the external phase shift varies by 2π over a total of J steps. For each step an interference pattern is recorded with and without the sample in the beam, giving a total number of $2J$ recorded patterns from which a single phase map is reconstructed using a simple algebraic expression. The number of patterns can be 8 ($J = 4$) or bigger [Mom95, Bec97]. In this way the phase is known except for a multiple of 2π. This uncertainty can be removed by phase unwrapping techniques [Bec98] if there are no sudden phase jumps on a scale smaller than the resolution.

The possibility to perform with an X-ray interferometer phase tomography and to reconstruct the local distribution of the refractive index decrement $\delta(x,y,z)$ was demonstrated by Momose *et al* and Beckmann et al in 1995 [Mom95, Bec95]. The interest of phase imaging compared to absorption imaging was frequently illustrated [Mom96]. The complexity of this technique is however a serious drawback. The fringe pattern can be totally changed by a displacement at the atomic level between the different slices of the interferometer, requiring extreme stability of the experimental environment (thermal, mechanical and acoustic stability). Up to now succesful operation of the interferometers was only obtained when they are cut out of a single crystal block. The space available for the sample and its environment between the slices is thus limited by the ingot to a few centimeters. The sample must be immersed in a liquid that matches the refractive index of the sample. Without this immersion liquid large phase jumps at an air-sample edge perturb the interference fringes and the large deflection in the sample reduces the visibility of the fringes. Such interference patterns can not be described and disentangled by the usual description that supposes a point to point relationship between object and image. This relationship is also broken by Fresnel diffraction due to propagation from sample to detector. This effect becomes important only when the size of the first Fresnel zone is bigger than the resolution.

The resolution is limited intrinsically by the passage of the beam through the analyser crystal. Dynamical diffraction occuring in this crystal spreads the energy of each point at its entrance over a triangle whose width will limit the resolution. This limits the resolution up to now to about 15 µm (10% of the MTF) in the best case [Bec97]. The resolution is further limited by the detector resolution. The volume of the interferometer implies a minimum distance between sample and detector, leading to some blurring due to the source size and Fresnel diffraction. The covered frequency range is not limited towards the low frequencies and a spatially homogeneous phase shift can be measured with respect to the reference beam.

The requirements on the beam incident on the interferometer are not extreme. The beam incident on the sample is intrinsically monochromatic because of Bragg diffraction in the slices of the interferometer. Normally the beam is already made monochromatic upstream of the interferometer. The interference occurs ideally between points of the reference and phase shifted wave that originate from the same point of the original wave. Bragg diffraction assures the coherence between these points. There is no superposition of waves originating from laterally separated portions of the incident wave and thus the beam needs little lateral coherence. Increasing too much the beam divergence will however affect the geometrical resolution. The main interest of synchrotron radiation for interferometric phase imaging is the available flux. Interferometric phase tomography requires a very large number of images to be recorded (about 2.*J*.number of angular steps), and became only possible with synchrotron radiation.

The same interferometric principle was applied with neutrons by Schlenker *et al* [Sch80] to image magnetic domains in a Fe, 3 % Si crystal. They also showed that, after suppression of the reference beam, the phase jumps or gradients remain visible. Very recently hard X-ray interferometry by division of wavefront, where the interfering beams originate from laterally separated portions of a beam, was demonstrated in the configuration of Fresnel's mirrors [Fez97].

2.1.2 Schlieren technique

This differential phase contrast method is sensitive to the angular deviations of the X-ray beam. Phase gradients present in the object deviate locally the beam through refraction, as known from the simple expression

$$\Delta\alpha = -\frac{\lambda}{2\pi}\frac{\partial\varphi}{\partial x} \tag{2.1}$$

that links the angular deviation $\Delta\alpha$ to the derivative of the phase. Förster et al [För80] used a double crystal arrangement similar to the one shown in Fig 2.2. The first, collimator, crystal limits the angular and spectral range of the incident beam, i.e. if the beam is monochromatic it will select the direction of the beam incident on the sample; if the beam is collimated but polychromatic, the crystal selects the used wavelength. The second, analyser, crystal, downstream of the object acts as an angular filter that accepts only a narrow range of incident directions. The angular acceptance of the crystals is described by their reflection curve. If the second crystal is rocked through a specific reflection, the intensity profile as a function of the angular setting $\Delta\theta$ is the well-known rocking curve [Tan76]. This curve corresponds to the convolution of the reflection curves of the two crystals. The angular deviations introduced by the sample change the incidence angle with respect to the analyser. In a geometrical-optical approach the diffracted intensity changes in each point of the image as a function of the local angular deviation $\Delta\alpha$ and the rocking curve. The contrast depends on the exact form of this rocking curve and the angular setting $\Delta\theta$ [För80]. The nomenclature's creativity has to be noted: Schlieren-imaging [Goe79, För80, Clo96], refraction contrast [Som91], phase dispersive imaging [Ing95, Ing96, Bus96], phase contrast imaging [Dav95] and diffraction enhanced imaging [Cha98] are the most common names.

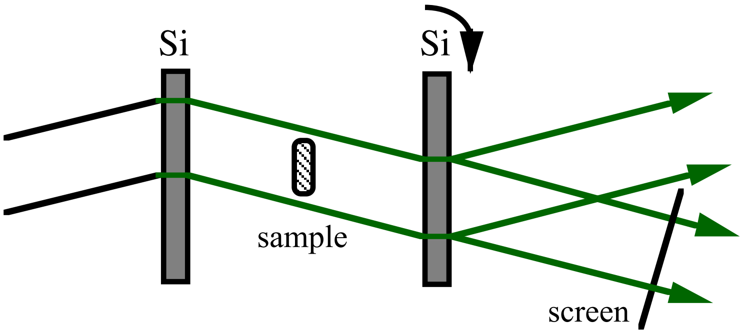

Fig 2.2 Principle of Schlieren imaging using a double crystal diffractometer.

To a certain extent the images can be exploited qualitatively without any processing. Contrast is expected at the edges and boundaries in the sample where phase gradients are present. Symmetrical objects may appear however non-symmetric because the sign of the angular deviation changes for an edge compared to its mirror. Simple combinations of the images, such as the subtraction of two images obtained on either side of the maximum of the rocking curve, solve this problem partially [Cha98]. The sensitivity of the method is different for angular deviations in the plane of diffraction and in the perpendicular plane. This also changes the symmetry of the image compared to the object, hindering easy interpretation of the images. The possibility to visualise phase gradients was shown by many groups, but no reconstructed (differential) phase map was presented and the method was never extended to three-dimensional imaging through tomographic techniques. Some quantitative analysis of the images was reported [För80, Bus96] but the extracted information remains limited. This kind of analysis requires a wave-optical description where the propagation of the waves in the crystals is described by the dynamical X-ray diffraction theory. The intensity distribution can be simulated if the object is known. It is possible to introduce a geometrical model for the object and to determine precisely [För80, Bus96, Dav95] unknown parameters such as the inner and outer radii of a sphere. The passage through the analyser crystal is equivalent to the application of a filter on the wave exiting the sample and the detector records the squared modulus of this filtered wave. The inverse problem, i.e. determining the wave exiting the sample from the intensity distribution, seems not feasible in general. By recording images for different values of the angular setting $\Delta\theta$ it must be possible to determine the modulus of the spectrum of the object function, i.e. the information remains partial in the best case.

Compared to the interferometric technique, the experimental set-up is simplified and the stability requirements are less stringent. To obtain a good sensitivity to phase gradients however the width of the rocking curve should be small, typically 2-10 µrad, and the angular stability should be about 0.2 µrad [Ing96]. As the alignment is less critical, the collimator and analyser crystal do not need to be monolithical and the space available for the sample and its environment increases. The samples are in general not immersed in a liquid, although this would be useful to eliminate angular deviations corresponding to the overall form of the sample.

The resolution is again affected by the passage of the wave through the analyser crystal. In the geometrical-optical approximation, every point of the image is determined by the angular deviation in the corresponding point of the projected object if the free space propagation is neglected. In reality each point at the entrance of the analyser crystal affects a range of points at the exit, and the relation is described by influence functions [För80, Aut78, Pin84]. If the dynamical diffraction fringes are not disentangled, the resolution is limited to the width of the influence function, whose value, of the order of 10 µm, depends on the reflection geometry and the energy used. Evaluation of the interference fringes allows to improve the resolution below this value [För80]. The resolution is limited by the detector as usual but it is possible to introduce a magnification in the direction corresponding to the plane of diffraction by using an asymmetric reflection. These astigmatic images are mainly useful for one-dimensional objects. The sample detector distance limits again the resolution through Fresnel diffraction and geometrical blurring. This method is less adapted than the previous one to cover the low spatial frequency range and very smooth variations of the phase may introduce a phase gradient that is too small to be detected. The presence of objects smaller than the resolution can be detected, mainly by the small angle scattering they produce. This scattering is rejected by the analyser crystal, and regions with small angle scatterers will give a lower intensity when the analyser is set at the maximum of the rocking curve [Cha98].

The beam incident on the sample must be quasi-monochromatic and its divergence in the diffraction plane be smaller than the angular deviations to be detected. Normally the incident divergence is smaller than the width of the reflection curve of the analyser crystal and can be as small as 0.5 µrad. This collimation is however performed by the first crystal and a well-chosen (asymmetric) reflection. The set-up creates the necessary coherence itself and the beam incident on the collimator can be either collimated and polychromatic or monochromatic and non-collimated. This imaging scheme can be used in combination with a classical laboratory X-ray source and most of the published results were obtained under these conditions, resulting in long exposure times of 15-30 minutes [Ing96]. The advantage of using synchrotron radiation resides again essentially in the much bigger available intensities. The photon flux delivered by the X-ray source is not effectively used in this configuration. The collimator and the analyser crystal select a narrow spectral and/or angular range within the total flux. This limits the number of photons contributing to the image, especially when the image is recorded at the tail of the rocking curve and the necessary exposure time (and suffered dose) may increase by a factor of 100.

This technique corresponds to Schlieren imaging in classical optics [Hec98]. Neutron radiography can be enhanced with the same experimental set-up as the one for X-rays, as shown by Podurets *et al* [Pod89]. It was noticed by Goetz and Zaumseil that image contrast could be recorded with the sample put in the highly collimated beam delivered by the crystals and the detector positioned at a certain distance downstream of the object without analyser crystal inbetween them [Goe79].

2.1.3 The propagation technique

The spatial redistribution of the photons due to deflections or more generally Fresnel diffraction is considered as a parasitic phenomenon in absorption contact and projection radiography and in interferometric and Schlieren phase imaging. It is however also a unique contrast mechanism for phase sensitive imaging with advantages concerning the simplicity of the set-up and the achievable resolution. In this case there is no distinct reference beam as in the interferometric technique, and the beam transmitted through the object plays this role itself. The occurrence of contrast can be understood as due to interference between parts of the wavefront that have suffered slightly different angular deviations associated to different phase gradients. The overlap between parts of the wavefront is only possible after propagation over a certain distance. As in previous case, this is a differential phase imaging technique. A homogeneous phase gradient can not be detected because it corresponds to an overal deflection of the beam; detectable contrast requires the second derivative of the phase to be different from zero. When the direction of the X-ray beam is tangential to the edge of structures in the sample, such a perturbation of the wavefront is expected and contrast will appear. Possible internal structures are holes and cracks, inclusions, reinforcing particles and fibers in a composite material. Experimentally the sample is set in a (partially) coherent beam and the transmitted beam is recorded at a given distance d with respect to the sample [Sni95, Clo96]. The experimental set-up shown in Fig 2.3 is thus essentially the same as for absorption radiography except for the increased sample to detector distance. The crystal system upstream of the sample selects a narrow spectral range, delivering a quasi-monochromatic beam to the sample and should not affect the collimation of the beam. The image is recorded with a two-dimensional detector.

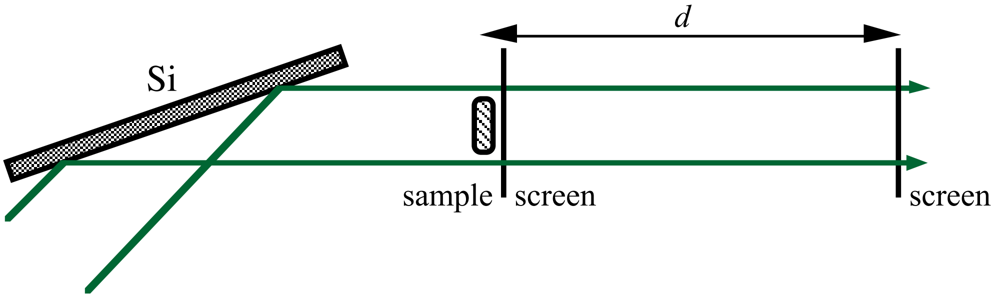

Fig 2.3 Experimental set-up for phase sensitive imaging using the propagation technique.

Fig 2.4 shows examples of Fresnel diffraction patterns obtained at several distances from a 850 µm diameter polymer sphere with two layers [Bar97]. The internal 30 µm thick layer consists of polystyrene, whereas the outer 15 µm thick layer consists of parylene. The contrast changes tremendously with the propagation distance. The absorption in the sample being very small compared to the dynamic range of the film used as detector, no contrast is visible on the absorption radiograph ($d \approx 0$). In the first enlargement (Fig 2.4d) recorded at a distance of 0.15 m, all the boundaries of the object are strongly enhanced and a distinct interference pattern corresponds to every edge, consisting mainly of a white/black fringe. This pattern is obtained in the *edge-detection regime*. The different boundaries (air-polymer or polymer-polymer) can easily be detected and the dimensions of the layers give valuable geometrical information on the sample. The inner polystyrene layer has many spherical inclusions corresponding to voids. The second enlargement (Fig 2.4e) obtained at a distance of 3.1 m resolves very well many interference fringes. It is no longer possible to attribute the fringes to a specific edge of the sample. The deformed image obtained in the *holographic regime* gives little direct information on the object. Such images need image processing based on the physics underlying the image formation process to make them exploitable. Combining images recorded at different distances with a suitable algorithm can give access to the phase.

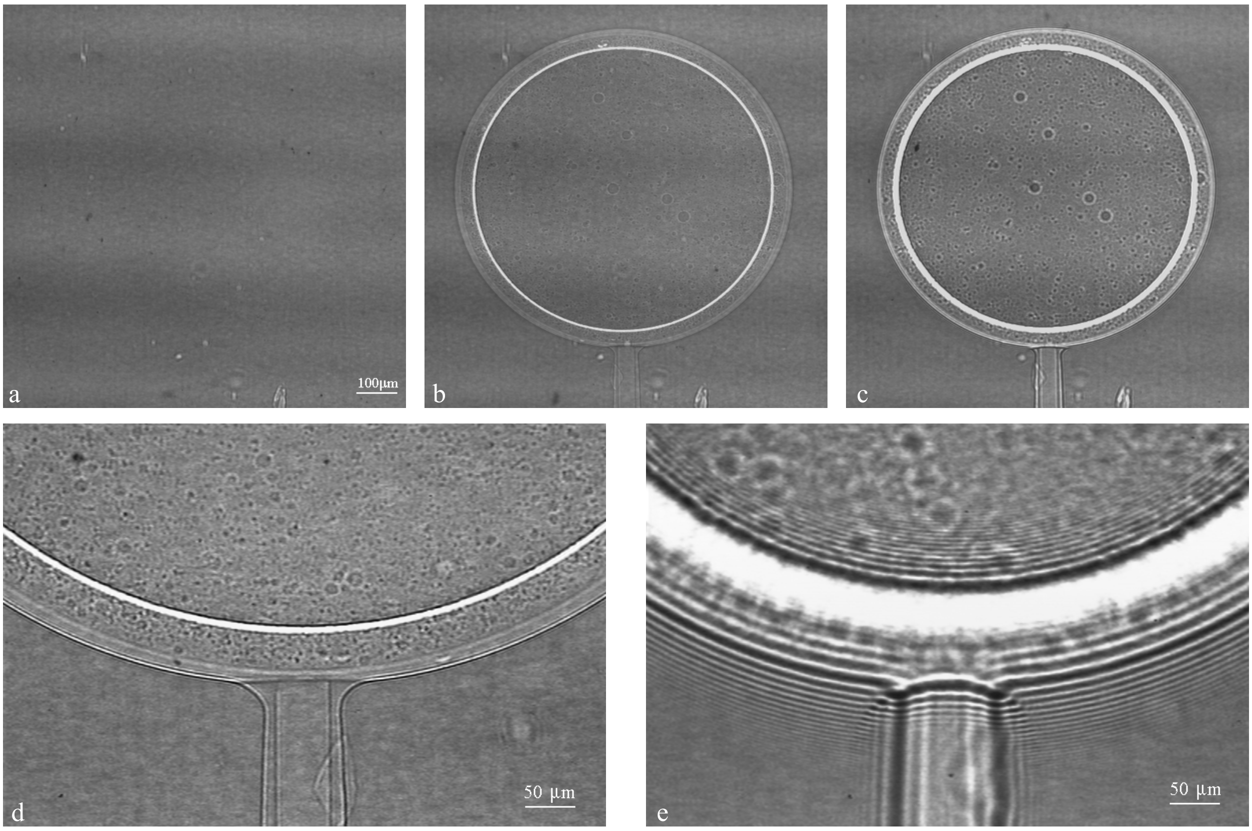

Fig 2.4 Phase sensitive radiographs of a 'double' 850 μm diameter sphere consisting of two plastic materials: a 30 μm thick polystyrene inner layer covered by a 15 μm thick parylene one, with the film at various distances *d* from the specimen. X-ray wavelength 0.7 Å, exposure time on film 30 s. a) $d = 0.003$ m ; b) $d = 0.19$ m; c) $d = 0.83$ m; with larger magnification: d) $d = 0.15$ m; e) $d = 3.08$ m.

This example shows that the information that can be extracted from the Fresnel diffraction patterns depends on the experimental conditions, edge-detection versus holographic regime. The complete quantitative information consisting in the amplitude and the phase of the wave exiting the sample can be reconstructed in many cases from a set of Fresnel diffraction patterns recorded at different distances *d*. The inverse problem, reconstructing the phase modulation from the recorded intensity distributions, will be discussed in § 4.3. Varying the distance is important to avoid undeterminations in the phase retrieval problem: at a given distance the image is 'blind' for certain frequency components of the object. Practically, it is a necessity to combine a set of images corresponding to a variable parameter in every coherent imaging technique that aims at retrieving the phase in a reliable way with sufficient reduction of the coherent noise. Here it is done by scanning the recording distance of the Fresnel diffraction pattern, whereas it is done by varying the external phase shift in the fringe scanning method for interferometric imaging. In general this holographic reconstruction is less straightforward for in-line holography than in the interferometric technique. For certain types of objects good results can however be obtained through simple filtering and summation of the images (see § 4.3). In many cases the characteristics of the object of main interest are the boundaries and the propagation technique gives directly access to them. The image formation process itself is isotropic, and horizontal and vertical edges give identical contrast under coherent illumination, avoiding the symmetry problems mentioned for Schlieren imaging.

The most striking advantage of this method is the extreme simplicity of the set-up. It is essentially the same as for absorption radiography. The transition between absorption and phase radiography or between the different regimes of phase imaging is simply obtained by changing the sample detector distance. The stability requirements on the (few) elements downstream of the monochromator, i.e. the sample and the detector, are easily met. The monochromator can be well upstream of the sample and the sample detector distance can often be chosen quite large. The free space around the sample can be used for all kinds of sample environments such as a furnace, a cryostat, a tensile device or coils to apply a magnetic field. This technique is thus well adapted for in-situ and real-time observations. The set-up can easily be combined with tomography. Reconstruction of the boundaries inside the volume is feasible with a simple algorithm. The complete reconstruction of the three-dimensional distribution of the refractive index decrement is more delicate and must be performed in two steps. In a first step, the phase modulation is reconstructed for every projection from a set of in-line holograms in a holographic reconstruction with numerical implementation. In a second step the projection or Radon transform is inversed using a classical tomographic reconstruction method, such as the filtered backprojection method. Experimentally, it is not necessary to surround the sample with an immersion liquid. This may however be useful to avoid the strong contrast from the phase jumps corresponding to the outer edges of the sample.

The example of Fig 2.4 shows that the images obtained at short distances (figs. b, c and d) are essentially sensitive to the edges and thus the high frequency components of the phase modulation. More generally it can be shown (see § 2.2.3) that for a given propagation distance the image is most sensitive to a specific frequency range. The optimum distance to be sensitive to phase features with spatial frequency *f* is such that

$$D \approx 1/2\lambda f^2 \tag{2.2}$$

where the defocusing distance *D* is determined by

$$D = \frac{d.l}{d+l} \tag{2.3}$$

In the case of a distant source, the source sample distance *l* is large compared to the sample detector distance *d*, hence *D* is approximatively equal to *d*. The X-ray wavelength λ is very small, typically 1 Å, and the features of interest are huge compared to this wavelength, typically 1 µm - 50 µm. This explains why the optimum distance is macroscopic and falls in a range that is experimentally well accessible. The optimum distance is 5.10^{-3} m and 12.5 m for a size of respectively 1 and 50 µm. This frequency selectivity will intrinsically limit the accessibility to the low frequency range, i.e. the smooth variations in the object's phase. The optimum distance, increasing as the square of the object size, will not be reached for these frequencies due to physical limitations (size of the experimental hutch) or the coherence conditions. This frequency selectivity does not exist in absorption imaging and is less pronounced in interferometric phase imaging. The low spatial frequencies are thus imaged with less contrast and it is more difficult to retrieve them. On the contrary the high frequencies contribute strongly to the image and the highest accessible frequency and the resolution are not limited by the method itself, but by the resolution of the detector. The image is not spoiled by the passage of the modulated wave through a crystal as is the case in the interferometric and Schlieren techniques. The resolution in the propagation technique depends on the image processing after recording. For untreated images recorded in the edge-detection regime the resolution is limited by the fringe spacing to about $\sqrt{\lambda D}$. This quantity corresponds to the radius of the first Fresnel zone [Bor80]. When the fringes are disentangled in a holographic reconstruction, the information limit towards the high frequencies is determined essentially by the detector resolution. For an ideal detector, the resolution would still be limited by the thickness of the sample t_s. The propagation inside the specimen over its thickness introduces a blurring equal to $\sqrt{\lambda t_s}$. This limit is 0.3 µm in the case of a 1 mm thick sample and a wavelength $\lambda = 1$Å. The smallest object detectable can be smaller than the resolution or pixel size. This can be understood from the fact that the diffraction fringes are sometimes large compared to the lateral extent of the object. This is an interesting feature to visalize and position isolated small objects with a large field of view. The observation of the interference fringes requires on the opposite sufficient resolution from the detector. For the typical distances in the meter-range this minimum resolution is about 20 µm if the imaging is performed with a quasi-planar wave and thus without X-ray magnification. This may be an important limitation for using this method in medical *in vivo* applications. In such clinical applications the resolution is normally worse than 40 µm in order to reduce the dose and such resolution is often insufficient to resolve the interference fringes. On the other hand, this phase technique may be very adapted for imaging in medical *in vitro* applications and materials science applications where thick (several mm) samples are to be investigated with ‘high’ resolution (µm-range).

The stringent requirements on the beam incident on the sample explain why this technique emerged only recently [Har94, Sni95, Clo96, Nug96] with the appearance of partially coherent X-ray beams delivered by third generation synchrotrons. For observation of the interference patterns the wave incident on the sample must fulfil monochromaticity and source size conditions. The angular source size plays the most important role. Incident beams with different directions that are mutually incoherent will form images translated by an amount proportional to the object detector distance and the angle between the beams. The blurring is described as a convolution of the image for a point source with the projection of the angular source size s_α from the object to the detector. The geometrical resolution in the Fresnel diffraction pattern is then equal to $D\, s_\alpha$. and the condition for observation of the frequency f is

$$D.s_\alpha < 1/f \tag{2.4}$$

Alternatively, the interference pattern involves the coherent superposition of laterally separated portions of the incident beam. The interfering waves must originate from points that are mutually coherent, and thus laterally separated by a distance smaller than the transverse coherence length l_t that can be defined as (see expression (2.84))

$$l_t \approx \lambda/2s_\alpha \tag{2.5}$$

Choosing the distance D equal to the optimum one from expression (2.2) and eliminating D from expression (2.4) yields

$$s_\alpha < 2\lambda f \tag{2.6}$$

as the condition on the angular source size to observe the spatial frequency f under optimum conditions.

This indicates that the finite angular source size will set a lower limit to the spatial frequency that can be imaged optimally. Eliminating the frequency f on the other hand, gives

$$l_t > \frac{\sqrt{\lambda D}}{2\sqrt{2}} \tag{2.7}$$

indicating that the incident beam must be coherent over the first Fresnel zone, the zone around a point of the object essentially contributing to the corresponding point of the image.

The angular source size s_α is determined both by the lateral source size s and the source sample distance l as $s_\alpha = s/l$. Due to the small source sizes and large distances between the source and the sample encountered at third generation synchrotrons, the complete angular extent of the beam can be used and the available flux is used efficiently. The beam is sufficiently coherent as it is. The blurring implies that this kind of phase imaging is difficult with classical X-ray sources or synchrotron sources of an older type. Some angular selection is necessary in these cases by limiting the visible source with a slit or by angular filtering with a crystal collimator, at the cost of incident flux [Nug96, Wil96].

The conditions on the monochromaticity are less stringent. The beam is usually monochromatised using a monochromator based on perfect silicon crystals. The energy spread $\Delta E/E \approx 10^{-4}$ is thus very small. Within this range all physical phenomena, such as the behaviour of the source, the object if it is not Bragg diffracting, the propagation and the detector, remain essentially unchanged and the beam can be considered as monochromatic. This simplifies the description of the image formation process and also the reconstruction of the in-line holograms. The wavelength spread limits the longitudinal coherence length $l_l = \lambda^2/\Delta\lambda$ to typically 1 µm. The thickness of the samples that can be investigated is however *not* limited to this value [Clo96]. The phase modulation φ is not affected considerably as long as

$$t_s.<\delta> << l_l \qquad (2.8)$$

with $<\delta>$ the mean refractive index decrement. The sample thickness t_s can thus be 10^5 as large as the longitudinal coherence length. The phase φ is approximately proportional to the wavelength λ, and a relative error on the wavelength results in the equal relative error on the phase. The propagation is not altered as long as $\Delta\lambda.D_{max}.f_{max}^2 << 1$. For typical conditions ($D_{max} = 1$ m, $\lambda = 1$ Å, $f_{max} = 1\ \mu m^{-1}$), the relative energy spread should be a fraction of 1 %. An increase in energy spread by one or even two orders of magnitude can still correspond to quasi-monochromatic conditions. This may be a way to increase considerably the flux, especially for qualitative imaging. A spectral filter with a wider pass-band than silicon monochromators and that conserves the homogeneity and coherence of the beam is however not readily available for hard X-rays. Multi-layer monochromators can be a solution in the future. Using the same propagation principle but working with the polychromatic radiation delivered by a laboratory X-ray microsource to retain some flux, deflection sensitive images were obtained [Wil96, Pog97]. This seems promising for work in the edge detection regime as the main contrast, a white and black fringe, is unchanged over a large spectral range. The contrast is however spoiled compared to monochromatic conditions as is the case in absorption imaging. In absorption imaging the use of mono-energetic radiation simplifies and improves quantitative and tomographic imaging as it makes the problem linear. Quantitative analysis of the Fresnel diffraction patterns under polychromatic conditions seems tedious. The observed pattern results from the incoherent superposition of the images at different wavelengths. In order to obtain some information on the object, the behaviour of the source, the detector and the object itself as a function of the energy of the radiation has to be known.

2.2 Image formation

The direct problem consists in determining the defocused image of a known object under known experimental conditions, such as the wavelength λ, the sample detector distance, the detector response ... It will be considered here. Although the wavelengths used are unusually small ($\lambda < 2$ Å), X-rays belong to the electromagnetic spectrum and their behaviour must be described in a wave optical approach by the formalism of Maxwell's equations or an adapted approximate description. Such a description was not familiar in the field of hard X-rays before the appearence of coherent X-ray beams, except for the propagation of X-rays in crystals.

The actual X-ray sources can rather well be described as incoherent, extended sources with a certain spatial distribution and a specific energy spectrum. The monochromator selects a narrow spectral range from this spectrum and makes the beam quasi-monochromatic ($\Delta E/E \approx 10^{-4}$). The propagation of the beam makes it partially coherent and the beam incident on the sample can be described by the complex degree of coherence $\gamma(\boldsymbol{x}_1,\boldsymbol{x}_2)$. The interaction of the X-ray beam with the sample is very complex but can be formalised by a transmission function $T(\boldsymbol{x})$. It is the complex ratio of the wave exiting and entering the sample and is determined by the projection of the complex refractive index distribution within the object. The propagation of the transmitted wave in free space over a distance d is well described in the Fresnel approximation by the convolution of the transmitted wave with a known propagator $P_d(\boldsymbol{x})$. A plane wave decomposition allows to describe the propagation also as a simple phase change of the plane wave components of the transmitted beam. The intensity distribution, the squared modulus of the wave, depends in an essentially non-linear way on the object characteristics. The recorded intensity distribution is blurred due to the response of the X-ray detector. This linear process corresponds to filtering the images with the mutual transfer function of the detector. To a good approximation the finite extent of the source and the resulting partial coherence can similarly be described as filtering the images with the degree of coherence.

The z-axis is chosen along the average propagation direction of the X-rays, the x-y planes are thus parallel to the detector that is set perpendicular to the z-axis. The x and y axis are chosen respectively horizontally and vertically. In the following we use a scalar wave description and consider a monochromatic component of this wave. It is thus convenient to use a complex representation of the wave. The time dependency of all waves being identical [$\exp(-\mathrm{i}\omega t)$] it is sufficient to consider the spatially variant part, i.e. the complex amplitude [Bor80].

2.2.1 The incident beam

Because of its small size and huge distance with respect to the sample, a third generation synchrotron X-ray source tends to behave as an ideal point source. The incident beam is an incoherent superposition of waves emitted by the electrons in the storage ring. The individual waves are spatially coherent. The electrons can not be forced to follow identical trajectories and this results in a certain lateral and angular extension of the electron beam. The effect of the resulting partial coherence of the incident beam on the Fresnel diffraction pattern will be discussed in § 2.2.4 and we will first consider the case of a completely coherent incident beam such as the one emitted by an individual electron. The light is emitted in a highly anisotropic way, i.e. merely in a cone with an opening of the order of 0.1 mrad for a 6 GeV electron energy synchrotron. This is however sufficient to illuminate the field of view homogeneously and a spherical wave approximation is well adapted. A monochromatic component of the incident wave u_{inc} in the plane $z = l$ just in front of the sample can thus be written:

$$\begin{aligned} u_{\mathrm{inc}}(x,y) &= c\, e^{\mathrm{i}kr}/r \\ &= c\, e^{\mathrm{i}\frac{\pi}{\lambda l}(x^2+y^2)} \end{aligned} \qquad (2.9)$$

The second expression corresponds to the Fresnel approximation and a parabolic incident wave. It is possible to consider the directionality of the coherent wave by the use of a gaussian wave description (far from the source, $\sqrt{\lambda l}$ >> waist w_{o}) :

$$u_{\mathrm{inc}}(x,y) \quad = c\ \exp\left[-\frac{x^2+y^2}{2w^2(l)}+\mathrm{i}\frac{\pi}{\lambda l}(x^2+y^2)\right] \tag{2.10}$$

The phase dependency is thus also parabolic, but the amplitude is no longer homogeneous but it has a gaussian distribution with a width w, given by

$$w(l)=\frac{\lambda}{2\pi w_{\mathrm{o}}}l \tag{2.11}$$

where w_{o}, the waist of the gaussian beam [Yar91], corresponds to its width at the level of the source. $\lambda/(2\pi w_{\mathrm{o}})$ is the sigma value of the angular distribution of the wave.

2.2.2 The object

Absence of Bragg diffraction

The interaction of the wave with matter may affect its amplitude and phase. The forward diffraction can formally be described by the complex refractive index n of the medium, usually written for X-rays as

$$n = 1 - \delta + \mathrm{i}\beta \tag{2.12}$$

This refractive index is defined so that the wavenumber k=2π/λ in vacuum and the wavenumber in the material k' are related by $k' = n\,k$. Hence a plane wave is of the form $e^{\mathrm{i}nkz} = e^{\mathrm{i}(1-\delta)kz}.e^{-\beta kz}$. The refractive index decrement δ results in a phase shift, and the absorption index β is linked to the linear absorption coeffiecient μ as

$$\mu = \frac{4\pi}{\lambda}\beta \tag{2.13}$$

The main contributions to the attenuation of the beam for the energy-range of interest (8 keV - 100 keV) are the photo-electric effect, and Rayleigh and Compton (coherent and incoherent) scattering. The cross section for photo-electric excitation varies abruptly near the characteristic edges of an element and this is often used in absorption imaging to image a specific element in the sample. The subtraction of two images taken on either side of the absorption edge results in a map of this specific element.

The polarisation of matter under the effect of an electric field is rather well described, for hard X-rays and far from the absorption edges, by the free electron model (Thomson scattering). The linear susceptibility χ, averaged over a representative volume, is thus proportional to the electron density in the material and it is very small (typically 10^{-6}). This results in a real part of the refractive index slightly smaller than 1, and the refractive index decrement ($n = (1+\chi)^{1/2}$) can be expressed as

$$\delta = \frac{r_c\lambda^2}{2\pi V}\sum(Z_j + f_j') \tag{2.14}$$

where $r_c = 2.8$ fm is the classical electron radius, the summation is over all the atoms contained in the representative volume V, Z_j is their number of electrons, f_j' is the real part of the wavelength-dependent dispersion correction [Par54].

Expression (2.14) can be rewritten in terms of the number N_j of atoms of a specific species:

$$\delta = \frac{r_c N_A}{2\pi} \lambda^2 \rho \frac{\sum N_j (Z_j + f_j')}{\sum N_j A_j} \tag{2.15}$$

ρ is the mass density of the material, N_A is Avogadro's number and A_j is the atomic weight. The summations are over the different atomic species in the material. If the composition of the material is known in terms of mass fractions q_j, the following equivalent expressions can be used

$$\delta = \frac{r_c N_A}{2\pi} \lambda^2 \rho \, \Sigma \, q_j \, (Z_j + f_j') \, / \, A_j \tag{2.16}$$

$$\delta / \rho = \Sigma \, q_j \, \delta_j / \rho_j \tag{2.17}$$

δ_j and ρ_j are respectively the refractive index decrement and mass density of the pure species.

In the case of a crystalline medium, the scattering properties are usually described by the structure factors (see expression 2.28). If no Bragg reflection is excited, propagation in the crystal is not affected by its crystalline structure and only the average scattering properties are relevant. The refractive index can be expressed in terms of the (complex) structure factor F_0 as

$$n = 1 - \frac{r_c \lambda^2}{2\pi} \frac{F_0}{V_c} \tag{2.18}$$

with V_c the volume of the unit cell in this case.

δ is always positive for the X-ray energy range of interest as Thomson scattering of 'free' electrons is the dominant process. The real part of the refractive index is thus always slightly smaller than 1. If one neglects the dispersion correction f', the index decrement δ has a very simple wavelength dependence, it is proportional to λ^2. The ratios Z_j/A_j appearing in expression (2.16) are similar for many atomic species ($\approx 1/2$), and δ is thus to a good approximation determined by the mass density ρ of the material [Gui94]

$$\delta \approx 1.3 \; 10^{-6} \, \rho \, \lambda^2 \qquad \rho \text{ in g/cm}^3, \lambda \text{ in Å} \tag{2.19}$$

The wavelength dependent dispersion correction f' accounts for the fact that the electrons are not free in the atom. It is linked to the absorption coefficient and thus the complex part f'' of the atomic scattering factor ($f_{at} = Z + f' + \mathrm{i} f''$ for forward scattering) by the Kramers-Kronig dispersion relation. The size of f' is in general small compared to Z except near the absorption edges. At an energy corresponding to such an edge, f' is negative and reaches a minimum. At its K-edge, the value of f' is about -8 for a niobium atom compared to its atomic number $Z = 41$.

This effect yields negative values of δ near the absorption edges for Be and C in the soft X-ray range [Spi94]. The global forward scattering is here considered as the simple sum of what is scattered by the individual atoms. This assumption is no longer valid near the absorption edges where the photoelectron emitted by an atom will interfere with the neighboring atoms (EXAFS [Sch87]). In this case f'' and f' depend on the local atomic order.

For numerical calculations of the absorption coefficients, use was made of the software program 'Xray' running under the 'Wingz' spreadsheet [Aks92]. The 'photon' method used, is based on analytical approximations for X-ray cross-sections [Big71]. The calculation of the refractive index decrement is based on expression (2.15) when f' can be neglected. The dispersion correction can be obtained with calculations based on the work of Cromer [Cro70] or Henke [Hen93] implemented in the program 'Fhkl' [Soy95].

Because the interaction of X-rays with matter is weak ($|1-n| \approx 10^{-6}$) and the lateral resolution is relatively poor, the propagation inside the sample can be assumed as being straight. It is thus possible to project the object onto a single plane perpendicular to the propagation direction and to introduce formally the transmission function of the object $T(x,y)$ [Bor80] such that

$$u_o(x,y) = T(x,y)\, u_{\text{inc}}(x,y) \tag{2.20}$$

with $u_o(x,y)$ the field just downstream of the object. The transmission function depends on the projection of the refractive index distribution through

$$T(x,y) = A(x,y)\, \mathrm{e}^{\mathrm{i}\varphi(x,y)} \tag{2.21}$$

with the amplitude

$$A(x,y) = e^{-B(x,y)} \qquad \text{and} \qquad B(x,y) = \frac{2\pi}{\lambda}\int \beta(x,y,z)\mathrm{d}z \tag{2.22}$$

and the phase modulation

$$\varphi(x,y) = \frac{2\pi}{\lambda}\int [1-\delta(x,y,z)]\mathrm{d}z = \varphi_o - \frac{2\pi}{\lambda}\int \delta(x,y,z)\mathrm{d}z \tag{2.23}$$

φ_o is the phase modulation that would occur in the absence of the object and it is a non-relevant constant for a differential phase method. The integrations are understood to be along the propagation direction z over the maximum thickness t_s of the object. The following inequalities hold for hard X-rays in simple transmission

$$B(x,y) \geq 0 \qquad \text{(no X-ray sources in the sample)} \tag{2.24}$$

$$\varphi(x,y) - \varphi_o \leq 0 \qquad \text{(Thomson scattering)} \tag{2.25}$$

These are important constraints that facilitate the retrieval of the amplitude and phase (see § 4.3)

The projection of the object onto a single plane is only a valid assumption up to a certain thickness of the sample. The following handwaving argument can be given. The maximum angular deviation occurs in the case of total external reflection and is about $\sqrt{2\delta}$. For the propagation in the sample to appear as straight, the lateral displacement should be small compared to the spatial resolution r, hence

$$\sqrt{2\delta}.t_s < r \tag{2.26}$$

This yields a thickness $t < 0.7$ mm, for $\delta = 10^{-6}$ and $r = 1$ µm. Equation (2.26) is very conservative as the angular deviation at a boundary under non grazing conditions is rather of the order of δ, hence the thickness t_s can be as large as 1 m for these conditions. Straight propagation in the sample implies also that Fresnel diffraction in the sample itself is negligible. The radius of the first Fresnel zone corresponding to propagation in the object has to be small compared to the resolution:

$$\sqrt{\lambda t_s} < r \tag{2.27}$$

This is the usual limitation on the resolution due to Fresnel diffraction [Mou97] and it limits the thickness to 10 mm at an X-ray wavelength of 1 Å and resolution of 1 µm. Samples that are thicker could still be treated with a technique similar to multi-slicing in electron microscopy [Cow57]. The sample is divided in slices that are sufficiently thin to project them onto a single plane and to describe them by a transmission function. The wave at the exit of the sample is obtained by multiplication with the successive transmission functions and propagation between the slices. In this case equation (2.20) is only valid for the slices and not for the complete object.

In the presence of Bragg diffraction

Scattering from a structure with long range order in its atomic positions can result in a strong enhancement of the scattered wave when the contributions of the ordered atoms interfere constructively. This imposes a precise condition on the scattering vector $\boldsymbol{h}$. Strong diffracted waves, i.e. comparable to the incident wave, are expected when the (3D) Fourier component of the electron density is strong for the vector $\boldsymbol{h}$. In the case of a crystal, this occurs when $\boldsymbol{h}$ is close to a node of the reciprocal lattice [Gui94]. The two beam case, where the incident wave and a single diffracted wave propagate simultaneously in the crystal, is by far the most usual one for X-ray Bragg diffraction. The wave diffracted by a unit cell of the crystal is proportional to the structure factor $F_{\boldsymbol{h}}$ defined as [Cop93]

$$F_{\boldsymbol{h}} = \sum f_{\mathrm{at},j}(\boldsymbol{h}).T_{\mathrm{t},j}(\boldsymbol{h}).e^{-2\pi i \boldsymbol{h}.\boldsymbol{r}_j} \tag{2.28}$$

The summation is over all the atoms in the unit cell, located at their average position $\boldsymbol{r}_j$. The atomic temperature factor $T_{\mathrm{t},j}$ accounts for the thermal vibrations of the atoms around their mean position. The phase term in expression (2.28) depends on the position of the atoms in matter. This term vanishes in the case of simple forward scattering ($\boldsymbol{h} = 0$) where only the average electron distribution counts.

Variations of the scattering properties inside a crystal, due to crystalline defects or structural phases in the sample, alter the propagation of the waves inside the crystal compared to the case of a perfect crystal. This is extensively used to image crystals of nearly perfect quality in X-ray topography, i.e. X-ray Bragg diffraction imaging [Tan76]. Usually only the intensity modulation of the waves exiting the sample is considered. Complementary information can be obtained by recording the topographs at a finite distance with respect to the crystal. In incoherent cases this yields information on the angular deviations due to curvatures of the diffracting planes [Zon98, Mat98]. If the beams exiting the crystal are still sufficiently coherent, the phase modulation of the diffracted wave can be imaged in a way identical to the case of simple transmission (see § 5.4).

The energy pendulates between the direct beam and the diffracted beam because of the presence of multiple scattering in the sample. The determination of the outgoing waves is far more complicated and it is not possible in general to express them as a function of the atomic structure in a simple way, as it is done in the case of transmission in expressions (2.22) and (2.23). An adequate but rather unphysical description of the propagation in a distorted crystal is given by the Takagi-Taupin equations, an adapted approximation of the Maxwell equations. For a known strain field and occupation of the atomic sites, the field inside the crystal can be numerically calculated in both amplitude and phase. This allows to simulate the contrast expected from a dislocation, stacking fault, domain boundary, ... when the strain field is known at the atomic level. It is however not feasible to determine an unknown atomic structure from the knowledge of the outgoing waves. The existing simulation programs [Gro80, Epe85] do calculate the phase of the wave and the phase is thus available (although previously unused) to determine the image contrast after free space propagation. There is no point to point relationship between the incoming and outgoing wave such as expression (2.20). The spread inside the crystal is determined by the Borrmann fan. The variation of Bragg diffraction phenomena as a function of the wavelength is very fast compared to the case of normal forward scattering. An energy variation $\Delta E/E = 10^{-5}$ - 10^{-6} can alter the wavefields significantly. If the spectral range of the diffracted wave is too large, the intensity must be calculated as a function of the wavelength and integrated over the relevant wavelength range.

2.2.3 Free space propagation

The recorded intensity is ideally the squared modulus of the wave at the level of the detector

$$I_\mathrm{d}(x,y) = |\, u_\mathrm{d}(x,y)\, |^2 \tag{2.29}$$

In the previous equation of the time-averaged intensity, we 'forgot' consciously all proportionality factors such as a factor 1/2 due to the complex representation of the wave. The amplitude information of the wave is in principle readily available in every plane and the phase information is completely lost. In particular at the exit of the sample ($z = l$), one obtains

$$I_o(x,y) = A^2(x,y).|\,u_{\text{inc}}(x,y)\,|^2 = A^2(x,y).I_{\text{inc}}(x,y) \tag{2.30}$$

The amplitude of the transmission function and consequently the projection of the absorption coefficient can be obtained if the incident intensity $I_{\text{inc}}(x,y)$ is independently measured. The phase modulation turns into an amplitude information through propagation. The effect on a quasi-monochromatic wave of free space propagation over a distance d is considered here.

Real space approach

In this approach the propagating wave is decomposed into point sources and the linearity of the propagation equations can be invoked to treat each point source individually. The Fresnel-Kirchhoff diffraction formula [Bor80] is the resulting superposition integral that links u_o and u_d

$$u_d(x,y) = \frac{1}{\mathrm{i}\lambda}\iint u_o(x_o,y_o)\frac{e^{\mathrm{i}kr_{od}}}{r_{od}}\cos(\boldsymbol{n},\boldsymbol{r}_{od})\mathrm{d}x_o\mathrm{d}y_o \tag{2.31}$$

The integration is over the object plane $z = l$ and the cosine term is the obliquity factor. For the cases of interest the Fresnel approximation of the previous formula is well adapted. The obliquity factor equals 1 as the diffraction angles are smaller than 1 mrad. The distance r_{od} equal to

$$r_{od} = [d^2 + (x-x_o)^2 + (y-y_o)^2]^{1/2} = d\,\{1 + [(x-x_o)/d]^2 + [(y-y_o)/d]^2\}^{1/2} \tag{2.32}$$

can be approximated in the exponential term of equation (2.31) as

$$r_{od} \approx d\,\{1 + 1/2[(x-x_o)/d]^2 + 1/2[(y-y_o)/d]^2\} \tag{2.33}$$

This yields the Fresnel integral

$$u_d(x,y) = e^{ikd}\frac{1}{\mathrm{i}\lambda d}\iint u_o(x_o,y_o)\exp\left\{\mathrm{i}\frac{\pi}{\lambda d}\left[(x-x_o)^2 + (y-y_o)^2\right]\right\}\mathrm{d}x_o\mathrm{d}y_o \tag{2.34}$$

The expansion (2.33) of r_{od} is valid if the distance d satisfies the condition

$$d^3 >> \frac{\pi}{4\lambda}\,[\,(x-x_o)^2 + (y-y_o)^2]^2_{\max} \tag{2.35}$$

The Fresnel approximation seems not very adapted for small distances considering the small wavelength λ of hard X-rays. Equation (2.34) remains however often valid when the condition on d is violated because the primary contribution of the integral will arise only from a zone near the point ($x_o = x$, $y_o = y$) according to the stationary phase principle [Bor80].

Free space propagation over a distance d can thus be described in real space as a convolution of the wave with a propagator P_d, such that

$$u_d\,(x,y) = P_d\,(x,y) * u_o(x,y) \tag{2.36}$$

with (neglecting a non relevant phase factor)

$$P_d(x,y) = \frac{1}{\mathrm{i}\lambda d}\exp\left[\mathrm{i}\frac{\pi}{\lambda d}\left(x^2+y^2\right)\right] \tag{2.37}$$

Fourier space approach

The propagating wave can alternatively be decomposed into plane waves [Goo68]. This is done by taking the two-dimensional Fourier transform of $u_o(x,y)$ with respect to x and y:

$$\tilde{u}_o(f,g) = \int\int_{-\infty}^{\infty} u_o(x,y)\exp[-\mathrm{i}2\pi(fx+gy)]\mathrm{d}x\mathrm{d}y \tag{2.38}$$

with spatial frequencies f and g corresponding to respectively x and y. The inverse Fourier transform allows to write the wave as a superposition of simple complex-exponential functions:

$$u_o(x,y) = \int\int_{-\infty}^{\infty} \tilde{u}_o(f,g)\exp[i2\pi(fx+gy)]\mathrm{d}f\mathrm{d}g \tag{2.39}$$

Each exponential function corresponds to a plane wave with a wavevector $\boldsymbol{k} = (k_x, k_y, k_z)$ and

$$k_x = 2\pi f \qquad k_y = 2\pi g \qquad k_z = \sqrt{k^2 - k_x{}^2 - k_y{}^2} = \frac{2\pi}{\lambda}\sqrt{1-(\lambda f)^2-(\lambda g)^2} \tag{2.40}$$

Propagation to the plane $z = d$, corresponds to a multiplication of a plane wave with the phase factor $\exp(\mathrm{i}k_z d)$, hence

$$u_d(x,y) = \int\int_{-\infty}^{\infty} \tilde{u}_o(f,g)\exp\left[i\frac{2\pi}{\lambda}\sqrt{1-(\lambda f)^2-(\lambda g)^2 d}\right]\exp[i2\pi(fx+gy)]\mathrm{d}f\mathrm{d}g \tag{2.41}$$

In Fourier space, this can be expressed as

$$\tilde{u}_d(f,g) = \tilde{u}_o(f,g).\exp\left[i\frac{2\pi}{\lambda}\sqrt{1-(\lambda f)^2-(\lambda g)^2 d}\right] \tag{2.42}$$

and free space propagation can be described by multiplication with a spatial-frequency dependent phase term. The angle θ_k between the wavevector and the incident beam for a given plane wave component is (equation (2.40))

$$|\sin(\theta_k)| = \lambda(f^2+g^2)^{1/2} \tag{2.43}$$

The length scales of interest in the object are macroscopic compared to the wavelength λ, the angles θ_k are thus small and can be approximated as

$$|\theta_k| = \lambda(f^2+g^2)^{1/2} << 1 \tag{2.44}$$

This last inequality suggests to expand the square root expression in the phase term of equation (2.42) to yield

$$\tilde{u}_d(f,g) = \tilde{u}_o(f,g).\exp(\mathrm{i}\frac{2\pi}{\lambda}d).\exp\left[-\mathrm{i}\pi\lambda d\left(f^2+g^2\right)\right] \tag{2.45}$$

The second order term of the expansion can be neglected as long as

$$d\lambda^3(f^2+g^2)^2_{\max}/8 << 1 \tag{2.46}$$

As an example, if $(f^2+g^2)^{1/2}_{\max} = (0.1\ \mu\mathrm{m})^{-1}$, d should be small compared to 800 m, which is obviously the case.

Free space propagation over a distance d can thus be described as a space invariant linear system [Kai80] for the wave. It corresponds in Fourier space to the multiplication

$$\tilde{u}_d(f,g) = \tilde{P}_d(f,g).\tilde{u}_o(f,g) \tag{2.47}$$

of the wave with the transfer function (neglecting an overall phase term)

$$\tilde{P}_d(f,g) = \exp\left[-\mathrm{i}\pi\lambda d\left(f^2+g^2\right)\right] \tag{2.48}$$

This transfer function is consequently the Fourier transform of the propagator $P_d\,(x,y)$ given by equation (2.37).

The expression (2.29) of the intensity as a function of the wave field is simple in real space. The Fourier transform of the intensity, the intensity spectrum, $\tilde{I}_d(f,g)$ corresponds to an autocorrelation of the wave in reciprocal space

$$\tilde{I}_d(f,g) = \int\int_{-\infty}^{\infty} \tilde{u}_d(p,q).\tilde{u}_d^{\,*}(p-f,q-g)\mathrm{d}p\mathrm{d}q \tag{2.49}$$

This autocorrelation is obviously not calculated explicitly. One calculates the propagation of the wave in reciprocal space where it corresponds to a simple multiplication. This wave is inverse transformed to direct space where the intensity is calculated with equation (2.29).

Mixed approach

In order to simplify the notations, we will assume $\boldsymbol{x} = (x\,,y)$ and $\boldsymbol{f} = (f\,,g)$. As proposed by Papoulis [Pap74] and Guigay [Gui77, Gui78], it is possible to express the intensity spectrum $\tilde{I}_d(\boldsymbol{f})$ as one 2D integral calculated in direct space on the wave $u_o(\boldsymbol{x})$. Taking the Fourier transform of expression (2.29) and replacing the wave $u_d\,(\boldsymbol{x})$ by the Fresnel integral of equation (2.34), yields the intensity spectrum as a sixfold integral. This sextuple integral simplifies to a double integral [Gui77]

$$\tilde{I}_d(\boldsymbol{f}) = \int e^{-\mathrm{i}2\pi\eta f} u_o(\eta - \frac{\lambda d f}{2}).u_o^{\,*}(\eta + \frac{\lambda d f}{2})\mathrm{d}\eta \tag{2.50}$$

or

$$\tilde{I}_d(\boldsymbol{f}) = e^{-\mathrm{i}\pi\lambda d f^2} \int e^{-\mathrm{i}2\pi\eta f} u_o(\eta).u_o^{\,*}(\eta + \lambda d f)\mathrm{d}\eta \tag{2.51}$$

The Fourier component $\boldsymbol{f}$ of the intensity involves the object and the complex conjugate of the object shifted by $\lambda d\boldsymbol{f}$. The exponential factor in the first expression is identical to the one in the definition of the Fourier transform. The expression is however not a Fourier transform because the remaining terms depend on the frequency $\boldsymbol{f}$ through the shifts. Expression (2.51) is similar to the definition of an ambiguity function, a concept familiar in radar theory [Fla93], defined for a function F as

$$A_F(\boldsymbol{f},\boldsymbol{x}) = \int e^{-\mathrm{i}2\pi\eta f} F(\eta).F^*(\eta-\boldsymbol{x})\mathrm{d}\eta \tag{2.52}$$

The first coordinate $\boldsymbol{f}$ corresponds to Fourier space, whereas the second one $\boldsymbol{x}$ corresponds to direct space. Disregarding a phase term in expression (2.51), the intensity spectrum $\tilde{I}_d(\boldsymbol{f})$ is thus equal to the ambiguity function $A_{u_o}(\boldsymbol{f}, -\lambda d\boldsymbol{f})$ of the wave $u_o(\eta)$ evaluated for $(\boldsymbol{f}, \boldsymbol{x} = -\lambda d\boldsymbol{f})$. The expressions (2.50) and (2.51) are useful for theoretical considerations and to find analytical expressions for the intensity spectrum for specific objects [Gui77].

Case of a weak object

The weak phase approximation can easily be derived from expression (2.50), if one considers the case of a phase object $T(\eta) = \exp[i\varphi(\eta)]$ and plane wave illumination of unit amplitude. This yields a linear expression for the intensity spectrum

$$\tilde{I}_d(\boldsymbol{f}) = \delta_D(\boldsymbol{f}) + 2\sin(\pi\lambda d\boldsymbol{f}^2)\tilde{\varphi}(\boldsymbol{f}) \tag{2.53}$$

with the condition [Gui77]

$$|\, \varphi(\eta+\lambda d\boldsymbol{f}) - \varphi(\eta)\,| << 1 \qquad\qquad \forall\ \eta \tag{2.54}$$

The 2D Dirac delta function $\delta_D(\boldsymbol{f})$ corresponds to the unaltered mean intensity. In this case there is a linear relationship between the spectrum of the intensity and the spectrum of the phase. If weak amplitude and phase modulations are present, it stands [Han72 ,Wad74]

$$\tilde{I}_d(\boldsymbol{f}) = \delta_D(\boldsymbol{f}) + 2\sin(\pi\lambda d\boldsymbol{f}^2)\tilde{\varphi}(\boldsymbol{f}) + 2\cos(\pi\lambda d\boldsymbol{f}^2)\tilde{B}(\boldsymbol{f}) \tag{2.55}$$

with as conditions expression (2.54) and $B(\eta) << 1\ \forall\ \eta$. The factors in this expression multiplying the spectrum of the phase modulation $\tilde{\varphi}(\boldsymbol{f})$ and the absorption 'length' $\tilde{B}(\boldsymbol{f})$ are the contrast factors for phase and amplitude modulation respectively. Fig 2.5 shows both contrast factors for a given distance d as a function of the spatial frequency $\boldsymbol{f}$. It can be seen that the two contrast mechanisms are in quadrature. The phase contrast factor can be as large as 2, first reached for the distance $d = 1/(2\lambda\boldsymbol{f}^2)$ (cfr. equation (2.2)). At this distance the Fresnel image is not sensitive to the amplitude modulation. The phase contrast factor is equal to zero at the origin and on circles in Fourier space, such that (p integer)

$$\lambda d\boldsymbol{f}^2 = p \tag{2.56}$$

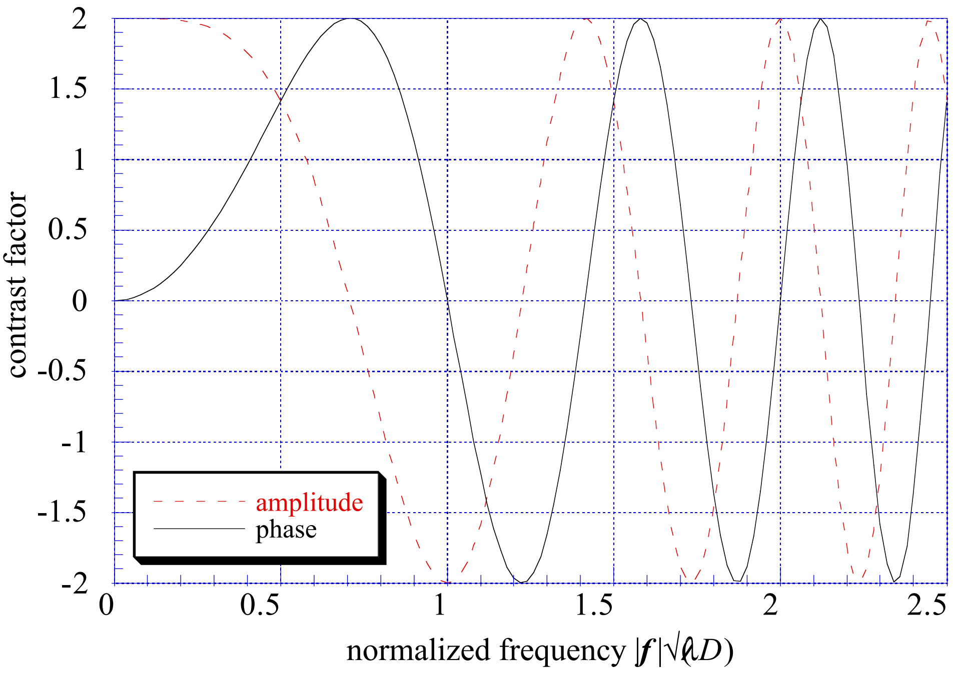

Fig 2.5 Contrast factor for the phase and amplitude modulation as a function of the spatial frequency ***f*** in the case of a weak object (see text). The frequency is normalised by multiplication with the radius of the first Fresnel zone.

Case of a spherical incident wave

If the incident wave has a parabolic phase dependency

$$u_{\mathrm{inc}}(\boldsymbol{x}) = \sqrt{I_{\mathrm{inc}}}\ \exp\left(\mathrm{i}\pi\frac{\boldsymbol{x}^2}{\lambda l}\right) \tag{2.57}$$

(see expressions (2.9)) its effects are a modification of the propagation distance and a magnification of the Fresnel image compared to the case of plane wave illumination. Substituting expressions (2.57) and (2.20) in the Fresnel integral (2.34) yields

$$u_d(\boldsymbol{x}) = \frac{1}{\lambda d \mathrm{i}} \int \sqrt{I_{\mathrm{inc}}(\eta)}\, T(\eta) e^{\mathrm{i}\frac{\pi}{\lambda l}\eta^2} e^{\mathrm{i}\frac{\pi}{\lambda d}(\boldsymbol{x}-\eta)^2}\, \mathrm{d}\eta \tag{2.58}$$

Reorganising the complex-exponential functions gives

$$u_d(\boldsymbol{x}) = \frac{1}{\lambda d \mathrm{i}} e^{\mathrm{i}\frac{\pi}{\lambda d}\boldsymbol{x}^2} \int \sqrt{I_{\mathrm{inc}}(\eta)}\, T(\eta) e^{\mathrm{i}\frac{\pi}{\lambda}(\frac{1}{l}+\frac{1}{d})\eta^2} e^{-\mathrm{i}\frac{\pi}{\lambda d}2\boldsymbol{x}\eta}\, \mathrm{d}\eta \tag{2.59}$$

This suggests introducing the defocusing distance *D*, defined by

$$\frac{1}{D} = \frac{1}{l} + \frac{1}{d} \tag{2.60}$$

and the magnification *M*

$$M = \frac{l+d}{l} \tag{2.61}$$

Expression (2.59) is now

$$u_d(x) = \frac{1}{M} e^{\mathrm{i}\frac{\pi}{\lambda(l+d)}\boldsymbol{x}^2} \cdot \frac{1}{\lambda D\mathrm{i}} \int \sqrt{I_{\mathrm{inc}}(\eta)}\, T(\eta) e^{\mathrm{i}\frac{\pi}{\lambda D}(\frac{\boldsymbol{x}}{M}-\eta)^2} \mathrm{d}\eta \tag{2.62}$$

The recorded intensity is a magnified version of the intensity distribution for plane wave illumination and a sample-detector distance equal to D. The non-uniform incident intensity results in a window $\sqrt{I_{\mathrm{inc}}}$ applied on the transmission function. In the case where the source-sample distance l is huge compared to the sample-detector distance d, the defocusing distance $D \approx d$ and $M \approx 1$.

The phase term in the integral determines the relative phase of the contribution of the disturbance in η. The main contribution to the field $u_d(\boldsymbol{x})$ in $\boldsymbol{x}$ comes from points close to the corresponding point $\boldsymbol{x}/M$ in the object such that their contribution is less but π out of phase [Bor80]. These points constitute the first Fresnel zone with radius r_{F}

$$r_{\mathrm{F}} = \sqrt{\lambda D} = \sqrt{\lambda \frac{d.l}{d+l}} \tag{2.63}$$

The contribution of more distant points oscillates rapidly as a function of η and the contributions of different points tend to cancel each other.

2.2.4 Partial coherence

Until now, a completely coherent incident wave, as the one emitted by a single electron, was assumed. The real beam can be decomposed into a large number of waves that are individually completely coherent but mutually incoherent. The resulting intensity is the incoherent superposition of the contributions of the individual waves.

It is useful to have at every distance from the source a complete description of the coherence properties of the quasi-monochromatic beam. This is given by the mutual intensity [Bor80], the superposition of the product of the waves at two points $\boldsymbol{x}_1$ and $\boldsymbol{x}_2$ in the plane at distance $l+z$ of the source

$$J_z(\boldsymbol{x}_1, \boldsymbol{x}_2) = \Sigma_p\, u_z^{(p)}(\boldsymbol{x}_1).u_z^{(p)*}(\boldsymbol{x}_2) \tag{2.64}$$

The sum is over all the individual waves. For $\boldsymbol{x}_1 = \boldsymbol{x}_2$, the mutual intensity is equal to the usual intensity

$$I_z(\boldsymbol{x}) = J_z(\boldsymbol{x},\boldsymbol{x}) \tag{2.65}$$

The degree of coherence $\gamma^{\mathrm{c}}(\boldsymbol{x}_1, \boldsymbol{x}_2)$ is the normalized version of the mutual intensity

$$\gamma^{c}(\boldsymbol{x}_1,\boldsymbol{x}_2)=\frac{J(\boldsymbol{x}_1,\boldsymbol{x}_2)}{\sqrt{I(\boldsymbol{x}_1).I(\boldsymbol{x}_2)}} \tag{2.66}$$

It is by definition equal to 1 when the two points coincide and it describes the coherence that remains between the two points when they are separated. It determines for example the visibility of the interference fringes formed behind an opaque screen with two identical point sources [Bor80].

The mutual intensity immediately downstream of the object is according to expression (2.20)

$$J_o(\boldsymbol{x}_1,\boldsymbol{x}_2)=J_{\text{inc}}(\boldsymbol{x}_1,\boldsymbol{x}_2).T(\boldsymbol{x}_1).T(\boldsymbol{x}_2)^{*} \tag{2.67}$$

The spectrum of the intensity can be expressed as one double integral involving this mutual intensity [Gui78] (see also equation (2.50))

$$\tilde{I}_d(\boldsymbol{f})=\int e^{-\mathrm{i}2\pi.\eta.f}.J_o(\eta-\frac{\lambda d f}{2},\eta+\frac{\lambda d f}{2})\mathrm{d}\eta \tag{2.68}$$

Every factor in the mutual intensity J_o that depends only on the difference $\boldsymbol{x}_1-\boldsymbol{x}_2$ results in a multiplicative factor for the intensity spectrum.

Incoherent source

In the case of an extended incoherent source with a source distribution $S(\boldsymbol{x}_s)$, the individual wave is the spherical wave emitted by a point of the source. The intensity contribution from different points is identical except for a weighting factor $S(\boldsymbol{x}_s)$ and a translation given by $\boldsymbol{x}_s d/l$. The average intensity is thus equal to the convolution of the intensity for a point source with the geometrical projection of the source distribution S through the object on the detector, i.e.

$$I_d(\boldsymbol{x})=S(\boldsymbol{x}\,l/d) * I_d^{\text{point}}(\boldsymbol{x}) \tag{2.69}$$

If s denotes a characteristic width of the source distribution S, the blurring of the Fresnel image is of the order of $s.d/l$ at the level of the detector. Considering the equivalence between plane wave and spherical wave illumination (see § 2.2.3), we can also write

$$I_d(\boldsymbol{x})=S[(\boldsymbol{x}/M).(l+d)/d] * I_D^{\text{coh}}(\boldsymbol{x}/M) \tag{2.70}$$

with $I_D^{\text{coh}}(\boldsymbol{x}/M)$ the intensity for plane wave illumination and a propagation distance equal to D. The blurring at the level of the object is consequently $s.d/(l+d)$, considering the magnification between the object and image planes.

The incident mutual intensity as a function of the source intensity $S(\boldsymbol{x}_s)$ of an extended incoherent source is given by the Van Cittert-Zernike theorem [Bor80]

$$J_{\text{inc}}(\boldsymbol{x}_1,\boldsymbol{x}_2)=e^{i\frac{\pi}{\lambda l}(x_1{}^2-x_2{}^2)}\int S(\eta)\exp\left[-2\pi i\eta\frac{(\boldsymbol{x}_1-\boldsymbol{x}_2)}{\lambda l}\right]\mathrm{d}\eta \tag{2.71}$$

The mutual intensity is disregarding a phase factor equal to the Fourier transform of the source intensity

$$J_{\text{inc}}(\boldsymbol{x}_1,\boldsymbol{x}_2) = e^{i\frac{\pi}{\lambda l}(x_1{}^2 - x_2{}^2)}\tilde{S}(\frac{\boldsymbol{x}_1 - \boldsymbol{x}_2}{\lambda l}) \tag{2.72}$$

The phase factor in front of the integral corresponds to a spherical wave propagating from the origin in the source. It leads to the defocusing distance *D* and magnification *M* discussed before (equations (2.60) and (2.61)). The amplitude of the mutual intensity and the degree of coherence are uniform, they are only function of the vector between the two points. The effect of the extended size of the source on the spectrum of the intensity is consequently a simple product with the amplitude of the mutual intensity, equal to the spectrum of the source intensity. Introducing expressions (2.72) and (2.67) into expression (2.68) and using the concept of *D* and *M*, yields

$$\tilde{I}_d(\boldsymbol{f}) = \tilde{S}(\frac{d}{l}\boldsymbol{f})\int e^{-\mathrm{i}2\pi\eta.M\boldsymbol{f}}.T(\eta - \frac{\lambda DM\boldsymbol{f}}{2})T^*(\eta + \frac{\lambda DM\boldsymbol{f}}{2})\mathrm{d}\eta \tag{2.73}$$

hence

$$\tilde{I}_d(\boldsymbol{f}) = \tilde{S}(\frac{d}{l+d}M\boldsymbol{f}).\tilde{I}_D{}^{\text{coh}}(M\boldsymbol{f}) \tag{2.74}$$

This is obviously the Fourier transform of expression (2.70). More generally, if $J_{\text{inc}}(\boldsymbol{x}_1, \boldsymbol{x}_2) = |J_{\text{inc}}(\boldsymbol{x}_1 - \boldsymbol{x}_2)|.\exp[\mathrm{i}\pi(\boldsymbol{x}_1{}^2 - \boldsymbol{x}_2{}^2)/\lambda l]$, it stands

$$\tilde{I}_d(\boldsymbol{f}/M) = |J_{\text{inc}}(\lambda D\boldsymbol{f})|.\tilde{I}_D{}^{\text{coh}}(\boldsymbol{f}) \tag{2.75}$$

Using equation (2.49), it is therefore possible to write the spectrum of the intensity as one double integral involving the spectrum of the object's transmission function

$$\tilde{I}_d(\boldsymbol{f}/M) = |J_{\text{inc}}(\lambda D\boldsymbol{f})|\int \tilde{T}(\boldsymbol{p} + \boldsymbol{f})\tilde{T}^*(\boldsymbol{p})\tilde{P}_D(\boldsymbol{p} + \boldsymbol{f}).\tilde{P}_D{}^*(\boldsymbol{p})\mathrm{d}\boldsymbol{p} \tag{2.76}$$

Introducing expression (2.48) for the propagator yields

$$\tilde{I}_d(\boldsymbol{f}/M) = |J_{\text{inc}}(\lambda D\boldsymbol{f})|e^{-\mathrm{i}\pi\lambda df^2}\int \tilde{T}(\boldsymbol{p} + \boldsymbol{f})\tilde{T}^*(\boldsymbol{p})e^{-\mathrm{i}2\pi\lambda D\boldsymbol{p}.\boldsymbol{f}}\mathrm{d}\boldsymbol{p} \tag{2.77}$$

This can be written in terms of the so-called transmission cross coefficient (TCC) $T_{\text{cc}}(\boldsymbol{p}+\boldsymbol{f}, \boldsymbol{p})$, well known in light optics [Bor80]

$$\tilde{I}_d(\boldsymbol{f}/M) = \int \tilde{T}(\boldsymbol{p} + \boldsymbol{f})\tilde{T}^*(\boldsymbol{p})T_{\text{cc}}(\boldsymbol{p} + \boldsymbol{f}, \boldsymbol{p})\boldsymbol{dp} \tag{2.78}$$

with $T_{\text{cc}}(\boldsymbol{p} + \boldsymbol{f}, \boldsymbol{p}) = |J_{\text{inc}}(\lambda D\boldsymbol{f})|.e^{-\mathrm{i}\pi\lambda Df^2}.e^{-\mathrm{i}2\pi\lambda D\boldsymbol{p}.f}$ (2.79)

The TCC is widely used in electron microscopy [Ish80] where it has a more complicated expression due to the presence of spherical and chromatic aberrations. In a lensless, quasi-monochromatic X-ray set-up these aberrations do not exist. Therefore only the last factor of the

TCC, corresponding to the defocusing, is included in the integral of expression (2.77) and the TCC is a less useful concept.

Synchrotron source

In the case of synchrotron radiation, the individual wave is the wave emitted by a single electron in the storage ring and the waves emitted by different electrons are mutually incoherent. The wave emitted by a single electron on the average trajectory is a deterministic wave that can be approximated by a gaussian wave (equation (2.10)). The electrons oscillate in position and angle around the mean trajectory with electron position and angular distributions that can be described as uncorrelated gaussians, respectively

$$g(\boldsymbol{x}) = \frac{1}{2\pi\sigma_{\mathrm{e}x}\sigma_{\mathrm{e}y}} \exp\left[-\frac{1}{2}\left(\frac{x^2}{\sigma_{\mathrm{e}x}{}^2} + \frac{y^2}{\sigma_{\mathrm{e}y}{}^2}\right)\right] \tag{2.80}$$

and $$\kappa(\theta) = \frac{1}{2\pi\sigma_{\mathrm{e}x}'\sigma_{\mathrm{e}y}'} \exp\left[-\frac{1}{2}\left(\frac{\theta_x{}^2}{\sigma_{\mathrm{e}x}'^2} + \frac{\theta_y{}^2}{\sigma_{\mathrm{e}y}'^2}\right)\right] \tag{2.81}$$

where $\sigma_{\mathrm{e}x}$ and $\sigma_{\mathrm{e}x}'$ are the horizontal electron beam size and beam divergence and $\sigma_{\mathrm{e}y}$ and $\sigma_{\mathrm{e}y}'$ are the vertical ones. Equation (2.72) originally derived for an incoherent source, is valid much more generally. A synchrotron source is not strictly incoherent otherwise the radiation would not be anisotropic. The angular distribution of the synchrotron radiation wave is of the order of $1/\gamma$ (see § 3.1), thus the width at the level of the source of an individual coherent wave (w_{o} in equation (2.11)) is of the order of $\lambda\gamma/2\pi$. This is about 0.2 µm for the case of interest and it is very small compared to the usual source sizes (> 10 µm). The source intensity will consequently not vary over the coherence width in the source and the source can be described as a quasihomogeneous source [Car77, Wol78]. Therefore equation (2.72) remains valid as long as $w_{\mathrm{o}} << \sigma_{\mathrm{e}}$. The complex degree of coherence is proportional to the Fourier transform of the electron position distribution

$$\gamma^{\mathrm{c}}_{\mathrm{inc}}(\boldsymbol{x}_1,\boldsymbol{x}_2) = e^{\mathrm{i}\frac{\pi}{\lambda l}(x_1{}^2 - x_2{}^2)}\,\tilde{g}\left(\frac{\boldsymbol{x}_1 - \boldsymbol{x}_2}{\lambda l}\right) \qquad w_{\mathrm{o}} << \sigma_{\mathrm{e}} \tag{2.82}$$

and is independent of the electron angular distribution. In the case of a gaussian position distribution, the degree of coherence is also a gaussian with a sigma-value σ_{c}

$$\sigma_{\mathrm{c}} = \frac{\lambda l}{2\pi\sigma_{\mathrm{e}}} \tag{2.83}$$

The transverse coherence length l_{t} gives a global appreciation of the spatial coherence conditions. It can be defined as the lateral separation between two points in the horizontal or the vertical plane such that $|\,\gamma^{\mathrm{c}}\,| = 1/2$. Expressed as a function of the fwhm size of the source s ($\approx 2.35.\sigma_{\mathrm{e}}$, see § 3.1 for other contributions to the source size), it is

$$l_{\mathrm{t}} = \frac{2\ln 2}{\pi}\frac{\lambda l}{s} \approx \frac{\lambda l}{2s} \tag{2.84}$$

The general case of a synchrotron source with a source coherence width that is not small compared to the source size is treated in [Coï95] and [Tak98]. In the case of gaussian distributions, the degree of coherence still depends only on the difference $\boldsymbol{x}_1 - \boldsymbol{x}_2$ (disregarding the spherical wave phase term), i.e. it fulfils the Schell condition [Coï95]. This is no longer true for the mutual intensity. The degree of coherence is also gaussian and depends now on both the position and angular distribution of the electrons. Its sigma value in one direction is [Coï95]

$$\sigma_{\mathrm{c}} = \frac{\lambda l}{2\pi}\frac{1}{\left(\sigma_{\mathrm{e}}^{\,2} + \frac{w_{\mathrm{o}}^{\,2}}{2} - \frac{1}{2(1/w_{\mathrm{o}})^2 + 4(k\sigma_{\mathrm{e}}')^2}\right)^{1/2}} \tag{2.85}$$

and the intensity of the synchrotron radiation beam has the following gaussian dependency, different in both directions [Coï95]

$$I_{\mathrm{inc}}(x) \propto \exp\left[-\frac{1}{2}\frac{x^2}{(l\sigma_{\mathrm{e}}')^2 + w^2/2}\right] \tag{2.86}$$

If the Schell condition is fulfilled, equation (2.68) and definition (2.66) yield

$$\tilde{I}_d(\boldsymbol{f}) = \gamma_{\mathrm{inc}}^{\mathrm{c}}(\lambda d\boldsymbol{f})\int e^{-\mathrm{i}2\pi\eta f}.\sqrt{I_{\mathrm{inc}}(\eta - \frac{\lambda df}{2})}T(\eta - \frac{\lambda df}{2})\sqrt{I_{\mathrm{inc}}(\eta + \frac{\lambda df}{2})}T^*(\eta + \frac{\lambda df}{2})\mathrm{d}\eta \tag{2.87}$$

The effect of the coherence and shape of the incident beam is thus a multiplication of the intensity spectrum with the degree of coherence and the object transmission function is replaced by $T(\boldsymbol{x})\sqrt{I_{\mathrm{inc}}(\boldsymbol{x})}$. If the incident intensity $I_{\mathrm{inc}}(\boldsymbol{x})$ does not vary on a scale given by the coherence length or the Fresnel zone, it will simply result in a multiplicative factor for the intensity $I_d(\boldsymbol{x})$.

2.2.5 Detection

A two-dimensional detector is used to acquire the complete image in a single exposure. Point by point imaging using a narrow incident beam and a scanning geometry can be used for absorption radiography. It is not adapted for phase sensitive imaging as the contrast is based on the interference between laterally separated portions of the beam. The beam must be at least some Fresnel zones wide. An image obtained with a beam of limited lateral extension and a scanning procedure was reported [Nug96]. The digitised (film) or digital (CCD-camera) images contain typically 10^6 pixels. A scanning procedure is consequently far too slow.

The response of the detector is supposed to be *linear* and *spatially invariant* as a function of the intensity of the beam impinging on it without offset. If this is not the case, it is assumed that the images are corrected for the offset, non-linearities and pixel response non-uniformity (see § 3.4.1). An important characteristic of the detector is its detection quantum efficiency (DQE) as a function of the spatial frequency, incident intensity,... This will determine the recorded image with its noise characteristics. For the time being, we consider only the detector transfer function, that describes how the information spreads spatially over the detector. The point spread function of the detector $R(x,y)$ gives the response of the detector to a Dirac pulse $\delta_{\mathrm{D}}(x,y)$ in a noiseless world. The recorded intensity $I_d^{\mathrm{rec}}(x,y)$ is obtained in real space as the convolution of the intensity impinging on the detector with the point spread function

$$I_d^{\mathrm{rec}}(x,y) = R(x,y) * I_d(x,y) \tag{2.88}$$

or equivalently in Fourier space

$$\tilde{I}_d^{\mathrm{rec}}(f,g) = \tilde{R}(f,g).\tilde{I}_d(f,g) \tag{2.89}$$

where the detector transfer function $\tilde{R}(f,g)$ is the Fourier transform of the point spread function.

2.2.6 Summary

As shown above every contribution to the image can be described as a multiplication either in real space or in Fourier space. The image is therefore calculated as a succession of multiplications with intermediate transformations between the two spaces. In the case of non uniform illumination, the incident wave and object transmission function are multiplied in real space. Propagation corresponds to a multiplication of the spectrum of the wave with the propagator (2.48) corresponding to the defocusing distance D (2.60). The intensity is the squared modulus of the wave in real space using (2.29). The partial coherence and detector response are considered by multiplying the spectrum of the intensity with respectively the degree of coherence (2.82) and the detector transfer function (2.89). This can be expressed as

$$I_d^{\mathrm{rec}}(M\boldsymbol{x}) = \underset{f\to x}{\Im}\left[\tilde{R}(\boldsymbol{f}/M).\left|\gamma^{\mathrm{c}}(\lambda D\boldsymbol{f})\right|.\underset{x\to f}{\Im}\left[\left|\underset{f\to x}{\Im}\left[\tilde{P}_D(\boldsymbol{f}).\underset{x\to f}{\Im}\left[T(\boldsymbol{x}).u_{\mathrm{inc}}(\boldsymbol{x})\right]\right]\right|^2\right]\right] \tag{2.90}$$

where $\Im$ denotes a Fourier transform. The transformations are two-dimensional and the arrow indicates if the transformation goes from direct space to reciprocal space ($\boldsymbol{x} \to \boldsymbol{f}$) or vice versa ($\boldsymbol{f} \to \boldsymbol{x}$). The scaling factor M accounts for the possible magnification (2.61).

As can be seen from this expression the simulation of an image starting form the object in real space involves four 2D Fourier transforms. The calculation of the spectrum using equation (2.68) followed by a single Fourier transform would be more time consuming and must consequently be avoided if possible (Schell condition). If the object is weak, the linear terms in expression (2.49) will dominate. The linear terms correspond to the interference of the plane wave components with the forward diffracted wave ($\boldsymbol{f} = 0$). The effect of the source and the detector can then be approximated by a multiplication of the spectrum of the wave amplitude instead of the intensity. This is called the quasicoherent approximation and would limit the number of required Fourier transforms to two. The objects being in general not weak, this approximation is *not* applied. The assumption of quasimonochromaticity is normally correct when working with a monochromator based on perfect crystal diffraction. If the energy range is too large, it is necessary to integrate over the energy range and to superpose the contributions corresponding to different wavelengths incoherently.

2.3 Tomography

One of the important advantages of hard X-rays for imaging is their relatively weak attenuation by materials, hence their ability to propagate through thick samples (several mm). In order to obtain a three-dimensional image of a thick object it is viewed under a large number of incidence angles. Each 2D image corresponds to an angular position ω of the sample in its rotation around the y-axis. It was shown theoretically in 1917 by Radon [Rad17], that it is possible to reconstruct the distribution of a quantity from its projections for different angles. The relevant quantity in this case is the complex refractive index $n(x,y,z)$, hence the refractive index decrement $\delta(x,y,z)$ and the absorption index $\beta(x,y,z)$ (see § 2.2.2). A 3D reconstruction is normally performed in two steps. First one determines for every angular position, from the recorded 2D *image(s)*, the 2D *projection* $R_\omega(x,y)$ of the relevant quantity

$$R_\omega(x,y) = \int n[x_\text{o}(\omega), y, z_\text{o}(\omega)]\mathrm{d}z$$

or $$R_\omega(x,y) = \int n(x\cos\omega - z\sin\omega, y, x\sin\omega + z\cos\omega)\mathrm{d}z \tag{2.91}$$

with the x_o, y_o, z_o coordinate system attached to the rotating object ($y = y_\text{o}$, see Fig 2.6). These integrals correspond to equations (2.22) and (2.23), but they now depend on the angular position ω of the object. The set of projections is called the Radon transform of the distribution $n(x,y,z)$ [Her80]. The second step is the tomographic reconstruction itself that consists in the determination of the 3D *distribution* from the available projections. This is the inversion of the Radon transform. The synchrotron beam can be considered as parallel for tomography. The largest incidence angle compared to the center of the image is reached at the edge of the image and is given by $N_\text{p}.s_\text{p}/(2.l)$, with N_p the width in pixels of the image, s_p the pixel size and l the source sample distance. This results in a lateral displacement in the specimen that should be small compared to the pixel size, yielding as condition for a parallel beam geometry

$$l > N_p^2.s_p/2 \tag{2.92}$$

This is certainly achieved with the source sample distances encountered at a synchrotron and it simplifies to a large extent the tomographic reconstruction. It is sufficient to acquire images over half a turn, because images recorded at 180° apart, are each other's mirror image, i.e. $R_{\omega+\pi}(x,y) = R_\omega(-x,y)$.

The first step consists in the determination of the projection $R_\omega(x,y)$ from the image $I_{d,\omega}(x,y)$ for each view. This is nearly a straightforward task for what concerns the imaginary part or the linear absorption coefficient μ. From an image at the exit of the sample and equation (2.30), one obtains in a simple way the projection of the linear absorption coefficient.

$$\int \mu(x_{\mathrm{o}}(\omega), y, z_{\mathrm{o}}(\omega))\mathrm{d}z = -\ln\frac{I_o(x,y)}{I_{\mathrm{inc}}(x,y)} \tag{2.93}$$

The recorded image is however $I_o^{\mathrm{rec}}(x,y)$ and depends on the detector response through expression (2.88). If the effect of this convolution is strong and if the images are not deconvolved (see § 3.4.1.3) the starting point of the tomographic reconstruction will not be a real Radon transform. This introduces artefacts when the absorption is strong, the ln-operator in expression (2.93) being non-linear. The determination of the phase modulation $\varphi(x,y)$, hence the projection of the refractive index decrement δ, from the image is a more delicate inverse problem. The holographic reconstruction will be discussed in § 4.3.

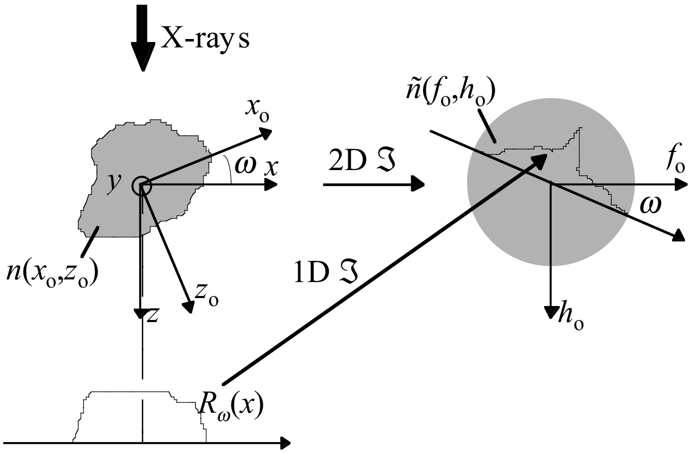

Fig 2.6 Principle of the tomographic acquisition and illustration of the Fourier-slice theorem. The sample is rotated around the vertical y-axis. Thanks to the parallel beam geometry slices at different heights can be treated independently. The x_{o}, y_{o}, z_{o} coordinate system rotates with the sample. f_{o} and h_{o} are the reciprocal coordinates with respect to x_{o} and z_{o} respectively.

The tomographic reconstruction corresponds to inversing expression (2.91), i.e. the determination of the distribution from a set of projections. In the parallel beam geometry, the slices of the sample corresponding to different heights in the sample can be treated independently. The problem reduces to a two-dimensional one to be solved for every value of y. An explicit expression of the solution can be written for continuous and complete data. The *analytical methods* are based on the discretisation of such an explicit expression [Her80]. If the sampling rates in the x and ω direction are sufficient, these direct methods are superior with respect to the speed and the quality of the reconstruction. If the data set is incomplete, an *algebraic method* can be used [Her80]. These iterative methods are slow and may diverge in the presence of noise. As the number of views is sufficient in our case, the analytical method of *filtered backprojection* is used. The fundamental theorem of the analytical methods is called the Fourier-slice theorem. It links the Fourier transforms of the distribution and the projections: the

1D Fourier transform of the projection corresponding to the angle ω is a cut in the 2D Fourier transform of the distribution at the angle ω

$$\tilde{n}(f_\mathrm{o} = f\cos\omega\,,\ h_\mathrm{o} = f\sin\omega) = \tilde{R}_\omega(f) \qquad \forall\ \omega \tag{2.94}$$

This expression is however not used in practice to implement the reconstruction. Instead the idea of backprojection is used. During backprojection one attributes the value of the projection $R_\omega(x)$ to every point $(x_\mathrm{o},z_\mathrm{o})$ in the sample that is projected onto the point x of the detector. This is repeated for every projection. The value in a point $(x_\mathrm{o},z_\mathrm{o})$ of the distribution obtained after backprojection can be calculated as

$$\mathbf{Bp}[R_\omega](x_\mathrm{o},z_\mathrm{o}) = \int_0^\pi R_\omega(x = x_\mathrm{o}\cos\omega + z_\mathrm{o}\sin\omega)\mathrm{d}\omega \tag{2.95}$$

The result of a simple backprojection is however not the distribution, but a blurred version of it. It is possible [Her80] to correct for this by filtering the projections before backprojection. The inverse of the Radon transform can be written

$$n(x_\mathrm{o},z_\mathrm{o}) = \mathbf{Bp}\left[\underset{f\to x}{\Im}\left[H(f).\underset{x\to f}{\Im}\left[R_\omega(x)\right]\right]\right] \tag{2.96}$$

with the filter $H(f) = |f|$ and where $\Im$ denotes a one dimensional Fourier transform. The filter amplifies the high frequencies and consequently the high frequency noise. Therefore it may be necessary to consider a different filter yielding an approximate solution. In practice a finite number of views N_v are recorded and the projection is sampled with a pixelsize s_p. The distribution is reconstructed on a square grid for $(x_\mathrm{o},z_\mathrm{o})$ with normally the same sampling rate s_p. The spectrum of the projections and the reconstruction is therefore limited to a maximum frequency $1/(2s_\mathrm{p})$ (Whittaker-Shannon sampling theorem [Whi15, Dai74]). The filter $H(f)$ is set to zero outside this band. This filter, the Ram-Lak filter, is the filter used for our reconstructions [Her80]. The Fourier theorem says that the spectrum of the distribution is sampled on a polar grid with a rate in angle π/N_v. This means that the sampling is less dense far from the origin of the spectrum. The required sampling rate for the spectrum is $1/(N_\mathrm{p}.s_\mathrm{p})$ and the minimum number of projections is therefore [Her80]

$$N_\mathrm{v} \approx (\pi/2).N_\mathrm{p} \tag{2.97}$$

The width of the projection in pixels imposes the number of views. In practice the gain of such a large number of views is small. Therefore we work with a smaller number of angular positions, approximately equal to the number of pixels, $N_\mathrm{v} \approx N_\mathrm{p}$.

3 Implementation

In this chapter the instrumentation used for phase sensitive radiography and tomography is described. The experiments were mainly performed at the ESRF beamline ID19 which is exceptionally long. It is optimised for imaging applications with a wiggler as source [Bar93a]. The small lateral extent of the source and the long source-specimen distance result in a small incident divergence as seen from a point of the sample. The transverse coherence length is consequently large. On its way to the sample, the X-ray beam 'sees' attenuators, windows, monochromator crystals,... In order to avoid parasitic images and to preserve the coherence, the optical elements are subject to stringent quality requirements. The problems identified and the way they were solved during the commissioning of ID19 are described. The experimental set-up strikes by its simplicity and versatility. An X-ray diffractometer is used to align the sample. The rotation for the tomographic acquisition is performed by a precision rotation stage. The detector is carried by a translation stage aligned with the X-ray beam in order to select the sample-detector distance. The recording medium is either high resolution film or a CCD-based camera. The latter is based on an X-ray visible light converter which is coupled to the CCD with a lens system. These detectors, with different spatial resolving power, are described, and the way their transfer function is determined and taken into account.

3.1 The source

A conventional X-ray laboratory source uses the impact of electrons on a metal as a source for X-rays. The interaction of the accelerated electrons with the electrons in the metal target results in a 'continuous' energy spectrum (Bremsstrahlung) with some narrow peaks ($\Delta E/E \approx 10^{-4}$) corresponding to the characteristic X-ray energies of the elements of the metal. The useful radiation created by X-ray anodes is limited by the efficiency of the X-ray generation process and the heat load in the metal target. Furthermore, the produced X-rays are emitted more or less isotropically and most of them will not reach the specimen. Synchrotron radiation is the wave produced by a relativistic accelerated charged particle [Rao93]. It was used from the early seventies in a parasitic way on particle accelerators for high energy physics (first generation). Afterwards, some dedicated, second generation machines appeared. A tremendous improvement in the stability and control of the trajectory of the charged particle beam, together with the appearance of multipole insertion devices to produce synchrotron radiation in a more efficient way, are the fundamental characteristics of third generation synchrotron radiation sources (ESRF in Grenoble, APS in Argonne, SPRING-8 in Hyogo, Elettra in Trieste). The charged particles used at the ESRF are simply electrons. Although the emittance is very small, the distribution in angle and especially in position of the electrons still smears out the characteristics of pure synchrotron radiation. A further improvement in the emittance will result in the next generation, diffraction limited, machines.

The electrons (or positrons) are accelerated to a relativistic speed in order to collimate the emitted electromagnetic field, as seen by an observer at rest, in a narrow cone. This increases tremendously the emitted flux per solid angle in a direction parallel to the trajectory of the electrons and shifts the emitted spectrum to the hard X-ray energy range. A non relativistic accelerated particle emits power isotropically with respect to its acceleration. When the electron energy E_e expressed with respect to its rest energy,

$$\gamma = \frac{E_e}{m_e c_1^2} \tag{3.1}$$

is huge, the radiation is sharply peaked in the direction of motion of the accelerated charge. This can be 'understood' from the space-time Lorentz transformations. The typical opening angle of the radiation in the laboratory frame is $1/\gamma$ in both directions. For 6 GeV electrons (case of the ESRF) γ is equal to 1.174 10^4 and the opening angle is only 85 µrad. The acceleration is imposed with a static magnetic field and the electron describes an orbit, normally in the horizontal plane, with a radius of curvature ρ_e. An observer in the plane of motion receives from the electron a short pulse of light during the time $\tau = 4/3\ \rho_e/(c_1\gamma^3)$ he is illuminated. The energy spectrum of the radiation, its decomposition in monochromatic components, is therefore broad with frequencies up to $1/\tau$. The critical wavelength λ_c and associated critical energy E_c are defined such that half of the power is radiated at higher energies. It is given by

$$\lambda_c = \frac{4\pi}{3} \rho_e / \gamma^3 \tag{3.2}$$

The high value of γ allows to obtain a spectrum in the hard X-ray range with a macroscopic radius of curvature ρ_e (≈ 20 m).

The distribution in position and angle of the electrons affect the ideal synchrotron radiation characteristics. The horizontal electron beam emittance ε_x is proportional (up to a factor π) to the surface occupied in phase space (x,dx/ds) by the electrons [Rao93]. The s-coordinate indicates the position along the trajectory of the electron. Whereas $\sigma_{ex}(s)$ and $\sigma_{ex}'(s)$, the sigma values of respectively the gaussian position and angle distribution of the electrons (see equations 2.80 and 2.81), vary along the storage ring, the emittance is approximately constant and is a global characteristic of the machine. Similar quantities exist in the vertical plane corresponding to the electron motions in the y-direction.

ε_x [nm.rad]	ε_y [nm.rad]	E_e [GeV]	σ_E/E
3.9	0.039	6	0.001

	β_e [m]		$\mathrm{d}\beta_\mathrm{e}/\mathrm{d}s$		η_e[m]		$\mathrm{d}\eta_\mathrm{e}/\mathrm{d}s$	
	H	V	H	V	H	V	H	V
Bending Magnet	2.2	34.9	0.75	-0.025	0.09	0	-0.08	0
Low Beta section	0.5	2.7	0	0	0.04	0	0	0
High Beta section	35.6	2.5	0	0	0.13	0	0	0

Table 3.1 Emittances ε, electron energy E_e and relative energy spread σ_E/E of the machine. Values of Beta β_e and the dispersion η_e, together with their derivatives obtained at the ESRF at different positions in the storage ring [Ell98]. These machine parameters are used in the calculation of the electron beam size and divergence. H and V stand respectively for horizontal and vertical.

The vertical emittance is due to coupling with the horizontal magnetic lattice. The coupling ($\varepsilon_y/\varepsilon_x$) is typically 1 %. The resulting betatron oscillations are described by the Beta-function $\beta_\mathrm{e}(s)$ [Rao93]. Table 3.1 shows the presently obtained values of the emittances and other machine parameters determining the electron beam size and divergence. In the vertical plane, they are expressed as

$$\begin{aligned} \sigma_{\mathrm{e}y}(s) &= \sqrt{\varepsilon_y \beta_{\mathrm{e}y}(s)} \\ \sigma_{\mathrm{e}y}'(s) &= \sqrt{\varepsilon_y \frac{1+\left(\frac{\mathrm{d}\beta_{\mathrm{e}y}(s)}{\mathrm{d}s}/2\right)^2}{\beta_{\mathrm{e}y}(s)}} \approx \sqrt{\frac{\varepsilon_y}{\beta_{\mathrm{e}y}(s)}} \end{aligned} \tag{3.3}$$

In the horizontal plane, the fluctuations in energy of the electrons induce fluctuations in the radius of curvature of the electron trajectories. This increases the horizontal electron beam size and divergence

$$\begin{aligned} \sigma_{\mathrm{e}x}(s) &= \sqrt{\varepsilon_x \beta_{\mathrm{e}x}(s) + \left(\eta_\mathrm{e}(s)\frac{\sigma_E}{E}\right)^2} \\ \sigma_{\mathrm{e}x}'(s) &= \sqrt{\varepsilon_x \frac{1+\left(\frac{\mathrm{d}\beta_{\mathrm{e}x}(s)}{\mathrm{d}s}/2\right)^2}{\beta_{\mathrm{e}x}(s)} + \left(\frac{\mathrm{d}\eta_\mathrm{e}(s)}{\mathrm{d}s}\frac{\sigma_E}{E}\right)^2} \end{aligned} \tag{3.4}$$

where σ_E is the standard deviation of the electron energy distribution and $\eta(s)$ is called the dispersion function [Rao93]. Table 3.2 shows the size and divergence in both horizontal and vertical directions of the electron beam for a bending magnet, a high Beta section (normally used for undulators) and a low Beta section (wiggler of ID19). The vertical electron beam size is in all cases small compared to the horizontal one.

	beam size σ_e [μm]		divergence σ_e' [μrad]	
	H	V	H	V
Bending Magnet	126	37	108	1
Low Beta section	57	10	88	4
High Beta section	395	10	10	4

Table 3.2 Standard deviations of the electron position and angle distributions in the horizontal and vertical planes calculated using equations (3.3) and (3.4) and the machine parameters given in Table 3.1.

3.1.1 The bending magnet

A constant magnetic field imposes in this device an angular deviation to the electrons. The storage ring is built as a succession of these electro-magnets with straight sections in between them. The field emitted by a single electron depends only on the vertical angle θ_y. In order to show the link with a monochromatic component of the incident wave (see § 2.2.1), we can express it as $u_\mathrm{inc}(y = l.\theta_y) \propto A_\mathrm{p}(\theta_y,E)/l$ with

$$A_\mathrm{p}(\theta_y,E)=\begin{pmatrix}A_\mathrm{p}^{\sigma}\\ A_\mathrm{p}^{\pi}\end{pmatrix}=\gamma\frac{E}{E_c}\left(1+(\gamma\theta_y)^2\right)\begin{pmatrix}-iK_{2/3}(m)\\ \dfrac{\gamma\theta_y}{(1+(\gamma\theta_y)^2)^{1/2}}K_{1/3}(m)\end{pmatrix}\quad m=(1+(\gamma\theta_y)^2)^{3/2}\frac{E}{2E_c}\tag{3.5}$$

where $K_{1/3}$ and $K_{2/3}$ are the modified Bessel functions of the second kind of order 1/3 and 2/3. The upper and lower term correspond respectively to horizontal and vertical polarisation. The beam is fully linearly polarised in the plane of motion and elliptically polarised out of this plane. The expression allows to assess whether the source can be described as an incoherent one. The angular width of the wave with σ-polarisation is approximately

$$\sigma_\mathrm{p}'\approx\frac{0.8}{\gamma}\left(\frac{E_c}{E}\right)^{0.43}\qquad\text{for } 1/100<E_c/E<5\tag{3.6}$$

The associated coherent width in the source w_o [see § 2.2.1 and equation (2.11)] is $\lambda/(2\pi\sigma_\mathrm{p}')$ and is small compared to the size of the electron distribution σ_e. A quasi-homogeneous source description is adapted (see § 2.2.4). Although the field radiated with π-polarisation has a different angular profile, the same reasoning holds.

3.1.2 Multipole insertion devices

The flux and brilliance can be improved a lot by imposing to the electrons a different trajectory than a circular arc. When the charged particle oscillates, radiation is emitted by each wiggle. This is achieved with a spatially periodic magnetic field from permanent magnets. The contributions of the different wiggles add up incoherently in the case of an ideal wiggler and coherently in the case of an ideal undulator.

Wigglers

An observer looking at this device receives the light pulses from the different wiggles separated in time. The radiation pattern is therefore the incoherent sum of the radiation fields emitted by the individual magnets (half-periods). This is the case if the transverse oscillations, characterised by the maximum angular deviation α_{os}, are large compared to the natural opening of the synchrotron radiation, hence

$$K = \alpha_{\mathrm{os}}.\gamma >> 1 \tag{3.7}$$

This dimensionless parameter can be expressed as a function of the maximum magnetic field B_{o} along the y-axis and λ_{os} the period in the z direction of the magnetic field

$$K = \frac{q_{\mathrm{e}}}{2\pi m_{\mathrm{e}} c_1} \lambda_{\mathrm{os}} B_o = 0.934 \lambda_{\mathrm{os}}[cm] B_o[Tesla] \tag{3.8}$$

with q_{e} the electron charge . The ideal trajectory of the electrons in the periodic magnetic field is given by

$$x(z) = \frac{K}{\gamma} \frac{\lambda_{\mathrm{os}}}{2\pi} \sin(2\pi \frac{z}{\lambda_{\mathrm{os}}}) \tag{3.9}$$

Most characteristics of a wiggler can be obtained from the corresponding one of a bending magnet, scaled with the number $2N_{\mathrm{os}}$ of magnetic poles. The radiation pattern depends now also on θ_x the angle with respect to the device axis in the horizontal plane. The wiggler radiates in the horizontal direction over a fan $2K/\gamma$ corresponding to the angular deviation of the electrons. The magnetic field and the radius of curvature seen by the observer change as a function of the horizontal observation angle. The spectral properties of the radiation depend on the horizontal angle through a simple change in the critical wavelength (expression (3.2)) [Rao98]

$$\lambda_c(\theta_x) = \frac{\lambda_c(\theta_x = 0)}{\left(1 - (\gamma\theta_x / K)^2\right)} \tag{3.10}$$

The contributions to the source size are due to the electron position distribution, the length of the device L_{os} (= $N_{\mathrm{os}}.\lambda_{\mathrm{os}}$) and the excursion of the electrons in the horizontal plane. Looking at the device from an angle θ with respect to its axis introduces an apparent size of the source equal to $L_{\mathrm{os}}\theta$. Its contribution (a multiplicative factor) to the mutual intensity can be expressed as

$$J_{\mathrm{inc}}(x_1, x_2) \propto \int_{-L_{\mathrm{os}}/2}^{L_{\mathrm{os}}/2} dz S_z(z) e^{i\frac{\pi}{\lambda}\frac{x_1^2 - x_2^2}{l-z}} \approx e^{i\frac{\pi}{\lambda l}\left(x_1^2 - x_2^2\right)} \int_{-L_{\mathrm{os}}/2}^{L_{\mathrm{os}}/2} dz S_z(z) e^{-2i\pi\frac{x_1^2 - x_2^2}{2\lambda l^2} z} \tag{3.11}$$

where $S_z(z)$ is the source intensity as a function of the depth of the device (assumption of incoherence). The mutual intensity is thus approximately the Fourier transform of the depth distribution evaluated at $(x_1^2 - x_2^2)/(2\lambda l^2)$

$$J_{inc}(x_1,x_2) \propto \tilde{S}_z\left(\frac{x_1^2-x_2^2}{2\lambda l^2}\right) \qquad (3.12)$$

In general the mutual intensity and degree of coherence can no longer be expressed as a function of the difference x_1-x_2 (violation of Schell condition, see § 2.2.4). Assuming the depth distribution constant over the length L_{os} of the wiggler yields

$$J_{inc}(x_1,x_2) \propto \frac{\sin(\pi m L_{os})}{\pi m L_{os}} \qquad m = \frac{x_1-x_2}{\lambda l}\frac{x_1+x_2}{2l} \qquad (3.13)$$

The 'source size' seen by a point of the sample depends on its position through the angle $\theta_y = (x_1+x_2)/2l$. It is only a useful concept if it is approximately constant over the field of view. The source can then be approximated in the vertical plane as a gaussian distribution with sigma value

$$\sigma_{sy} = \sqrt{\sigma_{ey}^2 + \frac{(L_{os}\theta_y)^2}{12}} \qquad (3.14)$$

The oscillations of the electrons in the horizontal plane introduce on axis two sources separated by a distance $K\lambda_{os}/(\pi\gamma)$ (equation (3.9)). The contribution to the mutual intensity is the Fourier transform of two Dirac distributions separated by this distance

$$J_{inc}(x_1,x_2) \propto 2\cos\left(\pi.\frac{K\lambda_{os}}{\pi\gamma}.\left(\frac{x_1-x_2}{\lambda l}\right)\right) \qquad (3.15)$$

The 'source size' using gaussian approximations is therefore in the horizontal plane

$$\sigma_{sx} = \sqrt{\sigma_{ex}^2 + \frac{(L_{os}\theta_x)^2}{12} + \left(\frac{K\lambda_{os}}{2\pi\gamma}\right)^2} \qquad (3.16)$$

We consider now the specific case of the wiggler of ID19 and will estimate the contribution of the different terms. The parameters of this wiggler are $\lambda_{os} = 0.15$ m, $N_{os} = 5.5$, $L_{os} = 0.825$ m with a variable magnetic field B_o from 0 to 1.4 T [Bar93a]. This magnetic field is varied by changing the gap between the permanent magnets. The maximum value of the critical energy is 33.5 keV ($K \approx 20$). The source-specimen distance l is approximately 145 m. This large distance is chosen in order to have a homogeneous beam of 40 mm (H) by 14 mm (V). The maximum value of the vertical angle θ_y is about 50 µrad and the depth of the device yields a contribution to the source size of 12 µm. This is of the same order as the contribution of the electron beam. If one restricts the field of view to 2 mm in the vertical direction, the effect on the coherence becomes negligible and the degree of coherence is uniform. On axis, the vertical source size (fwhm) is 24 µm and the transverse coherence length is 270 µm at $\lambda = 1$ Å. The maximum amplitude ($K = 20$) of the oscillations in the horizontal direction is 40 µm. Typical working conditions correspond to $B_o = 1$ T, hence $K = 14$ and $K\lambda_{os}/(2\pi\gamma) = 28$ µm. The source size is thus slightly dependent on the wiggler gap. At 20 mm from the point corresponding to the axis of the wiggler, the contribution of the length of the wiggler is 34 µm and rather small compared to the electron beam size. At the edge of the fan emitted in the horizontal direction ($\theta_x = K/\gamma$), the contribution of the wiggler length can be as large as 400 µm ($KL_{os}/(\gamma\sqrt{}12)$). It is consequently important to work near the axis of the wiggler to be at the maximum intensity in the vertical direction, but also to avoid coherence degradation due to the length of the device. For typical working conditions ($B_o = 1$ T), the horizontal source size (fwhm) is 150 µm and the transverse coherence length l_{tx} is 44 µm.

Undulators

In this case the angular deviations are comparable to the natural opening angle $1/\gamma$ of synchrotron radiation ($K \approx 1$). The field radiated by the electron along its trajectory superimposes in space and time near the axis of the undulator. Constructive interference appears for a specific wavelength and its harmonics (odd harmonics on axis). The wavelength depends on the angle θ ($= (\theta_x^2 + \theta_y^2)^{1/2}$) and the emitted field is axially symmetric with respect to the axis of the ideal device

$$\lambda_m = \frac{\lambda_{os}}{2\gamma^2 m}\left(1 + \frac{K^2}{2} + \gamma^2\theta^2\right) \tag{3.17}$$

where m denotes the harmonic number. A given wavelength or energy is emitted in rings around the device axis. The wavelength of interest is normally the one emitted in the central cone. At fixed observation angle, one sees a quasi-monochromatic beam delivered by N_{os} undulator periods with spectral bandwidth

$$\frac{\Delta\lambda}{\lambda} \approx \frac{1}{mN_{os}} \tag{3.18}$$

The energy spectrum, measured with a pinhole to select a specific angle θ, shows narrow peaks. A very collimated beam is emitted in the central cone corresponding to a specific wavelength. The angular width of this wave is (cf. expression (2.11))

$$\sigma_p' = \sqrt{\frac{1 + K^2/2}{2mN_{os}}}\frac{1}{\gamma} = \sqrt{\frac{\lambda_m}{L_{os}}} \tag{3.19}$$

This is about $\sqrt{N_{os}}$ times smaller than the natural opening angle of synchrotron radiation ($m = 1$). There is a considerable gain in brightness compared to a wiggler due to the concentration of a given wavelength in a narrow angular range. The small angular width of the useful central beam makes undulator radiation less suited for imaging applications with a large field of view (more than 1 mm). For an intensity distribution with a diameter of 2 mm (fwhm), the source-specimen distance l should be about 200 m for a 3 m long ideal undulator operated at 1 Å. This estimation does not take into account the angular fluctuations in the mean electron trajectory that would cause the beam position to change at that distance.

The source size is predominantly determined by the electron position distribution. The coherence width in the source w_o (= $\lambda/(2\pi\sigma_p')$) corresponding to the collimation of the beam is

$$w_o = \frac{1}{2\pi}\sqrt{\lambda L_{os}} \tag{3.20}$$

For a 3 m long undulator tuned at 1 Å, this is about 2.7 μm, still small compared to the vertical electron beam size of 9.9 μm. If they are comparable, one can use equations (2.85) and (2.86) to estimate the coherence length and the incident intensity. It has to be noted that in the case of a perfectly collimated electron beam ($\sigma_e' << \sigma_p'$), the degree of coherence is still only determined by the electron beam size [Coï95]. For correct undulator operation the angular divergence of the electron beam σ_e' should be small compared to σ_p', the angular width of the wave. This is more or less the case at low emittance machines and it is one of their major advantages. A bigger electron divergence will cause the number of coherently radiating periods to be smaller than N_{os}. The gain in brightness will then be situated between $2N_{os}$ and N_{os}^2 instead of the ideal gain of N_{os}^2. To minimise the electron angular divergence, undulators are normally placed in sections of the ring with a high Beta value in the horizontal plane. The horizontal beam size is consequently very large ($\sigma_{ex} \approx 400$ μm) and destroys the horizontal coherence. The vertical beam size is identical to the one in a low beta section and the source thus has a very elongated elliptical shape. A crude solution consists in limiting the horizontal extension of the source with a slit. An ideal undulator is coherent over its length and gives no depth contribution to the source size similar to expression (3.14). In the case of partial coherence, there will be some contribution. The intrinsic energy bandwidth of the undulator radiation ($\Delta E/E \approx 10^{-2}$ for $m.N_{os} = 100$ using equation (3.18)) can be sufficiently narrow for many phase sensitive applications. The suppression of the monochromator can increase the incident flux by two orders of magnitude. The harmonics of the wavelength used can be suppressed by working at low K value (only the fundamental radiates) or by using total external reflection by a mirror. It is presently still unlikely to find a mirror of sufficient quality for imaging applications (see § 3.2.3). The very collimated undulator beam only conditioned with a pinhole is however not compatible with a large field of view. The need for a narrow spectral bandwidth and a large angular width of the beam suggests using an undulator with a short period λ_{os} (N_{os} large while keeping L_{os} small).

3.2 Conserving the homogeneity and coherence of the beam

Spurious images from beryllium windows were reported [Clo96, Sni96a, Esp98], indicating that nearly everything on the X-ray path can act as a phase object, and lead to a degradation of the beam quality. The beam loses its spatial homogeneity and its angular distribution gets broader. This degradation is unacceptable for critical applications such as (coherent) imaging, X-ray focusing, dispersive EXAFS studies and high resolution diffraction. A flat-field correction (see § 3.4.1.1), consisting in a pixel by pixel division with an image recorded without object, does not give a complete solution. Phase imaging is a coherent process and the division should be made on the wave amplitudes and not on the intensities convolved with the detector transfer function. In the case of Bragg diffraction imaging, removing the object suppresses completely the diffracted beam. The culprits found are the protection foils located in the front end, the beryllium windows, the filters, the mirrors and the monochromators. The measures taken to alleviate the problems related to each element are discussed [Esp98]. The best solution is to image with a beam as clean as possible and therefore to restrict the optical elements to the strictly necessary ones.

3.2.1 Carbon filters

The total power emitted by an insertion device is big (> 1kW). The first beryllium window, separating the vacuum of the storage ring and the beamline, has low absorption for hard X-rays, but not in the soft part of the synchrotron radiation spectrum. Its cooling system is unable to dissipate the corresponding heat load. This window must therefore be protected by a filter. In most of the similar ESRF beamlines, two 0.25 mm thick pyrocarbon foils are placed just before the beryllium window, i.e. 25 m from the source. Fig 3.1a shows the image of a monochromatic beam obtained from a flat Si crystal diffracting, in symmetrical Bragg setting for the 111 reflection, in the horizontal plane, at 145 m from the source (photon energy $E = 20$ keV). A wavy structure and horizontal lines are clearly visible. The horizontal lines were known to come from the beryllium, as will be discussed in § 3.2.2. Therefore it was suggested that the diagonal ones were originating from the pyrocarbon filters. This was easily confirmed in Fig 3.1b by a test, performed when the machine was operated at low enough current (<100 mA) for operation without carbon filters to be safe.

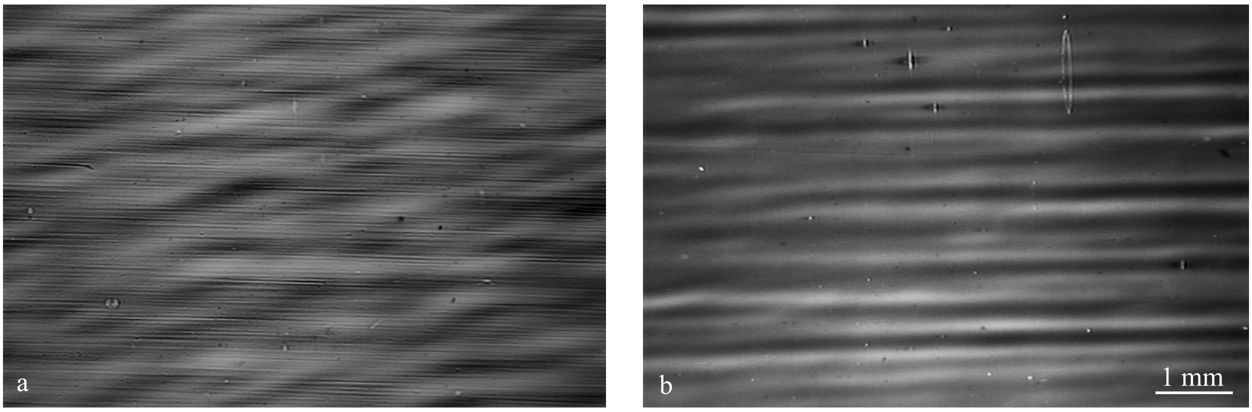

Fig 3.1 Image of a monochromatic ($E = 20$ keV) beam obtained from a flat Si (111) crystal diffracting, in symmetrical Bragg setting, in the horizontal plane, at 145 m from the source. (a) Horizontal lines due to the beryllium windows located at 26 and 135 m from the source and a wavy structure, associated with the carbon filters, located 25 m from the source, are clearly visible. (b) Same image after removing the second beryllium window and the carbon filters.

Using the propagation technique in our experimental hutch (sample-detector distance in the 1 to 4 m range), we tested several other filter materials. The observed wavy images appear to mainly correspond to internal density inhomogeneity, and polishing the foil does not improve the situation. Highly Oriented Pyrolitic Graphite (HOPG) introduces less pronounced spurious images, but is still not satisfactory. Diamond plates produced by chemical vapour deposition (CVD) appeared to be more promising. The specification of the plates was as follows: thickness 250 +/- 25 μm; surface finish 0.03 μm RMS; maximum peak to valley 0.4 μm; optical grade. Fig 3.2a shows that no phase image was introduced by a diamond plate set into the monochromatic beam. There were no general contrast features added to the image, but some occasional intensity drops (white in the figure). This local loss of intensity was assigned to Bragg diffraction from individual crystallites. When the diamond plate is rotated, the location and shape of the diffracting crystallites change, but their number and average size (50-100 μm) remain. Several diamonds, produced by the CVD technique, but provided by different suppliers, were tested. All of them display basically the same features. Nevertheless the diamond plates were a large improvement with respect to the graphite foils, and were installed in the front end. The local loss of intensity with these new protection filters located 25 m from the source and 120 m from the sample, though still observable (≈ 10 % over about 0.1 mm^2), is less dramatic than on Fig 3.2a because of the blurring associated with the source size. Possible solutions to avoid the intensity drops are the use of diamond with smaller crystallites or single crystal diamond.

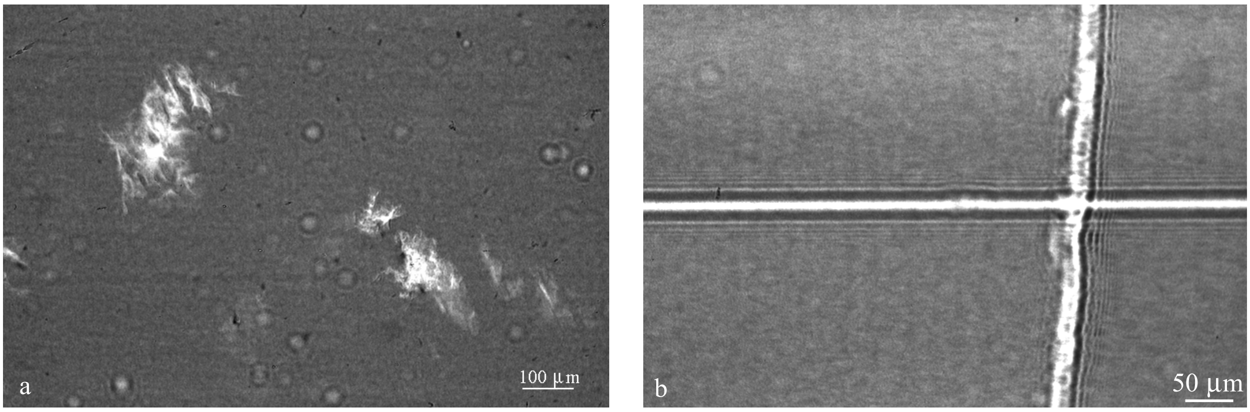

Fig 3.2 (a) Image of a monochromatic beam after passage through a CVD grown diamond plate. No diamond-related spurious phase images are observed, but local dips in the intensity are associated with Bragg diffraction by diamond crystallites (50-100 μm). The sample-detector distance was 2.4 m and the X-ray energy 20 keV. (b) Phase image of a polymer fibre, 13 μm in diameter, and of a circular Be window: the Fresnel fringes from the fibre are not affected by the presence of this polished beryllium plate, which was later used as the front end window of the beamline. The plate covers the left part of the image. The sample-detector distance was respectively 2.3 m and 2.8 m for the fibre and the plate and $\lambda = 0.7$ Å.

3.2.2 Beryllium and aluminium windows

Fig 3.1a and b show two sets of horizontal lines. They were traced to slight rolling defects in the two beryllium windows placed across the beamline, respectively 26 meters from the source (wide lines in Fig 3.1b) and 135 meters from the source (fine lines in Fig 3.1a). The thickness variations are known to be of the order of 10 μm. At the photon energy used, the absorption variation associated to this thickness variation is 0.05 % for PF60 beryllium (99.8 at% Be with small amounts of O, Fe,...) and consequently completely negligible. The variation in optical path-length, i.e. of phase, is however 0.9 rad and huge intensity variations are expected depending on the distance. The defocusing distance promotes certain spatial frequencies of rolling defects. The quasi-period of the lines, respectively about 380 µm and 45 µm, can be understood from the respective values of defocusing distance *D* (respectively 21 m and 9.3 m) and magnification *M* (respectively about 5.6 and 1). Using expression (2.2) to estimate the feature size to which the Fresnel image is most sensitive, and taking into account the magnification, yields respectively 290 µm and 35 µm for the expected image feature size. This type of artefact can be removed by using a 'random phase screen' [Clo96], which consists in a rotating inhomogeneous material. However, the use of such a device increases the incident divergence and reduces dramatically the beam coherence. We realised such a device based on rotating wood to create a statistically varying refractive index distribution. The statistical description based on Rytov et al. [Ryt89], together with measurements of the angular divergence as a function of the thickness of the screen can be found in [Clo96].

Several polished beryllium windows were tested in order to replace the defective ones. Fig 3.2b shows that the fringe visibility in the Fresnel diffraction pattern of a fibre is not altered when inserting into the monochromatic beam the circular Be window which was later used for the separation between the storage ring and the beamline in the front end. The presence of the window is only revealed by the edge contrast occurring at its border. This beryllium is Brush-Wellman grade PF60, with a specification of 0.02 µm RMS and an actual measured value of 0.01 µm on both faces.

It should be noted that just giving the polishing specification through the rms roughness is not enough for an imaging beamline: a single scratch nearly does not modify the rms, but is very detrimental for the image quality. The beryllium windows which appeared to be satisfactory and to fulfil our requirements were polished by the SAGEM company, and, for some of them, brazed by METACERAM. The rms value was specified to be less than 0.02 µm, and the peak-to-valley roughness to be less than 0.1 µm, which corresponds to a phase modulation of 0.017 rad at an X-ray energy of 10 keV.

Aluminium is also frequently used as window or filter material. When working at not too low energies (> 17 keV), it attenuates the unused lower energies and decreases the heat load on the monochromator or the sample. The aluminium or any other filter material must be internally homogeneous and carefully polished. Good results were obtained with A5 aluminium polished with the same mechano-chemical technique as for silicon crystals.

3.2.3 Mirrors

No mirror was included in the design of the beamline because tests performed at the Optics beamline (BM5) showed that, at that time, the state-of-the-art mirrors produced a rather inhomogeneous beam [Sch96]. For a given incidence angle, total external reflection occurs below a threshold energy and a mirror is thus a low pass filter for the energy spectrum. A height error Δe of the mirror surface reflecting X-rays at a grazing incidence angle α_{inc} (typically 3 mrad) generates a phase shift $\Delta\varphi$ equal to

$$\Delta\varphi = \frac{4\pi}{\lambda}\Delta e \sin\alpha_{\text{inc}} \tag{3.21}$$

A height error of only 1 Å introduces consequently a phase shift of 0.04 rad ($\lambda = 1$ Å, $\alpha_{\text{inc}} = 3$ mrad). This shift increases rapidly with the grazing angle of incidence. In order not to affect the small angular source size, the slope errors of the mirror should be small compared to half the angular source size (rms value slope error << ′ σ_s/l). This angular source size is 0.07 µrad vertically and 0.44 µrad horizontally at ID19. State-of-the-art surface manufacturing achieves presently at best 0.5 - 1 µrad slope errors and height errors of a few Å. The sensitivity to height variations at the Å level, although only in the direction of the diffraction vector, is a tremendous improvement compared to the transmission geometry. It can be the basis for a surface and interface metrology technique complementary to X-ray reflectometry [Sin88] and atomic force microscopy. Such a technique would benefit from a robust phase reconstruction algorithm.

3.2.4 Monochromators

The monochromatic beam is delivered by either of two monochromators. The 'horizontal' one, located in the experimental hutch, 145 m from the source, consists of one single crystal diffracting in the horizontal plane. The 'vertical' monochromator is a fixed-exit, double-crystal, system located in a vacuum enclosure in the monochromator hutch, 140 m from the source. Both monochromators are based on the use of perfect silicon crystals, mechano-chemically polished, set for reflection 111 in *symmetrical Bragg geometry*. This assures good monochromaticity at every point of the incident beam ($\Delta\lambda/\lambda \approx 1.5\ 10^{-4}$) and the beam is also spectrally homogeneous ($\Delta\lambda/\lambda \approx 1\ 10^{-4}$ over 2 mm).

Chromatic aberration

The symmetrical Bragg setting is the only one which does not introduce a supplementary divergence in the diffraction plane, and consequently a degradation of the apparent coherence properties [Che, Bra95]. This chromatic aberration corresponds to the fact that incident plane waves with identical wavevector directions but different wavelengths are diffracted into different directions except when the diffraction planes are parallel to the crystal surface. Fig 3.3 is a graphical representation, based on the dispersion surface approach. It is well known that the classical Huygens-Snell construction allows to determine, when knowing the dispersion surface and the incident plane wave in vacuum, which wavefields propagate into the crystal, and what waves come out from the crystal [Aut78]. Fig 3.3 shows the results of the same construction, restricted to the relevant small portions of the constant wavelength surfaces describing propagation in vacuum. Fig 3.3a describes the symmetrical Bragg setting (reflection geometry) and Fig 3.3b the symmetrical Laue case (transmission geometry). Actually two sets of vacuum surfaces are represented on each figure, corresponding to two energies (different length of the wavevectors $\boldsymbol{k}_{\mathbf{o1}}$ and $\boldsymbol{k}_{\mathbf{o2}}$) within the acceptance bandwidth of the crystal. The construction shows that when $\boldsymbol{k}_{\mathbf{o1}}$ and $\boldsymbol{k}_{\mathbf{o2}}$ have the same direction this is also the case for $\boldsymbol{k}_{\mathbf{h1}}$ and $\boldsymbol{k}_{\mathbf{h2}}$ in the symmetrical Bragg case (Fig 3.3a) whereas the Laue case introduces an extra divergence (Fig 3.3b).

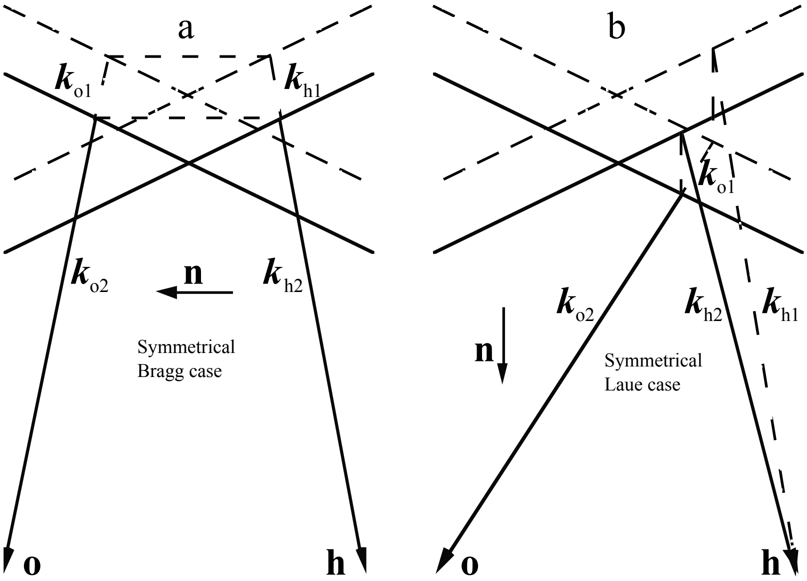

Fig 3.3 Vacuum dispersion surfaces for two wavelengths within the bandwidth corresponding to the intrinsic diffraction width of the monochromator in the a) symmetrical Bragg and b) symmetrical Laue cases. It can be observed that an additional divergence with respect to the incoming beam occurs in the diffracted beam in the Laue case but not in the symmetrical Bragg one. The vector **n** represents the outwards drawn surface normal.

The geometry of the reflection is characterised by the asymmetry factor b [Bat64],

$$b = \frac{\sin(\alpha_1 + \theta_B)}{\sin(\alpha_1 - \theta_B)} \tag{3.22}$$

with α_l the angle between the lattice planes and the crystal surface and θ_B the conventional Bragg angle (= $\sin^{-1}(\lambda/2d_B)$). The symmetric Bragg case of Fig 3.3a corresponds to $b = -1$ ($\alpha_l = 0$), whereas the symmetric Laue case of Fig 3.3b corresponds to $b = 1$ ($\alpha_l = \pi/2$). A relative variation in wavelength for a fixed incidence angle results in the following variation of the exit angle [Bra95]

$$\Delta\theta_{\text{out}} = |1 + b|.\tan(\theta_B).\frac{\Delta\lambda}{\lambda} \tag{3.23}$$

If the incident radiation is polychromatic and perfectly collimated (≈ case of ESRF), the accepted energy width is finite and determined by dynamical diffraction. On the other hand, at fixed wavelength, the angular width of the reflectivity as measured at the entrance side of the crystal is limited to the Darwin width ω_D. The relationship between both is simply $\Delta\lambda/\lambda = \omega_D/\tan(\theta_B)$. The polychromatic divergence introduced in the plane of diffraction is consequently

$$s_{\theta\lambda} = |1+b|.\omega_D \tag{3.24}$$

The divergence introduced in the symmetrical Laue configuration at $\lambda = 1$ Å and using the 111 reflection of silicon is 42 µrad, hence huge compared to the incident divergence. This anisotropic degradation of the coherence condition was observed experimentally. The maximum deviation from an exact symmetric Bragg cut that can be tolerated is obtained by deriving expression (3.22) with respect to α_l. This yields

$$\frac{\partial b}{\partial \alpha_l} = -\frac{\sin(2\theta_B)}{\sin^2(\alpha_l - \theta_B)} \tag{3.25}$$

and the divergence due to a miscut in the symmetrical Bragg case

$$s_{\theta\lambda} = 2.\Delta\lambda/\lambda.\Delta\alpha_l \tag{3.26}$$

The miscut $\Delta\alpha_l$ should be smaller than 350 µrad (0.02°) to keep the divergence below 0.1 µrad. The slope errors should also be below this value. This divergence is well defined as a function of the wavelength and it can be corrected when using a second reflection with opposite asymmetry in the (+n,–n) setting [Tan76]. A double crystal monochromator with two symmetrical Laue reflections is then acceptable. The divergence due to surface slope errors or a lattice angle α_l difference between the two crystals is smaller by a factor $\tan^2\theta_B$ compared to the Bragg geometry, as can be seen from expression (3.25).

Surface irregularities

The monochromatic beam is very sensitive to irregularities on the monochromator surfaces. These include dust, which turns out to be difficult to completely eliminate. Fig 3.4a shows the 'butterfly' like contrast of a dust particle deposited on the monochromator. This double contrast can be easily understood when considering that the dust particle introduces a phase shift both on the incoming (direct) beam and on the diffracted one [Sch96]. The path length of the X-rays inside the deposited particle is of the order of $2.t_n/\sin\theta_B$ for the symmetrical Bragg case with t_n the thickness of the particle measured along the surface normal and $\sin\theta_B$ typically 0.1. The portion of the crystal imaged to obtain a field of view s_v is obviously $s_v/\sin\theta_B$ and the small Bragg angle increases the probability to encounter irregularities. In the symmetrical Laue case, the path length is only $t_n/\cos\theta_B$ and the portion of the crystal imaged is $s_v/\cos\theta_B$. The transmission geometry is consequently much less ‘dust sensitive’.

A specific problem arose due to the deposition of a thin layer (estimated to be a fraction of a micrometer thick from the colour rings observed in visible light) of oil on the first monochromator crystal surface. The hydrocarbon originated from stepper motors that were badly encapsulated. Under the X-ray beam this deposit partly combined with the silicon and introduced spurious phase images. This deposition process could be retarded by encapsulating the motors properly and by substantially improving the vacuum at the monochromator position, making repolishing of the crystal less frequently necessary. Alternatively, when the monochromator is put under an inert helium atmosphere, contamination of the crystal surface is also avoided and the helium introduces only a slight increase in absorption and background. The impact of the X-rays itself accelerates the dust deposition, probably due to an electro-static effect. The low temperature of the crystal surface due to the cooling system and its nearly horizontal orientation when working with a vertical diffraction plane are also detrimental.

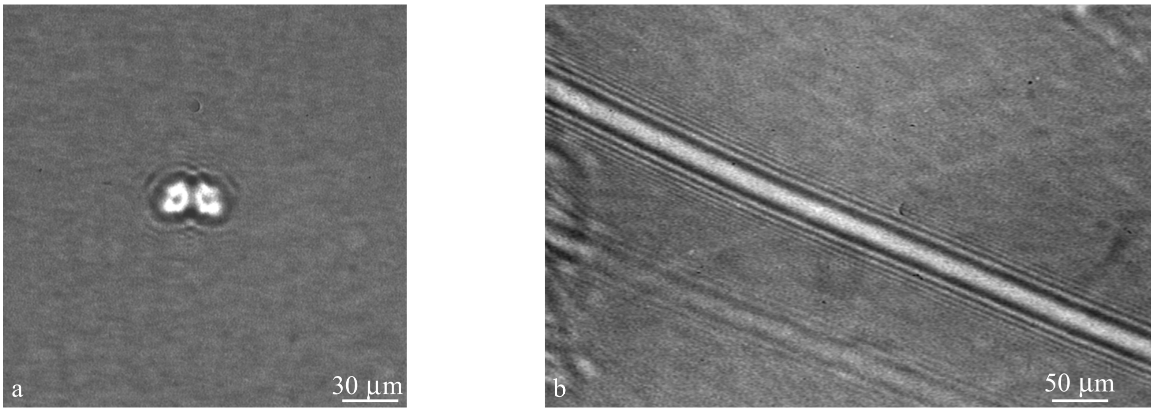

Fig 3.4 a) 'Butterfly' like contrast of a dust particle deposited on the horizontal monochromator; distance $D \approx 1.5$ m. b) Phase image of a faint scratch on the Si (111) monochromator surface; distance $D \approx 1$ m. Symmetrical Bragg setting, $\lambda = 0.7$ Å.

Surface flatness

The usual requirement in conventional Bragg-diffraction imaging is that the surfaces of the investigated crystal (and/or monochromator) be strain free; no specific requirement is made on the flatness of the surface. This is no longer true when dealing with high quality crystals and using a coherent X-ray beam. A surface slope error may increase the apparent divergence. Considering the symmetrical Bragg geometry, the height variations also introduce a phase modulation in a similar way as dust particles do. This principle is the basis of Bragg-Fresnel optics [Ari87] where a surface structure is introduced in order to simultaneously monochromatise and focus the beam. Here the height variations introduce unwanted perturbations of the wavefront. Fig 3.4b shows the image of a surface scratch, which is mainly a phase contrast image, associated to the height variation introduced by the scratch. The direct image component, associated with a gradient of distortion in the crystal [Tan76], is very weak in this case. The origin of the weaker parallel image visible in Fig 3.4b is probably due to a second scratch. The Laue geometry is not as sensitive to the surface flatness because of the geometrical reason invoked when considering the effect of dust.

In order to obtain an acceptable surface flatness and a distortion free crystal, the crystal surfaces are mechano-chemically polished. Via a recursive procedure of polishing and intermediate assessment of the quality through X-ray imaging, the polishing procedure has been optimised for coherent imaging applications.

Crystal vibrations

The intrinsic diffraction width ω_D of the symmetric Si (111) reflection is about 14 µrad at an X-ray energy of 18 keV. The vertical angular size of the source seen from the monochromator is only 0.2 µrad (fwhm). This implies that a vibration of 1 µrad does not affect the diffracted intensity, even when considering the diffraction by the second crystal. But this small vibration leads to an increase of the effective source size from 25 to 250 µm, or, correspondingly, to a drop of the lateral coherence length at wavelength $\lambda = 0.69$ Å from 200 to 20 µm. Such a vibration was observed to be associated with the water cooling of the vertical monochromator. The water flow was calculated to be sufficient for the maximum beam size (40 x 14 mm^2) and minimum gap. When reducing the beam size or opening the gap, it is possible to reduce the flow, through the regulation of the water pressure. The effect of the vibrations was experimentally checked by verifying that the lateral coherence length is a decreasing function of the water pressure [Esp98]. The measurement was based on the images of a periodic object (see § 4.1).

3.3 Experimental set-up

The experimental hutch located approximately 145 m from the source receives either the monochromatic beam delivered by the vertical diffractometer or the 'white' wiggler beam. In the white beam case, the wavelength is selected by the horizontal monochromator or by the sample itself. The latter is set on a diffractometer which allows to align it in the beam and to rotate it around a vertical axis for tomographic acquisition. In order to vary the propagation distance the sample is kept fixed while the detector moves. This option is preferable as the sample may be a diffracting crystal. The translation is performed by a stage carried and aligned by the camera manipulator. The latter and the diffractometer can move on air pads on the marble floor of the experimental hutch. Each ensemble can rotate around the previous one to which it is connected. The large number of motions or external parameters and the data / image acquisition are remote controlled. Nearly everything is unified under a single software package SPEC. This UNIX-based program from Certified Scientific Software is widely used for instrument control and data acquisition for X-ray and neutron diffraction. Common ESRF macros were developed by the Computing Services of this institute. Some specific beamline macros were written, including programs to automate the tomographic acquisition, the acquisition of flat field images, to perform the flat-field correction,... The SPEC package runs on a SUN UltraSparc 1 workstation, with a clock frequency of 166 Mhz, a total of 320 mega bytes (MB) internal memory and a 23 GB external hard disk. The relatively large internal memory allows to acquire and store images at high speed in the case of dynamic phenomena. The external hard disk enables to store large data amounts locally, a single tomographic scan representing a data volume of about 2 GB. Normally the data is however not stored locally but transferred to and stored on the ESRF central computer facility, called NICE (Networked Interactive Computer Environment). A high speed data connection between the beamline and the computer cluster consists in an optical fibre ATM

(Asynchronous Transfer Mode) link. Most hardware components (motors, encoders,...) are interfaced through the industrial VME standard under OS9 software. The VME crate assembles up to 20 cards with specific tasks:

- a microprocessor (Motorola 68040 CPU based)
- cards for digital input / output (ICV 196) to control for example the compressed air circuit
- cards for analog input (ICV 150) or output (AD and DA converters)
- stepper motor controllers (VPAP) for the stepper motor drivers (DPAP current boosters)
- read-out cards for incremental (CC-133) and absolute (VAROC) encoders
- a card (VCT-6) for counting (solid state detectors measuring integrated intensities) and timing (determination of the exposure time)

Most instruments were designed at ESRF (A. Draperi, J. Borrel and R. Chagnon). They have a modular concept and consist of a superposition or interconnection of independent elements.

3.3.1 The horizontal monochromator

A stage similar to a simple diffractometer allows to position and to adjust the monochromator crystal. This is normally a slice of perfect silicon, cut and positioned for the 111 reflection in symmetrical Bragg geometry (see § 3.2.4). A slice is typically 10 mm thick, 50 mm high and 150 mm long. Other crystals can easily be mounted. Operation under an inert nitrogen atmosphere and water cooling are possible. This monochromator has the disadvantage compared to the vertical one that the beam is not fixed when the energy changes. The beam leaves the monochromator with an angle of $2\theta_B$ with respect to the original beam. However, as the diffraction plane is horizontal, this monochromator preserves much better the optimum vertical coherence properties. A monochromator working in the vertical plane always affects to some extent the very small angular source size of 0.17 µrad (fwhm).

The monochromator stage is fixed to the marble floor. A rotation module (Institut Laue Langevin type) connects the diffractometer to the monochromator and allows the first one to rotate around the vertical axis of the second one. The *y*-stage adjusts the height of the ensemble. A precision rotation stage (Newport RTN-350) with a resolution of $5\ 10^{-4\circ}$ and an accuracy of 0.01° controls the Bragg angle. The exact energy, also when working with the vertical diffractometer, is determined with either of two methods. A first method consists in putting an element with a known absorption edge (e.g. a iodine solution) in the beam. The absorption edge can be localised by the abrupt change in transmitted intensity. This allows to calibrate the diffraction angle absolutely and to switch the energy to a specific value by an appropriate rotation. The second method is the Bond method [Bon60], which is based on Bragg diffraction from a known crystal with diffraction vector $\boldsymbol{h}$ and $-\boldsymbol{h}$. The error on the energy is consequently mainly due to the accuracy of the rotation stage. The error on the absolute energy and wavelength is only about 0.1 % at $\lambda = 1$ Å. This error increases at high energies. The *x-z* stage and the two tilts on top of the omega rotation allow to obtain coincidence between the vertical rotation axis of the monochromator and a specific axis at the crystal surface. The energy can then be changed without further lateral adjustments.

3.3.2 The horizontal diffractometer

This instrument carries the sample and its environment. The airpads allow to position it approximately with respect to the beam. Two rotation modules allow to connect the camera manipulator and/or a second detection column optimised for diffraction applications. The rotation module is used to adjust the horizontal angle of the detector translation stage. This is possible thanks to the precision of this module and the resolution and accuracy of its encoder. This incremental encoder consists of an optical scale and a fixed optical read-out head, both from the Renishaw company. The linear ruler used as scale has a resolution of 0.5 µm and is mounted on a 300 mm radius cylinder rotating with the turning element. This gives a theoretical angular resolution (1 step of the encoder) of 1.666 µrad ($95.5\ 10^{-6\circ}$). Both turning modules were measured in the metrology laboratory of the ESRF (M. Nicola, H.-P. Van Der Kleij). The average step size of the encoder is 1.6684 µrad and 1.6690 µrad respectively for the module used for the camera manipulator and the second module. The accuracy of the modules over a range of 300° is $10^{-3\circ}$. The rotation around the diffractometer is driven by a motorised wheel mounted on the camera manipulator a long distance (≈ 1.5 m) from the vertical axis of the diffractometer. Due to slipping between the wheel and the marble floor, the motor alone has a very poor accuracy. In combination with the encoder however, both the accuracy and the resolution (≈ 3 µrad) are excellent. The translation module clamps the arm that connects the diffractometer to the rotation module of the horizontal monochromator. The distance between both can be changed. The y-stage and omega rotation stage are identical to the ones on the monochromator. The rotation stage has a resolution of $5\ 10^{-5\circ}$ in this case. The x-z translation stage has a resolution of 5 µm. The repeatability is of the same order, but the accuracy is worse. The figures of the x-y translation stages are poor compared to the resolution obtained in the images. They are however sufficient to position the specimen. A specific problem arises from the flat field procedure when it is necessary to take the sample out of the beam and to bring it back at exactly the same location. The repeatability of the x-stage is in principle insufficient. It was used as a temporary solution. The translation error is determined after acquisition from the images themselves using cross-correlation techniques, and correction is made numerically as a function of the detected error. The two tilt stages (ω_x and ω_z) can describe circle segments of ± 20° with a common centre. The sample is placed at the circle centre and will consequently describe a pure rotation without translation when the tilts are used. The resolution of the tilts is 7 µrad and the accuracy is again poor. The tilts are used to align the rotation stage for the tomographic scan, i.e. to assure perpendicularity between the rotation axis, the X-ray beam and the rows of the image pixels. The angular accuracy of the rotation stage must be sufficient compared to the sampling period in ω_y of the tomographic scan equal to $\pi/N_V \approx 0.2°$ (see § 2.3), about one tenth of this value. This is easily obtained with standard rotation stages. However, the rotation axis must be a fixed line during the complete rotation over half a turn. In reality the axis oscillates in angle (wobble in ω_x and ω_z) and position (concentricity error in x, z and y) due to mechanical limitations of the device. The wobble is small and does not significantly change the angle of the projection of the rotation axis, but it also introduces an effective translation of the axis on the screen. This effect is proportional to the distance between the sample and the centre of the parasitic rotations, approximately situated at the middle of the bearings. The contribution of the wobble can therefore be decreased by limiting the height between the rotation stage and the sample, whereas the contribution of the concentricity is intrinsic. If l_y, w_z, c_x and c_y denote respectively the height of the sample with respect to the rotation centre, the wobble in ω_z and the concentricity in the x and y direction, the translation of the rotation axis in x and y direction is limited to

$$\begin{aligned} \Delta x &\leq l_y.w_z + c_x \\ \Delta y &\leq c_y \end{aligned} \tag{3.27}$$

The translation errors should be small compared to the pixel size s_p. The errors of the Newport RTN-160 rotation stage are typically ± 5 µm for the concentricity c_x and ± 40 µrad for the wobble w_z. The height l_y was originally about 170 mm, resulting in a possible error range of 24 µm. The actual figures measured are better. We measured the x and y displacement of a 'perfect' sphere mounted at the level of the sample using dial gauges with submicron accuracy (≈ 0.1 µm). From the x motion we subtracted a sinusoidal motion with a period of one turn. This sinusoidal motion corresponds to the fact that the centre of the sphere was not mounted exactly on the rotation axis. The error in x has a 6 µm total range and a 1 µm RMS value. The error in the y direction has also a 6 µm total range and a 1.1 µm RMS value. This must be considered as an exceptional case and normally the axial errors are small compared to the radial ones. The error has a mechanical origin and is very reproducible, with a repeatability of about 0.4 µm. A possible solution consists in characterising the error as a function of the angular position of the rotation stage and using the error map to correct for the translation errors after acquisition. The errors depend strongly on the mounting and environmental conditions (temperature, humidity, ...), such an error calibration should therefore be done in-situ and repeated frequently. The measurements were performed in the metrology laboratory at constant temperature (Δtemp ≈ 0.1°C). During a failure of the air-conditioning system, the temperature changed by several degrees, introducing huge translation drifts (> 20 µm). The temperature of the experimental hutch is kept constant within ± 0.1°C. Because the errors with the original rotation stage are large compared to the spatial resolution (≈ 1 µm), it was replaced by the 'ultra-precision' rotation stage PM500-360R by Newport. This DC-motor driven stage offers closed-loop positioning thanks to an integrated optical encoder mounted on the turning platform. The resolution is 1 arcsec (≈ 5 µrad) and the accuracy is better than $5\ 10^{-3\circ}$. The high velocity (200°/s maximum) is an important advantage during the alignment and scans compared to a stepper motor driven device. We also decreased the specimen height with respect to the platform to about 80 mm. Both wobble and concentricity (at a height of 72 mm with respect to the platform) were measured for this element. The measurement was performed over two bi-directional cycles and indicated a total wobble range of 9.1 µrad and a concentricity range of 1.6 µm. Restricted to a single rotation direction, the translation error is 1 µm. The errors introduced by this stage are thus compatible with the final resolution and it is not necessary to correct for them. An alternative solution consists in adding a marker to the sample. For an ideal rotation stage this reference point has a sinusoidal motion on the detector. The discrepancies with respect to the pure sinusoidal motion correspond to the translation errors. It was not necessary to adopt this solution. When no specific sample environment is requested, the sample is mounted on an X-ray goniometer head. It offers six manual degrees of freedom and is used to centre the sample on the rotation axis within the field of view without modifying the alignment of the rotation stage underneath. The elements of the diffractometer are bulky, but this makes it compatible with heavy sample environments such as a furnace, a cryostat, magnetic coils or a traction device. Such a machine, working both in compression and traction, was designed at INSA, Lyon (see § 5.2). It is optimised for tomographic scans. In order to avoid absorbing obstacles in the field of view over an angular range of 180°, the outer part of the machine consists of 2 mm thick plexiglass cylinder with a diameter of 100 mm. This choice is a compromise between minimum absorption of the softer X-rays, minimum sample-detector distance and minimum creep under load. Both surfaces of the plexiglass were polished in order to avoid parasitic contrast.

3.3.3 The camera manipulator

This table was especially designed for phase sensitive imaging at a variable sample-detector distance. The device is built from a modified ESRF table resting on three airpads in contact with the marble floor. A wheel driven by a motor with reducer can be put into contact with the floor by compressed air to rotate the table around the sample. This motion is monitored by the precision encoder mounted on the turning module of the diffractometer and allows to set the ω_y angle of the translation stage. The translation module holds the arm with adjustable length that connects the table to the diffractometer. The height of the complete table can be adjusted as the table rests on three motor driven jack-screws. The horizontality of the translation stage is adjusted by a manual tilt system. The simple and economic realisation consists of a 15 mm thick aluminium plate mounted on adjustable screws. This lockable system was preferred for reasons of rigidity and because the beam is emitted in a fixed plane that corresponds to absolute horizontality. The ω_x alignment of the table is consequently approximately fixed. Thanks to the rotation module it is possible to align the translation stage also with a beam diffracted by a (quasi-)crystal when the diffraction plane is approximately horizontal. As translation stage a NCB 100 Schneeberger table (200 mm platform length, 1200 mm total length) was chosen. It gives a usable sample-detector distance range of 0.9 m, a resolution of 12 µm and an accuracy better than 150 µm over the total range. It is therefore compatible with an absolute sample-detector distance accuracy of 1 mm.

3.3.4 The alignment procedure

Tomographic scan

If the rotation axis, the direction of the X-ray beam (// z) and the rows of the image pixels are mutually perpendicular, every row of the projection corresponds to a slice of the object. Assuring this orthogonality simplifies the tomographic reconstruction. The tilt errors $\Delta\omega_x$ and $\Delta\omega_z$ must be small compared to the angle corresponding to a row of N_p pixels, hence

$$\Delta\omega_x < 1/N_\text{p} \qquad\qquad \Delta\omega_z < 1/N_\text{p} \tag{3.28}$$

The rotation axis must be projected approximately on the central column of the image pixels. The exact position is not important, but it must be known within a fraction of a pixel. Finally the sample must be mounted on the rotation axis in such a way that its image remains within the field of view for every angular position of the scan. This limits the maximum width of the sample in the x-z plane to the $N_\text{p}.s_\text{p}$. The 3D field of view after reconstruction is a cylinder with $N_\text{p}.s_\text{p}$ as diameter and height. One has to make a compromise between the size of the object and the spatial resolution. This restriction can be overcome by making a scan in the x-y plane with the detector or the sample. The amount of data and the acquisition time increase rapidly in this case. Another solution that will be implemented in the future combines two tomographic scans with different pixel sizes and resolutions. There exists a contribution to the projections of the part of the sample outside the high resolution cylinder. The contribution is approximately known from the low resolution reconstruction. This allows to determine with better resolution a part of the sample volume.

Two procedures are used to minimise the tilt errors and to determine the position of the rotation axis. In the case of a 1024 by 1024 CCD, the tilts should be small compared to 1 mrad (0.05°). The first procedure enables to correct both tilts [Pat98]. A point of the sample describes in space a circle around the rotation axis. Its projection will describe a line corresponding to a single row of pixels if the alignment is correct. If this is not the case, the point will describe an ellipse. Its characteristics, centre, angle and ellipticity are directly linked to the position of the rotation axis, $\Delta\omega_z$ and $\Delta\omega_x$ respectively. The ellipse is determined from an even number (typically 8) of images of a tungsten needle or wire deliberately positioned off-centre. The position of the top of the needle is determined with an edge detection procedure and corresponds to a point of the ellipse. From the ellipse parameters, the alignment errors are determined and correction is made with the corresponding motors of the horizontal diffractometer. This cycle is repeated until the errors are undetectable. The second procedure allows to determine the $\Delta\omega_z$ error more accurately and gives also the position of the rotation axis. It uses two images, recorded at ω and $\omega+\pi$, of the object itself. This fast procedure is repeated at every scan. The two images are each other's mirror with respect to the projection of the rotation axis. To determine the mirror axis, one of both images is mirrored numerically with respect to the central column. For every row, the mirror position is measured by a 1D cross-correlation between the corresponding lines of the two images. The shift between the signals is equal to twice the distance of the mirror at that row with respect to the middle of the image. A linear fit through the mirror positions allows to determine the position and angle of the projection of the rotation axis very accurately. The shift can be determined within a fraction of a pixel and the number of lines N_p is large (typically 1024), this gives a sufficient precision of about $1/(10N_\mathrm{p})$ in $\Delta\omega_z$ and 1/10 of a pixel in the axis position.

Holographic scan

This procedure concerns the alignment of the long translation stage with the direction of the X-ray beam (z-axis). Ideally the quality of the translation stage and the alignment should be such that a point is projected on the same detector pixel independent of the chosen sample-detector distance. In reality the image undergoes a translation error due to the horizontal and vertical run-out of the table, but also due to alignment errors and the compliance of the table. The wobble of the translation stage contributes significantly to the error. The stage was not measured in the metrology laboratory but under actual experimental conditions. The angular error ω_z around the translation axis introduced by the translation is known to be smaller than 100 µrad. Therefore there is only a translation and no appreciable rotation between the images. In order to minimise the translation errors the stage is aligned with a simple procedure. The position of a reference feature is monitored during a scan of the sample-detector distance. From a linear fit of the horizontal and vertical position as a function of d, one deduces the horizontal ($\Delta\omega_y$) and vertical ($\Delta\omega_x$) angular errors. Correction is made with respectively an encoded motorised rotation of the camera manipulator and a tilt of the table.

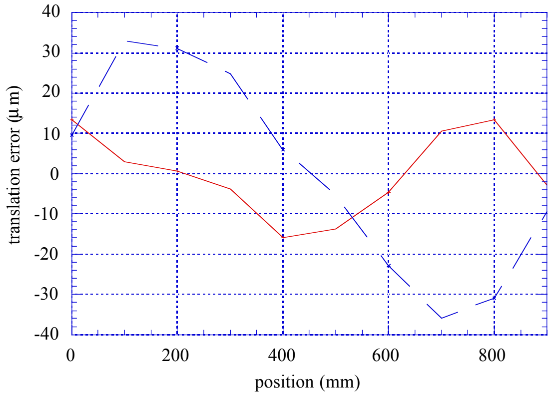

Fig 3.5 Lateral translation errors in the horizontal (full curve) and vertical (dashed curve) direction as a function of the position along the translation stage.

The translation errors remaining after alignment are presented in Fig 3.5. In the horizontal plane the alignment error vanishes ($\Delta\omega_y = 1$ µrad) and the total translation range is 29 µm. This value corresponds to the mechanical quality of the bench itself. In the vertical direction the alignment error is about 65 μrad and the translation error is 70 μm over the full translation length of 900 mm. If one subtracts a linear term corresponding to the angular error, the total error reduces to 42 μm. The fault is bigger in the vertical direction mainly because of the deformation of the aluminium plates of the table. Increasing the stiffness of these plates, can further reduce the error. The translation faults are huge compared to the pixel size and it is necessary to take them into account. The correction is performed after acquisition. Another solution consists in making the opposite translation with the detector or the same translation with the sample including the rotation stage. Moving the detector would require two supplementary high quality x-y translation stages put on top of the long z translation stage. This increases in an unacceptable way the load of the z translation stage. Moving the sample must be avoided when working in reflection or diffraction conditions and also requires precise x-y translation stages underneath the ω_y sample rotation stage. The translation errors are in principle reproducible and a x-y correction could be added to every z translation. The correction is performed numerically by translating the recorded images. The translation error between successive images of the scan is determined using the cross-correlation technique. The maximum of the 2D cross-correlation (calculated by Fourier transformation) of two images corresponds to the translation that makes them as much alike as possible. The images of the series are compared in this way two by two and the translation of every image with respect to the mean origin is determined. The origins of the images are aligned by applying the opposite translation implemented with a bicubic interpolation or Fourier transformation [Bri74].

3.4 The high resolution X-ray detector

The large source-sample distance encountered at a synchrotron reduces the blurring by the source to a fraction of its size. On the other hand the magnification M is approximately equal to 1 and the resolution in the recorded Fresnel images (the information limit) is mainly set by the detector resolution. Two types of high resolution ($r < 20$ μm) X-ray detectors are commonly used: photographic film and CCD based detectors with on-line conversion from X-rays to visible light. The linearity of the response of the detector with the incident intensity is a prerequisite for quantitative imaging (holographic reconstruction, tomography). Correction for non-linearities (off-set, film response, non-uniformity,...) is made in the flat-field correction. The spatial resolution of the detector is described by the optical transfer function. It is measured indirectly through the edge spread function obtained in a simple way with an absorbing edge. The detective quantum efficiency (DQE) describes how well the detector preserves the signal to noise ratio (SNR) present in the incident photons. A large DQE reduces the necessary dose and exposure time to achieve a given SNR and resolution in the recorded images. The advantages of photographic film are its nearly infinite field of view, the easy positioning and good spatial resolution ($r \approx 1$ μm). The drawbacks are the non-linearity and the off-line development. The difficulty to store a large number of images with a fixed field of view makes film inappropriate for tomographic acquisition. With on-line CCD based detectors one makes intrinsically a compromise between the field of view and the obtainable resolution because of the limited number of pixels. The detector is bulky and more difficult to position. The dynamic range of the detector itself can be as large as 14 bits with excellent linearity within this range using a cooled CCD camera. The detector is fixed and the image can be read and transferred to a storage medium within a fraction of a second (down to 50 ms). Such an on-line detector is therefore well adapted for real-time and tomographic acquisition. Three detector systems with pixel sizes s_{p} of 10 µm, 6.5 µm and 0.5-2 µm were developed. Once their transfer function is measured, it is possible to deconvolve the images and to correct for the spatial-frequency dependent response.

3.4.1 Detector characteristics

3.4.1.1 Linearity and uniformity

Films

The response of the detector should be proportional to the incoming intensity without off-set and spatially uniform. The response of photographic film is non linear because of saturation effects and because the amount of transmitted light is measured [Dai74]. The response is uniform except when the resolution becomes similar to the grain size. A uniform background (fog) is present independent of the received exposure. In order to exploit the images, one looks at them in transmission mode under incoherent illumination with a light microscope. It is thus possible to explore a large field of view under the microscope and to adapt the optical magnification to the case of interest. The images are digitised with a plain CCD camera (Hitachi, KP-M1E/K-S10) and a cheap 8-bit analog-digital converter.

In order to quantify the images, the use of a densitometer is avoided because this would be unpractical and the resolution would be poor. Instead, the grey level response of the film under the light microscope is calibrated. For this several exposures with increasing duration are made of the same portion of the beam and preferably on the same film as the actual image. The grey level value is determined for each exposure time and the functional relationship between grey level and exposure is determined by fitting the observation points with a simple function (third or fourth order polynomial). This calibration curve is then used to translate the grey levels of the actual image into relative exposures. This procedure is correct for monochromatic illumination and because the film response for hard X-rays depends for a given energy only on the exposure, the product of the impinging intensity and the exposure time. This characteristic is called the reciprocity law [Dai74]. The X-ray energy, film development procedure, microscope settings and illumination conditions must be fixed. The films used are Kodak high resolution SO-343 and Kodak Industrex SR films.

CCD cameras

CCD cameras are normally linear before saturation when the full well capacity is reached. The linearity errors are smaller than ± 0.3 % for the cameras used [Lab96]. The gain is not necessarily identical for every pixel. This fixed sensitivity pattern gives a *multiplicative* contribution to the image [Dab91]. It is exactly corrected for by dividing the image signal with an image I^{flat} obtained under uniform illumination of the detector. An output signal is present without incoming photons, corresponding to the time dependent dark current of the CCD and an electronic off-set. This is an *additive* contribution. A dark image I^{dark}, recorded without incoming beam, is subtracted from every image. Both contributions are corrected for with the flat field procedure:

$$I_d^{\text{corr}}(\boldsymbol{x}) = \frac{I_d^{\text{rec}}(\boldsymbol{x}) - I^{\text{dark}}(\boldsymbol{x})}{I^{\text{flat}}(\boldsymbol{x}) - I^{\text{dark}}(\boldsymbol{x})} \tag{3.29}$$

In order not to increase the noise with this correction, a number of dark images, about 20, are averaged. The choice of I^{flat} depends on the purpose of this correction. If one wants to know the intensity distribution of the wave including the effect of the incoming beam, real homogenous illumination is necessary to obtain the flat image. If one wants to retain only the contribution of the sample, the contrast present in the incoming wave (see § 3.2) is unwanted. This parasitic contrast gives a contribution that is also approximately multiplicative. The flat image is in this case replaced by an image recorded without sample in the beam, I_d^{blank}. In the case of absorption imaging, the intensity impinging on the detector is equal to the squared modulus of the transmission function of the object multiplied by the incident beam intensity. The recorded image is however convolved with the detector point spread function and the correction will not be perfect if both the object and incident beam contrast are strong. In the case of phase imaging, the contribution of the object and the incident intensity are only approximately multiplicative, because the imaging process is coherent. This flat field procedure improves however to a large extent the quality of the images and is adopted. The incident beam is nearly perfectly stable. Small motions with time of the beam impose to update the flat field image regularly. The approximations concerning the multiplication and the variations with time result in an imperfect correction for an image. This leads to artefacts in the tomographic reconstruction: rings centred around the rotation axis in the plane of rotation. A more rigorous flat-field procedure for absorption imaging includes a deconvolution for the detector response:

$$I_d^{\text{corr}}(\boldsymbol{x}) = \Re^{-1}\left(\frac{I_d^{\text{rec}}(\boldsymbol{x}) - I^{\text{dark}}(\boldsymbol{x})}{I^{\text{flat}}(\boldsymbol{x}) - I^{\text{dark}}(\boldsymbol{x})}\right) \Bigg/ \Re^{-1}\left(\frac{I_d^{\text{blank}}(\boldsymbol{x}) - I^{\text{dark}}(\boldsymbol{x})}{I^{\text{flat}}(\boldsymbol{x}) - I^{\text{dark}}(\boldsymbol{x})}\right) \tag{3.30}$$

where $\Re^{-1}$ denotes a deconvolution for the detector point spread function. This procedure increases the noise due to the large number of images involved and the deconvolutions. If I_d^{blank}, I^{flat} and I^{dark} are truly fixed patterns, they can be averaged over many observations and the noise increase is limited. A general correction, in the case of defocused images, includes in principle the holographic reconstruction. The wave amplitude exiting the object is determined from images with the object. Images without the object give similarly the wave incident on the sample. The ratio of both *amplitudes* gives access to the transmission function according to expression (2.20). The practical flat field procedure used is simply

$$I_d^{\mathrm{corr}}(\boldsymbol{x}) = \frac{I_d^{\mathrm{rec}}(\boldsymbol{x}) - \left\langle I^{\mathrm{dark}}(\boldsymbol{x})\right\rangle}{\left\langle I_d^{\mathrm{blank}}(\boldsymbol{x})\right\rangle - \left\langle I^{\mathrm{dark}}(\boldsymbol{x})\right\rangle} \tag{3.31}$$

followed eventually by a deconvolution. The averaging of the 'fixed' patterns avoids a noise increase.

3.4.1.2 Detective quantum efficiency and signal to noise ratio

The DQE is the signal to noise ratio (SNR) gain of the detector [Dai74, Arn79]:

$$\mathrm{DQE}(E, It, \boldsymbol{f}, \ldots) = \frac{\mathrm{SNR}_{\mathrm{out}}^{\;2}}{\mathrm{SNR}_{\mathrm{in}}^{\;2}} \tag{3.32}$$

It depends on the operating conditions of the detector through the energy, the spatial frequency ***f***, the exposure *It*, ... An ideal detector has the same SNR at the output compared to the input, hence DQE = 1. The signal to noise ratio at the input is determined by photon statistics. The number of incident photons obeys Poissonian statistics. The statistical error on a number of N_X incident X-ray photons is therefore $\sqrt{N_X}$. The latter value is equal to the SNR at the input. A low DQE increases the time necessary to obtain a sufficient signal to noise ratio in the output image. When the signal is predominant compared to the detector noise the DQE is equal to the fraction of incident photons that contributes to signal events. For X-ray detectors with high spatial resolution, this fraction is normally limited by the absorption in the active layer of the detector. The thickness is reduced to preserve the spatial resolution.

When the detection involves several conversion processes, a decrease of the DQE must be avoided in every step. This implies that the number of information carriers (photons, electrons,...) produced by a single incident X-ray photon must be at least 1 at all levels of the detector. The DQE can be expressed as a function of the gain G_i of each process and its relative variance $\mathrm{rv}(G_i)$. For a noiseless detector [Bre55, Arn74]

$$\mathrm{DQE} = \left[1 + \mathrm{rv}(G_1) + \frac{1}{G_1}\mathrm{rv}(G_2) + \frac{1}{G_1.G_2}\mathrm{rv}(G_3) + \ldots\right]^{-1} \tag{3.33}$$

with $\mathrm{rv}(G_i) = 1/G_i$ (Poisson statistics)
and $\mathrm{rv}(G_i) = (1-G_i)/G_i$ (binomial statistics)

with the processes ordered from the input to the output. A small DQE does not necessarily limit the obtainable signal to noise ratio. For a noiseless detector it is determined by the square root of the number of minority information carriers accumulated before saturation is reached. This is often the number of absorbed (not incident) photons that fill the dynamic range of the detector completely. A small DQE will increase the exposure time and dose required to obtain a given signal to noise ratio.

3.4.1.3 Detector transfer function and deconvolution

The frequency response of a (linear and spatially uniform) imaging system was introduced in § 2.2.5. For quantitative imaging it is necessary to consider the detector response. As the relationship between the object function and the image is non-linear (both for absorption and phase imaging), a blurring of the image by the detector does not simply result in a blurred reconstructed object, but it may introduce artefacts. It is therefore important to be able to measure the optical transfer function (OTF) and to correct for it in a deconvolution procedure. For qualitative imaging, deconvolution improves the visibility of fine details in the image.

Transfer function determination

It is not straightforward to realise a sinusoidal modulation of the X-ray intensity in order to measure directly the transfer function. At low spatial resolution a binary absorption grid is often used to measure the contrast transfer function that must be converted into the real transfer function [Dai74]. This method is not suited to measure the response over a large frequency range and at high spatial resolution because it is difficult to realise the corresponding absorption grids. Measuring the point spread function directly, on the other hand, requires two dimensional focusing of the X-rays to a submicron spot size without tails. This is presently not feasible with hard X-rays. An absorbing edge can quite easily be achieved even for fairly high X-ray energies. The advantages of an absorbing edge compared to another (phase) object are that the absorption image is independent of the coherence conditions and that the object is known. The edge spread function (ESF) $R_e(x)$, the response of the detector to a vertical totally absorbing edge, can easily be related to the line spread function (LSF) $R_l(x)$, response to a linear illumination

$$R_l(x) = \frac{\mathrm{d}R_e(x)}{\mathrm{d}x} \tag{3.34}$$

A line can be written as an integral of points. Using the assumption of linearity and spatial invariance the LSF can be obtained from the PSF $R(\mathrm{x},y)$ through integration over y

$$R_l(x) = \int R(x,y)\,\mathrm{d}y \tag{3.35}$$

Taking the Fourier transform of the LSF with respect to x yields the transfer function along the f-axis

$$\tilde{R}_l(f) = \tilde{R}(f,0) \tag{3.36}$$

If the detector response displays radial symmetry, hence if

$$R(x,y) = R\left(\sqrt{x^2+y^2}\right) \qquad \text{and} \qquad \tilde{R}(f,g) = \tilde{R}\left(\sqrt{f^2+g^2}\right), \tag{3.37}$$

a single measurement of the line spread function is sufficient to determine the transfer function (and PSF)

$$\tilde{R}\left(\sqrt{f^2+g^2}\right) = \tilde{R}_1\left(\sqrt{f^2+g^2}\right) \tag{3.38}$$

The PSF can then be determined from the transfer function by taking a two dimensional Fourier transform or, using the radial symmetry, a one dimensional Hankel transform [Dai74]

$$R(r) = 2\pi \int_0^\infty v\, \mathrm{J}_0(2\pi r v)\, \tilde{R}(v)\, \mathrm{d}v \tag{3.39}$$

with J_0 the Bessel function of the first kind of order zero. With the assumption of radial symmetry it is thus possible to determine the transfer function of the detector completely from the measured ESF (equations (3.34) and (3.38)). The line and point spread function have not necessarily the same shape and width. If there is no radial symmetry, the transfer function can still be determined from ESF's, measured now for a large number of orientations of the edge. Equation (3.35) is equivalent to equation (2.91) encountered in tomography (see § 2.3). The relationship between the spectra of the LSF and PSF corresponds to the Fourier-slice theorem (equation (2.94)). The two dimensional transfer function and the PSF can thus be retrieved with a particular kind of tomographic reconstruction. The symmetry assumption seems fair and was experimentally checked by setting the edge vertical and horizontal.

The derivative in equation (3.34) amplifies the high frequency noise in the measurement. The observed ESF is therefore fitted with analytical functions containing some unknown parameters. The analytic representation allows to switch easily from one detector function to another without new calculations or supplementary noise. A low noise level in the transfer function is important when it is used afterwards for a deconvolution. The ESF is written as a sum of error functions. With this choice the PSF, ESF and OTF simply correspond to a sum of gaussians. Other possibilities are found in literature [Boo94]. It is assumed that the images are normalised with respect to the incident beam. The ideal detector response is therefore equal to 0 for $x < x_0$ and equal to 1 for $x > x_0$ with x_0 the position of the edge. The expression used for the ESF is

$$R_\mathrm{e}(x) = c_1 + \sum_{p=1}^{J} \frac{b_p}{2}\left(1 + \mathrm{erf}\left(\frac{x - x_0}{\sqrt{2}\, a_p}\right)\right) \tag{3.40}$$

$$\text{with } b_J = c_2 - c_1 - \sum_{1}^{J-1} b_p \tag{3.41}$$

The constants c_1 and c_2 correspond to the value of the normalised intensity far from the edge, respectively in the non-illuminated and illuminated zone. They are ideally equal to respectively 0 and 1. The differences correspond to a small homogeneous background (about 1 %) in the image attributed to very long tails in the PSF or scattered light in the optical system. The *c*-values are set equal to the asymptotic values of the ESF. The other parameters (*a* and *b* values) are determined through minimisation of the squared differences between the observed and fitted values of the ESF. In order to obtain a better fit of the steep intensity variation at the edge the function to be minimised by the fit includes a term with the numerical derivative of the ESF. The parameter x_0 is identical for all terms in equation (3.40). The fitted curve has therefore the symmetry expected from the assumption of radial symmetry for the PSF. The fitting procedure rejects to some extent spurious contributions to the measured ESF, such as fluorescence from the edge. The image is recorded as close as possible (few mm) from the edge in order to avoid defocusing effects. The scattered radiation is on the other hand not avoided. The number of terms included J is normally set to 4. The height of the last term is not a free parameter but determined from the total height of the jump (equation (3.41)). The LSF, OTF and PSF can easily be expressed in terms of the determined parameters, they are respectively

$$R_1(x) = \sum_1^J b_p \frac{1}{\sqrt{2\pi}\, a_p} \exp\left(-\frac{x^2}{2\, a_p^2} \right) \tag{3.42}$$

$$\tilde{R}(v) = \sum_1^J b_p \exp(-2\pi^2 a_p^2 v^2) \tag{3.43}$$

and $$R(r) = \sum_1^J b_p \frac{1}{2\pi\, a_p^2} \exp\left(-\frac{r^2}{2\, a_p^2} \right) \tag{3.44}$$

Correction for the detector response

Image restoration aims at recovering an optimum estimate of the ideal image from a recorded image. The latter may be *blurred* due to the detector response and *noisy* due to the detector and/or due to photon statistics. An exhaustive literature exists, describing many algorithms to tackle the deconvolution problem. An overview can be found in [Jans97] and a description of their physical origin in [Mei86]. The transfer function of the detector is assumed to be known and the blind deconvolution methods, without complete knowledge of the OTF, are not considered. The available methods can be split into linear and non-linear methods. The first ones have the advantage to be direct and consequently fast, but they can not take advantage of general constraints. Taking into account a priori knowledge about the ideal image allows to restore images in the presence of more noise. General constraints give rise to the non-linear methods that do not consist in simple filtering of the images. They are recursive in most cases. The best known linear filter is the **Wiener-type filter**. It is the optimum linear method if the noise is additive and

Gaussian distributed. The inverse filter applied to the recorded image spectrum in order to retrieve the ideal image is [Jans97]

$$\tilde{Y}_{\mathrm{w}}(\boldsymbol{f}) = \frac{\tilde{R}^*}{|\tilde{R}|^2 + \dfrac{\phi_N}{\phi_I}} \tag{3.45}$$

with ϕ_I and ϕ_N the power spectra of respectively the ideal image and the noise, the image power spectrum is for example

$$\phi_I(\boldsymbol{f}) = |\tilde{I}(\boldsymbol{f})|^2 \tag{3.46}$$

If the power spectra are unknown the ratio ϕ_N / ϕ_I is sometimes replaced by a small constant. This method was occasionally used for deconvolutions (see § 4.2).

Many recursive methods use the discrepancy between the recorded image and the calculated image from a previous estimate of the ideal image to find a new estimate [Mei86]. The relationship can be linear, but it is simple to constrain a recursive method and to make it non-linear by applying the constraints between the recursion steps. The discrepancy between the recorded and the calculated image can be the numerical difference or the ratio. We used the following recursion formula, expressed in Fourier space, [Mei86]

$$\tilde{I}^{p+1}(\boldsymbol{f}) = \tilde{I}^p(\boldsymbol{f}) + C\tilde{R}^*(\boldsymbol{f})[\tilde{I}^{\mathrm{rec}}(\boldsymbol{f}) - \tilde{R}(\boldsymbol{f})\tilde{I}^p(\boldsymbol{f})] \tag{3.47}$$

It corresponds to Van Cittert's method with **reblurring** [Jans97]. The relaxation factor C is a positive constant. The expression between square brackets is the remaining error. Van Cittert initially considered $C = 1$ and no filtering of the remaining error. Reblurring with the conjugate of the transfer function itself removes noise at frequencies where the transfer function is small and where the recorded image carries little information on the ideal image. It is possible to write the estimate after p iterations explicitly as a function of the recorded image and the initial estimate $\tilde{I}^0$

$$\tilde{I}^p = \frac{1-(1-C|\tilde{R}|^2)^p}{\tilde{R}}\tilde{I}^{\mathrm{rec}} + (1-C|\tilde{R}|^2)^p\,\tilde{I}^0 \tag{3.48}$$

This recursion formula converges to a solution under the condition ($C > 0$)

$$C|\tilde{R}|^2 < 2 \tag{3.49}$$

The OTF being smaller than 1, the relaxation factor must be positive and smaller than 2. It is important to study the behaviour of the filter applied to $\tilde{I}^{\mathrm{rec}}$ in equation (3.48) as a function of p and C. When the transfer function is not close to zero, i.e. when $|\tilde{R}| > 1/\sqrt{Cp}$, the filter is simply equal to $1/\tilde{R}$, corresponding to a direct inversion of the convolution formula in Fourier space. The second term in expression (3.48) vanishes under this condition and the solution is independent of the initial estimate. For those spatial frequencies such that $|\tilde{R}| < 1/\sqrt{Cp}$, the restored image is approximately

$$\tilde{I}^{p} \approx Cp\tilde{R}^{*}\tilde{I}^{\mathrm{rec}}+\tilde{I}^{0} \tag{3.50}$$

Therefore, the contribution of the recorded image vanishes when the transfer function vanishes and the restored image is equal to the initial estimate for those frequencies. This occurs thanks to the reblurring without which the solution would diverge at zeros of the transfer function due to noise. To a good approximation, the maximum of the applied filter is reached for $|\tilde{R}| = 1/\sqrt{Cp}$ and it is

$$\tilde{Y}_{\max} \approx \sqrt{Cp}\,\frac{\mathrm{e}-1}{\mathrm{e}} \tag{3.51}$$

The best value for p consequently depends on the acceptable noise amplification. At spatial frequencies where the transfer function is small, reblurring will however suppress the noise. Better noise behaviour can be expected from a non-linear method. The non-linear constraints can be applied to the present estimate and the constrained estimate is used as a new initial estimate for the reblurring restoration. We propose the deconvolution procedure

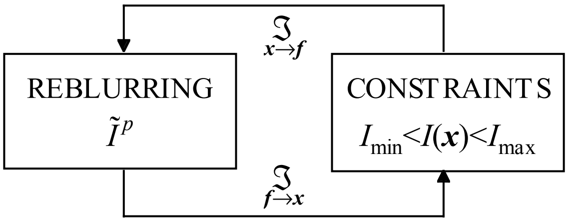

(3.52)

An important advantage of this scheme is the speed. The p reblurring iterations are implemented with a single filter (see expression (3.48)) and each loop needs only two 2D Fourier transforms. Constraints on the image intensity are most effective [Jans97]. Nonnegativity is applicable to any intensity image and the upper limit of 1 for the normalised intensity in an absorption image is another useful constraint (cf. equation (2.24)). The constraints are applied by simple clipping, i.e. the pixel value is set to the corresponding boundary value when the bounds are crossed. An optimisation consists in applying the constraints in a less abrupt way. This is for example done in Jansson's method [Jans97]. The nonnegativity is not implicit in expression (3.48) and negative values can be obtained without constraining.

The **Richardson-Lucy Algorithm** is an example of a non-linear method that intrinsically yields nonnegative results [Ric72]. It is deduced from Bayes's probability theorem and is adapted to Poisson processes. This is a good representation of the noise in the images when noise is limited by photon statistics. Negative values as number of counts have zero probability in a Poisson process. When the Richardson-Lucy method converges, it yields the image with the highest probability assuming Poisson statistics. The method is iterative and uses the *ratio* of the recorded image and its present estimation to yield a better estimate of the ideal image. Implemented with Fourier transforms, the present calculated image is

$$I^{\mathrm{rec},p} = \underset{f\to x}{\Im}[\tilde{R}\underset{x\to f}{\Im}(I^p)] \tag{3.53}$$

and the new estimate of the ideal image given by the Richardson-Lucy iteration is

$$I^{p+1} = I^p \underset{f\to x}{\Im}\left[\tilde{R}^* \underset{x\to f}{\Im}\left(\frac{I^{\mathrm{rec}}}{I^{\mathrm{rec},p}}\right)\right] \tag{3.54}$$

For each iteration step one has to perform four 2D Fourier transforms but acceleration techniques exist [Jans97]. The initial estimate of the image is normally the recorded image itself, i.e. $I^0 = I^{\mathrm{rec}}$. An interesting modification of the Richardson-Lucy method (or other iterative methods) consists in correcting the image only in these spatial regions where the recorded image and its estimate are still sufficiently different. This suppresses noise amplification when the number of iterations increases. Sufficiently different means more different than expected from the noise level. Other than Poisson distributed noise sources exist in the recorded image, such as additive gaussian noise due to the CCD read-out. Further benefit can be expected from methods that consider a more complete description of the image formation process with appropriate probability distributions for each contribution to the image.

The convergence can be monitored by the residual error in the estimation of the recorded image

$$R_{\mathrm{w}}{}^{p} = \left[\frac{<(I^{\mathrm{rec}} - I^{\mathrm{rec},p})^2>}{<(I^{\mathrm{rec}})^2>}\right]^{\frac{1}{2}} \tag{3.55}$$

with the angle brackets indicating the (weighted) mean in the image. The residual error, together with the computing time and the noise level in the estimated image, are used as termination criteria. An example of deconvolution for the detector response is given in § 3.4.2.3. In the case of images recorded at a series of distances for holographic reconstruction, the correction for the detector response can be included in the phase retrieval algorithm. This global solution is preferred to correction of the individual images before the holographic reconstruction (see § 4.2).

3.4.2 X-ray image converters

3.4.2.1 Principle

The principle of the presently described on-line detectors is a conversion of X-ray photons in visible photons that are detected with a charge coupled device (CCD). This conversion step is preferred to direct detection of the X-rays with the CCD for several reasons. The main ones are: 1) the number of electrons created for a single absorbed X-ray would be very large. Few X-ray photons lead to saturation of the detector and the SNR is extremely poor due to Poisson statistics, 2) the radiation damage for the CCD is unacceptable, 3) the smallest pixel size of CCD's available for direct detection is about 6 µm and consequently too large. The converter screen is coupled to the CCD by light optics. When using CCD's with a finite pixel number of N_{p} pixels, one makes intrinsically a compromise between the field of view, $N_{\mathrm{p}}.s_{\mathrm{p}}$ in width, and the obtainable resolution, the Shannon-Nyquist frequency being $1/(2s_p)$. The magnification of the light optics allows to realise the desired pixel size s_p.

The general principle of the detector systems is shown in Fig 3.6. The incident X-rays are partly absorbed in the active layer of the converter screen and create visible photons of a specific wavelength thanks to a scintillating element. The X-rays that are not absorbed in the active layer are stopped by the substrate of the converter screen or additional lead glass. The first lens system collects the light emitted by the scintillator screen and projects an image at infinity. The second lens system also works at infinity but at the entrance side. It focuses the image onto the active layer of the CCD. A mirror positioned between the two lens systems deflects the visible light beam by 90 degrees. The CCD and the second lens are thus not in the direct X-ray path in order to reduce further the direct interactions with the CCD and the radiation damage. The magnification realised by the light optics ranges from about 2 to 40. Coupling with fibre optics results in a higher gain, but it is not used because of the limited obtainable resolution, the strong fixed pattern, radiation damage and the impossibility to change easily the magnification. Too high a gain also reduces the obtainable signal to noise ratio.

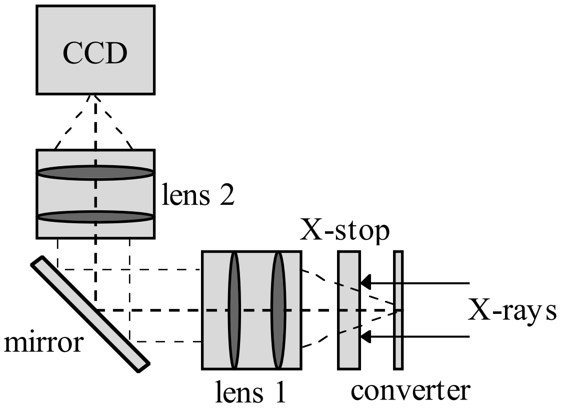

Fig 3.6 Principle of the detector system including an X-ray/visible light converter, an optical lens coupling and a cooled CCD camera.

3.4.2.2 Elements of the detector

The converter screen

Two kinds of scintillator screens are used: phosphor screens and transparent screens. Screens based on powder phosphors are used for resolutions down to about 5 µm. Structured screens were not used but simply thin layers of Gd_2O_2S:Tb (Gadox) grains deposited on 16 mm thick lead glass. The terbium doping assures the scintillation efficiency. The achievable resolution with such a screen is limited by scattering in the powder to about the thickness of the screen when the resolution is expressed in terms of the FWHM of the LSF [Swa73]. We used screens with a nominal thickness of 5 and 10 µm (supplier: Thomson, France). The packing density of the powders is only about half of that of the solid material. Fig 3.7 shows the absorbed energy fraction $\eta_{abs}(E)$ for several detector screens as a function of the X-ray energy. Only the X-ray attenuation corresponding to an effective energy deposition in the layer is considered. The characteristic X-ray radiation for example will most likely escape from the layer without creating visible light photons. The requirement of a thin layer to maintain good resolution clearly results in a decreased DQE (see below) for common converter materials.

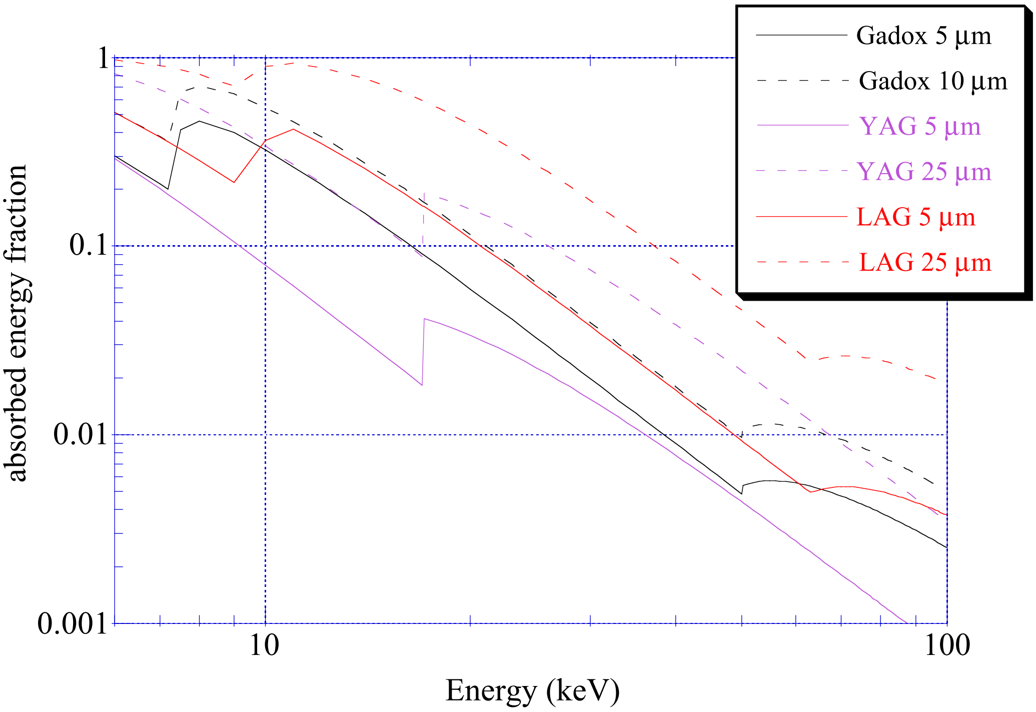

Fig 3.7 Fraction of the X-ray energy absorbed η_{abs} as a function of the energy for several powder (Gadox) and transparent (YAG and LAG) screens. They are presently used or under development (LAG).

The energy efficiency is high, about 10 % of the absorbed X-ray energy is converted into green light ($\lambda_{\text{v}} = 550$ nm). The gain of the X-ray/visible light conversion $\eta_{\text{X/v}}$ is the number of created visible light photons per absorbed X-ray. It can be expressed as

$$\eta_{\text{X/v}} = \varepsilon_{\text{X/v}} \frac{E}{E_{\text{v}}} \tag{3.56}$$

with E_{v} the energy of the visible photons and $\varepsilon_{\text{X/v}}$ the conversion efficiency. A phosphor surface behaves approximately as a Lambertian surface, the received light flux decreases proportionally to the cosine of the observation angle with respect to the normal. This directionality results in a better (factor 2) light collection efficiency compared to a transparent screen.

Better resolution can be achieved with transparent scintillator screens. In combination with an optical system which does not accept all angles of view (finite numerical aperture or *NA*), this can give a resolution better than the scintillator thickness. As pointed out in [Koc98], the same visible object is formed at different depths in the converter, although with gradually decreasing intensity due to attenuation of the X-rays. The light optics are focused on part of the active layer and planes downstream or upstream of the focused plane are out of focus. The thickness of the layer is thus limited by the depth of focus of the optical system. The depth of focus in the object space decreases proportionally to the inverse square of the *NA* according to [Müc97]

$$d_{\mathrm{foc}} = \frac{\lambda_{\mathrm{v}}\, n_{\mathrm{v}}}{(NA)^2} \tag{3.57}$$

with λ_{v} the wavelength of the light emitted by the scintillator and n_{v} the refractive index of the layer. Too small a *NA* on the other hand limits the light collection efficiency and the resolution. The transparent screens used are crystals of $Y_3Al_5O_{12}$ (YAG) doped with Cerium. A thin active layer is grown on a YAG substrate by liquid phase epitaxy (supplier: Crismatec, France). Layer thicknesses of 5 and 25 µm were realised. The characteristics of the converter screens used are tabulated in Table 3.3. An increased X-ray absorption (see Fig 3.7) is obtained by deposition of a heavier layer of doped $Lu_3Al_5O_{12}$ (LAG). The processing of the converter screens is the following: the YAG substrate surfaces are polished, then the YAG:Ce layer is deposited, only the 25 µm thick layers are polished and finally both surfaces are coated with an anti-reflection coating.

	Gadox	YAG
material	Gd_2O_2S:Tb	$Y_3Al_5O_{12}$:Ce
thickness	5 / 10 µm	5 / 25 µm
λ_{v}	550 nm	550 nm
n_{v}	(substrate: 1.5)	1.85
$\varepsilon_{\mathrm{X/v}}$	0.1	0.05
ρ (g/cm^3)	7	4.5
E edges (keV)	9.3 (L_I) 50.2 (K)	17.1 (K)
substrate	16 mm Pb glass	0.5 / 1 mm YAG

Table 3.3 Scintillator characteristics for Gadox powder phosphors and transparent YAG crystals.

The visible-light lens coupling

In combination with powder screens and pixel sizes above 5 µm, we used photography-type objectives specially developed for X-ray imaging. The optical magnification M_{v} in the set-up of Fig 3.6 is given by the ratio of the focal lengths of optical elements 2 and 1

$$M_{\mathrm{v}} = \frac{f_{\mathrm{v}\,2}}{f_{\mathrm{v}\,1}} \tag{3.58}$$

The use of bulky optics with a large entrance diameter is compatible with the large field of view required (> 5 mm at the entrance). This would not be the case with microscope objectives (see below). The light collection efficiency η_{col}, the fraction of the light collected by the lens system is determined by the *f*-numbers of the objectives (*f*-number = 1/(2*NA*)). For a Lambertian emitter it is given by

$$\eta_{\mathrm{col}} = \frac{1}{2}\min\left[\left(\frac{1}{2f\text{-number}_1}\right)^2, \left(\frac{M_{\mathrm{v}}}{2f\text{-number}_2}\right)^2\right] \tag{3.59}$$

where the minimum corresponds to the fact that the light cone collected by the first lens system should also be accepted by the second one. The transmission in the lens system is about 1. Table 3.4 lists the objectives used, their focal lengths and *f*-numbers. The magnifications are modest, 1.9 and 2.9 respectively with the 210 and 320 mm lens

function	type	f_{v} (mm)	*f*-number
lens 1 + mirror	Rodenstock XR-Heliflex	112	1.8
lens 2 M_{v}=1.9	Kinoptik	210	2.8
M_{v}=2.9	Rodenstock Rotelar	320	6.8

Table 3.4 Objectives used in combination with phosphor screens, their focal lengths and *f*-numbers.

To obtain a higher magnification with a smaller field of view, microscope objectives are better adapted. The case when they image a fluorescent layer of a transparent screen through this screen is of interest. The light collection efficiency of an objective with numerical aperture *NA* in combination with a transparent screen with refractive index n_{v} is

$$\eta_{\mathrm{col}} = \frac{1}{4}\left(\frac{NA}{n_{\mathrm{v}}}\right)^2 \tag{3.60}$$

type	M_{v}	*NA*	image at	cover	lens 2
LB ULWD CD Plan	20×	0.4	150 mm	0-2 mm	PE 1.67×
UIS LCPLFL	20×	0.4	∞	1.2 mm	Telan lens + PE 2×
UIS UPLFL	10×	0.3	∞	–	Telan lens + PE 2×

Table 3.5 Microscope objectives used as lens 1 in combination with transparent screens. The magnification corresponds to the nominal one. All objectives are manufactured by Olympus. PE stands for photo-eyepiece. The two first objectives are corrected for a (variable) cover glass thickness.

In order to obtain a given spatial resolution with a sufficient DQE, it is necessary to consider carefully the influence of three optical phenomena: diffraction, defocusing over the layer thickness and the aberration due to the substrate. It is introduced by the transparent screen which has a refractive index different from air. The resolution limit due to diffraction has the form [Müc97]

$$r = c\frac{\lambda_{\mathrm{v}}}{NA} \tag{3.61}$$

with c a constant close to 1 that depends on the resolution definition. This implies to use a high NA exactly opposite to the requirement of a small numerical aperture to maintain a large depth of focus (equation (3.57)). The optimum solution consists in choosing the smallest possible NA and maximum layer thickness w compatible with the required spatial resolution. Simulations indicate that the finite layer thickness will in an initial stage increase the tails in the PSF without affecting its FWHM. The tails correspond to an OTF value reduced well below the diffraction limit. A diffraction limited objective has the optical transfer function [Hop55]

$$\tilde{R}_{\mathrm{diff}}(\nu) = \frac{2}{\pi}\left[\arccos(\nu) - \nu\sqrt{1-\nu^2}\right] \qquad \nu = \frac{|f|}{f_{\mathrm{c}}} < 1 \qquad (3.62)$$

The spatial frequency is normalised by the cut-off spatial frequency f_{c}. The transfer function is exactly zero above this frequency

$$f_{\mathrm{c}} = \frac{2\,NA}{\lambda} \qquad (3.63)$$

This implies that the pupil function of the objective [Hop55, Bor80] is uniform within a circle determined by the NA and vanishes outside this circle. A defect of focus or aberrations disturb the uniformity of the pupil function and will lower the transfer function. It is possible to calculate the OTF when the pupil function is known, the OTF being its autocorrelation function. The case of an aberration free system with a defect of focus has been considered by Hopkins [Hop55]. The pupil function can be expressed as a function of the distance ρ_{p} with respect to its centre, normalised such that the pupil function vanishes for $\rho_{\mathrm{p}} > 1$. The system is characterised by the phase of the pupil function $\phi(\rho_{\mathrm{p}})$. If the defocus in the object plane equals z_{d}, this phase is

$$\phi(\rho_{\mathrm{p}}) = 2\pi\, w_0(z_{\mathrm{d}})\,\rho_{\mathrm{p}}^2 \qquad \rho_{\mathrm{p}} < 1 \qquad (3.64)$$

with $w_0(z_{\mathrm{d}}) = \frac{1}{2}\frac{(NA)^2}{\lambda_{\mathrm{v}}\, n_{\mathrm{v}}} z_{\mathrm{d}}$

The expression of the defocused transfer function can be found in [Hop55], the shape of the transfer function depends on the value of w_0 and is in general complicated, with negative values possible. The expansion of the transfer function as a function of the spatial frequency is [Hop55]

$$\tilde{R}(\nu) \approx 1 - \frac{4}{\pi}\nu - 8\pi^2 w_0^2(z_{\mathrm{d}})\,\nu^2 \qquad (3.65)$$

The first order term corresponds to the diffraction contribution, whereas the second order term corresponds to the contribution of the defect of focus. To obtain the actual transfer function, it must be averaged over the layer thickness t_{l}. This approach is exact because the imaging is incoherent and linear. If the focused plane corresponds to the middle of the layer, the average transfer function is

$$\tilde{R}(\nu) \approx 1 - \frac{4}{\pi}\nu - \frac{2}{3}\pi^2 w_0^2(t_\mathrm{l})\, \nu^2 \tag{3.66}$$

With equations (3.63) and (3.64) the transfer function can be expressed explicitly as a function of the spatial frequency f and the NA

$$\tilde{R}(f) \approx 1 - \frac{2}{\pi}\frac{\lambda_\mathrm{v} f}{NA} - \frac{\pi^2}{24}(NA)^2\left(\frac{t_\mathrm{l}}{n_\mathrm{v}}\right)^2 f^2 \tag{3.67}$$

A reasonable design goal is to impose a minimum value ε_m to the transfer function up to a certain spatial frequency f_m

$$\tilde{R}(f) > \varepsilon_\mathrm{m} \qquad \forall f < f_\mathrm{m} \tag{3.68}$$

and to realise this with the thickest possible layer. Setting expression (3.67) for the transfer function equal to ε for $f = f_\mathrm{m}$ yields an expression of the layer thickness t_l as a function of the NA in order to respect the imposed constraint. The maximum of this expression is reached for the optimum numerical aperture

$$NA_\mathrm{opt} = \frac{3}{\pi\,(1-\varepsilon_\mathrm{m})}\lambda_\mathrm{v} f_\mathrm{m} \tag{3.69}$$

and the largest acceptable layer thickness is

$$t_\mathrm{l,opt} = \frac{\sqrt{8}\,(1-\varepsilon_\mathrm{m})^{3/2}}{3}\frac{n_\mathrm{v}}{\lambda_\mathrm{v} f_\mathrm{m}^2} = \frac{3\sqrt{8}}{\pi^2\sqrt{1-\varepsilon_\mathrm{m}}}\frac{\lambda_\mathrm{v}\, n_\mathrm{v}}{(NA)^2_\mathrm{opt}} \tag{3.70}$$

The latter expression is in agreement with the usual definition of the depth of focus (expression (3.57)). The high refractive index of YAG is an advantage with respect to the defect of focus. In order to obtain for example a transfer function not smaller than 0.5 up to a frequency of 250 lp/mm (0.25 μm^{-1}), the optimum NA is about 0.25 for a maximum thickness of 20 μm. Working with a smaller optical wavelength allows to reach a better resolution and/or to use a thicker layer.

The aberrations of the objective itself are very small for state-of-the-art microscope objectives. The infinity corrected 20× objective listed in Table 3.5 was checked using an interferometric set-up. The parasitic phase of the pupil function was found to be smaller than $2\pi/20$ [Hig97] and is consequently negligible. The substrate of the converter screen can however introduce an aberration. At the exit face the refractive index changes from n_v to 1. Due to refraction the rays with an important angle with respect to the optical axis originate apparently from a different depth in the screen. The shift of focus due to a substrate with thickness t_b is from simple geometrical considerations

$$\Delta z = t_\mathrm{b}\left[1 - \frac{\tan(\theta_\mathrm{s})}{\tan(\theta_\mathrm{a})}\right] \tag{3.71}$$

with θ_s and θ_a the angles of the ray respectively in the screen and in air. The ratio of the sines of these angles is given by Snell-Descartes's law. The focus shift is therefore approximately

$$\Delta z \approx t_b \frac{n_v - 1}{n_v} + t_b \frac{n_v^2 - 1}{2\, n_v^3} \sin^2(\theta_a) \tag{3.72}$$

The first term corresponds to a fixed change of the plane of focus. The second term corresponds to the angle dependent variation of the focus and corresponds formally to spherical aberration. The variation of focus should be small compared to the layer thickness for all collected rays ($\sin\theta_a < NA$). The spherical aberration is expected to be negligible compared to the defect of focus in the layer when

$$t_b \frac{n_v^2 - 1}{2\, n_v^2} (NA)^2 << t_l \tag{3.73}$$

The layer thickness is divided by its refractive index because expression (3.72) gives the equivalent focus shift in *air*. With an NA of 0.25 and a layer thickness of 20 µm, the substrate should be thinner than 900 µm. The phase in the pupil function introduced by the variation in focus is, using $\sin\theta_a = NA\ \rho_p$ and expression (3.64),

$$\phi(\rho_p) = 2\pi A_s \rho_p^4 \qquad \rho_p < 1 \tag{3.74}$$

with $A_s = \frac{1}{4}\frac{t_b}{\lambda_v}(NA)^4 \frac{n_v^2 - 1}{n_v^3}$

This corresponds to the formal definition of spherical aberration [Bor80]. Including both spherical aberration and defect of focus yields the following phase of the pupil function

$$\phi(\rho_p) = 2\pi \left[A_s \rho_p^4 + w_0(z_d)\, \rho_p^2 \right] \qquad \rho_p < 1 \tag{3.75}$$

where $z_d = 0$ corresponds to the in-focus setting for paraxial rays. The effect of spherical aberration and defect of focus on the transfer function is shown in [Bla57] with numerical simulations. It is again possible to consider an expansion of the transfer function valid for small spatial frequencies:

$$\tilde{R}(\nu) \approx 1 - \frac{4}{\pi}\nu - 8\pi^2 \left[w_0^2(z_d) + \frac{8}{3} w_0(z_d)\, A_s + 2 A_s^2 \right] \nu^2 \tag{3.76}$$

The defect of focus can partly compensate the spherical aberration. According to the expansion the highest transfer function at low frequencies is obtained for a defocus such that $w_0(z_d) = -\frac{4}{3}A_s$. The response must again be averaged over the layer thickness. It is assumed that the layer is very thin compared to the complete substrate ($t_l << t_b$), hence that A_s is independent of the depth in the layer. The middle of the layer can be displaced by an amount z_f from paraxial focusing in order to optimise the response. The expansion of the averaged transfer function is

$$\tilde{R}(\nu) \approx 1 - \frac{4}{\pi}\nu - 8\pi^2 \left[w_0^2(z_f) + \frac{8}{3} w_0(z_f)\, A_s + 2 A_s^2 + \frac{1}{12} w_0^2(t_l) \right] \nu^2 \tag{3.77}$$

At the optimum layer position z_f the expansion is

$$\tilde{R}(\nu) \approx 1 - \frac{4}{\pi}\nu \; - \frac{2}{3}\pi^2\,[w_0^2(t_l) + \frac{8}{3}A_s^2]\,\nu^2 \tag{3.78}$$

This expansion can be compared with (3.66), valid in the absence of spherical aberration. The condition to preserve 80 % of the contrast at the spatial frequency f yields an upper limit to A_s and the (uncorrected) substrate thickness

$$A_s < 0.21\frac{NA}{\lambda_v f} \qquad \text{hence} \qquad t_b < 0.85\,\frac{n_v^3}{n_v^2 - 1}\,\frac{1}{(NA)^3 f} \tag{3.79}$$

This limitation must be considered especially when using a high numerical aperture. If one accepts some deterioration of the response due to the defect of focus in the layer, the decrease in contrast due to the spherical aberration is smaller than the one due to defocusing if

$$A_s < \sqrt{\frac{3}{8}}\,w_0(t_l) \qquad \text{hence} \qquad t_b < \sqrt{\frac{3}{2}}\,\frac{n_v^2}{n_v^2 - 1}\,\frac{t_l}{(NA)^2} \tag{3.80}$$

Commercial microscope objectives are either not corrected for this kind of spherical aberration, or corrected for a fixed cover glass thickness ($t_b = 170$ µm) and refractive index $n_v = 1.5$. Some objectives allow to correct for variable glass thicknesses (see Table 3.5).

The CCD camera

Quantitative imaging applications, such as X-ray tomography and holography, require a digitisation with a large dynamic range and a low noise. The dynamic range of the detector should therefore be large (12 bits or more) and the read-out noise should be small [about 1 grey level or 1 adu (analog digital unit)]. The additional noise accumulated during the exposure must remain small compared to the signal over a large range of exposure times. The noise characteristics of the images are then limited by photon statistics, rather than the characteristics of the camera, and one gets the best out of the available X-rays. Dynamic ranges of 16 bits (65000:1) can be reached with cooled (e.g. -40°C) slow scan CCD-cameras. They are read at a typical speed of 200 kpixels/s, yielding a total read-out time of 5 - 10 seconds. For real-time experiments and when it is necessary to collect a large number of images as for tomography, slow scan cameras are thus excluded. Exposure times as small as 100 ms can be sufficient and a detector with a comparable read-out time is necessary. Plain video cameras take images at a rate of 25 images/s but their dynamic range is poor (7-8 bits). Up to recently it was therefore necessary to make a compromise between a low noise level and a short read-out time. The Frelon camera, developed at ESRF by the group of J.C. Labiche, allows to overcome this limitation and offers a real dynamic range of 14 bits (16000:1) with a read-out time of 50 ms (20 Mpixels/s) [Lab96]. The humble-bee (frelon in French) is optimised to collect images with Fast REad-out and LOw Noise. These noise characteristics, comparable with those offered by most slow scan cameras, are achieved by the choice of Thomson CCDs (initially TH7896A-H) and adapted signal processing and analog electronics. The 1024×1024 pixels CCD and the whole camera have four independent channels, each reading one quarter of the image. This results in a quadruple read-out speed. The electronic design uses standard technology but in an optimised way. For most applications we used this camera while reading with only one channel in 200 ms. The camera is Peltier cooled to -20°C in order to reduce the dark current. The transmission between the camera and workstation is done by fibre coupling. This assures galvanic insulation of the camera from the outer world and is compatible with the high data transfer rate (40 Mbytes/s). It also admits a long working distance between camera and workstation. The gain of the CCD as visible light to electron converter can be expressed as the average number of electrons created for one incident visible light photon $\eta_{\mathrm{v/e}}$. At a wavelength of 550 nm (emitted by the converter screen) this gain is about 0.3. The response of good quality CCD chips in terms of the spatial distribution of the incident light is approximately ideal. This means that each pixel gives a signal proportional to the incident light intensity integrated over the pixel surface. The PSF, the response to a pencil beam, of the CCD is consequently a square box corresponding to one pixel. This analog step (integration on CCD) is followed by a two-dimensional discretisation with the usual folding of the Fourier spectrum on itself and a risk of aliasing if the Shannon-Nyquist condition is not fulfilled [Dai74]. The ideal CCD transfer function approaches the Fourier transform of a square

$$\tilde{R}(f,g) = \frac{\sin(\pi s_{\mathrm{p}} f)}{\pi s_{\mathrm{p}} f} \frac{\sin(\pi s_{\mathrm{p}} g)}{\pi s_{\mathrm{p}} g} \tag{3.81}$$

with s_{p} the pixel size (at the level of the converter). At the Nyquist frequency ($1/(2s_{\mathrm{p}})$), corresponding to half the sampling frequency, the transfer function is equal to 0.64.

The electrons collected in the CCD without illumination during long exposures (dark current) introduce additional noise and loss of dynamic range when the exposure is longer than about 10 s with the camera working in normal mode. Our need for a single camera operating over a large range of exposure times with 14 bit dynamic range accelerated the development of an adapted Frelon camera with a smaller dark current. This was realised using MPP (multi-pinned phase) technology. Applying a potential to the CCD substrate reduces on the other hand the dynamic range. The characteristics of both types of cameras and a 2048×2048 camera currently being developed are listed in Table 3.6.

Type	Normal 1024×1024	MPP 1024×1024	MPP 2048×2048
Dynamic range	14800	12000	16000
Gain	40 e^- / adu	22 e^- / adu	20 e^- / adu
Read-out noise	44 e^- - 1.1 adu	31 e^- - 1.4 adu	20 e^- - 1 adu
Dark current	200 e^- / s	3 e^- / s	3 e^- / s
Full well capacity	6 10^5 e^-	3.5 10^5 e^-	3.2 10^5 e^-
Non linearity	+/– 0.4 %	+/– 0.5 %	+/– 0.5 %
PRNU	0.3 %	0.5 %	0.5 %
CCD	TH7896A-(H)	TH7896M-(H)	TH7899M-(H)
Pixel surface	(19 µm)^2	(19 µm)^2	(14 µm)^2

Table 3.6 Main characteristics of the CCD cameras used. The MPP version is preferred for exposure times > 10 s. The 2048×2048 is under development. The figures can be obtained at a read-out speed of 20 Mpixels/s. The non linearity indicates the maximum error range valid over the complete dynamic range (e^- stands for electrons, 1 adu corresponds to 1 grey level). The pixel response non-uniformity (PRNU) characterises the non-uniformity in the gain of the different pixels.

The standard acquisition system is a EDT-SDV board plugged into the SUN workstation. In this case, only one of the four available channels is operating and the read-out speed is 5 Mpixels/s. The images are stored with 2 bytes for each pixel, corresponding to 2 Mbytes for a single image. For real-time experiments the images are stored in the RAM memory at a maximum rate of 3.5 images/s (1024×1024 pixels). For tomographic acquisitions the images are either stored locally on a hard disk, or transmitted on the computer cluster through ATM.

Different non-standard solutions were developed to use the camera in four channel mode and to read at the maximum speed of 20 Mpixels/s. A VME system based on the VCCD3 card, developed at ESRF [Her95] was used. This card allows to rebuild the 14 bits images and store them in a buffer memory at the maximum rate of the camera (17 images/s ≈ 40 Mbytes/s). A 8-bit real-time video-display allows to follow and track dynamical events. A trial experiment was performed exploring the possibilities of *real-time phase sensitive radiography* [Clo98a]. The 10 µm optics were used (see below) in order to obtain the smallest possible exposure time. This time was varied between 10 and 100 ms. An adapted laser-type shutter was used to avoid exposure during read-out time. We tried to recreate the conditions of a real experiment in which we would have some phase objects which move in some unpredictable way and whose behaviour we were interested to track at a given moment. We found these characteristics in the gas bubbles which appear inside a glass of white beer. Fig 3.8 shows a series of images of a region in the beer where new bubbles appear. The exposure time of 50 ms yields, together with the readout time, a lapse of time of 100 ms between consecutive images. The sample-detector distance was set to 2.5 m and the phase sensitive images are obtained in the edge detection regime, where black/white contrast appears at the border of the gas bubbles. The emerging bubble can be recognised when it has a diameter of 30 µm and we can perfectly track its movement as it grows up to a diameter of 150 µm while its speed increases. Of course, when this speed becomes too high, the contrast arising from the bubble becomes less defined, but is still appreciable.

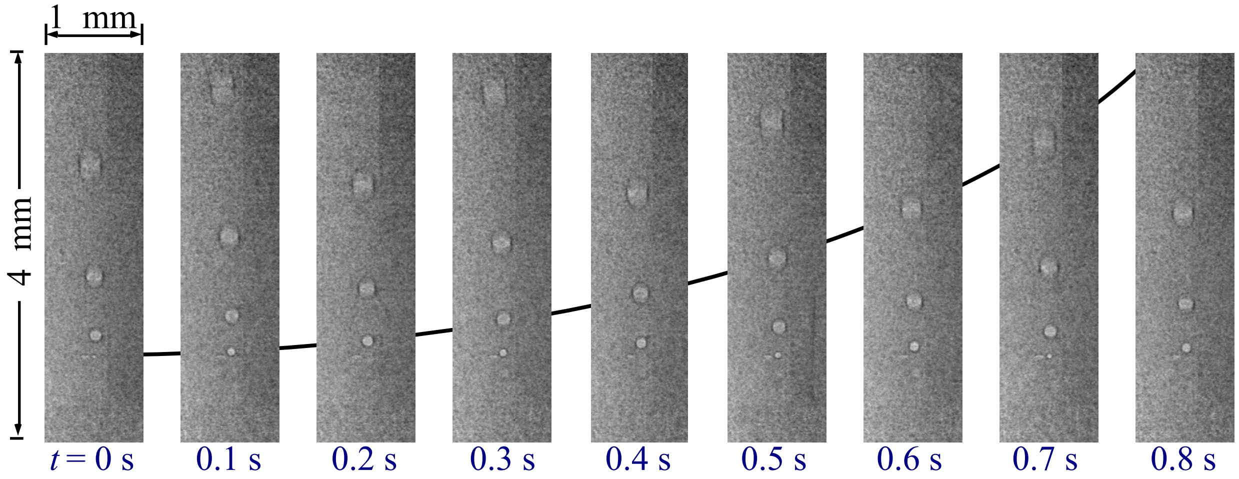

Fig 3.8 Region of interest of a series of phase sensitive images showing the formation and evolution of gas bubbles inside white beer. The time lapse between the images is 100 ms (50 ms for both read-out and exposure). The interpolated track of one bubble is indicated. Sample camera distance d = 2.5 m, X-ray energy E = 20 keV.

Gain and DQE

The number of electrons per pixel N_e as a function of the exposure can simply be obtained by multiplication of the 'gains' of the different conversion steps [Swa73]. Under homogeneous illumination it is given by

$$\frac{N_e}{It} = s_p^2 \, \eta_{abs}(E) \; \varepsilon_{X/v} \frac{E}{E_v} \; \eta_{col} \; \eta_{v/e} \tag{3.82}$$

The first term is the pixel surface at the converter level, the second term is the absorbed energy fraction in the layer. The following terms correspond respectively to the deposited energy-visible light conversion, the light collection by the optics and the visible light-electron conversion in the CCD. Note that without the first term this expression corresponds to the total number of electrons created per *incident* X-ray photon, whereas without the first two terms it corresponds to the number of electrons created per *absorbed* X-ray photon, denoted $\eta_{X/e}$. It is possible to estimate the important value of the DQE with expression (3.33) when the detector noise is negligible. The number of X-rays and of created visible photons and electrons follow Poisson statistics, whereas the other processes are ruled by binomial statistics. Recombination of the terms in expression (3.33) yields (see also [Koc98])

$$\mathrm{DQE}(E) = \eta_{\mathrm{abs}}(E)\left[1+\frac{1+\eta_{\mathrm{v/e}}}{\varepsilon_{\mathrm{X/v}}\dfrac{E}{E_{\mathrm{v}}}\,\eta_{\mathrm{col}}\,\eta_{\mathrm{v/e}}}\right]^{-1} = \eta_{\mathrm{abs}}(E)\left[1+\frac{1+\eta_{\mathrm{v/e}}}{\eta_{\mathrm{X/e}}}\right]^{-1} \qquad (3.83)$$

The main factor limiting the DQE in such a detector is consequently the fraction of X-rays absorbed in the sensitive layer (see Fig 3.7). In order not to deteriorate further the DQE, the number of electrons created per absorbed X-ray photon $\eta_{\mathrm{X/e}}$ should be larger than 1 ($\eta_{\mathrm{v/e}} \approx 0.3$). This is normally the case. The low absorption in the converter screen limits the SNR in the recorded images when the dose on the sample is limited or if the exposure time becomes unacceptably long. If dose is not a constraint, the low DQE can simply be compensated for by increasing the incident flux or exposure time. The maximum number of electrons that can be collected in a pixel, N_{sat}, is called the full well capacity (see Table 3.6). The corresponding number of X-ray photons at the entrance can be deduced from the gain (expression (3.82)). The square of the SNR at the input is equal to this number (Poisson statistics). The best SNR at the output is obtained just before detector saturation

$$\mathrm{SNR}^2_{\mathrm{out}} = \mathrm{DQE}\; It\, s_{\mathrm{p}}^2 = \frac{N_{\mathrm{sat}}}{\eta_{\mathrm{X/e}}}\left[1+\frac{1+\eta_{\mathrm{v/e}}}{\eta_{\mathrm{X/e}}}\right]^{-1} = \frac{N_{\mathrm{sat}}}{1+\eta_{\mathrm{v/e}}+\eta_{\mathrm{X/e}}} \qquad (3.84)$$

Note that the low absorption efficiency disappeared from this expression and does not necessarily limit the obtainable SNR. It is rather limited by the number of electrons per absorbed X-ray, which should not be too *large*. We assumed the detector noise to be negligible. This requires a minimum exposure. The variance of the number of signal electrons is N_{e} (given by expression 3.82), whereas the detector noise is $\sigma_{\mathrm{er}}^2 + S_{\mathrm{ed}}\, t$ (see Table 3.6). The first noise term corresponds to the read-out noise whereas the second one corresponds to the dark current. The minimum exposure in order to overcome the detector noise is consequently

$$It > \frac{\sigma_{\mathrm{er}}^2 + S_{\mathrm{ed}}\, t}{s_{\mathrm{p}}^2\, \eta_{\mathrm{abs}}\, \eta_{\mathrm{X/e}}} \qquad (3.85)$$

This expression indicates the need of a high incident flux and/or a low (dark current) noise especially at high magnifications (effective pixel size s_{p} small).

3.4.2.3 The set-ups: efficiency, transfer function and deconvolution

10 µm set-up

This detector is build around a 5 or 10 µm thick Gadox screen together with a Rodenstock objective (lens 1, see Fig 3.6 and Table 3.4) and a Kinoptic objective (lens 2). The mirror is included in the first optical element. The motorised focusing is performed by adjusting the distance of the converter screen with respect to the first lens. The magnification is 1.9 and the effective pixel size is 10.1 µm. Vignetting is not observed within the 10 mm field of view. The light collection efficiency is 0.04 (expression (3.59)). This results in a maximum SNR per pixel of

240 at 18 keV (expression (3.84)). The use of a fibre coupling instead of a lens coupling can increase the light collection efficiency to about 0.5 but this would result in a deterioration of the SNR to only 70. The number of electrons created per absorbed X-ray photon of 18 keV is about 9. The DQE is thus at all energies limited to the absorbed energy fraction (see Fig 3.7). At 18 keV, the DQE is 0.14 and 0.07 respectively with a 10 and 5 μm thick screen. The calculated gain (expression (3.82)) is about 30 % higher than the measured value (see Table 3.7). It is useful to express the sensitivity as the energy density that must be absorbed in the converter screen in order to create 1 electron per pixel because this value is rather energy independent. It is about 19000 keV/mm^2. The smallest exposure to overcome the read-out noise (MPP, $E = 20$ keV and 10 μm Gadox) is about 10^7 ph/mm^2 (expression (3.85)). This corresponds for an incident monochromatic flux of 10^{10} ph/mm^2/s to an exposure time of 1 ms.

The detector response was determined with the image of an absorbing edge. Half of the beam was hidden with a cleaved 500 μm thick GaAs crystal. The edge-detector distance was minimised in order to avoid Fresnel diffraction. On the other hand some fluorescence can hit the scintillator. Fig 3.9 shows the measured ESF obtained with the 5 μm thick converter screen. The intensity profile was averaged over the image parallel to the edge direction. The response is in fact slightly better in the middle than for the borders and the detector response is not strictly shift invariant. The full line in Fig 3.9 corresponds to a fit of the ESF using expression (3.40) with 4 terms. The shape of the fitting curve does not correspond to a possible fluorescence distribution and such a fit rejects partly the fluorescence contribution.

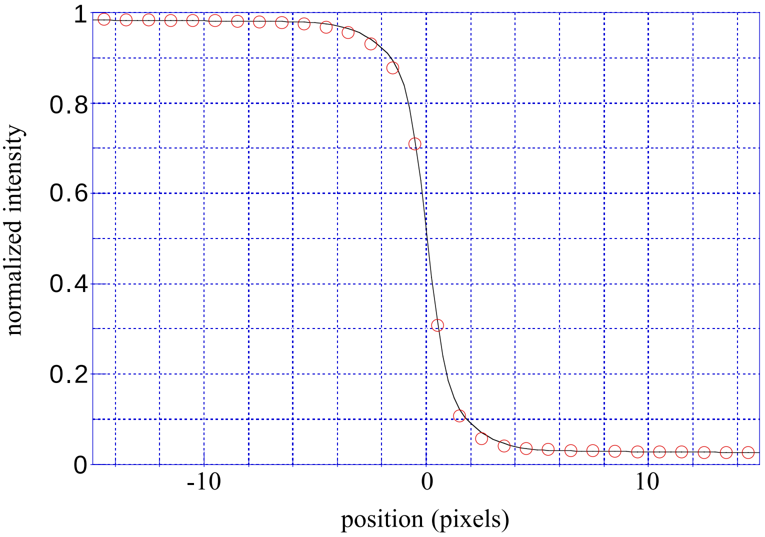

Fig 3.9 Normalised intensity profile along the direction perpendicular to an absorption edge. Half of the beam is stopped with a cleaved GaAs crystal. This corresponds to the edge spread function (ESF). The full line is obtained by fitting the ESF with equation (3.40). This procedure gives analytical expressions for the different response functions (LSF, PSF, OTF). $E = 20$ keV, $d \approx 0.02$ m.

From the fitting procedure the line and point spread functions can be obtained analytically (expressions (3.42)-(3.44)). This avoids problems in calculating the derivative in the presence of noise and with a finite sampling rate. The corresponding curves are shown in Fig 3.10. The width of the LSF and PSF are approximately equal when expressed as a FWHM. It is 1.6 pixels (16 µm). The tails of the LSF are however more pronounced compared to the PSF. It is not possible to obtain correctly the tails in the LSF by numerical differentiation of the ESF because the differences between the successive pixel values become too small. Working with finite differences gives an overestimated width of 1.8 pixels for the LSF. The 10 % level in the OTF (see Fig 3.10b) is reached at 0.47 f_s (46 lp/mm). The OTF curve is shown for frequencies smaller than the Nyquist frequency ($f_s/2$).

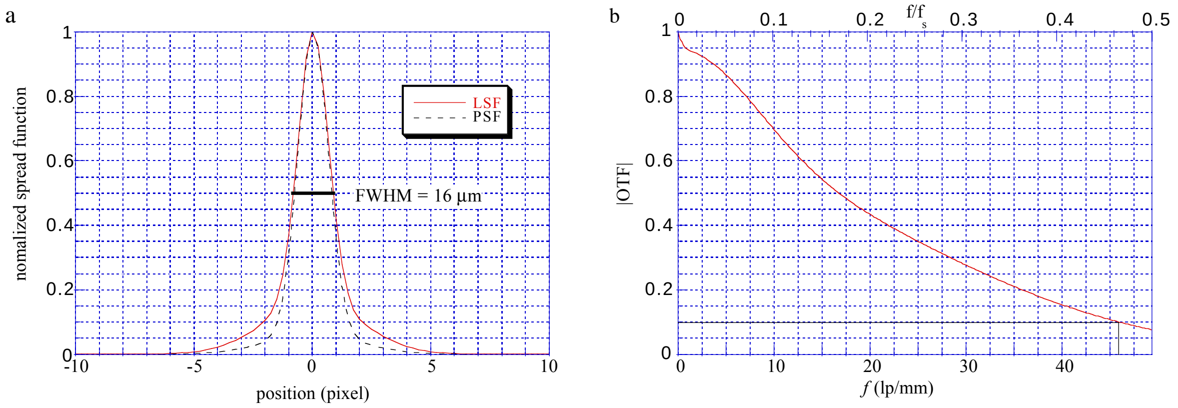

Fig 3.10 (a) Response of the 10 µm set-up in direct space, the point and line spread function. There maximum value is normalised to 1 in order to compare their shapes. (b) Response of the system in reciprocal space, the optical transfer function. The sampling frequency f_s is about 100 lp/mm.

<u>6.5 µm set-up</u>

This detector is very similar to the previous one with the second lens replaced by a 320 mm Rodenstock lens. The 5 µm thick Gadox screen is preferred in order to preserve the optimum resolution. The magnification is now 2.9 and the effective pixel size is 6.65 µm. Vignetting is not observed within the 6.8 mm field of view. The smaller light collection efficiency and the ratio of the pixel surfaces result in a gain 4 times smaller than in the 10 µm set-up. The number of electrons created per absorbed X-ray decreases to 5 at 18 keV. This reduces the DQE slightly (expression (3.83)), but results in a better SNR.

set-up	gain $e^-/(ph/mm^2)$	DQE	SNR	width LSF µm	10 % OTF lp/mm
10 µm	$4.8\ 10^{-5}$	0.07	240	16	46
0.7 µm	$1.5\ 10^{-8}$	0.02	460	1.5	410
1 µm	$7.5\ 10^{-8}$	0.07	530	2	340

Table 3.7 Some characteristics of the different detector configurations. The gain corresponds to the measured value (measured at respectively 20 keV, 18 keV and 18 keV) and is expressed as the ratio of the number of electrons collected per pixel and the exposure. The DQE is the calculated value at 18 keV using expression (3.83). The SNR is calculated with expression (3.84) for $N_{sat} = 6\ 10^5\ e^-$. The resolution is deduced from the measured edge spread function.

High resolution set-up

In this case the pixel size is of the order of 1 µm with a field of view of about 1 mm. The choice of the transparent screen, microscope objective and photo-eyepiece allows to select the spatial resolution and corresponding pixel size. In the set-up the converter screen is kept fixed and its mounting allows to approach the sample to about 1.5 mm for pure absorption images. The microscope objective with a long working distance is mounted on a translation stage. Focusing of the optical system is thus done by translating the objective. The stage is motorised with a resolution of about 0.25 µm and allows to focus automatically by optimising the image of an edge. A mirror deflects the visible light beam in the vertical direction. In combination with objectives corrected for finite distance (older type), the mirror is followed by a photo-eyepiece and the camera. With infinity corrected objectives (present type), the image at infinity from the objective is collected by a supplementary lens (Telan lens) followed by a photo-eyepiece and the camera. The camera is mounted on a manual tilt system in order to correct for angular errors of the optical elements with respect to the optical axis. The photo-eyepiece assures a more homogeneous image quality by correcting for field curvature [Bor80]. It also introduces supplementary magnification and thus allows to select the effective pixel size. The photo-eyepiece is sometimes removed from the system in order to magnify less when a large field of view is necessary.

The first high resolution experiments were performed with an objective (*NA* = 0.4) corrected for finite distance and a 5 µm thick sensitive YAG:Ce layer on a 1 mm thick substrate. The magnification used was about 26 yielding a pixel size of 0.7 µm. The light collection efficiency of the objective is 0.012 and the cut-off frequency is 1450 lp/mm. It is approximately equal to the sampling frequency. We used this system mainly at an energy of 18 keV in order to take benefit of the K-absorption edge of Yttrium. The calculated gain is about 80 % higher than the measured one. The exact origin of this discrepancy is not known.

The depth of focus as given by equation (3.57) is 6 µm for this objective. It seems thus well adapted to the 5 µm thick converter screen. The effect of defocus is characterised by the dimensionless number $w_0(t_1)$ equal to 0.4 in this case (equation (3.64)). At the Nyquist frequency ($\nu \approx 0.5$) we expect a decrease in the OTF of the order of 60 % due to diffraction and 25 % due to defocus (equation (3.67)). The obtainable OTF should be close to the one imposed by the diffraction limit. Simulations performed with optical design software confirm this and give a width of 0.7 µm for the LSF before sampling. The spherical aberration introduced by the 1 mm thick substrate is important. It can be characterised by the dimensionless number A_s which has a value of 4.5. The adjustable collar on the objective to correct for cover glass thicknesses is consequently very important. In order to limit the effect of spherical aberration to the one of the defocusing, the remaining A_s value should be smaller than 0.24 (equation (3.80)). This corresponds to an uncorrected substrate thickness of 50 µm.

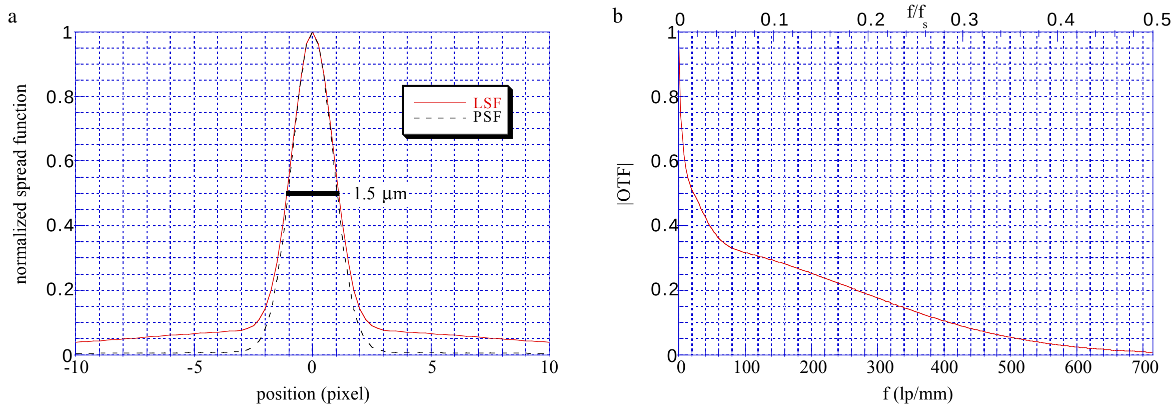

Fig 3.11 (a) LSF and PSF of the 0.7 µm pixel set-up (*NA* = 0.4, 5 µm thick YAG). The width of both spread functions is about 1.5 µm. Pronounced tails appear in the LSF. (b) OTF of this detector indicating a early drop in the contrast. Sufficient contrast remains up to a spatial frequency of 410 lp/mm (10 % limit).

Fig 3.11 shows the LSF and PSF obtained at an X-ray energy of 18 keV with the absorbing edge procedure. The edge spread function was obtained by averaging the intensity profile over 100 lines in a central part of the detector. The most outer lines of the detector give only slightly worse figures. The widths of the spread functions are narrow: 1.5 µm FWHM in both cases. Long tails can however be observed in the line spread function. This corresponds to a drop and fast decrease of the OTF at frequencies well below those expected from diffraction or defocusing in a 5 µm thick layer. Two main origins for the long tails appearing with transparent converter plates were suggested. 1) Total internal reflection occurs for a large fraction of the fluorescence light created in the YAG:Ce layer because of the high refractive index of YAG. This light is captured between the parallel surfaces limiting the crystal and ideally leaves the crystal at its extremities. In reality it can leave the plate when it encounters imperfections [Dab96]. Both sides of the YAG crystal were polished before the deposition of the sensitive layer. The latter was to thin to be polished after the growth. One surface was therefore not perfect. 2) The substrate may be slightly fluorescent itself due to impurities. Only a small fraction of the X-rays is stopped in the doped layer. Thus weaker but strongly defocused contributions can occur if the substrate fluoresces. The penetration depth ($1/\mu_{abs}$) of the X-rays in the YAG crystal is about 125 µm at 18 keV.

In order to increase the DQE of the detector and to obtain shorter exposure times, the converter screen is replaced by a 25 µm thick layer in combination with an infinity corrected objective ($NA = 0.3$). With a total magnification of 20 the effective pixel size is 0.95 µm. The cut-off frequency is 1090 lp/mm. The absorbed fraction in the layer increases by a factor of 5 to 18 %. The light collection efficiency of 6.6 10^{-3} is smaller due to the smaller numerical aperture of the objective. It is not possible to increase the *NA* because of the depth of focus. The number of electrons created per absorbed X-ray photon is 0.8. This small value deteriorates the DQE, but there is still a gain of 3.5 compared to the previous system ($NA = 0.4$, $t_l = 5$ µm). The depth of focus as given by equation (3.57) is 11 µm. The value of $w_0(t_l)$ is equal to 1.1. Defocusing deteriorates slightly the response compared to a diffraction limited system. The objective is not corrected for the presence of a plate with a different refractive index. The 500 µm thick substrate introduces spherical aberration with $A_s = 0.7$, a rather low value.

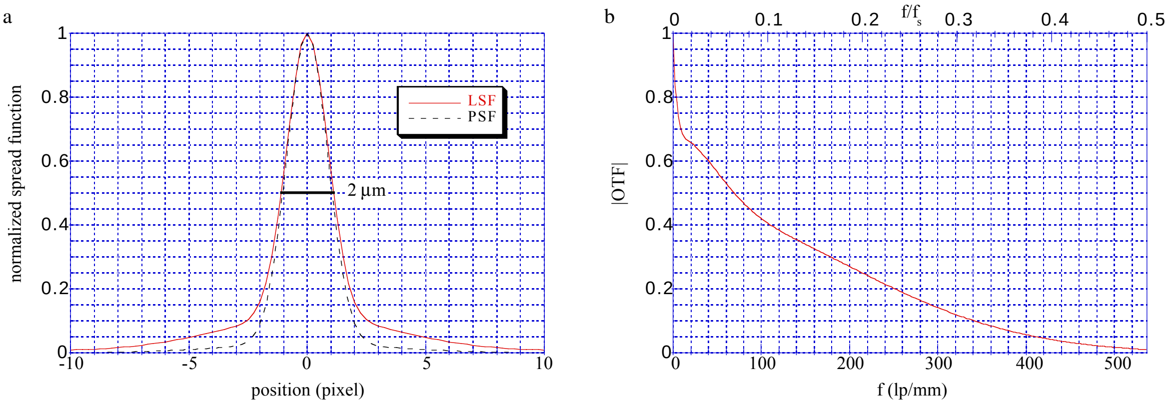

Fig 3.12 (a) LSF and PSF of the 0.95 µm pixel set-up ($NA = 0.3$, 25 µm thick YAG). The width of both spread functions is 2 µm. The tails appearing in the LSF are less pronounced, but still appreciable. (b) OTF of this detector indicating an early drop 30 % in the contrast. Sufficient contrast remains up to a spatial frequency of 340 lp/mm (10 % limit).

The spread functions represented in Fig 3.12a indicate a slight increase in the width of the LSF and PSF. The optics limit ideally the width to 1.3 µm. This figure can anyway not be reached because of the pixel size used. The tails in the LSF, although still present, are weaker in this case. This is attributed to a better surface quality of the converter screen. Because of the thicker sensitive layer it was possible to polish the surface after the growth. The improvement can also be seen in the transfer function (Fig 3.12b). The OTF drops to 0.7 at low frequencies, compared to 0.4 for the 5 µm thick layer it is about. The best value of 0.9 is reached with the Gadox screen.

Deconvolution

Thanks to the relatively low noise level of the recorded images it is possible to correct for the detector response with a deconvolution procedure. It is especially useful to correct for the tails in the spread functions of detectors based on transparent screens. Special attention was given to the method of constrained reblurring and the Richardson-Lucy algorithm (see § 3.4.1.3). The results shown correspond to images obtained with the 5 µm thick YAG layer and the 10 × objective. No eyepiece was used and this gave an effective pixel size of about 2 µm. The sample consisted of a 1 mm thick piece of polystyrene. A hologram recorded at a sample-detector distance of 0.83 m was tentatively corrected for the detector response. The reconstruction of the phase modulation introduced by this sample is given in § 4.2. Here the purpose is only to obtain values in the image that are as close as possible to the relative intensity impinging on the detector. Fig 3.13a shows the recorded image. The only processing is the flat-field correction. An analytical approximation of the transfer function was obtained with the edge procedure. The image b is obtained from the recorded image with the constrained reblurring method (3.52) using this OTF. The improvement in contrast and visibility of details is evident. The recovered image is also in better agreement with the measured OTF. The residual error R_w (defined by expression (3.55)) is 0.11 for the recorded image. It decreases to 0.015 in the recovered image after only four iterations. The only constraint used is positivity. This constraint is necessary; the final image has values in the range between 0 and 3.7 whereas the original image was limited between 0.5 and 2. The average intensity in these normalised phase images is 1 of course. The number of intermediate reblurring operations was set to 10 with a relaxation factor $C = 1$. These operations were implemented with a single filter. With our choice of parameters the filter has a reasonable maximum value of 2 (expression (3.51)). The total number of 2D Fourier transforms to obtain the recovered image was 8. The noise in the recovered image is higher for some spatial frequencies but still acceptable. The Richardson-Lucy algorithm was employed on the same image. The recovered image is essentially equivalent but the same residual error is only obtained after about 40 iterations and 160 2D Fourier transforms. In this case the recovered image is intrinsically positive (minimum recovered value = 0.04). The maximum value is 3.9 and close to the value obtained with the reblurring method. The Richardson-Lucy algorithm gives a recovered image with the same noise characteristics as obtained by reblurring. In this case there is no benefit in the Richardson-Lucy algorithm and the constrained reblurring method is preferred because of the much higher speed.

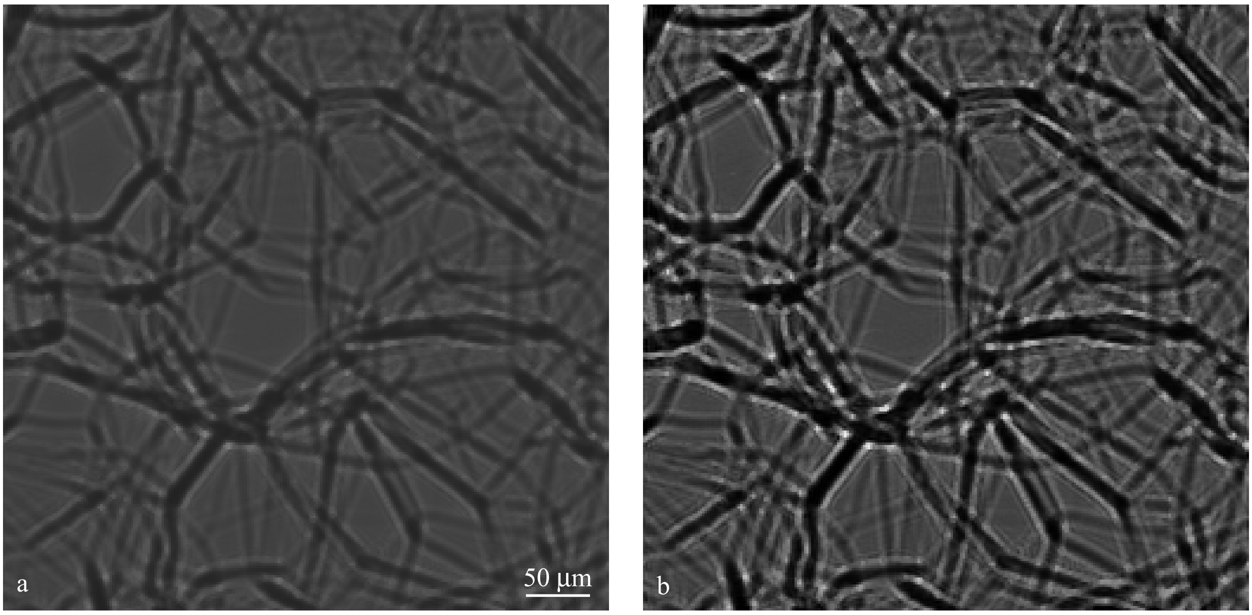

Fig 3.13 Recorded (a) and recovered (b) Fresnel diffraction patterns of a piece of polystyrene foam. The deconvolution is performed with the constrained reblurring method (expression (3.52), $C = 1$, $p = 10$, positivity constraint). The OTF of the detector was previously determined under an analytical form from the edge spread function. The images are presented with identical contrast. The deconvolution requires 8 2D Fourier transforms. $E = 18$ keV, $d = 0.91$ m, pixel size ≈ 2 µm.

Conclusion and possible improvements

CCD-based detectors are a tremendous step forward compared to film with respect to the obtainable linearity, signal to noise ratio, the possibility of real-time imaging ... The flat-field procedure allows to image small contrast variations when a (parasitic) background is present. In the presented set-ups the pixel-size is rather large compared to the intrinsic resolution of the detector before sampling. This is done in order to maintain a sufficiently large field of view. Therefore a risk of aliasing exists. However this effect is attenuated in the case of CCD based detectors because of the averaging over the physical pixels and equation (3.81) can be considered as an anti-aliasing filter. In the case of microscope objectives a solution consists in chosing the cut-off frequency of the objective (equation(3.63)) equal to the Nyquist frequency ($1/(2s_p)$) in order to supress all high spatial frequencies that can be confused with low spatial frequencies. This will be possible, keeping in mind the field of view, when a 2048×2048 camera is available. The set-ups with medium resolution (10 and 6.5 µm pixel sizes) with a powder phosphor as converter screen perform very well regarding the shape of the transfer function and the achievable SNR. Their DQE is limited because of the small energy absorption in the powder screen. A possible improvement of these detectors consists in replacing the converter with a more absorbing (structured) screen that should not deteriorate the spatial resolution. A resolution of the order of 1 µm is easily obtained with films. This is less straightforward with on-line X-ray image converters. Transparent luminescent screens allow in principle to obtain a resolution which is significantly better than their thickness. The choice of microscope objective is based on a compromise between the resolving power as limited by diffraction and by defocusing in the converter. Our set-up with a 5 µm thick sensitive YAG layer has a narrow PSF (1.5 µm). It performs however below the theoretical expectations, especially due to the presence of long tails in the LSF. The origin is probably total internal reflections in the YAG crystal and a bad surface quality. Another explanation is (weak) luminescence of the YAG substrate. The use of a well polished screen is a straightforward improvement and was shown to be effective for the 25 µm thick converter screen. It performs very well in combination with a 10× ($NA = 0.3$) objective. The tails are weaker and can possibly further be reduced by the deposition of a light absorbing, index matched layer on the converter screen in order to avoid total reflections [Dab96, Koc98]. The DQE can further be improved by the replacement of Yttrium with Lutetium in the sensitive layer. The small light collection efficiency of the objective reduces the DQE. It can be compensated by an increase of the conversion efficiency of the luminescent screen (expression (3.56)) or/and of the CCD efficiency (back instead of front illumination [Dab96]).

4 Methods

4.1 Introduction

This chapter deals with important quantitative aspects of coherent X-ray imaging. The advent of coherent hard X-ray beams allows to repeat classical experiments in the field of light optics with wavelengths about 10000 times smaller. The Talbot effect, a special manifestation of Fresnel diffraction occurring with periodic objects, is an example of this. Talbot images show a double periodicity, both in the direction of the object periodicity and in the propagation direction. Quantitative evaluation of the data obtained as a function of defocusing distance provides information about the lateral coherence of the beam as well as on the phase modulation in the object.

The determination of the phase in the case of an arbitrary object, not necessarily periodic or weak, is the purpose of the holographic reconstruction. This is done on an actual sample using the method of focus variation, as applied in high resolution electron microscopy. It consists in recording at different sample detector distances a series of images which are combined through a suitable algorithm to reconstruct the wave exiting the sample. This gives directly access to the projection of the complex refractive index. In combination with a tomographic technique, i.e. the holographic reconstruction is repeated for a large number of angular positions of the sample, the three dimensional distribution of the refractive index decrement in a polymer foam sample is mapped.

A reconstructed phase map can be interpreted straightforwardly as a projection image of the object. The resolution is no longer limited by the Fresnel fringes but by the resolution in the Fresnel diffraction patterns, usually imposed by the detector response. The possibility to overcome this limitation through magnification by projection is demonstrated. The divergent but coherent beam exiting an X-ray waveguide is shown to be effective, at least in one direction, for this purpose.

4.2 The case of a periodic object: the Talbot effect

The Talbot effect, i.e. the self-imaging of periodic structures under coherent illumination, was discovered 160 years ago by H. F. Talbot [Tal1836] and first analytically explained by Lord Rayleigh in 1881 [Ray1881]. It is a spectacular manifestation of Fresnel diffraction and the basis for useful applications in visible light [Liu89, Arr95, Ham95, Pat89] and soft X-ray [Ari85] optics. A single Fresnel diffraction image of a grating, obtained with a micro-focus X-ray generator in reflection geometry, was published [Har94]. We reported the first reasonably full observation of the Talbot effect with hard X-rays [Clo97b]. The ‘Talbot effect’ is the fact that, in illumination by a quasi-monochromatic plane wave, perfect images of a periodic object are observed if the distance from the object to the recording plane is an integral multiple of the

'Talbot distance' $D_T = 2a^2/\lambda$, where a is the period of the object. More generally, the complex amplitude is periodic both in the direction of the object periodicity (period a) and in the direction of propagation (period D_T). The periodicity in the propagation direction is not perfect due to the partial coherence of the beam, and the decrease of contrast provides a precise measure of the degree of spatial coherence.

4.2.1 Modelisation

For the theoretical description, we will consider the case of a one-dimensional object, though extension to specific types of two-dimensional objects is straightforward. First the calculations are done for plane wave illumination of unit amplitude. As shown in § 2.2.3, the case of a spherical incident wave can always be reduced to this one. The effect of the partial coherence is considered afterwards and a practical method to measure the degree of spatial coherence is deduced.

Case of perfect coherence

Reasoning in reciprocal space, a periodic object is characterised by the absence of spatial frequencies different from

$$f = \frac{m}{a} \qquad \forall \text{ integer number } m \tag{4.1}$$

Such an object can be described in terms of a spectrum with Dirac distributions or more correctly in terms of a Fourier series. The usual definition of the (complex) Fourier coefficient of order m of the periodic object transmission function $T(x)$ is

$$T^{(\mathrm{m})} = \frac{1}{a}\int_0^a T(x)\exp(-2\pi\mathrm{i}\, m\frac{x}{a})\,\mathrm{d}x \tag{4.2}$$

The periodicity in the direction of propagation follows directly from the periodicity of the complex exponential function appearing in expression (2.48) of the propagator $P_D(f) = \exp(-\mathrm{i}\pi\lambda D f^2)$. The propagator is clearly unaltered for all frequencies of the form given in expression (4.1) if the defocusing distance changes by a multiple of the Talbot distance

$$D_\mathrm{T} = \frac{2\,a^2}{\lambda} \tag{4.3}$$

The numerical calculations of the Fresnel diffraction patterns are implemented by Fourier transformations and simple operations in either direct or reciprocal space (see § 2.2.6). This approach (Fourier optics) is especially adapted to periodic objects. The finite window (field of view) does not introduce any calculation errors if the window size is equal to a multiple of the period. For periodic functions we systematically chose the window size equal to one period. For non-periodic objects the discrete Fourier transformation replaces the real object by a periodic repetition of the portion of the object within the field of view. The error introduced by this periodic repetition is usually termed leakage [Bri74]. It can thus easily be avoided for periodic objects.

In direct space, the diffraction integral (equation (2.34)) reduces to a finite sum. The reduced defocusing distance D/D_T can be restricted to the range between 0 and 1 because of the periodicity. Images simply related to the object are expected at reduced distances equal to a simple fractional number (n_1/n_2). The wave amplitude at a distance D with respect to the sample can be expressed as [Gui71, Arr92]

$$u_D(x) = \frac{1}{\sqrt{2\,\mathrm{i}\,n_1 n_2}} \sum_{p\,=\,0,1,\ldots n_2-1} T\left(x+p\frac{a}{n_2}\right) C(n_2,n_1,p) \tag{4.4}$$

with the fractional Talbot coefficients

$$C(n_2,n_1,p) = \sum_{j\,=\,0,1,\ldots 2n_1-1} \exp\left[\mathrm{i}\,\pi\frac{(p+j\,n_2)^2}{2\,n_1\,n_2}\right] \tag{4.5}$$

The amplitude (and intensity) have the same periodicity as the object. The wave consists of a superposition of n_2 replicas of the object laterally shifted by a multiple of a/n_2. The fractional Talbot coefficients give the weight of the corresponding replica. In the case $n_1 = 1$, they have the simple expression

$$C(n_2,1,p) = [\,1+(-1)^p\,\mathrm{i}^{n_2}\,]\,\exp\left(\mathrm{i}\,\pi\frac{p^2}{2\,n_2}\right) \tag{4.6}$$

At the Talbot distance itself, i.e. $n_1 = n_2 = 1$, equation (4.4) reduces to $T(x)$ and a self-image is obtained. Fractional Talbot effects appear for other simple values of (n_1/n_2), for example,

$$u_D(x) = T(x+a/2) \qquad\qquad D = \frac{a^2}{\lambda} \tag{4.7}$$

$$u_D(x) = \frac{1}{\sqrt{2\mathrm{i}}}[\,T(x) + \mathrm{i}\,T(x+a/2)\,] \qquad\qquad D = \frac{a^2}{2\lambda} \tag{4.8}$$

Expression (4.7) shows that identical intensities except for a translation of $a/2$ are obtained in planes separated by $D_\mathrm{T}/2$. The moduli of the Fourier coefficients are then identical

$$|I_\mathrm{coh}^{(m)}(D_\mathrm{o} + p\,D_T/2)| = |I_\mathrm{coh}^{(m)}(D_\mathrm{o})| \qquad\qquad \forall \text{ integer number } p \tag{4.9}$$

with the defocusing distance appearing as the argument of the Fourier coefficient.

At a quarter of the Talbot distance, the intensity distribution is from expression (4.8)

$$I_D^{\text{coh}}(x) = \frac{A^2(x)}{2} + \frac{A^2(x+a/2)}{2} + A(x)A(x+a/2)\sin[\,\varphi(x) - \varphi(x+a/2)\,] \tag{4.10}$$

This profile is similar to a two-beam interference pattern appearing in, e.g., Young's experiment [Bor80].

In the case of a pure phase grating, for which $T(x)= \exp[i\varphi(x)]$, we expect no contrast immediately downstream of the object but also if D is an integral multiple of $D_T/2$. For $D = a^2/2\lambda$, we recover the very simple result [Gui71, Arr92]

$$I_D^{\text{coh}}(x) = 1 + \sin[\,\varphi(x) - \varphi(x+a/2)] \qquad D = \frac{a^2}{2\lambda} \tag{4.11}$$

However this formula does not provide the determination of $\varphi(x)$ from $I(x)$, since adding an arbitrary function of period $a/2$ to $\varphi(x)$ leaves $I(x)$ invariant. If the 2π indetermination due to the inversion of the sine can be solved with a continuity constraint, it yields $\varphi(x) - \varphi(x+a/2)$ and thus the phase modulation up to such an arbitrary function. The particular case of a symmetric rectangular phase profile (i.e. $\varphi(x) = 0$ for $0 < x < a/2$ and $\varphi(x) = \Delta\varphi$ for $a/2 < x < a$) results in an intensity distribution with identical shape and a minimum and maximum value respectively equal to $1 - \sin\Delta\varphi$ and $1 + \sin\Delta\varphi$. This is one of the rare cases of direct imaging of the phase modulation using Fresnel diffraction. In general a phase retrieval method is necessary. With a triangular periodic phase profile it is in principle possible to create a sinusoidal intensity modulation. This is useful for measuring directly the optical transfer function (see § 3.4.1.3).

Case of partial coherence

In a real situation the X-ray beam is only partially coherent and deviations from perfect periodicity in the defocusing direction are expected. We will consider the case of homogeneous illumination conditions, i.e. the incident mutual intensity depends only on the difference between the two considered points (see § 2.2.4). In the case of normalised images with unit incident intensity, the mutual intensity is equal to the degree of coherence $\gamma^{\text{c}}_{\text{inc}}$. The effect of the partial coherence can most easily be described on the Fourier coefficients of the intensity distribution. Expressions (2.75) and (2.89) give

$$I^{(m)} = \tilde{R}(m/a)\ \gamma^{\text{c}}_{\text{inc}}(\lambda D m/a)\ I^{(m)}_{\text{coh}} \tag{4.12}$$

The resolution of the detector is taken into account by its optical transfer function evaluated at the spatial frequency m/a. In the case of a significant magnification M (see expression (2.61)) the period at the level of the detector is Ma and the optical transfer function must be evaluated at $m/(Ma)$. We suppose that the magnification is sufficiently close to one for the effect on the detector response to be negligible. In general it is not straightforward to deduce from a Fresnel diffraction pattern the degree of coherence. It requires to know the detector and the object, respectively the first and third term in the expression, precisely. However using the Talbot effect it is possible to alter the coherence conditions without any change in the object or detector contribution by comparing images in planes separated by a multiple of half the Talbot distance. The ratio of the moduli of the Fourier coefficients is using expression (4.9)

$$\left|\frac{I^{(m)}(D_o + p\,D_T/2)}{I^{(m)}(D_o)}\right| = \left|\frac{\overset{c}{\gamma}_{\mathrm{inc}}\left[\lambda\,(D_o + p\,D_T/2)\frac{m}{a}\right]}{\overset{c}{\gamma}_{\mathrm{inc}}\left[\lambda\,D_o\,\frac{m}{a}\right]}\right| \tag{4.13}$$

This ratio is independent of the (periodic) object and the detector, it is only determined by the degree of coherence. In the case of an absorbing periodic object, contrast exists at distance zero and it is possible to choose $D_o = 0$. Hence, using $\overset{c}{\gamma}_{\mathrm{inc}}(0) = 1$ and the definition of D_T,

$$\left|\frac{I^{(m)}(p\,D_T/2)}{I^{(m)}(0)}\right| = |\overset{c}{\gamma}_{\mathrm{inc}}(p\,m\,a)| \qquad I^{(m)}(0) \neq 0 \tag{4.14}$$

The degree of coherence can be sampled with a period a, either by taking images in successive planes separated by $D_T/2$, or by calculating the ratio for higher order (non zero) Fourier coefficients. The ratio of the first Fourier coefficient of the image at half the Talbot distance and the absorption image gives the degree of coherence between two points laterally separated by one object period. If this choice of D_o is not possible (p.e. for a phase object), the specimen-detector distance must be increased until sufficient contrast appears. When $\lambda D_o m/a$ is small and does not introduce a decrease of the degree of coherence, it is still possible to measure directly the degree of coherence. In the other case or when a single value characterising the partial coherence is preferable, a model for the degree of coherence can be introduced. The X-ray beam is often well described as a set of mutually incoherent plane waves with a gaussian angular distribution

$$S_\alpha(\theta) = \frac{1}{\sqrt{2\pi}\,\sigma_\alpha}\exp\left(-\frac{\theta^2}{2\sigma_\alpha^2}\right) \tag{4.15}$$

This is the case when the ideal coherence is conserved and determined through $\sigma_\alpha = \sigma_s/l$ by the source with a gaussian distribution (see § 2.1.3). The degree of coherence (cf. expression (2.72)) is also a gaussian in this case

$$\overset{c}{\gamma}_{\mathrm{inc}}(\lambda D\frac{m}{a}) = \tilde{S}_\alpha(D\frac{m}{a}) = \exp\left[-2\left(\pi\,\sigma_\alpha D\frac{m}{a}\right)^2\right] \tag{4.16}$$

The ratio of the first Fourier coefficients gives the angular divergence through a simple algebraic expression

$$\sigma_\alpha = \frac{a}{\sqrt{2}\,\pi\sqrt{D_p^2 - D_o^2}}\left[\ln\left|\frac{I^{(1)}(D_p)}{I^{(1)}(D_o)}\right|\right]^{1/2} \qquad D_p = D_o + pD_T/2 \tag{4.17}$$

Two-dimensional case

In the case of a two-dimensional periodic object (fractional) Talbot images can be observed if there exists a relationship between the periodicity in horizontal and vertical direction. It is easy to show that the squared ratio of the horizontal and vertical period must be a rational number. The degree of coherence can be determined in both directions from ratios of Fourier coefficients in a similar way.

4.2.2 Experimental results

We used pure phase gratings (Hilger & Watts Student Diffraction Gratings) consisting of plastic replicas of 2000 LPI (line pairs per inch, $a = 12.7\ \mu\text{m}$) and 4000 LPI ($a = 6.35\ \mu\text{m}$) gratings, sandwiched between glass slides. They were set perpendicular to the beam, with the lines of the grating horizontal. The corrugation of the plastic replica was independently observed after one of the glass slides had been removed from the 2000 LPI grating, using scanning electron microscopy and atomic force microscopy [A. Liénard and O. Fruchart, Lab. Louis Néel, Grenoble]. The maximum thickness variation was found to be 2.4 µm. The X-ray beam of wavelength $\lambda = 0.69$ Å ($E = 18$ keV), selected with the vertical monochromator, is therefore not modulated in amplitude.

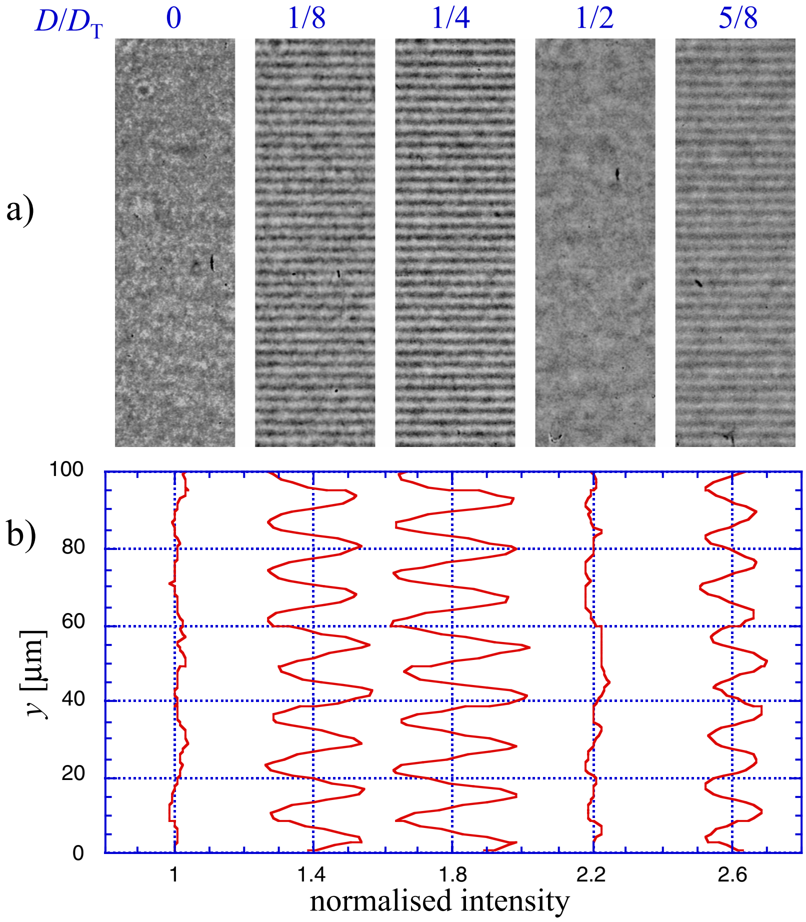

Fig 4.1 (a) Fractional Talbot images obtained on a 2000-LPI phase grating at increasing distance with respect to the sample, corresponding to simple fractions of the Talbot distance $D_T = 4.68$ m. (b) The curves represent the normalised intensity versus the coordinate perpendicular to the lines with a shift of 0.4 between them. $\lambda = 0.69$ Å (X-ray energy 18 keV) and period $a = 12.7\ \mu\text{m}$.

Fig 4.1a shows the images recorded on KODAK high resolution film at increasing distances. The qualitative features are in full agreement with expectation. There is indeed no contrast at all due to the sample when the film is set right after the grating (a phase object gives no variation in intensity until Fresnel diffraction has taken over to produce interference between different parts of the beam). Contrast then builds up as the film is set further from the specimen (increasing d), decreases again to zero exactly for $D = D_T/2$, and reappears as D is further increased. However, the contrast is not strictly identical in the second and the last image although they correspond to planes separated by a distance $D_T/2$. This is due to the partial coherence of the quasi-monochromatic incident beam [Fuj74]. The normalised intensity profiles of Fig 4.1b show this in more detail. To obtain them the film response was calibrated by recording the same portion of the beam, without the sample, for different exposure times (see § 3.4.1.1).

Going over to a more quantitative view, the amplitude of the first Fourier coefficient of the periodic intensity distribution is plotted vs distance in Fig 4.2. In order to combine data obtained on different samples (2000 and 4000 LPI gratings) the defocusing distance is scaled by the Talbot distance, respectively 4.68 m and 1.17 m, and the Fourier coefficient is scaled by the maximum possible contrast (see below). When using the vertical monochromator (square data points), the behaviour is not strictly periodic. This can be related to the deviation from perfect coherence of the beam as mentioned above. The value of the angular width (FWHM) s_α obtained with expression (4.17) for the 2000 LPI grating and reduced defocusing distance 1/8 and 5/8 is 1.5 µrad, in good agreement with the value of 1.4 µrad obtained with the 4000 LPI grating and reduced defocusing distances 1/4, 3/4 and 5/4. This angular width corresponds to a value of the transverse coherence length, defined as $\lambda/(2s_\alpha)$ of 25 µm at $\lambda = 0.69$ Å (cf. expression (2.84)). From the size of the source and its distance from the sample we would expect the angular width to be 0.17 µrad and the coherence length to be 200 µm. It is believed that the angular broadening is due to vibrations of the monochromator caused by the cooling system. Much better figures are obtained when the water pressure in the cooling circuit is reduced or when the horizontal monochromator is used. A decrease is hardly visible with the non-vibrating, uncooled horizontal monochromator (circular data points). This clearly shows that the origin of the decrease is indeed the partial coherence of the beam and not the object quality. The Fourier coefficients obtained at $D_p/D_T = 1/4 + p/2$ $(p = 0,1,2,3)$ are fitted with expression (4.12) and with the degree of coherence given by (4.16). The contribution of the object and the detector are constant. The resulting estimation of the angular width under 'perfect' coherence conditions is 0.2 ± 0.1 µrad, in agreement with the source characteristics. The amplitude of the first Fourier coefficient is calculated using a discrete Fourier transform procedure. In order to minimise leakage the width of the sampling window was chosen so to include an entire number of periods. The width is decreased and the Fourier component is calculated again until a maximum value (and minimum leakage) is reached. The position of the first Fourier component also results in a precise measurement of the image period. Working with a CCD based detector, the magnification due to the finite source-specimen distance can easily be detected. The largest value of the magnification in the results presented is 1.02. The object period a as given by the image period is in agreement with the value indicated by the manufacturer.

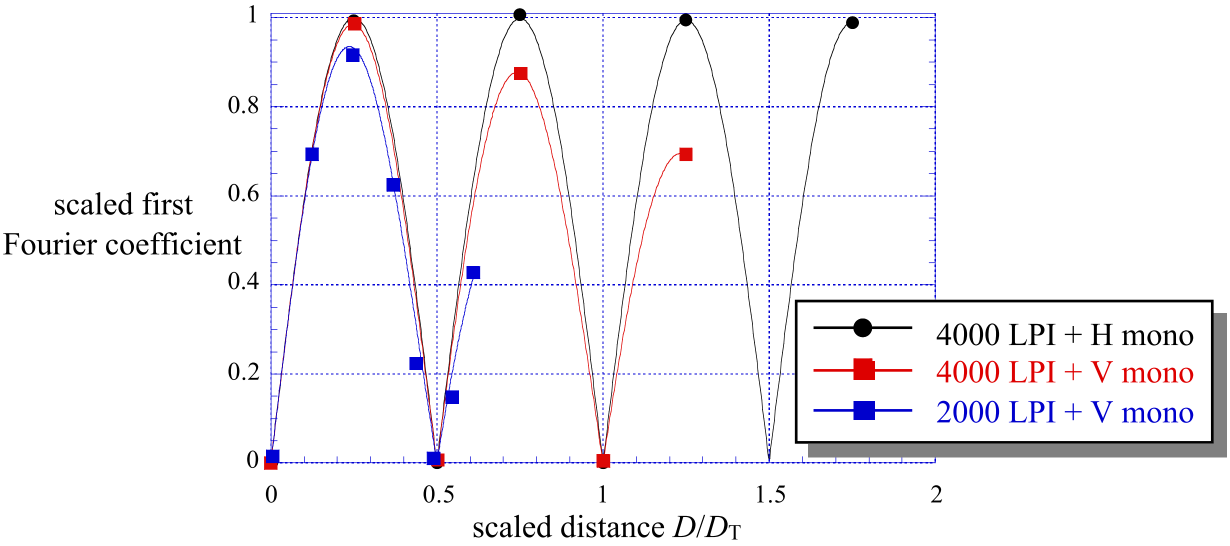

Fig 4.2 Amplitude of the fundamental of the intensity distribution versus the scaled distance using either the vertical monochromator and a 2000 LPI grating (blue squares) or a 4000 LPI grating (red squares) or the horizontal monochromator and a 4000 LPI grating (black circles). The X-ray wavelength λ is 0.69 Å. The Fourier coefficient was scaled for the maximum possible contrast. D_T is 4.68 m and 1.17 m for respectively the 2000 LPI and 4000 LPI grating. The fitted lines correspond to the simple analytical expression (4.18) which includes the effect of the degree of coherence at the position of the sample. (with σ_α respectively 0.65 µrad, 0.6 µrad and 0.07 µrad)

To estimate the phase modulation for the gratings we use the weak phase approximation ($\varphi(x,y) << 1$). In this case the Fourier coefficients $I^{(m)}$ and $\varphi^{(m)}$ of respectively the periodic intensity and phase modulation are linearly related by the phase contrast factor. Combining expressions (2.53) and (4.16) yields, in the case of the fundamental and a perfect detector at the spatial frequency $1/a$:

$$I^{(1)} = 2\,\varphi^{(1)} \sin\left(2\pi \frac{D}{D_T}\right) \exp\left[-8\left(\pi\,\sigma_\alpha \frac{a}{\lambda}\frac{D}{D_T}\right)^2\right] \tag{4.18}$$

The maximum obtainable value of $I^{(1)}$ is $2\varphi^{(1)}$, reached at $D_T/4$ under coherent illumination. This results in the fitted curves for $|\,I^{(1)} / 2\varphi^{(1)}\,|$ presented in Fig 4.2. The values obtained for $\varphi^{(1)}$ are 0.046 rad and 0.019 rad respectively for the 2000 LPI and 4000 LPI grating, corresponding to peak to peak modulations of the fundamental of 0.185 rad and 0.075 rad respectively, consistent with the weak phase assumption. Assuming the plastic of the replica has a density of 1 g/cm³, these phase modulations correspond to thickness modulations of respectively 2.7 µm and 1.1 µm, also consistent with the thickness variation of 2.4 µm obtained by AFM on the 2000 LPI grating. Note that the weak phase assumption is **not** used to measure the degree of coherence.

The expression of the phase contrast factor indicates that a non-periodic, weak phase object displays the Talbot effect for each spatial frequency separately. The distances with zero contrast are identical for a given spatial period in a weak, non-periodic phase object and a non-weak but periodic phase object.

Fig 4.3 shows the results obtained at $\lambda = 0.85$ Å on a two dimensional gold grid (Agar G2786A 2000 mesh gold) when both amplitude and phase modulation are present [Clo99]. The horizontal and vertical periods are identical ($a = 12.5$ µm) for this grid and the images are recorded at simple fractions of the Talbot distance ($D_T = 3.7$ m). The first image (0) is a pure absorption image ($d = 4$ mm). The same image, slightly blurred, is found at half (1/2) and once (1) the Talbot distance. The images recorded at $D/D_T = 1/4$ and 3/4 are dominantly determined by the phase modulation of the grid. The vertical monochromator was used for the experiment and the vertical coherence is deteriorated. It is only slightly better than the horizontal one whereas it should be significantly better due to the smaller vertical source size.

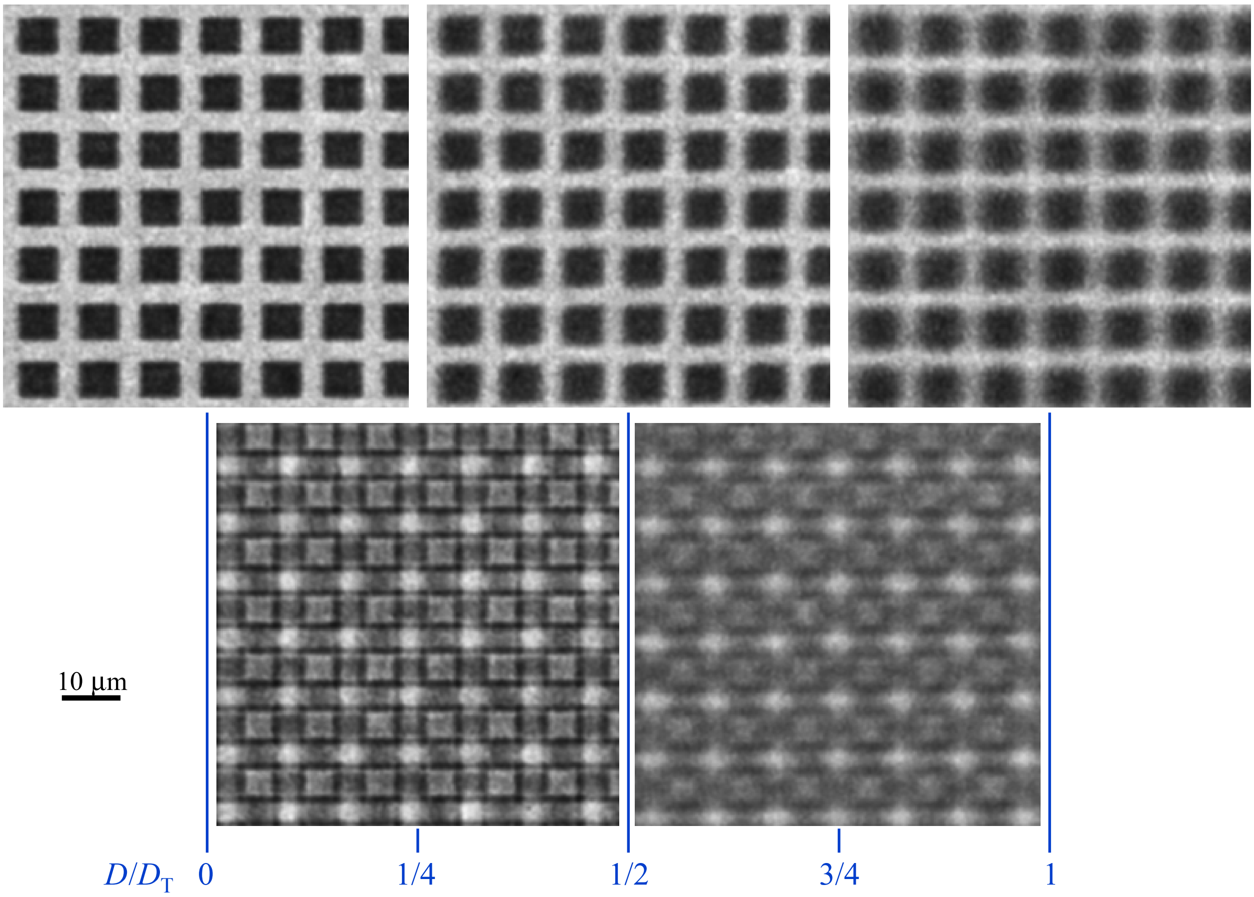

Fig 4.3 Fractional Talbot images obtained on a 2000 mesh gold grid at simple fractions of the Talbot distance D_T. Period $a = 12.5$ µm, $\lambda = 0.85$ Å, $D_T = 2a^2/\lambda = 3.7$ m. The origins of the images are not aligned and they are not corrected for the occurring magnification.

4.2.3 Conclusions

It is no surprise to confirm that Talbot imaging is essentially the same in the hard X-ray range as with visible light, in spite of a factor 10^4 in the wavelength or energy. The observations can qualitatively and quantitatively be interpreted as Fresnel diffraction on a periodic object. It is satisfactory to find a value for the first Fourier coefficient of the phase modulation introduced by the gratings in agreement with the surface corrugation determined by atomic force microscopy. The absence of contrast for a phase object at specific distances indicates clearly that a single Fresnel diffraction pattern can contain little (or no) information on a certain frequency range.

But the main result of these experiments is that the Talbot effect can be a very useful tool for the measuring the lateral coherence of an X-ray beam. For pure phase gratings, we showed that the ratio of the first Fourier coefficients of two images corresponding to planes separated by $D_T/2$ yields the angular divergence of the X-ray beam through a simple analytic formula. The use of an absorption grating yields the coherence properties in an even more complete way (cf. expression (4.14)).

Other techniques to estimate the degree of coherence of hard X-ray beams were proposed recently. The most direct approach, Young's double-slit experiment, is not feasible with hard X rays, but a complex variant, where two beams reflected by mirrors under grazing incidence interfere [Fez97], was realised. One can also estimate the transverse coherence length from the visibility of the Fraunhofer fringes produced by a circular aperture with size comparable to this coherence length [Sut91, Grü94]. The Fresnel diffraction pattern of a simple object, such as a phase jump [Clo96] or a fibre [Sch96], can also be used for this purpose. From such a pattern, obtained with a nylon fibre 100 µm in diameter, the coherence length was measured as approximately 30 µm under experimental conditions similar to those described in the present paper, where the value of 25 µm was obtained.

The originality of the method based on the Talbot effect is the use of Fourier techniques and of two measurements. It results in an excellent signal-to-noise ratio because the useful information is concentrated in the Fourier domain, whereas the noise is uniformly distributed. And, since only ratios of Fourier coefficients corresponding to the same spatial frequency are used, via expression (4.14) or (4.17), the result is independent of the detector transfer function. Exact knowledge of the object is not required insofar as it is periodic.

4.3 The holographic reconstruction

We now consider the inverse problem, i.e. the determination of the phase (and the amplitude) of the transmission function from the recorded intensities. At least two images are needed since they are real. For a pure phase object a single image could appear to be sufficient. However the contrast factor valid for weak phase objects (cf. expression (2.53) and Fig. 2.5) has positive and negative values with zero crossings, hence the image at a given distance contains no or little information on certain spatial frequency ranges or the contrast may be reversed. Combining images at different defoci allows to image and retrieve information in a larger frequency range. Thus in order to minimise problems of unicity of the solution, non-linear contributions and twin images, we consider a series of N defocused images corresponding to defocus distances D_m. The redundancy also improves the quality of the reconstruction and partly tackles the noise problem, crucial in all coherent imaging methods. This holographic reconstruction problem is similar to the one encountered in the soft X-ray range [Jac88, Joy88] and in high resolution electron microscopy [Gab48]. We basically use algorithms of the focus variation method developed for the latter [Sch73, Kir84, Coe92, Opd96]. However some simplifications occur in the X-ray case because of the absence of spherical aberration and the good monochromaticity of the X-ray beam. A defocal spread occurs in electron microscopy because the focal length of the objective lens fluctuates due to variations in the energy of the electrons and in the lens current. We include these simplifications and will give special attention to constraints valid for X-rays. If no Bragg diffraction occurs, the object transmission function is a very useful concept. Its modulus is smaller than or equal to 1 and its phase has only negative values if a path in vacuum is taken as reference (cf. expressions (2.24) and (2.25)). The case of a non absorbing, pure phase object is a good approximation for low Z materials. Otherwise the modulus of the object function can easily be measured from an image close to the sample, and only the determination of the phase is problematic. In electron microscopy the determination of the modulus is not straightforward either because of the presence of spherical aberration and defocus. Recently electron microscopes with a correction for the spherical aberration became available [Hai97]. The use of physically relevant constraints appeared to be crucial in order to compensate for the low sensitivity of the defocusing method for smooth variations in the sample.

In a recent paper [Nug96], some quantitative low frequency information was extracted from a single image obtained with hard X-rays on a pure phase object under weak defocus and weak contrast conditions. The authors considered the intensity variations to be proportional to the Laplacian with respect to x and y of the phase modulation (see § 4.4.2) and retrieved it essentially by double integration of the image. Their approach is based on the transport of intensity equation [Tea82, Gur95, Gur96], also introduced in electron microscopy [Van87]. For a phase object this equation links the derivative of the intensity distribution with respect to the defocus distance at $D = 0$ to the Laplacian of the phase. The experimental determination of the derivative is of course sensitive to noise. In order to extract information over a large spatial frequency range with optimal contrast for the different frequencies, it is more appropriate to record images at different defocus in the Fresnel diffraction regime and to combine the information entangled in these interference patterns to reconstruct a single transmission function.

The fundamentals of the algorithms are given elsewhere [Opd96]. The procedure consists of two parts: first a non-iterative 'paraboloid' method is applied to obtain *in a direct way* a first 'good guess' of the solution. It is based on backpropagation of the images what tends to linearise the object-image relationship. If necessary the object estimation is *iteratively* optimised through a non-linear least squares procedure [Kir84]. We consider the case of a unit intensity illumination with spatial coherence properties described by the degree of coherence. The images are assumed to have identical magnification, hence preliminary corrections have to be made if the magnification varies significantly with the defocusing distance.

4.3.1 Paraboloid method

4.3.1.1 General approach

The spectrum (Fourier transform) of the intensity distribution at defocus D_m is (cf. equation (2.77)), neglecting temporarily the detector and coherence contributions (multiplicative terms),

$$\tilde{I}_{D_m}(\boldsymbol{f}) = \exp(-\mathrm{i}\pi\lambda D_m \boldsymbol{f}^2) \int \tilde{T}(\boldsymbol{p}+\boldsymbol{f})\, \tilde{T}^*(\boldsymbol{p}) \exp(-\mathrm{i}2\pi\lambda D_m \boldsymbol{p}\boldsymbol{f})\, \mathrm{d}\boldsymbol{p} \tag{4.19}$$

with $\tilde{T}(\boldsymbol{f})$ the spectrum of the object transmission function. The intensity spectrum consists of interferences between the plane wave components of the transmission function multiplied with a distance dependent phase term. The first term is the propagator $P_{D_m}(\boldsymbol{f})$. If the images are backpropagated, hence if their spectrum is multiplied by $P_{-D_m}(\boldsymbol{f})$, the complex exponential term in front of the integral disappears. Summing the backpropagated intensity spectra introduces in the integral a sum of complex exponential terms of the form $\exp(-\mathrm{i}2\pi\lambda \mathrm{D}_m \boldsymbol{p}\boldsymbol{f})$. Using several defocus distances, the sum will approach zero except for $\boldsymbol{p}.\boldsymbol{f} = 0$, when it is equal to the number of images. This is in particular the case for $\boldsymbol{p} = 0$. Backpropagation and summation promote therefore the interference between the plane wave component $\tilde{T}(\boldsymbol{f})$ and the DC component of the wave $\tilde{T}^*(0)$, whereas most other interferences are attenuated ($\boldsymbol{p}.\boldsymbol{f} \neq 0$). It is thus useful to write the object transmission function as

$$T(\boldsymbol{x}) = \kappa + \psi(\boldsymbol{x}) \tag{4.20}$$

with κ the average of the transmission function and $\psi(\boldsymbol{x})$ its variations with zero mean. The Fourier transform of the object function is splitted in

$$\tilde{T}(\boldsymbol{f}) = \kappa\, \delta_{\mathrm{D}}(\boldsymbol{f}) + \tilde{\psi}(\boldsymbol{f}) \tag{4.21}$$

with $\tilde{\psi}(\boldsymbol{f}=0)=0$ and $\delta_{\mathrm{D}}(\boldsymbol{f})$ the Dirac distribution. The first term corresponds physically to the central, unaffected beam and the second one to a diffracted beam. κ has a modulus smaller than 1 and in the case of weak phase and amplitude modulation it is approximately unity. Introducing this decomposition in the expression of the backpropagated intensity yields

$$\begin{aligned}\exp(\mathrm{i}\pi\lambda D_m\boldsymbol{f}^2)\,\tilde{I}_m(\boldsymbol{f}) = \;& |\kappa|^2\,\delta_{\mathrm{D}}(\boldsymbol{f}) \\ &+\ \kappa^*\,\tilde{\psi}(\boldsymbol{f})\ +\ \kappa\exp(\mathrm{i}2\pi\lambda D_m\boldsymbol{f}^2)\,\tilde{\psi}^*(-\boldsymbol{f}) \\ &+\ \int\tilde{\psi}(\boldsymbol{p}+\boldsymbol{f})\,\tilde{\psi}^*(\boldsymbol{p})\exp(-\mathrm{i}2\pi\lambda D_m\boldsymbol{p}\boldsymbol{f})\,\mathrm{d}\boldsymbol{p}\end{aligned} \tag{4.22}$$

where the subscript m replaces the subscript D_m for notational simplicity.

The last term corresponds to the non-linear contributions due to interference between diffracted beams. The second and third term are linear in the object spectrum and are due to interference with the central beam. The second term is the object spectrum that one wants to reconstruct multiplied by the average of the object. The third term is unwanted. Both $\tilde{\psi}(\boldsymbol{f})$ and $\tilde{\psi}^*(-\boldsymbol{f})$ (or equivalently the object $T(x)$ and its complex conjugate $T^*(x)$) contribute and this constitutes the so called twin-image problem intrinsic in the conventional optical reconstruction [Gab48, Liu87]. The third term is actually the Fourier transform of the complex conjugate of the object propagated over a distance $-2D_m$. One principal idea of the paraboloid method is that these contributions to the intensity have different dependencies on the defocus D_m. Variation of this defocus will therefore make it possible to disentangle the different contributions and to retrieve $\tilde{\psi}(\boldsymbol{f})$. For example, if two images are recorded and if the non-linear terms are neglected, one obtains two linear equations with two unknowns which can be solved for the unknown $\tilde{\psi}(\boldsymbol{f})$. This is possible for those spatial frequencies for which the corresponding determinant is sufficiently different from 0. With an increasing number of images, the non-linear and the twin-image contributions tend to cancel (so far $\boldsymbol{p}.\boldsymbol{f}\neq 0$). It is thus more easily justified to neglect the non-linear contributions and it is possible to solve the twin-image problem over a large frequency range. Backpropagation and summation of N images yields for $\boldsymbol{f}\neq 0$

$$\frac{1}{N}\sum_{m=1..N}\exp(\mathrm{i}\pi\lambda D_m\boldsymbol{f}^2)\,\tilde{I}_m(\boldsymbol{f}) = \kappa^*\,\tilde{\psi}(\boldsymbol{f}) + \left[\frac{1}{N}\sum_q\exp(\mathrm{i}2\pi\lambda D_q\boldsymbol{f}^2)\right]\kappa\,\tilde{\psi}^*(-\boldsymbol{f}) + \tilde{I}_{\mathrm{NL}}(\boldsymbol{f}) \tag{4.23}$$

If the non-linear terms $\tilde{I}_{\mathrm{NL}}(\boldsymbol{f})$ are negligible, this equation and its complex conjugate at the spatial frequency $-\boldsymbol{f}$ give an equation determining $\kappa^*\,\tilde{\psi}(\boldsymbol{f})$ as a function of the experimental images

$$\Delta(\boldsymbol{f})\,\kappa^*\,\tilde{\psi}(\boldsymbol{f}) = \frac{1}{N}\sum_m\Delta_m(\boldsymbol{f})\,\tilde{I}_m^{\mathrm{exp}}(\boldsymbol{f}) \tag{4.24}$$

with

$$\Delta(\boldsymbol{f}) = 1 - \left| \tfrac{1}{N} \sum_{q} \exp(\mathrm{i}2\pi\lambda D_m \boldsymbol{f}^2) \right|^2 \tag{4.25}$$

$$\Delta_m(\boldsymbol{f}) = \exp(\mathrm{i}\pi\lambda D_m \boldsymbol{f}^2) - \left[\tfrac{1}{N} \sum_{q} \exp(\mathrm{i}2\pi\lambda D_q \boldsymbol{f}^2) \right] \exp(-\mathrm{i}\pi\lambda D_m \boldsymbol{f}^2)$$

The determinant $\Delta(\boldsymbol{f})$ is close to 1 except at specific frequencies ($\boldsymbol{f} = 0$ and resonance frequencies) when a large number of images is used. If the determinant is not close to zero the spectrum of the object is retrieved by multiplying the spectrum of the experimental images with the ideal filters $\Delta_m(\boldsymbol{f})/\Delta(\boldsymbol{f})$ and summing all contributions. The different dependency on the defocusing distance of the various linear and non-linear contributions to the image spectrum can clearly be visualised by considering a supplementary Fourier transform of the images with respect to the defocus D [Van97]. The considered three-dimensional reciprocal space has the coordinates f, g and ζ, conjugated to x, y and D respectively in direct space. Taking the Fourier transform with respect to D of expression (4.19) and using the decomposition of expression (4.21) yields

$$\begin{aligned} \tilde{I}(\boldsymbol{f};\zeta) = \; & |\kappa|^2\, \delta_{\mathrm{D}}(\boldsymbol{f}) \\ & + \kappa^*\, \tilde{\psi}(\boldsymbol{f})\, \delta_{\mathrm{D}}(\zeta + \tfrac{1}{2}\lambda \boldsymbol{f}^2) + \kappa\, \tilde{\psi}^*(-\boldsymbol{f})\, \delta_{\mathrm{D}}(\zeta - \tfrac{1}{2}\lambda \boldsymbol{f}^2) \\ & + \int \tilde{\psi}(\boldsymbol{p}+\boldsymbol{f})\, \tilde{\psi}^*(\boldsymbol{p})\, \delta_{\mathrm{D}}(\zeta + \tfrac{1}{2}\lambda[\boldsymbol{f}^2 + 2\boldsymbol{p}\boldsymbol{f}])\, \mathrm{d}\boldsymbol{p} \end{aligned} \tag{4.26}$$

The linear contribution of $\tilde{\psi}(\boldsymbol{f})$ is thus located on the paraboloid $\zeta = -\tfrac{1}{2}\lambda \boldsymbol{f}^2$. The twin linear contribution of $\tilde{\psi}^*(-\boldsymbol{f})$ is located on a second paraboloid given by $\zeta = \tfrac{1}{2}\lambda \boldsymbol{f}^2$ on the opposite side of the $\zeta = 0$ plane. The non-linear contributions are more homogeneously distributed over this reciprocal space.

The contribution of the detector and the degree of coherence are correctly taken into account by multiplying of the intensity spectrum with the factor (cf. expressions (2.89) and (2.75))

$$\tilde{R}_m(\boldsymbol{f}) = \tilde{R}(\boldsymbol{f})\, \gamma^{\mathrm{c}}_{\mathrm{inc}}(\lambda D_m \boldsymbol{f}) \tag{4.27}$$

Taking into account that the Fresnel diffraction patterns are blurred the equivalent of equation (4.23) is

$$\tfrac{1}{N} \sum_{m=1..N} \tilde{R}_m(\boldsymbol{f}) \exp(\mathrm{i}\pi\lambda D_m \boldsymbol{f}^2)\, \tilde{I}_m(\boldsymbol{f}) = Q_1(\boldsymbol{f})\, \kappa^*\, \tilde{\psi}(\boldsymbol{f}) + Q_2(\boldsymbol{f})\, \kappa\, \tilde{\psi}^*(-\boldsymbol{f}) + \tilde{I}_{\mathrm{NL}}(\boldsymbol{f}) \tag{4.28}$$

with

$$Q_1(\boldsymbol{f}) = \tfrac{1}{N} \sum_{m} \tilde{R}_m^2(\boldsymbol{f}) \tag{4.29}$$

$$Q_2(\boldsymbol{f}) = \tfrac{1}{N} \sum_{m} \tilde{R}_m^2(\boldsymbol{f}) \exp(\mathrm{i}2\pi\lambda D_m \boldsymbol{f}^2) \tag{4.30}$$

Expression (4.24) is still valid to obtain the object spectrum but with

$$\begin{aligned} \Delta(\boldsymbol{f}) &= |Q_1(\boldsymbol{f})|^2 - |Q_2(\boldsymbol{f})|^2 \\ \Delta_m(\boldsymbol{f}) &= \tilde{R}_m(\boldsymbol{f})\,[\,Q_1(\boldsymbol{f})\exp(\mathrm{i}\pi\lambda D_m \boldsymbol{f}^2) - Q_2(\boldsymbol{f})\exp(-\mathrm{i}\pi\lambda D_m \boldsymbol{f}^2)] \end{aligned} \tag{4.31}$$

In the spatial frequency range where the determinant $\Delta(\boldsymbol{f})$ is not close to zero, the object is obtained by applying the ideal filters $\Delta_m(\boldsymbol{f})/\Delta(\boldsymbol{f})$ to the experimental images. If the determinant is close to zero, as when $\boldsymbol{f}$ approaches zero, the equivalent of a deconvolution must be performed (see § 3.4.1.3). If a Wiener type filter is chosen, the estimation of the object spectrum is directly obtained by filtering the experimental images

$$\kappa^*\,\tilde{\psi}(\boldsymbol{f}) = \tfrac{1}{N}\sum_m \tilde{Y}_{\mathrm{W},m}(\boldsymbol{f})\,\tilde{I}_m^{\exp}(\boldsymbol{f}) \tag{4.32}$$

In expression (4.28) the images are backpropagated and multiplied by the detector transfer function and the degree of coherence. This is similar to the reblurring concept used for the deconvolution. It is in agreement with a least square minimisation [Opd96] where the non-linear terms are neglected, and results in giving a higher weight to the images which are less blurred.

4.3.1.2 Determining the object average κ

The previous expressions yield the object spectrum up to a multiplicative factor κ^* representing the interference with the central beam. The phase of κ can be chosen arbitrarily because a constant phase shift does not alter the recorded intensities. Restricting κ to real, positive values smaller than 1 is thus correct. Its modulus is determined by the average image intensity. Expression (4.22) evaluated for $\boldsymbol{f} = 0$ and averaged over N images yields

$$\tfrac{1}{N}\sum \mathrm{E}\tilde{I}_m(0) = |\kappa|^2 + \frac{1}{|\kappa|^2}\mathrm{E}\int |\kappa^*\,\tilde{\psi}(\boldsymbol{p})|^2\,\mathrm{d}\boldsymbol{p} \tag{4.33}$$

where the quantities that are Dirac distributions are preceded by the letter E to indicate that the weight of the distribution is taken (e.g. $\tilde{I}_m(\boldsymbol{f}\to 0) = \mathrm{E}\tilde{I}_m(0)\,\delta_{\mathrm{D}}(\boldsymbol{f})$; see also equation (4.21)) Solving for $|\kappa|^2$ yields

$$2\,|\kappa|^2 = \tfrac{1}{N}\sum \mathrm{E}\tilde{I}_m(0) + \sqrt{\left[\tfrac{1}{N}\sum \mathrm{E}\tilde{I}_m(0)\right]^2 - 4\,\mathrm{E}\int |\kappa^*\,\tilde{\psi}(\boldsymbol{p})|^2\,\mathrm{d}\boldsymbol{p}} \tag{4.34}$$

where only the solution with the strongest central beam was retained. More generally the linearisation is possible if the central beam is sufficiently strong. In the case of a pure phase object the normalised intensity average is 1 and the previous expression simplifies to

$$2\,|\kappa|^2 = 1 + \sqrt{1 - 4\,\mathrm{E}\int |\kappa^*\,\tilde{\psi}(\boldsymbol{p})|^2\,\mathrm{d}\boldsymbol{p}} \tag{4.35}$$

The initial estimation of the object transmission function is now complete. It is of interest to consider specific situations, i.e. to introduce constraints

4.3.1.3 Using the directly determined object modulus

Thanks to the absence of spherical aberration the modulus $A(\boldsymbol{x}) = |T(\boldsymbol{x})|$ of the transmission function is directly obtained from an image at $D = 0$. In reciprocal space the modulus information can not be expressed trivially, expression (4.22) gives for $\boldsymbol{f} \neq 0$

$$\tilde{I}_0(\boldsymbol{f}) = \tilde{R}(\boldsymbol{f}) \left[\kappa^* \, \tilde{\psi}(\boldsymbol{f}) + \kappa \, \tilde{\psi}^*(-\boldsymbol{f}) + \int \tilde{\psi}(\boldsymbol{p}+\boldsymbol{f}) \, \tilde{\psi}^*(\boldsymbol{p}) \, \mathrm{d}\boldsymbol{p} \right] \tag{4.36}$$

If the non-linear contributions are neglected, this determines $\kappa \, \tilde{\psi}^*(-\boldsymbol{f})$ as a function of $\kappa^* \, \tilde{\psi}(\boldsymbol{f})$ and substitution in expression (4.28) yields

$$[\, Q_1(\boldsymbol{f}) - Q_2(\boldsymbol{f})] \; \kappa^* \, \tilde{\psi}(\boldsymbol{f}) = \tfrac{1}{N} \sum \tilde{R}_m(\boldsymbol{f}) \exp(\mathrm{i}\pi\lambda D_m \boldsymbol{f}^2) \, \tilde{I}_m(\boldsymbol{f}) - \frac{Q_2(\boldsymbol{f})}{\tilde{R}(\boldsymbol{f})} \tilde{I}_0(\boldsymbol{f}) \tag{4.37}$$

The division by the detector transfer function is only apparent because it appears as a multiplicative factor in $Q_2(\boldsymbol{f})$. The object spectrum can be determined from this expression with κ given by equation (4.34).

In the case of a non absorbing object the second term in expression (4.37) disappears because no contrast is present at zero defocus ($\tilde{I}_0(\boldsymbol{f}) = 0$ for $\boldsymbol{f} \neq 0$). Neglecting the non linear contribution in expression (4.36) introduces then the relationship $\tilde{\psi}^*(-\boldsymbol{f}) = -\tilde{\psi}(\boldsymbol{f})$ in the spectrum of the object. The object is thus described in direct space as the sum of a real constant κ and a purely imaginary function $\psi(\boldsymbol{x})$. This approximation is only slightly better than the usual weak phase approximation $\exp[\mathrm{i}\varphi(\boldsymbol{x})] \approx 1 + \mathrm{i}\varphi(\boldsymbol{x})$. It is a coarse description, but it is useful as a first estimation, especially when the phase modulation is not strong.

4.3.1.4 Correction for non-linear terms

As shown above the contribution of the non-linear terms, i.e. the interference among diffracted waves, are attenuated when a large number of images are combined except for $\boldsymbol{f} = 0$. When a limited number of images are used and when the object is not weak it may be necessary to correct for the non-linear terms. A straightforward way of doing this is to use the initial estimate of the object to calculate the non-linear contributions and to introduce this calculated term in expression (4.23). This yields a new estimation of the object and the correction for non-linear terms is done in an iterative way. Introducing the calculated intensity distribution $\tilde{I}_m^j(\boldsymbol{f})$ based on the estimated object in expression (4.23) yields

$$\frac{1}{N} \sum_{m=1..N} \tilde{R}_m(\boldsymbol{f}) \exp(\mathrm{i}\pi\lambda D_m \boldsymbol{f}^2) \, \tilde{I}_m^j(\boldsymbol{f}) = Q_1(\boldsymbol{f}) \, \kappa^* \, \tilde{\psi}^j(\boldsymbol{f}) + Q_2(\boldsymbol{f}) \, \kappa \, \tilde{\psi}^{*j}(-\boldsymbol{f}) + \tilde{I}_{\mathrm{NL}}^j(\boldsymbol{f}) \tag{4.38}$$

Subtraction from equation (4.23) and setting the non linear terms equal to the calculated ones gives a correction to the object spectrum

$$\Delta(\boldsymbol{f}) \, [\kappa^* \, \tilde{\psi}^{j+1}(\boldsymbol{f}) - \kappa^* \, \tilde{\psi}^j(\boldsymbol{f})] = \tfrac{C}{N} \sum \Delta_{\mathrm{m}}(\boldsymbol{f}) \, [\tilde{I}_m^{\exp}(\boldsymbol{f}) - \tilde{I}_m^j(\boldsymbol{f})] \tag{4.39}$$

The convergence parameter C is chosen smaller than 1 because the estimation of the non-linear terms is only approximate. The expression for the object spectrum correction is thus identical to (4.24) for the initial estimate but the experimental images are replaced in the right hand side by the difference between the experimental and calculated images at the j-th iteration step. The purpose of the iterative process consists in minimising this difference. The paraboloid method can be deduced from a least square estimate where only the linear terms in the image are retained. These linearisations are very effective in retrieving the object information from the images when the linear contributions are dominant. In other cases it is necessary to minimise the squared differences (or another cost function) more completely. This is done by the non-linear least squares method (see § 4.3.3)

4.3.2 A variant for phase objects

4.3.2.1 The least square estimate for 'weak' phase objects

When the absorption in the object is negligible, i.e. when $T(\boldsymbol{x}) = \exp[\mathrm{i}\varphi(\boldsymbol{x})]$ the procedure can be simplified as only one real function $\varphi(\boldsymbol{x})$ needs to be determined instead of two. It is useful in this case to consider the weak phase approximation (cf. expression (2.53))

$$\tilde{I}_m(\boldsymbol{f}) = \delta_{\mathrm{D}}(\boldsymbol{f}) + \tilde{R}_m(\boldsymbol{f})\, 2\sin(\pi\lambda D_m \boldsymbol{f}^2)\, \tilde{\varphi}(\boldsymbol{f}) + \tilde{I}_{\mathrm{nl}_m}(\boldsymbol{f}) \tag{4.40}$$

where the last term includes the contributions that are non-linear in the Fourier transform of the phase $\tilde{\varphi}(\boldsymbol{f})$. The validity of this expression, more general than strictly weak phase (cf. condition (2.54)), is discussed in [Gui77]. The purpose consists in minimising the difference between the observed and calculated intensity distributions in a least squares sense, hence to minimise the cost functional

$$S_{\mathrm{c}} = \tfrac{1}{N}\sum_m \int \left| \tilde{I}_m^{\exp}(\boldsymbol{f}) - \tilde{I}_m[\tilde{\varphi}(\boldsymbol{f})] \right|^2 \mathrm{d}\boldsymbol{f} = \tfrac{1}{N}\sum_m \int \left| \delta\tilde{I}_m(\boldsymbol{f}) \right|^2 \mathrm{d}\boldsymbol{f} \tag{4.41}$$

$$= \tfrac{1}{N}\sum_m \int \left| \delta I_m(\boldsymbol{x}) \right|^2 \mathrm{d}\boldsymbol{x}$$

with respect to $\tilde{\varphi}(\boldsymbol{f})$. $\delta I_m(\boldsymbol{x})$ denotes the difference between the experimental image and the calculated image. This is in general tremendously complex because the intensity spectrum for a given spatial frequency depends in principle in a non-linear way on the complete spectrum of the phase. However if the non linear term in expression (4.40) is negligible, the relationship is linear and the least square estimate is given by

$$\Delta'(\boldsymbol{f})\, \tilde{\varphi}(\boldsymbol{f}) = \tfrac{1}{N}\sum \Delta'_m(\boldsymbol{f})\, \tilde{I}_m^{\exp}(\boldsymbol{f}) \tag{4.42}$$

with

$$\begin{aligned} \mathit{\Delta}'_m(\boldsymbol{f}) &= \tilde{R}_m(\boldsymbol{f})\sin(\pi\lambda D_m\boldsymbol{f}^2) \\ \mathit{\Delta}'(\boldsymbol{f}) &= \tfrac{1}{N}\sum\tilde{R}^2_m(\boldsymbol{f})\,2\sin^2(\pi\lambda D_m\boldsymbol{f}^2) \end{aligned} \tag{4.43}$$

These equations can be obtained by minimisation of the cost functional (expression (4.41)) with respect to the spectrum of the phase. Note that the multiplication of the images with the phase contrast factor itself is similar to the concept of reblurring used in § 3.4.2.3. This expression based on N images is better than expression (4.40) for a single image because the zeros in the contrast function $2\sin(\pi\lambda D\boldsymbol{f}^2)$ are avoided and because the non-linear contributions tend to cancel out. The smooth variations in the object remain problematic. This is implicit for a differential phase method. The filters $\mathit{\Delta}'_m(\boldsymbol{f})/\mathit{\Delta}'(\boldsymbol{f})$ can not be applied to the images for the low frequencies. The inverse of these ideal filters are zero for $\boldsymbol{f} = 0$ and they grow initially with the square of the spatial frequency. If all distances of the defocus series can be written as an integral multiple of a distance D_o, the denominator of the filters $\mathit{\Delta}'(\boldsymbol{f})$ is zero and retrieval problems occur at the resonance spatial frequency

$$f_\mathrm{res} = \frac{1}{\sqrt{\lambda D_\mathrm{o}}} \tag{4.44}$$

If equidistant planes are chosen, their separation D_o should be chosen small enough such that the first resonance frequency occurs above the highest frequency to be reconstructed. If one wants to retrieve the object up to the Nyquist frequency the maximum interdistance is $4\,s_p{}^2/\lambda$. If the pixel size s_p is 0.5 µm (hence the optimum resolution about 1 µm) this distance is 10 mm for $\lambda = 1$ Å.

The determination of the phase from $\exp[\mathrm{i}\varphi(\boldsymbol{x})]$ is possible by looking for the most continuous solution. In this way phase jumps of 2π can be removed. Retrieving directly the (Fourier transform of) the phase instead of the object function $T(\boldsymbol{x})$ has the advantage that the phase unwrapping is implicit. This is correct insofar as expression (4.42) is valid for this phase modulation.

If the images are backpropagated and summed and if the non-linear terms in expression (4.40) are neglected the expressions for the nominator and denominator of the ideal filters are slightly different [Clo97c]

$$\begin{aligned} \mathit{\Delta}'_m(\boldsymbol{f}) &= \exp(\mathrm{i}\pi\lambda D_m\boldsymbol{f}^2) \\ \mathit{\Delta}'(\boldsymbol{f}) &= \mathrm{i}\tfrac{1}{N}\sum\tilde{R}_m(\boldsymbol{f})\,[\,1-\exp(\mathrm{i}2\pi\lambda D_m\boldsymbol{f}^2)] \end{aligned} \tag{4.45}$$

4.3.2.2 Correction for non-linear terms

Correction for non-linear terms can again be performed recursively. A perturbation $\partial\varphi(\boldsymbol{x})$ of the phase $\varphi(\boldsymbol{x})$ introduces a variation of the intensity spectrum given, according to expression (2.50), by

$$\partial\tilde{I}_m(\boldsymbol{f}) = \tilde{R}_m(\boldsymbol{f})\, 2 \int \tilde{I}_m(\boldsymbol{f}-\boldsymbol{p}) \sin(\pi\lambda D_m \boldsymbol{f}\boldsymbol{p})\, \partial\tilde{\varphi}(\boldsymbol{p})\, \mathrm{d}\boldsymbol{p} \tag{4.46}$$

Note that the weak phase approximation is a special case of this with $\tilde{I}_m(\boldsymbol{f}-\boldsymbol{g}) = \delta_\mathrm{D}(\boldsymbol{f}-\boldsymbol{g})$. As long as the DC component in the *intensity* distribution is dominant the linearisation (restricting $\boldsymbol{p}$ to $\boldsymbol{f}$ in the integral (4.46)) seems correct. The iterative correction can than be done in a similar way as in § 4.3.1.4

$$\varDelta'(\boldsymbol{f})\, [\tilde{\varphi}^{j+1}(\boldsymbol{f}) - \tilde{\varphi}^{j}(\boldsymbol{f})] = \tfrac{C}{N} \sum \varDelta'_m(\boldsymbol{f})\, [\tilde{I}_m^{\mathrm{exp}}(\boldsymbol{f}) - \tilde{I}_m^{j}(\boldsymbol{f})] \tag{4.47}$$

If the domain of the integral is not restricted, each iteration step to obtain the least square estimate involves the solution of a very large system of linear equations. We never attempted this solution. It might be a feasible method if the integral is limited to the dominant contributions.

4.3.3 Non linear least squares method

To find the optimum complex object given N recorded images is in general a tremendous task because 1) the number of unknown (2 N_p^2) and the number of measurements ($N\ N_\mathrm{p}^2$) are huge (millions; N_p is the width of the images in pixels) 2) the object-image relationship is non-linear. Approximate methods that are direct (non-iterative), such as the paraboloid method described above, are thus crucial in order to obtain, if not the optimum solution, at least a solution that is reasonably close to the best one. The solution given by the direct method, followed if necessary by few iterative corrections for the non-linear terms, can be used as the final solution or, if the non-linear contributions are too strong, as the initial estimate for a non-linear iterative optimisation.

A scheme to retrieve the Bayesian or maximum a-posteriori estimate was proposed in [Kir84]. This implies to have some a-priori knowledge about the object. We will assume that this information is not available. The noise characteristics are also not straightforwardly modelled because several (not necessarily additive) contributions occur such as Poisson noise, additive gaussian detector noise, ... Therefore a simpler least squares optimisation is used and the optimum solution consists in the complex object function $T(\boldsymbol{x})$ that minimises the squared differences between the measured and calculated images (or equivalently their spectra, cf. Parseval's theorem) as expressed in equation (4.41). This corresponds of course to the maximum likelihood solution if one assumes gaussian additive noise with zero mean [Kir84, Coe92].

The method used for the minimisation is essentially a steepest descent procedure. Expressing the calculated intensity with the help of the transmission cross coefficient $T_{\mathrm{cc,m}}(\boldsymbol{p},\boldsymbol{f})$ (cf. equation

(2.78)) and minimising the cost functional with respect to the object $\tilde{T}(\boldsymbol{f})$ yields as condition on the optimum object [Kir84]

$$-2\frac{1}{N}\sum_m \int T_{\mathrm{cc,m}}(\boldsymbol{p},\boldsymbol{f})\,\tilde{T}(\boldsymbol{p})\,\delta\tilde{I}_m(\boldsymbol{f}-\boldsymbol{p})\,\mathrm{d}\boldsymbol{p} \;=\; 0 \tag{4.48}$$

If a discrete and finite number of spatial frequencies $\boldsymbol{f}_q$ are considered, the left hand side can be interpreted as the derivative of the cost function with respect to $\tilde{T}^*(\boldsymbol{f}_q)$ [Kir84]. Inserting the appropriate expression for the transmission cross coefficients (cf. expression (2.79)) yields

$$-2\frac{1}{N}\sum_m \tilde{P}^*_{\mathrm{m}}(\boldsymbol{f})\int\Big[\tilde{P}_{\mathrm{m}}(\boldsymbol{p})\,\tilde{T}(\boldsymbol{p})\Big]\Big[\tilde{R}_{\mathrm{m}}(\boldsymbol{f}-\boldsymbol{p})\,\delta\tilde{I}_m(\boldsymbol{f}-\boldsymbol{p})\Big]\,\mathrm{d}\boldsymbol{p} \;=\; 0 \tag{4.49}$$

The integrals are the cross-correlation functions for each image plane of the spectrum of the field $\tilde{u}_{\mathrm{m}}(\boldsymbol{f}) = \tilde{P}_{\mathrm{m}}(\boldsymbol{f})\,\tilde{T}(\boldsymbol{f})$ and of the difference image $\tilde{R}_{\mathrm{m}}(\boldsymbol{f})\,\delta\tilde{I}_m(\boldsymbol{f})$. The latter one is reblurred. The term in front of each integral is the backpropagator of the corresponding plane. For the optimum object the difference images carry no information on the object because they contain only noise. The steepest descent method adds at each iteration step a fraction of the opposite of expression (4.49) to the object spectrum. Given a prior estimate of the object, the new estimate is obtained from

$$\tilde{T}^{j+1}(\boldsymbol{f}) \;=\; \tilde{T}^{j}(\boldsymbol{f}) + \frac{C}{N}\sum_m \tilde{P}^*_{\mathrm{m}}(\boldsymbol{f})\int \tilde{u}^j_{\mathrm{m}}(\boldsymbol{p})\Big[\tilde{R}_{\mathrm{m}}(\boldsymbol{f}-\boldsymbol{p})\,\delta\tilde{I}^j_m(\boldsymbol{f}-\boldsymbol{p})\Big]\,\mathrm{d}\boldsymbol{p} \tag{4.50}$$

with C a convergence parameter. The cross-correlations are calculated by Fourier transformation, hence

$$\tilde{T}^{j+1}(\boldsymbol{f}) \;=\; \tilde{T}^{j}(\boldsymbol{f}) + \frac{C}{N}\sum_m \tilde{P}^*_{\mathrm{m}}(\boldsymbol{f})\,\underset{\boldsymbol{x}\to\boldsymbol{f}}{\Im}\Big\{u^j_m(\boldsymbol{x})\,\underset{\boldsymbol{f}\to\boldsymbol{x}}{\Im}\Big[\tilde{R}_{\mathrm{m}}(\boldsymbol{f})\,\delta\tilde{I}^j_m(\boldsymbol{f})\Big]\Big\} \tag{4.51}$$

with

$$\begin{aligned}\delta\tilde{I}^j_m(\boldsymbol{f}) &= \tilde{I}^{\mathrm{exp}}_m(\boldsymbol{f}) \;-\; \tilde{R}_{\mathrm{m}}(\boldsymbol{f})\,\underset{\boldsymbol{x}\to\boldsymbol{f}}{\Im}\Big\{\,|u^j_m(\boldsymbol{x})|^2\Big\}\\ u^j_m(\boldsymbol{x}) &= \underset{\boldsymbol{f}\to\boldsymbol{x}}{\Im}\Big[\tilde{P}_{\mathrm{m}}(\boldsymbol{f})\,\tilde{T}^j(\boldsymbol{f})\Big]\end{aligned} \tag{4.52}$$

One iteration step requires 4 two-dimensional Fourier transformations for each distance. If the detector response and the coherence are perfect this number is only 2. The possibility to calculate the correlations appearing in expression (4.48) with Fourier transformations results in a tremendous gain in calculation time [Coe92]. This is **not** an approximation thanks to the good monochromaticity of the beam and the absence of spherical aberration and defocus spread. The convergence parameter C can in principle be determined by various techniques to speed convergence. However more elaborate methods are often less adapted to complex systems with a large number of parameters [Hun77]. We used a constant value of C or a value that is increased at every successful iteration step with a maximum value of 1. The iterative procedure is stopped after a fixed (small) number of iterations (10-20) or when the decrease of the cost function becomes too small. If constraints are known, they modify the least squares estimate. They can be included by the use of Lagrange multipliers (cf. the linear case treated in [Haw74]). When constraints were used on the experimental results, it was done by using an adapted model (see § 4.3.2) in the direct part of the reconstruction. For the recursive part it was done by applying the constraints to the current estimate in between successive iteration steps.

4.3.4 Experimental results

4.3.4.1 A test fibre

The first test sample was a single polymer fibre extracted from a commercial string. Inspection with an optical microscope showed a diameter of approximately 12 µm and a nearly perfect cylindrical shape. Fig 4.4a shows a series of 9 images, recorded at increasing distance with respect to the sample, used for the reconstruction [Clo97c]. Equidistant planes were chosen starting at 32 mm from the sample and with an increment of 100 mm. The sample is expected to be a pure phase object since the absorption is smaller than 0.1 % at the X-ray wavelength $\lambda = 0.7$ Å ($E = 18$ keV) used. Images with and without sample were recorded on high resolution film to allow for flat-field correction. For this, the normal procedure of absorption imaging was used (i.e. pixel by pixel division), an acceptable solution because the beam inhomogeneity was small and concerned basically low frequencies which are not convolved with the object information in the propagation process. The complete defocus series including calibration measurements were recorded on the same film which was automatically translated between the different images. The intensity plots (dots) in Fig 4.4b correspond to averages in the direction parallel to the one-dimensional fibre, considerably reducing the noise. Digitisation of the films was performed with an 8-bit AD-converter and 0.88 µm pixel size. Alignment errors were kept as small as possible and the remaining faults were detected using cross correlation techniques and corrected for. The first two images correspond to the edge-detection regime in which each edge of the fibre gives a separate fringe structure. Further away the edges can no longer be recognised and the Fresnel diffraction pattern varies strongly with the defocusing distance D. The contrast increases gradually and stabilises at around 80 %, a factor 1000 higher than the expected, undetectable absorption contrast.

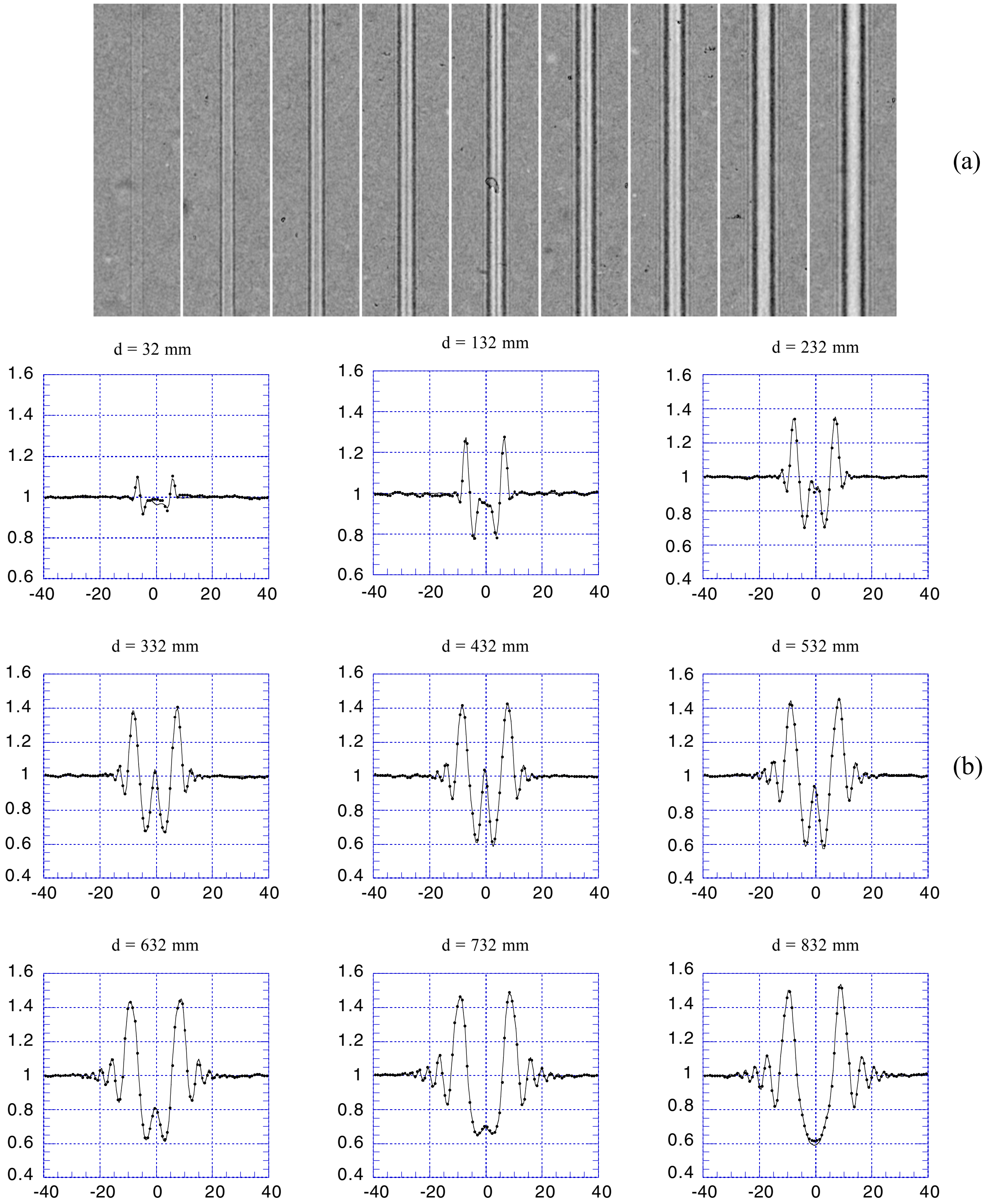

Fig 4.4 Defocus series for a polymer fibre. The images were recorded in equidistant planes separated by 100 mm with the first plane at 32 mm with respect to the sample. Fig. (a) corresponds to the images recorded on HR-film considering the film response and after flat-field correction. The intensity plots (dots) in Fig. (b) correspond to the experimental images averaged in the direction parallel to the one-dimensional fibre (distance in microns). The full lines correspond to the intensity distributions calculated from the reconstructed complex amplitude. $\lambda = 0.7$ Å; horizontal monochromator.

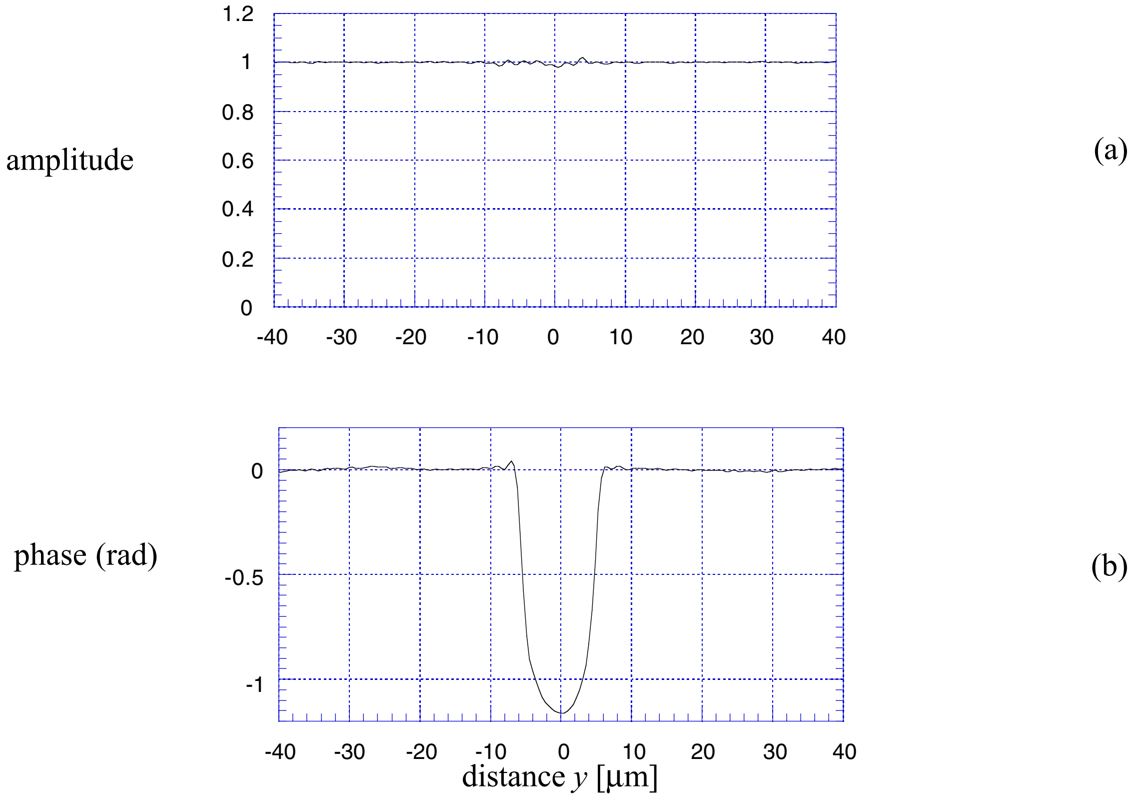

Fig 4.5 Reconstructed amplitude (a) and phase (b) of the object transmission function for a test sample consisting of a polymer fibre. The diameter is approximately 12 µm and the maximum phase modulation is -1.15 rad.

Fig 4.5 shows the reconstructed amplitude (a) and phase (b) of the object transmission function. The initial guess was directly retrieved with expressions (4.42) and (4.45). Using the horizontal monochromator, the vertical coherence was about perfect. The lowest frequencies could not be determined because the images are not sensitive to them at the distances used. Their contribution to the image is too small compared to the dynamic range and the noise level when recording the images on film. The spectrum of the phase in this small frequency range was determined through extrapolation from the spectrum at slightly higher frequencies. The initial guess was iteratively improved using the non-linear least squares method which corrects both amplitude and phase of the wave (equation (4.51)). The detector transfer function was approximated by a gaussian with a width (FWHM) of 1.6 µm. No constraint was imposed although the absorption was known to be negligible. The amplitude remains constant as expected. The form of the phase modulation of the fibre corresponds approximately to the ideal cylindrical shape. The Fourier transform of the reconstructed phase is similar to the expected Bessel function. From the zeros in the spectrum of the phase the diameter of the fibre was found to be 11.8 µm. The maximum phase modulation at the centre of the fibre is -1.15 rad, corresponding to a value for δ of 1.1 10^{-6}, in agreement with the theoretical value of 0.9 10^{-6} for nylon ($\rho = 1.15$ g/cm^3) at this energy. Thus the object is not a weak phase object but rather strong, indicating that the non-linearity was correctly handled. The full lines in Fig 4.4b correspond to the intensity distributions calculated from the reconstructed object. Very good agreement with the experimental data is obtained over the complete series of images, confirming the validity of the solution.

4.3.4.2 A two-dimensional example

A piece of polystyrene foam, an object of industrial interest with a rather complex three dimensional structure, was used to test the phase retrieval procedure on two-dimensional images [Cloe98b]. The 1 mm thick sample with negligible attenuation was set in the X-ray beam monochromatised at 18 keV. A total of 16 images were recorded for *D* ranging from 0.01 to 0.91 m. The separation between the planes was not regular. The CCD based high resolution detector (see § 3.4.2) with a pixel size of 1.9 µm was used. The spatial frequency response of the detector was precisely measured in order to account for it during the phase determination. The width of the LSF was 3 µm. The images were previously corrected for the OTF (see § 3.4.2.3) using the reblurring technique (equation (3.52) and Fig. 3.13). About identical results were obtained if the correction for the detector response was done as part of the phase retrieval procedure. The images were corrected for the (small) magnification introduced by the projection. The largest value of M (for $D = 0.91$ m) is only 1.006. The origins of the Fresnel diffraction patterns were aligned using cross-correlation techniques. The distance between the successive planes is small enough, hence the corresponding images are sufficiently similar for this to be successful.

Fig 4.6a shows 3 of the 16 recorded images. None of them is representative of the edge-detection regime, due to the small size of the features in the foam (2-10 µm from inspection with visible light microscopy). The contrast and the width of the interference fringes increases strongly with the distance. A direct interpretation of the images is therefore subject to errors. At small distance and with weak contrast, it seems possible to individualise some features but little can be said about their sizes. At larger distance, on the other hand, the contrast is strong but the width of the interference fringes makes it difficult to isolate features, hence all resolving power is lost. The purpose of the phase determination is 1) to obtain an image that contains more correctly interpretable information on the sample than each of the individual images 2) to obtain quantitative information on the sample, a prerequisite for three-dimensional imaging.

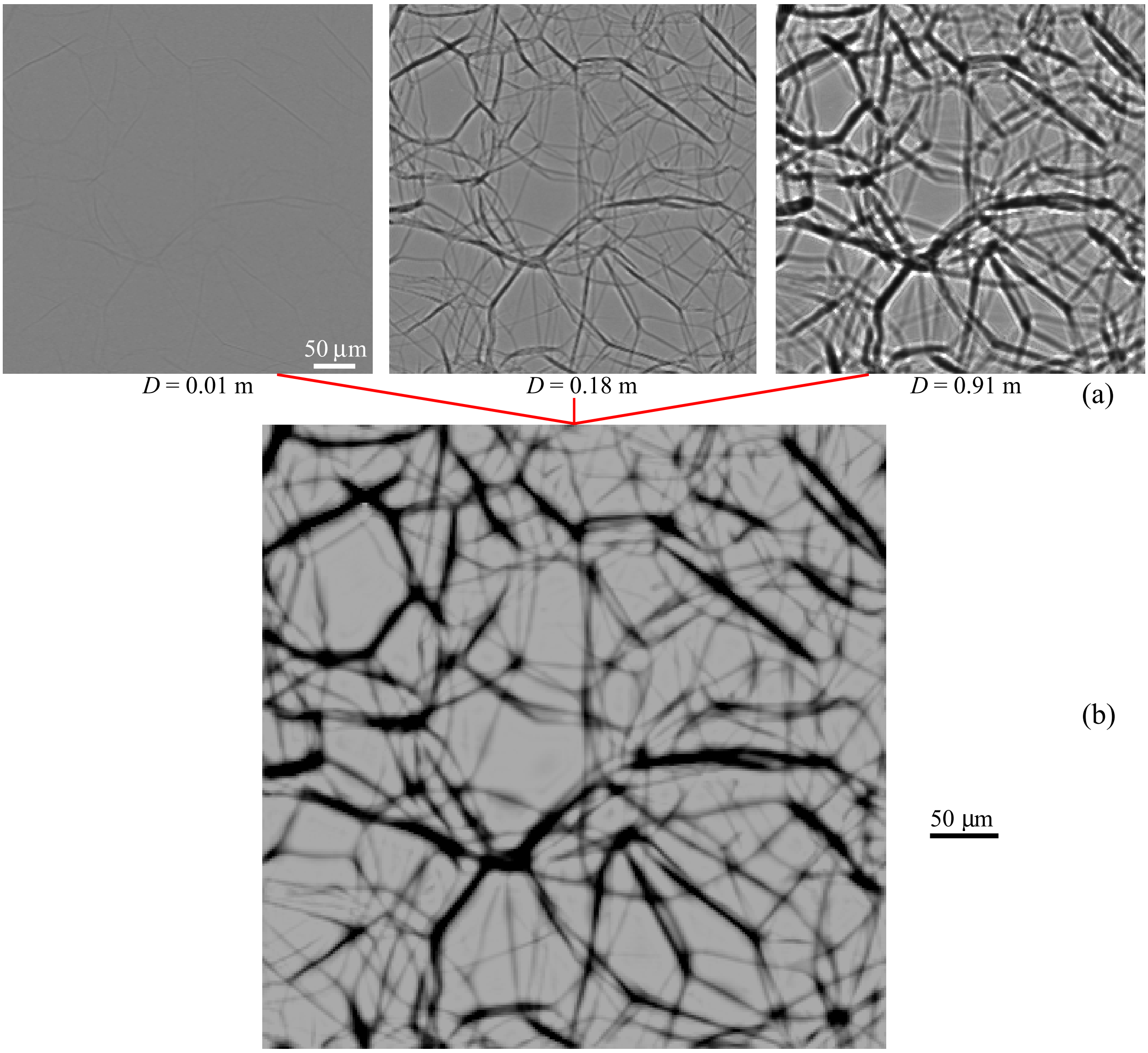

Fig 4.6 Principle of quantitative phase imaging. A series of images are recorded at different distances from the sample. Some of the 16 images of a 1 mm thick piece of polystyrene foam recorded at distances varying from 0.01 m to 0.91 m are shown in (a). An adapted numerical algorithm (see text) allows to combine these images and to retrieve the phase modulation introduced by the sample, shown in (b). Because linear grey scales are used, it is not possible to visualise the weakest phase modulations without saturation in the regions where the phase is strong. $E = 18$ keV, X-ray on-line detector with a pixel size = 1.9 µm.

The reconstructed phase map is shown in Fig 4.6b. A first estimate was directly retrieved from equations (4.42) and (4.45). An indetermination in the retrieval occurred only for $\boldsymbol{f} = 0$ because resonance frequencies were avoided by the choice of the distances (see equation (4.44)). The theoretically zero denominator $\Delta'(\boldsymbol{f})$ of the filters constituted less of a problem compared to the previous case with images recorded on film. The low frequency noise seems thus to be smaller. A Wiener -type filter (see § 3.4.1.3) was used to solve the divergence problem. In order to correct for the remaining non-linear contributions, three iterative corrections to the first estimate were made (expression (4.47)). This approximation of the object was used as initial estimate in the following non linear least squares minimisation (equation (4.51)). Good results could only be obtained by constraining the solution. The amplitude modulation was kept equal to zero and the phase of the object with respect to a portion of the image without sample was forced to have only negative values. These constraints are in agreement with the underlying physics (see § 2.2.2 and equation (2.25)). The constraints were applied after each iteration step, i.e. the amplitude of the object was set to one and only negative values of the relative phase were retained. The final result was obtained after 10 such iterations.

The image in Fig 4.6b has a straightforward interpretation, it is a projection of the electronic density in the sample. The projection is made along the X-ray path over the sample thickness as defined by equation (2.91). The features in the sample can now be individualised. Their width corresponds to the real (projected) size and is in agreement with observations of the surface by light microscopy. The limitation is now due to the projection of the object over its thickness. The colour map in Fig 4.7a represents the same phase modulation and is better adapted to span the complete dynamic range it involves. The wider structures correspond to a stronger phase modulation indicating that this foam has a skeleton consisting of rod-like structures. The rods are thin; most of them have a projected width smaller than 10 µm. They determine cells in the foam with a much larger size (100-200 µm). From a projection image it is not clear whether the cells are interconnected or if they are enclosed by thin walls. The phase modulation becomes very strong ($> 2\pi$) and difficult to follow with the available spatial resolution at the nodes where several rods meet. This would be less of a problem with a better spatial resolution, which would avoid sudden variations of the phase compared to the resolving power. A small portion of the phase map displayed in Fig 4.7a is shown magnified in b. This reveals the excellent spatial resolution obtained: the algorithm allows to retrieve the object information down to the level of the pixel size. The highest accessible spatial frequency is determined by the resolution of the detector. The lowest frequencies or smooth variations in the sample are more difficult to retrieve as they require an increasing propagation distance. The profile presented in Fig 4.7c is the phase profile obtained along the arrow shown in Fig 4.7b. It shows the quantitative character of the reconstruction and the very low noise level reached thanks to the use of a large number of images. The phase modulation is quantitatively determined and constitutes the correct input for a tomographic reconstruction in order to retrieve the three dimensional distribution of the refractive index decrement which is proportional to the local electron density.

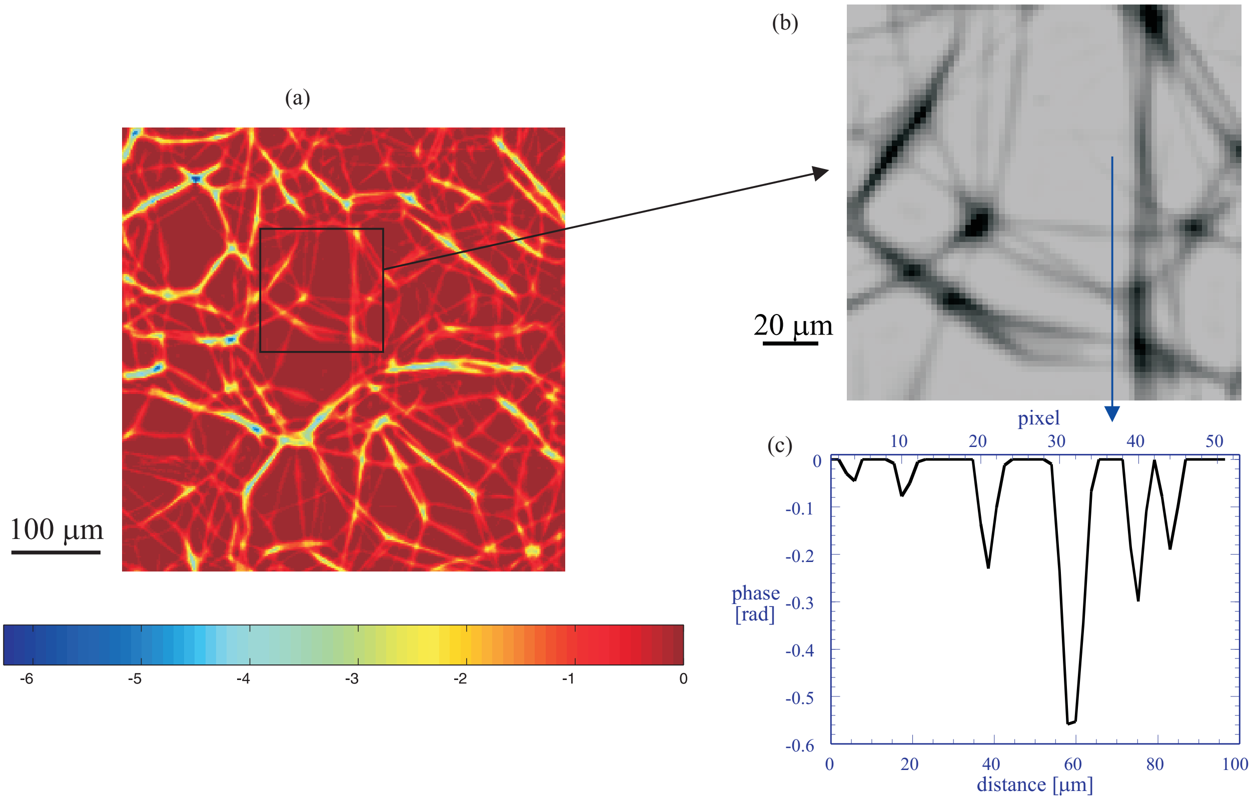

Fig 4.7 (a) Colour map representing the same retrieved phase map. The colour bar indicates the phase-colour correspondence. The foam skeleton is built of interconnected rods with variable thickness. (b) Magnified portion of the image. (c) Phase profile obtained along the arrow shown in (b). The noise level is low and the thinnest rods are well resolved.

4.4 The tomographic reconstruction

Computed tomography, based on a large number of projections recorded at different angular positions of the sample, reveals the three dimensional structure of the object. Adapted algorithms exist to treat the case of absorption tomography. As an unsatisfactory but provisional solution the same methods were at first used for the phase sensitive case. This results in a workable solution for some cases [Clo97a, Buf97], but gives rise to artefacts and does not reveal quantitatively the inner structure of the object. The combination of a 'holographic' and the classical 'tomographic' reconstruction allows to determine completely the distribution of the electronic density in the sample. In § 4.4.1 we show first experimental results using this technique. Then we give in § 4.4.2 a mathematical justification why under weak defocus conditions the use of the absorption algorithm can give a meaningful result. We also propose a method based on two tomographic scans, respectively in absorption and weak defocus conditions, in order to retrieve two 3D representations of the sample. The first one is the distribution of the linear absorption coefficient $\mu(x,y,z)$, the second is the three dimensional Laplacian of the refractive index decrement .

4.4.1 Holo-tomography

4.4.1.1 Principle

The correct input for a tomographic reconstruction is a set of projections (the Radon transform) of a local quantity such as the linear absorption coefficient or the electron density (see § 2.3). The tomographic reconstruction, usually implemented with the filtered backprojection algorithm, then allows to calculate without artefacts and in a unique way the three dimensional distribution of this quantity in the sample. If two-dimensional images of the sample that are not projections (integrals along the path of the beam, expression (2.91)) of a local quantity are used as input for the tomographic reconstruction, artefacts arise due to the non-linearity and the retrieved 3D map has no quantitative meaning.

When sufficient experimental data are available, i.e. if for each angular position in the tomographic scan enough Fresnel diffraction patterns are recorded to retrieve the object transmission function, it is possible to retrieve the three-dimensional distribution of the complex refractive index. The reconstruction problem can be split into two steps:

1) The object transmission function $T_\omega(x,y)$ is retrieved using the **holographic reconstruction** of § 4.3. This function depends on the angular position in the tomographic scan. Its modulus gives the amplitude modulation $B_\omega(x,y)$ proportional to the projection of the linear absorption coefficient $\mu(x,y,z)$ (equation (2.22)). The phase $\varphi_\omega(x,y)$ of the transmission function is proportional to the projection of the refractive index decrement $\delta(x,y,z)$ (equation (2.23)). Using the complex logarithmic function this can formally be written

$$\ln\left[\tilde{T}_\omega(x,y)\right] = \mathrm{i}k\int[\,n_\omega(x,y,z)-1\,]\,\mathrm{d}z = -k\int\beta_\omega(x,y,z)\,\mathrm{d}z - \mathrm{i}k\int\delta_\omega(x,y,z)\,\mathrm{d}z \tag{4.53}$$

where it is assumed that the optical path length is measured relative to a path in vacuum and with k the wave number in vacuum. The holographic reconstruction is repeated for each angular position of the sample, hence a total of N_V times.

2) From the projections the 3D distribution of the complex refractive index is determined with a classical **tomographic reconstruction** procedure, such as the filtered backprojection algorithm. The final result is thus the distribution of the linear absorption coefficient $\mu(x,y,z)$ $(=2k\beta)$ and the distribution of $\delta(x,y,z)$ which is to a good approximation (see § 2.2.2) proportional to the electron density $\rho_\mathrm{e}(x,y,z)$.

The more complex step is the first one, the latter one being in fact analytical. It is thus preferable to reduce the three-dimensional problem to a large number (N_V) of two dimensional problems. Thanks to the parallel beam geometry the second part can actually also be split into two-dimensional problems (see § 2.3). It is possible to check the final 3D distribution for self consistency by calculating from it the transmission function (expression (2.21)) for a specific angle and the corresponding Fresnel diffraction patterns (expression (2.90)) at the recording distances. They can be compared to the experimental images.

4.4.1.2 Experimental results

A three-dimensional study was performed of the polystyrene foam sample used earlier (see § 3.4.2.3 and § 4.3.4.2). The sample was slightly reduced in width to 700 μm by 500 μm to fit into the field of view of 1 mm (pixel size = 0.95 μm). The elements of the system were carefully characterised in order to account correctly for them. The wavelength λ of the incoming beam was set to 0.69 Å with the use of the vertical monochromator. The degree of coherence was determined with a grating using the method based on the Talbot effect (see § 4.2). The angular divergence was 1.9 μrad and 1.2 μrad in respectively the horizontal and vertical direction. As detector we used a CCD based X-ray image converter with a transparent YAG:Ce screen (see § 3.4.2). The OTF of the detector was determined from the measured edge spread function and is shown in Fig. 3.14. The angular position of the sample and the defocus distance were remotely controlled with an adapted set-up (see § 3.3). 4 tomographic scans of 700 views each were automatically recorded at defocusing distances D of 0.027, 0.207, 0.505 and 0.901 m. The number of defocusing distances is reduced in order to limit the acquisition and data processing time. The recorded images, 1024 by 1024 pixels in size, were flat-field corrected and corrected for the small magnification (maximum 1.006) due to projection (equation (2.61)). For each angular position of the sample the corresponding phase map was retrieved using the holographic reconstruction presented in § 4.3 with 4 image planes. The approximate phase was directly retrieved using a paraboloid method (equation (4.45)) with 3 iterations to correct for non-linear contributions (equation (4.47), $C = 0.5$). This first estimate was optimised using the non linear least squares method (equation (4.51), $C = 1$) and 5 iterations. The constraints were identical to those in § 4.3.4.2: no amplitude modulation and only negative relative phases. The phase retrieval included correction for the detector response and the partial coherence (see equation (4.27)). The determination of each phase map took about 25 minutes. It was easy to distribute the workload over different machines because the holographic reconstructions for each angular position were considered as independent. The 700 phase maps, projections of the refractive index decrement, were used to determine the 3D δ-distribution in the sample with a filtered backprojection algorithm (see § 2.3).

Fig 4.8a shows a slice of the reconstructed volume. The grey scale is linear with the index decrement δ, more black corresponds to a higher electron and mass density. The interpretation of the reconstructed slices is thus straightforward and the 3D distribution is well adapted for further automatic processing such as binarisation or building the foam skeleton. This is not the case with the edge contrast appearing when an incomplete reconstruction scheme is used (see § 5.2). The contrast of the polymer foam is excellent. This would certainly not be the case in absorption tomography, the ratio of the refractive index decrement and the absorption index δ/β being 2500.

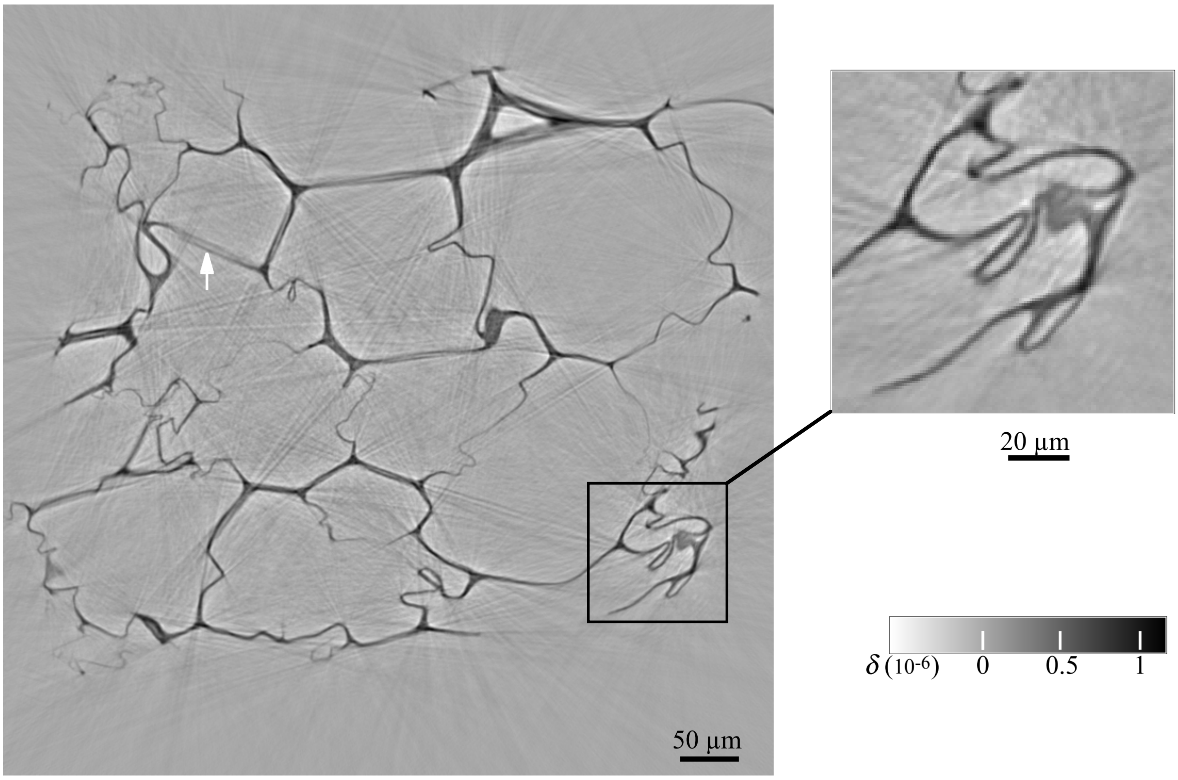

Fig 4.8 Quantitative coherent 3D imaging: (a) a slice of the reconstructed distribution of the refractive index decrement δ of a polystyrene foam. δ is essentially proportional to the electron and mass density in the polymer. A phase map was determined for each of the 700 angular positions using the holographic reconstruction of § 4.3 based on 4 defocus distances. From the projections the 3D distribution was determined with a filtered backprojection algorithm. (b) Magnified portion of the reconstructed slice shown in a. Some artefacts are visible (see text). Pixel size = 0.95 µm, $\lambda = 0.69$ Å.

Some features are artefacts. Occasionally stripes appear in the direction of the tomographic projection, especially when the direction is such that the amount of traversed polymer is high. This corresponds to sudden, large phase modulations ($> \pi$) with some absorption (still < 1 %). The phase determination may contain errors for those projections due to the spatial sampling rate and the limited number of distances and iterations used in the holographic reconstruction. A possible solution consists actually in increasing the photon energy in order to lower the contrast (!). Some regions appear incorrectly with a slightly negative index decrement (more white than regions without polymer). This corresponds to faults in the low frequency range in the determination of the spectrum of the index distribution. A negativity constraint was applied (with a small tolerance of 0.01 rad) in the retrieval of the phase maps. This is apparently not sufficient to assure only positive values of the refractive index decrement after tomographic reconstruction. It might be preferable to constrain the 3D distribution. Solving directly the three-dimensional problem, instead of splitting it in a large number of 2D problems, is on the other hand highly unpractical. The value of the index decrement in regions that apparently contain only polymer varies from $4\ 10^{-7}$ to $9\ 10^{-7}$. This decrement corresponds to, using expression (2.15) and neglecting the dispersion corrections, a density value varying from 0.5 to 1.25 g/cm^3. The expected density value for polystyrene is about 1 g/cm^3. The experimentally obtained number is the average in a 1 µm^3 voxel.

The tomographic slice of Fig 4.8 cuts several cells of the foam. It is now clear that the cells are in most cases completely closed by a polymer wall. In some regions the wall is rather thick (10 50 µm) where the slice cuts the rod-like skeleton structures. In other regions it becomes very thin and occasionally it seems to disappear probably due the rather large pixel size. The thin walls were not evident in the projection images (see phase map of Fig 4.7), but they appear correctly after tomographic reconstruction. The shape of the cells is irregular and very distorted. It is thus not only determined by a simple principle such as minimisation of the surface tension from which a simpler shape of the cells would be expected. The closed cell structure may be only apparent and interconnections could occur at a different depth in the sample. Therefore the reconstruction must be visualised and studied further in a three dimensional manner. The cell walls are not homogeneous and density variations occur inside. Several walls (an example is indicated with an arrow) appear with a double contrast. This double rod structure could also be observed at the surface by visible light microscopy. The magnified portion of the slice shown in Fig 4.8b, indicates an excellent 3D isotropic spatial resolution that can be obtained thanks to the detector resolution but also because the holographic reconstructions disentangled the object information from the recorded defocused images.

4.4.2 Justification of the approximate approaches

As a first and obviously unsatisfactory approach, the reconstruction algorithm of absorption tomography was used directly on the recorded phase sensitive images for some applications (see § 5) without holographic reconstruction. We give a theoretical justification of the validity of this approach for phase sensitive tomography under specific conditions [Clo97a]. The reason is that the recorded intensity may, for weak defocusing conditions, be approximated by the product of an absorption and a phase contribution. The first is identical to the one in absorption radiography. The latter involves the two dimensional Laplacian of the phase. This is of interest for situations where completely quantitative coherent tomography, as described in previous section, is not necessary or not feasible due to insufficient data collection.

We will assume that the incident amplitude is an ideal plane monochromatic wave such that $|u_{\mathrm{inc}}(x,y)|^2 = i_o$, the incident intensity. If $D = 0$, the intensity, recorded with an ideal detector, is simply (recall expression (2.30))

$$I_0(x,y) = i_o\, A^2(x,y) = i_o \exp\left[-\int \mu(x,y,z)\,\mathrm{d}z\right] \tag{4.54}$$

identical to what is obtained in conventional X-ray radiography. We will consider a simplified expression for $I_D(x,y)$ valid under weak defocusing conditions, hence we determine the first order term in its expansion as a function of defocus D. In reciprocal space the propagator $\tilde{P}_D(\boldsymbol{f})$ can be approximated as $1 - \mathrm{i}\pi\lambda D \boldsymbol{f}^2$ (cf. expression (2.48)). The wave amplitude at distance D is thus (expression (2.47))

$$\tilde{u}_D(\boldsymbol{f}) \approx \tilde{u}_0(\boldsymbol{f})\,[\,1 - \mathrm{i}\pi\lambda D\boldsymbol{f}^2] \tag{4.55}$$

Fourier transformation gives

$$u_D(x,y) \approx u_0(x,y) + \mathrm{i}\frac{\lambda D}{4\pi}\,\mathrm{D}^2_{xy}u_0(x,y) \tag{4.56}$$

where $\mathrm{D}_{xy} = (\partial/\partial x, \partial/\partial y)$, denotes the gradient operator in the (x,y)-plane. The operator applied to the complex amplitude is thus the two-dimensional Laplacian. The intensity is (equation (2.29))

$$I_D \approx |u_0|^2 - \frac{\lambda D}{2\pi}\,\mathrm{Im}\Big[u_0\;\mathrm{D}^2_{xy}u_0^*\Big] \tag{4.57}$$

where Im[ ] denotes the imaginary part. Introducing the modulus and the phase of the object transmission function (expression (2.21)) yields

$$I_D \approx i_o A^2\left(1 - \frac{\lambda D}{2\pi}\,\mathrm{D}^2_{xy}\varphi\right) - i_o\frac{\lambda D}{2\pi}\,(\mathrm{D}_{xy}A^2\;.\;\mathrm{D}_{xy}\varphi) \tag{4.58}$$

This expression is in agreement with the transport of intensity equation [Tea82] and the usual expression for weakly defocused images of phase objects [Cow75]. If the absorption term A varies slowly compared to the phase modulation φ, the last term in the expression can be neglected, giving in combination with expression (4.54)

$$I_D(x,y) \approx I_0(x,y)\left[1 - \frac{\lambda D}{2\pi}\,\mathrm{D}^2_{xy}\varphi(x,y)\right] \tag{4.59}$$

This means that initially the defocusing does not practically affect the absorption image. Consequently the image is a product of a in-focus absorption term ($I_0(x,y)$) and a phase sensitive defocusing term.

If a single image is recorded at distance D it is not possible to separate both contributions. It is then convenient to use for I_D the following expression, equivalent to the previous one if $\frac{\lambda D}{2\pi}\,\mathrm{D}^2_{xy}\varphi(x,y) << 1$

$$I_D \approx I_0\exp\left[-\frac{\lambda D}{2\pi}\,\mathrm{D}^2_{xy}\varphi\right] \tag{4.60}$$

Thus, taking the logarithm as for absorption tomography

$$\ln\left(\frac{i_o}{I_D}\right) \approx -\ln A^2 + \frac{\lambda D}{2\pi}\,\mathrm{D}^2_{xy}\varphi \tag{4.61}$$

Using expressions (4.54) and (2.23), one obtains the projections used as input for the tomographic reconstruction

$$\ln\left(\frac{i_o}{I_D}\right) \approx \int \mu(x,y,z)\,\mathrm{d}z - D\ \mathrm{D}^2_{xy}\left[\int \delta(x,y,z)\,\mathrm{d}z\right] \tag{4.62}$$

The reconstruction of the first term provides $\mu(x,y,z)$, the distribution of the linear absorption coefficient in the object. The second term corresponds to the two-dimensional Laplacian of the projection of $\delta(x,y,z)$. In 2D, it is known that the second derivatives of the projections of a distribution allow to recover the 2D Laplacian of this unknown distribution [Her80]. This property may be extended to 3D, thus the reconstruction of the second term provides the 3D Laplacian of the real part of the refractive index decrement $\delta(x,y,z)$. In summary, the 3D reconstructed distribution $o(x,y,z)$ is approximately, under weak defocus conditions,

$$o(x,y,z) \approx \mu(x,y,z) - D\left(\frac{\partial^2}{\partial^2 x}+\frac{\partial^2}{\partial^2 y}+\frac{\partial^2}{\partial^2 z}\right)\delta(x,y,z) \tag{4.63}$$

Since interfaces between materials correspond to singularities in the refractive index, they are amplified by the Laplacian operator, and appear as black/white contrasts in the reconstructed images (see § 5.2).

The artificial introduction of the exponential function in expression (4.60) allows to describe the phase effect as a pseudo-attenuation with a coefficient given by the second term in expression (4.63). If two images are recorded, respectively in absorption ($D = 0$) and weak defocus conditions, it is possible to avoid this supplementary approximation and to separate the attenuation and phase contributions in expression (4.59). The ratio of the weakly defocused image and the absorption image yields, up to a constant, the two dimensional Laplacian of the phase

$$\frac{I_D(x,y)}{I_0(x,y)} - 1 \approx -\frac{\lambda D}{2\pi}\mathrm{D}^2_{xy}\varphi(x,y) \tag{4.64}$$

If this ratio is used as input for the tomographic reconstruction (*without* introducing the logarithmic function), the retrieved distribution is approximately

$$o_2(x,y,z) \approx D\left(\frac{\partial^2}{\partial^2 x}+\frac{\partial^2}{\partial^2 y}+\frac{\partial^2}{\partial^2 z}\right)\delta(x,y,z) \tag{4.65}$$

hence it is directly proportional to the three dimensional Laplacian of the refractive index decrement. The absorption images yield of course the distribution of μ. This method based on two tomographic scans was successfully applied to an absorbing PVC foam sample [Lud98].

4.5 Sub-micron resolution using an X-ray waveguide

The resolution in the Fresnel diffraction patterns is essentially limited by the blurring due to the incident angular source size and the detector. A phase reconstruction algorithm allows to reach about the same resolution in the retrieved object as in the diffraction patterns. At synchrotron beamlines the source-sample distance is huge compared to the sample-detector distance, hence the blurring due the source is limited to a fraction of its size. On the other hand the magnification M is always close to 1 and the resolution in the Fresnel diffraction patterns (the information limit [Dai74]) is imposed by the detector. With film or an X-ray image converter it is in the best case of the order of 1 µm. In fact, the performance of existing focusing devices after the sample implies a perturbation of the imaging process and does not allow to improve the resolving power significantly. The main raison is the very low value of the refractive index decrement ($\approx 10^{-6}$) for hard X-rays. Diffractive optics such as (phase) zone plates are successfully applied in the soft X-ray range. Several soft X-ray microscopes [Say95, Sch95] exist with an optimum spatial resolution of about 50 nm. The low efficiency of the lenses, the still significant radiation damage and the limitation in sample thickness restrict their use. Zone plates for hard X-rays lately improved in quality but their absolute performances are still poor [Lai95]. The material thickness required to introduce appreciable phase shifts increases to several microns and this leads to ratios of the height and width of the zones that are difficult to realise. A magnifying set-up using circular Bragg-Fresnel lenses was reported, but no real improvement in the resolving power could be obtained and the quality of the optical elements is not in a satisfactory way compatible with imaging applications [Sni97]. Refractive lenses suffer also from the relatively weak effect of matter on the propagation of X-rays. The focal length of a circular lens given by $r_1/(2\delta)$ is huge. A radius of curvature r_1 of the lens of 100 µm results in a totally unpractical focal length of 50 m. Compound refractive lenses consist of a succession of a large number of lenses (up to 200) in order to divide the focal length by this same number [Sni96b]. They seem practical for focusing applications down to spot sizes of 1 µm and were very recently used as an actual lens for imaging applications [Len98]. A gain in resolving power compared to existent systems was not reported until now and the imperfections of the lenses introduce aberrations.

By lensless geometrical projection we could circumvent the detector resolution and demonstrate a resolution in the defocused images of 0.14 µm in one direction [Lag97]. The principle is illustrated in Fig 4.9. This microscope is based on the principle originally proposed by Gabor for high resolution electron microscopy [Gab48]. There is also similarity with low voltage projection electron microscopy [Spe95]. The object is illuminated by a coherent divergent beam which forms a magnified image through projection on the detector. Magnification is also obtained in projection radiography but the specificity here arises from the coherence of the beam. The recorded image is therefore a magnified Fresnel diffraction pattern sensitive to the phase modulation by the object.

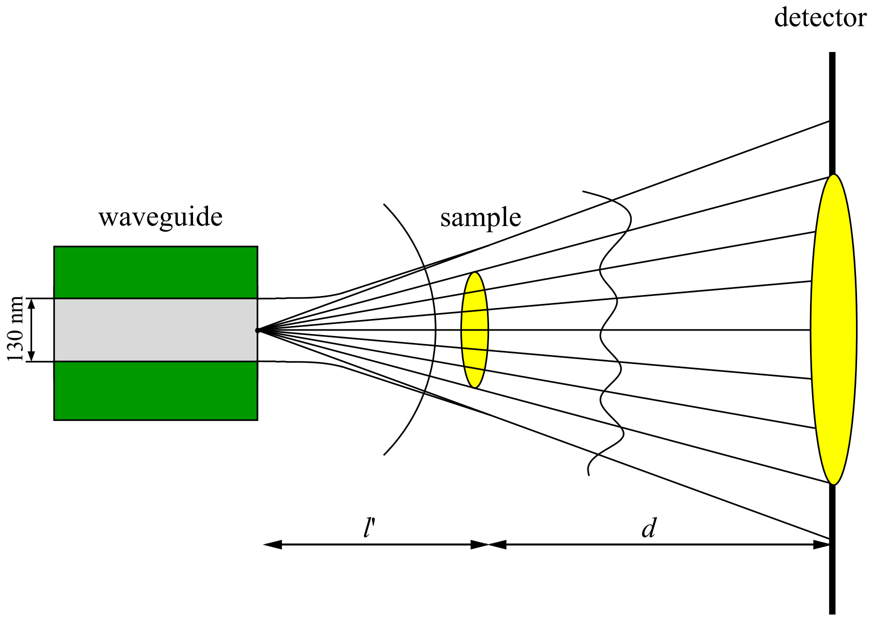

Fig 4.9 Schematic illustration of the hard X-ray magnifying set-up. A waveguide delivers a coherent and divergent beam which is transmitted through the sample and propagates towards the position sensitive detector. The magnification M due to the projection is given by $M = (l' + d) / l'$. As shown in the picture, the beam at the level of the sample is well approximated by a cylindrical wave which is generated by a line source coincident with the exit of the waveguide.

The effective source is formed by a hard X-ray waveguide [Fen95, Lag96, Jar96], i.e. a thin film resonator in which a low absorbtion material is enclosed between two metal layers with smaller refractive index. Due to the small differences in refractive index the critical angles below which total reflection occurs are small, but as in the visible light case X-ray waveguides can perfectly operate with small index variations [Sny83]. Several modes can be excited in the guiding structure and can travel with small loss towards the exit of the guide. Good coupling to a specific mode in the guide is obtained over a narrow angular range (1-2 µrad) of the incidence angle with respect to the cover layer. The various modes can be selected by changing this angle. In the direction of the layered structure, the beam

1) leaves the waveguide with a vertical size limited by the resonator layer thickness t_w, which can be of the order of 100 nm

2) is diffracted at the end of the waveguide and becomes divergent with a divergence of about 1 mrad

3) is highly coherent.

The last property implies that the spatial resolution is *not* limited to the source size as would be the case for an incoherent source in a magnifying set-up. Because of the magnification, no high resolution detector is needed. However magnification occurs only in the direction in which the beam is compressed.

The experiments were carried out on the microfocus beamline (ID13) at the European Synchrotron Radiation Facility (ESRF), with an unfocused 13 keV beam from a Si (111) channel-cut monochromator and with the experimental set-up operating in air. The waveguide, which is efficient for photon energies between 10 keV and 30 keV, was composed of a $t_w = 130$ nm thick carbon layer deposited onto 20 nm of chromium and covered with 4 nm of chromium [Jar96]. The layers were deposited onto an ultra smooth plane Zerodur mirror by sputtering at Sincrotrone Trieste. It was adjusted for maximum output flux on the first resonance, the TE_0 (transverse electric) mode. This mode has nodes at both interfaces and will give the simplest, approximately gaussian, amplitude distribution at the level of the sample. The higher order modes have at least one node inside the guiding layer and their diffraction pattern is more complicated. These profiles were observed experimentally and are essentially the Fraunhofer diffraction patterns of the expected mode profiles [Jar96]. The waveguide-sample distance l' could range from a few micrometers to a few millimeters. A piezoelectric transducer with a repeatability better than 0.1 µm was used to scan the sample across the beam. The images were recorded on the X-ray image converter with 6.5 µm pixel size (see § 3.4.2). The converter screen was positioned at a distance $l' + d = 0.99$ m from the end of the waveguide. The exposure time for each image was 5 s.

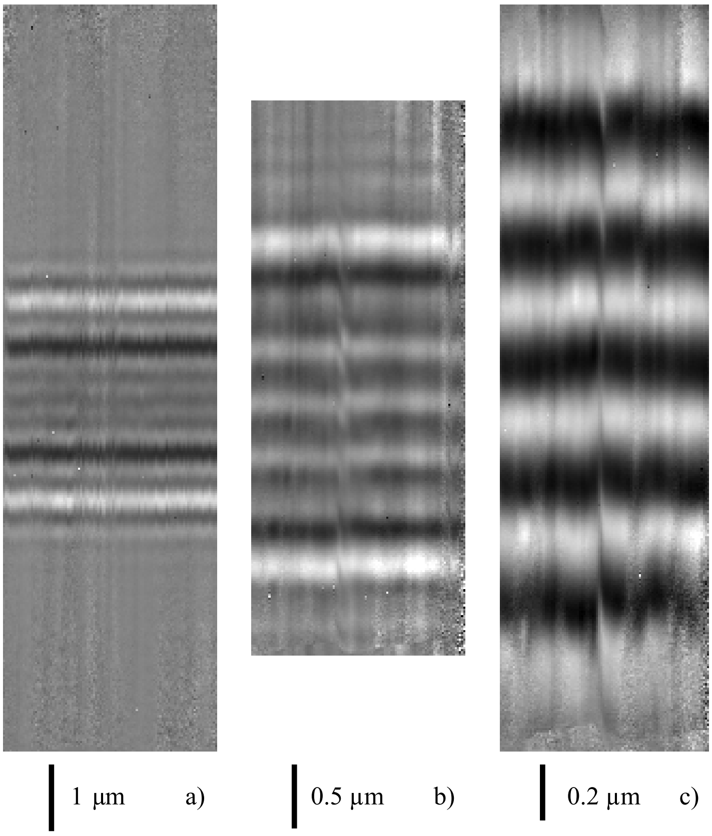

Fig 4.10 Defocused images of a grating pattern composed of five 0.3 µm wide gold strips separated by 0.2 µm. The magnification is 190 times for $l' = 5.3$ mm (a), 350 times for $l' = 2.8$ mm (b) and 760 times for $l' = 1.3$ mm (c). The images were recorded for a fixed waveguide-detector distance $l' + d$ of 0.99 m with an exposure time of 5 seconds at an X-ray wavelength of 0.95 Å (13 keV). The interference pattern changes with the defocusing distance, practically coincident with l'.

Results from a test pattern and a nylon fibre are presented [Lag97, DiF98]. The test pattern consisted of five 0.3 µm wide gold strips (thickness 0.3 µm) separated by 0.2 µm and deposited onto a silicon nitride mask. Fig 4.10a), b) and c) show the defocused images obtained, for three different values of *l*'. The beam without sample was strongly inhomogeneous due to the quality of the beam incident on the waveguide and due to imperfections of the guide itself. In order to correct for this and for variations in detector efficiency, these images were corrected using the flat-field procedure based on an exposure without sample. The images were taken with magnifications *M* of 190, 350 and 760, corresponding to values for *l*' of 5.3, 2.8 and 1.3 mm, respectively. Identical values for the magnifications were obtained in three independent ways. They were measured by imposing to the sample a calibrated piezo-driven displacement. The pseudo-periodicity in Fig 4.10c is in agreeement with the known object pitch. They correspond to equation (2.61) for the magnification with *l*' the effective source-sample distance. Fig 4.11a), b) and c) show the vertical intensity profile integrated horizontally over 6 pixels of the corresponding images in Fig 4.10.

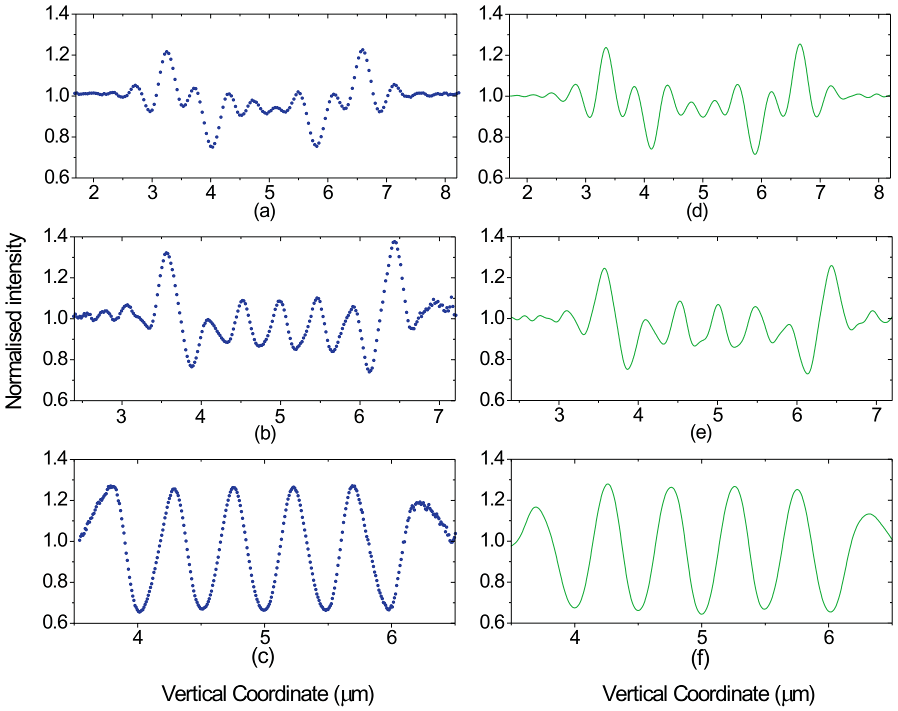

Fig 4.11 a, b and c represent the vertical intensity profiles integrated horizontally over 6 pixels of the images in Fig 4.10. Fig 4.11d, e and f show the corresponding simulations calculated with the procedure discussed in the text using the structural parameters of the gold strips as obtained from SEM images. The theoretical intensity needed to be convolved with a resolution function in order to obtain the present agreement between experimental data and simulations. While a resolution of 0.14 μm is taken for Fig 4.10e and f, for Fig 4.10d a resolution of 0.2 μm was used.

Fig 4.12 shows interference contrast at the edges of a nylon fibre 12 μm in diameter (see § 4.3.4.1), placed at the distance *l*' = 4.1 mm corresponding to a magnification of 240. The vertical beam dimension at the specimen position is limited by the divergence of the beam. The latter is of the order of 1 mrad and is determined through diffraction by the ratio of the wavelength λ and the width of the TE_0 mode. The beam size is about 4 μm, insufficient to illuminate the entire fibre. Fig 4.12 is thus the superposition of several images recorded in a vertical scan of the fibre. The bottom edge appears straight, with Fresnel interference fringes. The fringes at the top edge are strongly deformed, indicating damage of the fibre at this position.

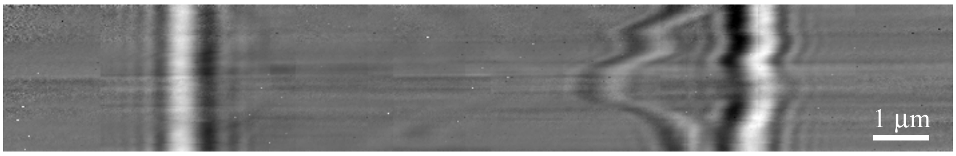

Fig 4.12 Phase sensitive image of a 12 μm diameter nylon fibre for $l' = 4.1$ mm and $d = 986$ mm ($M = 240$) at an X-ray energy of 13 keV. The figure is the superposition of different images recorded during a vertical scan of the fibre. Fresnel diffraction fringes are visible at the edges of the fibre. The radius of the first Fresnel zone r_F is 0.6 μm. The fringes appear deformed at the top edge indicating a defect of the fibre at this position. For layout reasons the image is rotated by 90 degrees with the top edge appearing on the right.

The wave incident on the sample is well described by expression (2.57) with, in one direction, a parabolic phase dependency and a non-homogeneous modulus. This is valid for an arbitrary mode profile at the exit of the waveguide with a size limited by the layer thickness t_w if $\sqrt{\lambda l'} >> t_w$ and Fraunhofer diffraction applies. Closer to the sample the incident wave can be calculated using the Fresnel diffraction formalism or a gaussian beam approximation can be used [Yar91]. Thus if l' is not too small the recorded intensity is a magnified version (cf. equation (2.61)) of the intensity distribution for plane wave illumination and a defocusing distance equal to $D = l' \times d / (d + l')$ (cf. equation 2.60). The non-uniform incident intensity results in a window applied to the object. In our case the magnification is large ($d >> l'$) and the defocusing distance is practically equal to the source-sample distance, whereas with the unfocused synchrotron beam it was approximately equal to the sample-detector distance. The radius of the first Fresnel zone, as given by expression (2.63), ranges from 0.3 μm to 0.7 μm in these experiments and is comparable to the size of the object. The images are thus recorded in a Fresnel diffraction regime and they are similar to the object in some cases (Fig 4.10c and Fig 4.12). The defocused images change significantly with the distance and this redundancy is of interest for a phase retrieval procedure (see § 4.3). This deviates sharply from the approach originally proposed by Gabor and applied in low-voltage electron microscopy, where Fraunhofer diffraction conditions are selected ($r_F >>$ object size).

Fig 4.11d),e) and f) show the simulations calculated using the equivalence with a magnified image for plane wave illumination. The structural parameters of the gold strips obtained from SEM images were used. The stripes introduce an amplitude modulation of 0.04 and a phase modulation of 0.35 rad. Note that the normalised intensity variations in Fig 4.11 are of the same order as the phase expressed in radians. The values of the defocusing distance D leading to the good-fit simulations shown are in agreement with the values of l' obtained from direct measurement as well as from the magnification. The calculated intensity distribution was convolved with a resolution function of gaussian form. While a resolution of 0.14 µm (FWHM) is obtained for magnifications $M = 350$ (Fig 4.11b) and $M = 760$ (Fig 4.11c), a resolution of 0.2 µm is needed for magnification $M = 190$ (Fig 4.11a). In the latter case additional vibrations were accidentally induced by the vacuum system of the beamline. We attribute the present resolution limit of 0.14 µm mainly to imperfections in the experimental set-up which can be corrected for in the future. Similar agreement was obtained between the calculations and the measured patterns at the good nylon fibre edge [DiF98]. For the simulations shown we assumed a homogeneous illumination of the sample whereas the experimental profiles are obtained as the ratio of the intensity distributions recorded with and without sample. The latter was, due to imperfections in these first experiments, only approximately gaussian and very perturbed. We also made simulations assuming a gaussian incident beam. After normalisation with respect to the incident intensity this yields profiles similar to those of Fig 4.11d-f. Proper imaging through reconstruction of the object transmission function using an adapted numerical algorithm is in principle possible. We used the methods of § 4.3, neglecting in a first stage the inhomogeneity of the beam. The reconstructed amplitude modulation contains essentially noise (maximum $A = 4$ %). The phase profile is deformed compared to the expected profile but shows clearly the presence of 5 strips. The retrieved maximum phase modulation is close to the expected value of 0.35 rad. The quality of the reconstructions can be improved with images recorded under better experimental conditions and by modelling the incident beam correctly. This will need an adaptation of the paraboloid method because the incident beam changes with the defocusing distance (waveguide-sample distance). Recently a phase retrieval method that allows to overcome the Rayleigh resolution limit was proposed [Bat89, McC92] for scanning transmission electron microscopy. It is based on the Wigner distribution [Fla93], obtained by recording the (Fraunhofer) diffraction patterns in a series of points of the sample. Fresnel diffraction patterns recorded in different regions of the sample can easily be obtained with the waveguide set-up and it is expected that they can be treated in a similar way.

So far our experiments showed the possibility of coherent hard X-ray projection microscopy with submicron resolution. It uses the coherent and divergent beam emerging from an X-ray waveguide to overcome the detector resolution. Variation of the source-sample and sample-detector distance allows to control both the defocusing distance and the magnification. Defocused images with a spatial resolution of 0.14 µm were recorded, but a better figure should be obtained with an improved experimental set-up. The contrast is mainly produced by variations in optical path length. For the moment this resolution is achievable in only one direction, but extension to two dimensions is envisaged.

5 Applications

5.1 Introduction

In parallel with the development of phase imaging as a technique it is simultaneously used as a tool to investigate natural and artificial materials introducing only weak attenuation contrast but significant phase variations across the transmitted X-ray beam. Among the ‘soft tissues’ we studied so far are wood, bone, lung and brain tissue, and ... fruit because of the similarity with the latter ones. We investigated artificial materials such as (quasi-)crystals and a variety of composites based on polymers, metal alloys or ceramics that exhibit inclusions, composition variations, holes, cracks, ...

Phase (sensitive) radiography and tomography applies not only to light materials (polymers, plants, ...) but also to heavier ones, such as metallic systems. The mean attenuation in the latter is appreciable but the difference in attenuation coefficient between two metallurgic phases is often small. Fresnel fringes can also signal the presence and the position of isolated features with a transverse dimension small compared to the spatial resolution such as cracks with submicron opening. The possibility to obtain 2D and 3D information about the internal structure of non-transparent samples with a sensitivity much greater than classical X-ray absorption imaging is of great interest for materials science samples. This applies especially when the spatial resolution improves well below the normal limits of non-destructive imaging. In-situ volume observations of the microstructure and damage in strained **composites** is now possible with a 3D resolution similar to that of optical microscopy. This contributes, in combination with surface techniques such as scanning electron microscopy and strain sensitive X-ray diffraction techniques, to a better understanding and modelling of the damage behaviour of these composites. This work results from a collaboration with the following laboratories: GEMPPM, INSA, Lyon, France; CNDRI, INSA, Lyon, France and CREATIS, INSA, Lyon, France.

New microstructural information could similarly be obtained on **quasicrystals**. When investigating AlPdMn icosahedral single quasicrystals through phase sensitive imaging, we observed in the bulk crystalline precipitates and several families of holes with a shape (dodecahedra) featuring the point symmetry of the material. A surprising feature is that the size distribution of the holes is discrete, exhibiting a hierarchy probably related to the very nature of the quasicrystalline state itself. A corresponding Bragg diffraction image (X-ray topograph) shows the strain field around the holes and precipitates. Joint use of these images thus provides information about the microstructure (holes, precipitates) and the structural defects. This allows to determine their relationships. To the investigation of quasicrystals several people from ESRF; CRMC2-CNRS, Marseille, France and Lab. Louis Néel, Grenoble, France contributed.

The combination of Bragg-diffraction and phase sensitive imaging is invaluable when the sample behaves as an inhomogeneous phase object only when set to Bragg diffract. The inhomogeneities can originate from defects, domains, structural phases, ... This was used to image the distribution of **ferroelectric domains** in periodically poled lithium niobate crystals. The phase shifts are due to the differences in phase of the structure factors of adjacent domains. The value of the phase shift was retrieved through simulation of the image contrast as a function of the defocusing distance. This study of materials for applications in the field of non-linear optics involves people from ESRF and LPCML, Université Claude Bernard, Lyon, France.

Technical and methodological improvements were made in parallel with the application of phase imaging to actual scientific and industrial problems. Therefore some reported observations contain artefacts or could now be improved. However these results and the quantitative 3D imaging of a polymer foam (see § 4.4.1) illustrate the possibilities of coherent hard X-ray imaging as a useful recent member of the large family of microscopy techniques.

5.2 Observation of microstructure and damage in materials

Phase feature detection in its simplest form is used to image, both in projection and in computed tomography, a cracked silicon single crystal and metal matrix composites strained in tension. Strain-induced cracks even with openings below the micrometer range are visible through the phase modulation they introduce, illustrating the potential of the technique for assessing damage in materials with improved resolution and sensitivity [Clo97a]. The non-invasive, three dimensional, high spatial resolution, observations are compared with scanning electron microscopy (SEM) images on the surfaces or on slices cut out of the samples. In particular, cracks with an opening of less than 1 μm are found to be clearly visible in phase sensitive tomography. Special attention is given to the study of an aluminium alloy matrix composite reinforced with silicon carbide particles [Buf97]. The initiation and the development of damage inside such a composite has been studied during in-situ mechanical tests using phase sensitive tomography [Buf98, Buf99].

5.2.1 The model case: a crack in a silicon single crystal

The formation and propagation of cracks being an important scientific issue, the first attempt at crack observation was performed on a simple sample, a silicon single crystal with a crack resulting from limited cleavage [Clo97a]. The cleavage plane was expected to be (110).

Two dimensional images of a (001) plate shaped silicon (30 x18 x 0.6 mm^3) single crystal where a crack was introduced approximately along the (110) plane by limited cleavage, have been obtained. This sample was kindly provided by A. Jacques (ENSMIN Nancy, France), and was originally produced to investigate, by X-ray diffraction topography, the crack tip plasticity [Mic88a, Mic88b]. The double cantilever beam test piece was mechanically and chemically polished on both sides. After pre-cracking, propagation was obtained by loading under mode I opening [Bro86].

Fig 5.1 shows a white beam X-ray topograph [Lan78] of the sample. Bragg diffraction occurs simultaneously for many reflections at different energies. This image obtained with one of them is essentially sensitive to the lattice distortions and a strong contrast associated with the plastically deformed zone is observed. On the other hand little can be extracted about the morphology of the crack itself.

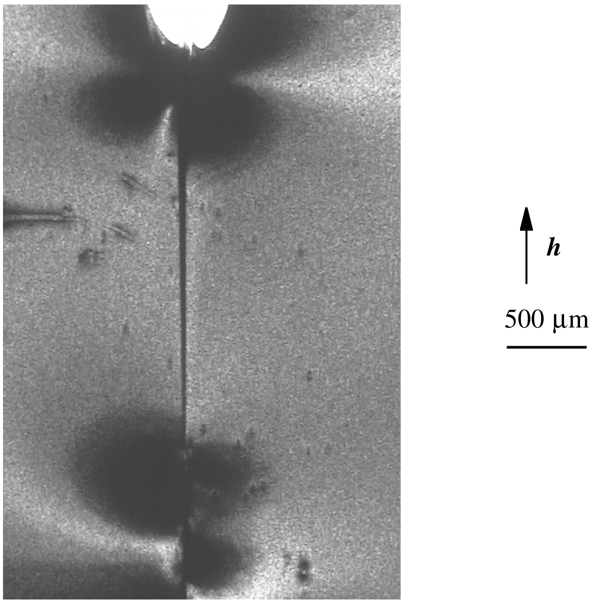

Fig 5.1 White beam topograph of a (001) silicon single crystal with a crack along the (110) plane. The crystal diffracts in the vertical plane for the $3\bar{3}1$ reflection, $E = 40$ keV ($\lambda = 0.31$ Å).

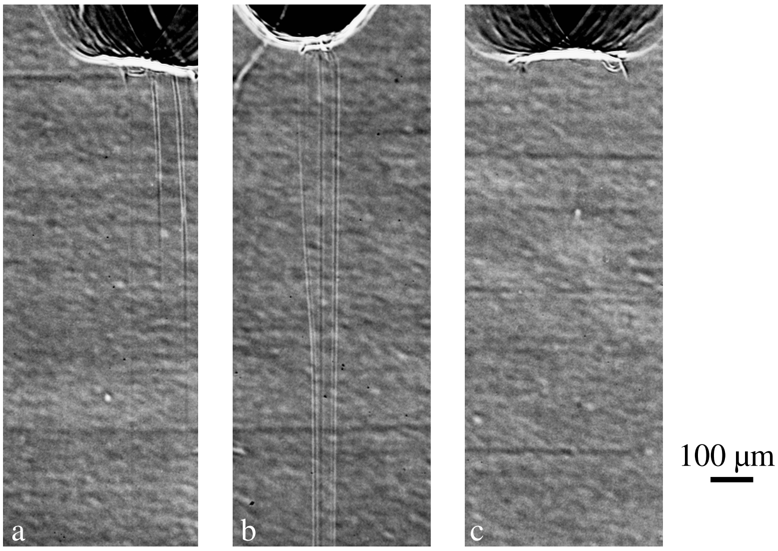

Fig 5.2 Phase sensitive radiographs of a cracked silicon crystal. The crack is imaged as sets of vertical lines with less-more-less intensity. The sample surface was placed at -25° (a), 0° (b), 25° (c) from perpendicularity with respect to the incident monochromatic beam. The X-ray energy used was 24 keV ($\lambda = 0.53$ Å) and the sample-film distance was 0.92 m.

Fig 5.2 shows phase sensitive radiographs of the crack region obtained at a sample-detector distance d of 0.92 m and an X-ray energy of 24 keV ($\lambda = 0.53$ Å): the sample was set nearly perpendicular to the incoming beam (Fig 5.2b), or at - or +25° (Fig 5.2a and c) with respect to this position. In Fig 5.2b, the contrast is weaker than on the topograph, but the crack is clearly visible as an ensemble of linear images, each of these images consisting of a set of lines (lines with less-more-less intensity). They can more easily be seen at higher magnification. Three of these linear images are observed in the initial part of the crack, two of them joining when going along the crack path. The contrast of the two remaining linear images decreases gradually while approaching the crack tip. In Fig 5.2a the set of lines can still be observed in the upper part of the crack, whereas in Fig 5.2c no contrast can be detected.

The features of the crack image can be explained by noting that the used technique is mainly sensitive to jumps (as opposed to gradual variations) in the phase. These jumps, corresponding to abrupt variations in the optical path, only occur when the X-rays are nearly tangent to the crack. The phase modulation can be approximated, in this case, by a narrow pulse-like function. It can be shown that such a function leads to a single set of lines with less-more-less intensity in the image. The observed images thus suggest that the crack is not flat but undulating. This undulation, schematically indicated on Fig 5.3, is such that the beam runs tangentially to the crack at three locations in the initial part of Fig 5.2b, and only at two once the crack has propagated and simplified. In addition the undulation angle is big enough, in the initial section, to allow visibility (i.e. occurrence of tangential areas) of the crack even at -25° of its expected cleavage plane. The geometry of the crack is such that no tangential area exists at +25°. The assumed shape of the crack was verified after the X-ray experiment by direct visualisation of the crack surface, after complete separation of the two parts.

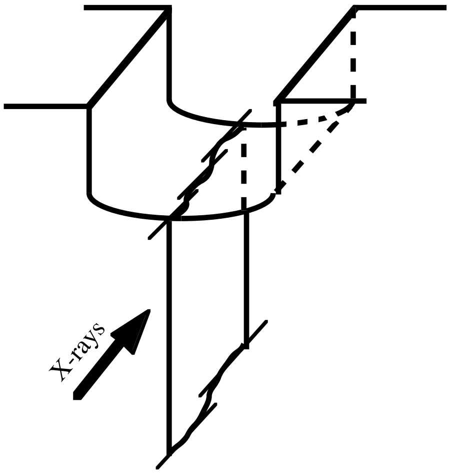

Fig 5.3 Model for the crack geometry explaining the observed set of lines occurring on Fig 5.2. The initial part of the crack deviates strongly from the expected (110) plane and in three regions (indicated by fine lines) the beam direction is approximately tangential to the crack surface. Deeper in the crystal the surface is more perfect and only two such regions are found.

5.2.2 Metal matrix composites

5.2.2.1 Introduction

Compared to monolithic metallic materials, metal matrix composites exhibit some advantages, such as a high specific strength and stiffness, an increased creep and wear resistance or a tailorable thermal conductivity, which make them very attractive materials, for example in transportation technologies where a gain in weight is highly desirable [Cly93]. However, so far, the industrial use of metal matrix composites has been greatly restricted by poor fracture properties, namely ductility and toughness, which stem from the presence, within a ductile matrix, of brittle ceramic particles. As a consequence, much attention has been paid, in the scientific literature, to the failure mechanisms of metal matrix composites during stress/strain application. One of the most fundamental properties of high strength structural materials is their durability, and lifetime predictions require a sound understanding of the microscopic damage mechanisms leading to failure, hence good characterisation of the damage occurring in materials during strain/stress application.

Various experimental methods are available: acoustic emission, eddy current, density or resistivity measurements, neutron scattering, post mortem observations, in situ surface observations during mechanical tests, X-ray imaging... Among all these methods, the three last ones provide direct observation of damage features.

Post mortem observation techniques like serial sectioning give some very useful but rather limited information; for instance, no indication on the time sequence of damage occurrence can be obtained by this method. They are in general time consuming. They are not free of artefacts such as cracks or voids blunting during polishing [Kin90, Clo97a]. The spatial resolution is poor in one direction because it may be difficult or too time consuming to polish very thin layers in between two sections. **In situ observations** during mechanical tests with for example a scanning electron microscope provide a better description of damage initiation and development. This technique has been applied successfully to metal matrix composites [Mai95, Moc95]. The complex stress state which prevails at the surface of the samples (where in situ observation is performed) may bias the damage mechanisms observed [Mum94]. Therefore the relevance of surface observations has still to be checked by destructive post mortem observations.

Some authors have tried to monitor the occurrence of damage in micro-heterogeneous materials using **non destructive techniques** like stiffness measurements [Llo91], density measurements [Hun91], acoustic emission measurements [Mum91], or X-ray computed tomography. The two first techniques correspond to non local measurements which are not necessarily representative of local phenomena [Mum93]. Acoustic emission can provide local information on damage mechanisms such as reinforcement cracking but the precise identification of the damage for which a signal is detected often requires destructive observations as mentioned above. Therefore, there is an obvious need for an experimental method such as X-ray tomography which provides 3D images and quantitative information on damage or microstructural features within materials with micrometer resolution. It has been used, in its classical form based on X-ray attenuation, to characterise, in various materials, defects resulting from processing [Kin93, Bre93a, Liu93] as well as to assess damage resulting from thermal cycling or from deformation [Lon90, Bre93b, Baa95, Hir95]. In these studies, defects such as voids, fibre-matrix debonding or fibre cracks have been imaged with a resolution varying from tens to a few micrometers depending on the kind of X-ray source used, either laboratory sources or synchrotron sources. One of the factor also influencing the resolution of the images obtained by X-ray tomography is the contrast in attenuation between the material and the phases/features that one wants to observe. This contrast is high in the case of a large void or crack and has enabled some authors, for example, to monitor fatigue crack closure in an Al-Li alloy [Guv97]. However, the X-ray attenuation coefficients of the reinforcement and of the matrix can be very similar in the case of Al/SiC composites. It is therefore of interest to improve the particle and crack contrast using the coherence of the beam.

In the particular case of particle reinforced metal matrix composites, the failure mechanisms can be broadly divided in three classes [Cly93]: 1) particle cracking 2) matrix reinforcement de-cohesion 3) ductile failure of the matrix. The flow behaviour of these materials can be strongly affected by the progressive cracking of the particles during the deformation, especially in tension, and properties such as the maximum tensile stress depend on the extent of this phenomenon. Recent theoretical studies [Bao92, Mai95, Kis96] have enabled the modelling of this effect. In each of these studies an important input parameter is the *evolution of the fraction of damaged particles during strain application*. This parameter is difficult to measure experimentally. This underlines the need for in-situ observations of the volume of these materials with good spatial resolution and sufficient contrast.

5.2.2.2 Samples and experimental conditions

Three-dimensional images of damage resulting from monotonic tensile tests have been obtained on two types of metal matrix composites consisting of a 6061 aluminium alloy reinforced by

1) a unique silicon carbide (SiC) fibre, 140 µm in diameter, with a 30 µm diameter graphite core, produced by Textron (SCS-2). This is an example of a fibre reinforced composite and was kindly provided by S. Cardinal (GEMPPM Lyon, France).

2) a 10 % volume fraction of SiC particles with a mean size of 150 µm. This particle reinforced composite, produced by rheocasting and kindly provided by L Salvo (GPM2 Grenoble, France), was first studied in its "as cast" state. Some helpful conclusions could be drawn from this first study, but the poor ductility of the material in this state led us to study it in an "extruded" state.

The fibre reinforced composite was a slim cylinder 1 mm in diameter and 4 mm long, carved out of a larger specimen strained in tension to a total strain of 1 %. After the non-destructive tomographic investigation, it was mechanically polished using SiC paper and 3 µm diamond paste to allow examination in a scanning electron microscope (SEM) operated at 20 kV.

The particle reinforced composites were small double shouldered specimens with a gauge length of 5 mm and a cross section of 1.5 x 1.5 mm^2. Before testing, the samples were mechanically ground following the same procedure as for the fibre reinforced composite. After the tomographic scans, damage features induced on the surface were characterised by SEM.

For the tomographic scans we used the CCD-based detector in the 6.5 µm configuration (see § 3.4.2.3). For each sample, 600 images of 512 x 512 pixels (from the 1024 x 1024 pixels available) were acquired over 180° (angular step : 0.3°). 3D images with isotropic voxels (6.6 x 6.6 x 6.6 µm^3) were reconstructed from the corrected projections using the algorithm for conventional absorption X-ray tomography. Although this is a temporary and obviously unsatisfactory approach, it works effectively for detecting the edge contrast associated with phase singularities (see § 4.4 for a detailed discussion of this approach). Constant strain rate tensile tests were conducted at room temperature on a specially designed in-situ tensile testing machine set directly on the goniometer and experiencing the same rotation as the sample during the scans (see § 3.3.2). The force and the crosshead displacement were recorded on a computer and monitored during the test. A crosshead displacement rate of 150 µm/min was used for all the tests, corresponding to an average strain rate of 5 10^{-4} s^{-1}. The true plastic strain $\varepsilon_p = \ln(A_{sp}/A_{s0})$, was calculated at each deformation stage from the area of undeformed (A_{s0}) and deformed (A_{sp}) sections, perpendicular to the applied stress. The values of A_{s0} and A_{sp} were measured from a reconstructed volume of the sample containing the same particles all along the deformation. The relative error $\Delta\varepsilon_p / \varepsilon_p$ on the plastic strain was estimated to be 2 %.

5.2.2.3 Experimental results

a. Fibre reinforced composite

The fibre reinforced composite was imaged after a monotonic tensile test. A sharp drop on the stress-strain curve recorded during the test suggested that the fibre was broken. A radiograph obtained in absorption mode ($d = 0.005$ m) is shown in Fig 5.4a. The contrast is too poor to investigate in a reasonable way the microstructure and possible cracks. Phase sensitive radiography, obtained with a specimen-detector distance d of 0.13 m and shown in Fig 5.4b, clearly reveals the microstructure of the sample. It confirms that the SiC fiber was broken during the tensile test. As shown on the tomographic slice directed along the fibre (Fig 5.5a), three cracks were detected in the fibre. Careful examination of this figure and Fig 5.4b reveals, within the central crack, some SiC fragments. It is important to notice that those fragments had disappeared, obviously during the grinding stage, when the specimen was examined in the SEM (Fig 5.5b). Voids in the aluminium matrix were also clearly imaged on the radiograph (Fig 5.4b) and the reconstructed slice (Fig 5.5a), as confirmed by SEM. No obvious correlation was found between the presence of those voids and the cracks in the fibre. The dark central part of Fig 5.5a, corresponding to less absorption, can easily be recognised as the graphite core of the fibre.

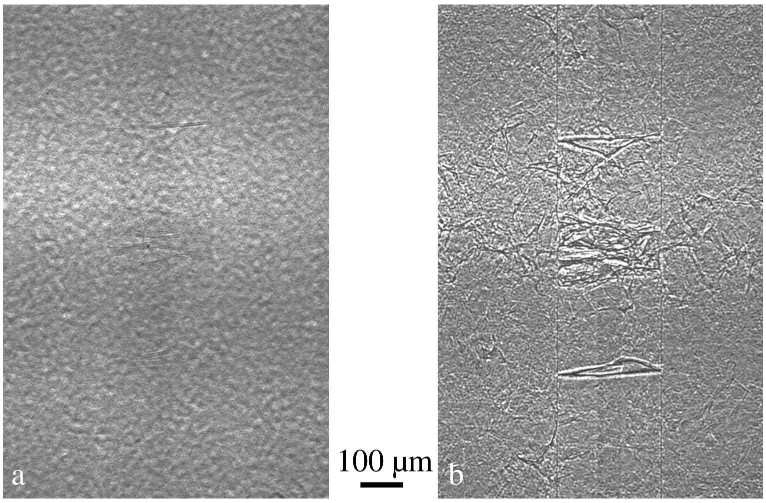

Fig 5.4 Radiographs corresponding to the absorption mode (a) and the phase sensitive mode (b) of a single-filament Al/SiC composite after monotonic room temperature tensile testing, up to the fibre rupture. The images were obtained at an X-ray energy of 25 keV ($\lambda = 0.5$ Å), at a sample-film distance d of 0.005 m (a) and 0.13 m (b).

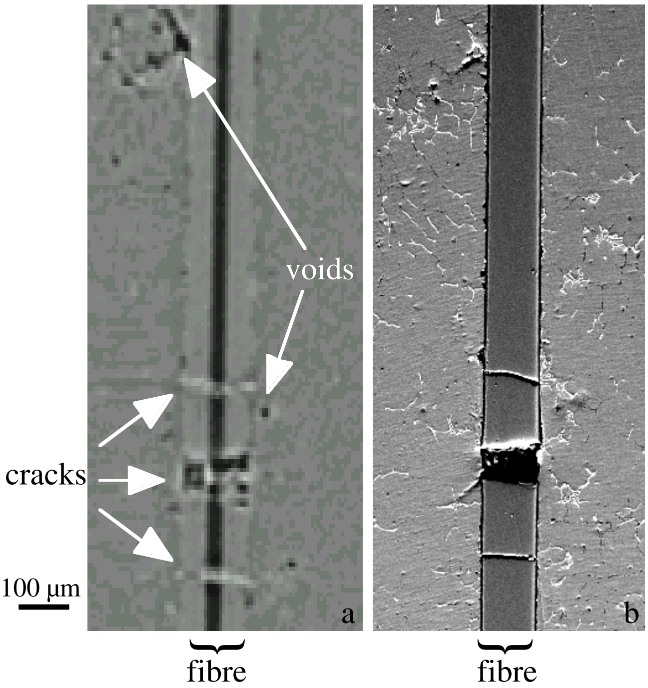

Fig 5.5 Tomographic slice (a) and SEM micrograph (b) of a fibre reinforced composite. Matrix pores and fibre cracks are clearly visible on both pictures. The actual opening width of the smallest detected crack is 5 µm. Within the central fibre crack, computed tomography reveals the presence of some SiC fragments which have disappeared during specimen polishing for SEM observations. The fibre carbon core (30 µm in diameter) is clearly visible as a zone with less absorption. The tomographic scan was performed at an X-ray energy of 25 keV ($\lambda = 0.5$ Å) and a pixel size of 6.5 µm, the sample-detector distance d was 0.82 m.

b. Particle reinforced composite

An example of an absorption radiograph (a) and a phase sensitive radiograph (b) of the particle reinforced composite, recorded on high resolution film, is shown in Fig 5.6. An energy of 25 keV was chosen in order to have sufficient transmission through the sample. At this energy the particles are only seen with reasonable contrast in the phase sensitive image, because the difference in attenuation coefficient between the aluminium alloy and the silicon carbide is too weak ($\mu \approx 0.49$ and $\mu \approx 0.55$ mm^{-1} respectively). In the phase sensitive radiograph recorded at $d = 0.83$ m (Fig 5.6b) a huge enhancement of the edge contrast can be observed. However due to the projection over the sample thickness it is difficult to extract microstructural information from a single radiograph and a tomographic approach is necessary.

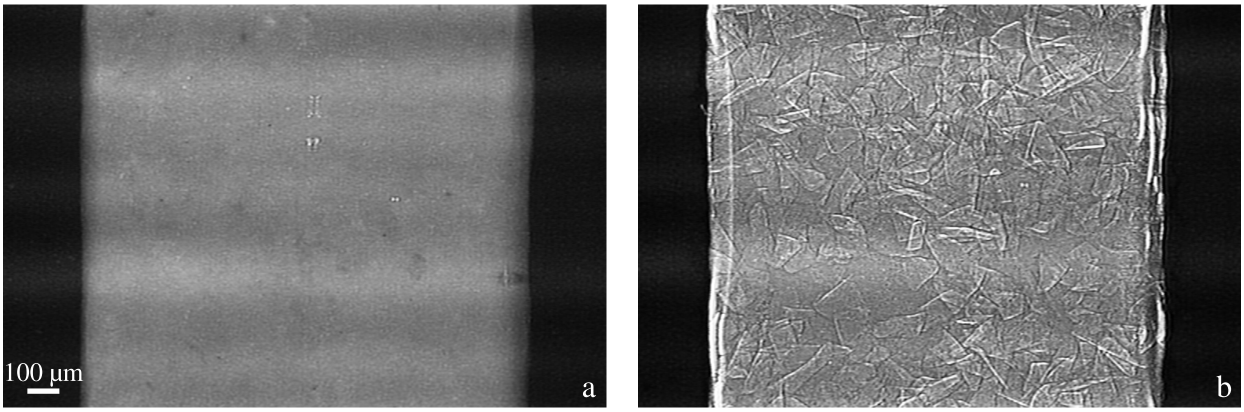

Fig 5.6 a) Absorption ($d = 0.003$ m) and b) phase sensitive radiograph ($d = 0.83$ m) of an aluminium-based SiC particle reinforced composite sample; $\lambda = 0.53$ Å.

Fig 5.7 shows two tomographic slices from the reconstructed volumes in absorption mode (Fig 5.7a) and the phase sensitive mode (Fig 5.7b). Although the contrast was strongly enhanced in Fig 5.7a the presence of particles is hardly revealed. Circular contrast appears centred around the rotation axis of the tomographic scan. This is an artefact associated with imperfect flat-field correction (see § 3.4.1.1). Edge contrast reveals the reinforcements in Fig 5.7b.

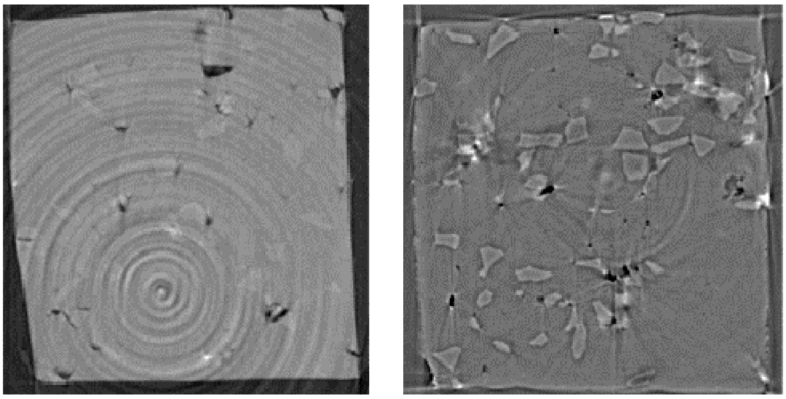
(a) 200 μm (b)

Fig 5.7 Tomographic slices of the studied composite obtained by a) attenuation tomography ($d = 0.003$ m) and b) phase sensitive tomography ($d = 0.83$ m). On the left image, the contrast was enhanced to make the weak absorption contrast visible. The X-ray energy was 23 keV.

Fig 5.8b-e show several slices of the reconstructed 3D volume of the “as cast” particle reinforced composite after a plastic deformation ε_p of 1 %. The SiC particles and cracks in the matrix (detail C) and in a particle (detail A and B) are clearly detected by the microtomographic method. The tomographic reconstruction of the sample surface (Fig 5.8b), is very similar to the corresponding SEM micrograph (Fig 5.8a), hence the reconstructed slice remains in excellent agreement with the real material.

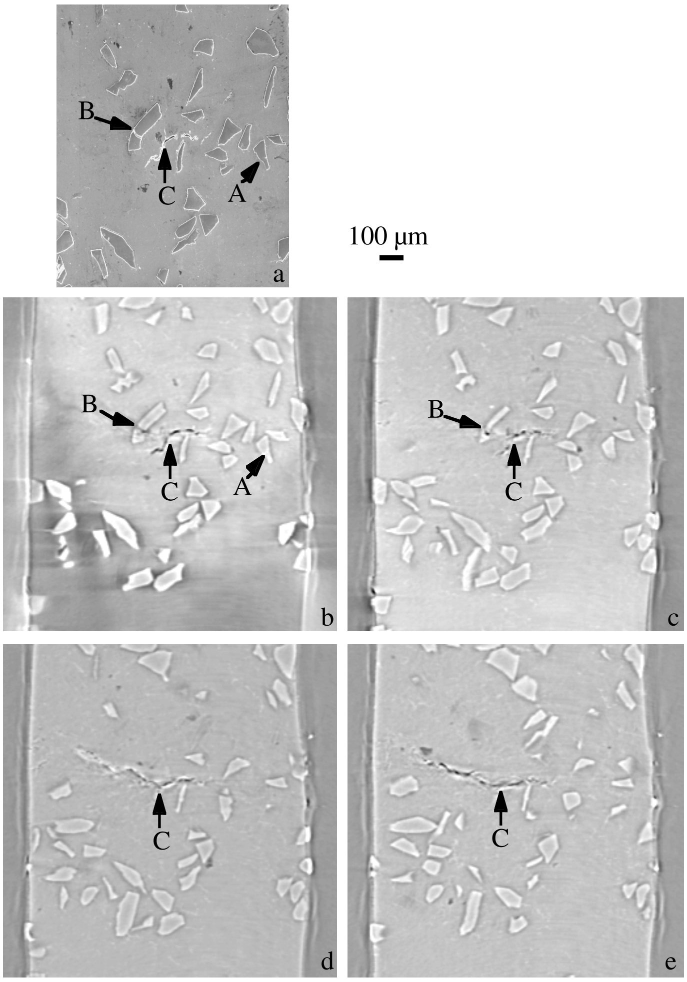

Fig 5.8 One SEM micrograph (a) and four tomographic slices (b-e) of an Al/SiC particulate composite after a room temperature monotonic tensile test ($\varepsilon_p = 1\%$). The slices, taken from the reconstructed 3D volume, correspond to zones at the surface (b), 25 µm (c), 50 µm (d) and 75 µm (e) beneath the surface. A crack in the aluminium matrix is indicated by arrow C; arrows A and B show cracked SiC particles. The tomographic scan was performed at an X-ray energy of 25 keV ($\lambda = 0.5$ Å) and the sample-detector distance *d* was 0.82 m.

A study of the pixel grey level across a SiC particle reveals, at each particle/matrix interface, a set of bright and dark fringes (Fig 5.9b) [Pei98]. The bright fringe, corresponding to a higher value for the pseudo-absorption, is located on the inner side of the particle. The width and contrast of those interface fringes depends on the experimental conditions and particularly on the specimen-detector distance *d*. Inside the particles, the grey level is roughly constant and slightly higher than that of the matrix, due to the slightly larger absorption and the tails of the fringes appearing at the edge.

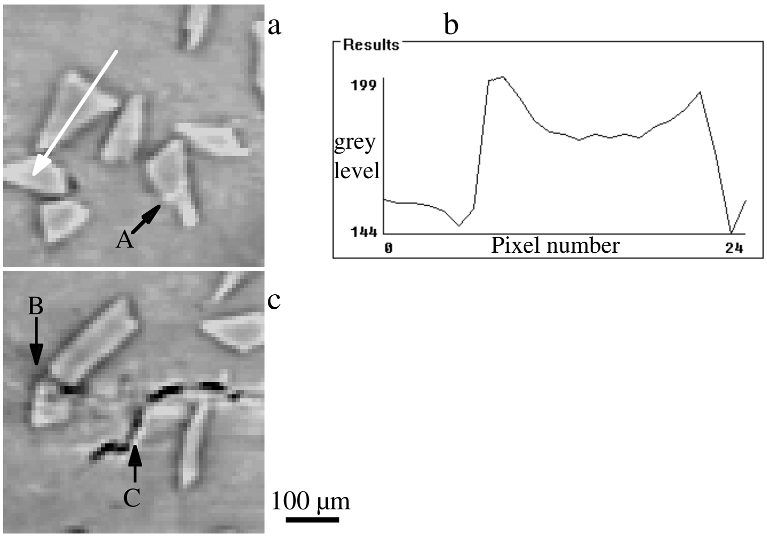

Fig 5.9 (a) Magnified detail extracted from Fig 5.8b showing sound SiC particles. The bright fringe (detail A) detected within the particle corresponds to a crack the opening of which is an order of magnitude smaller than the pixel size: 0.5 µm as determined by SEM observation. (b) Evolution of the pixel grey level along the axis shown in (a) through a SiC particle. The Al/SiC interfaces generate a set of dark and bright fringes. (c) Magnified detail extracted from Fig 5.8b showing cracks with wider openings (> 8 µm). They are underlined by a set of bright-dark-bright fringes.

At the onset of global plastic deformation of the particle reinforced composite, cracks have been detected within SiC particles (Fig 5.8 details A and B). As some of these cracks emerge at the surface of the sample, their openings have been measured in a SEM. When its opening is small, a crack appears as a bright fringe on the reconstructed picture (Fig 5.9a), while wide cracks appear as a set of bright and dark fringes (Fig 5.9c). Thanks to this fringe structure, cracks with an opening as small as 0.5 µm, much smaller than the experimental pixel size of 6.6 µm, can be detected (see for example detail A on Fig 5.8b and Fig 5.9a).

For the experimental conditions investigated, no particle/matrix debonding has been observed when the strain was increased. Instead, the presence within the matrix of alumina resulting from the rheocasting process, induced the cracking of the matrix (Fig 5.8 detail C). The path of these large matrix cracks as well as their interaction with reinforcing particles can be easily followed within the sample. It can be seen, for instance, that the crack in particle B (Fig 5.8b-c) originates on a larger matrix crack, underneath the surface (Fig 5.8d-e). It is noteworthy that internal voids do not appear to act as crack initiators for the experimental conditions investigated. All observed matrix cracks are initiated on the sample surface. The presence of these large matrix cracks led to the early rupture of the sample, precluding any observation of damage development through particle cracking or particle matrix decohesion.

Therefore the experiments were repeated on an extruded composite. Extrusion is known to break up oxide layers and improve the ductility of aluminium alloys. The set-up featured a specially designed tensile testing machine in order to perform the volume observations *in-situ*. Once the sample was set in the machine, a first tomographic scan was performed, without any load applied, in order to characterise the initial non deformed state. At the end of this first scan, the load was increased and another scan was performed while the crosshead position was maintained constant. A stress drop of less than 10 % was recorded during the scan time (≈ 1.5 h) due to classical stress relaxation phenomena inside the sample. On the whole, five scans corresponding to increasing strain levels were performed on the same sample.

Fig 5.10a-e presents reconstructed images of the same internal section of the sample at five different stages of deformation. The images show the chronology of damage initiation and development in the interior of the sample. In the initial state (Fig 5.10a) one can first notice a global alignment of the SiC particles due to the extrusion process, the direction of which is vertical on the figure. Two kinds of pre-existing damage can be observed in the sample before deformation. First, nearly all matrix/particle interfaces perpendicular to the extrusion direction are debonded (detail A on Fig 5.10a). Those voids were also observed at the surface of the sample during SEM examination, but in a much lower proportion probably because the majority of them had been filled, during the polishing process, by the ductile Al matrix. Those voids are clearly induced by the extrusion process. Second, the analysis of the reconstructed images revealed that 11 % of the SiC particles located at the surface of the sample contained a crack in the initial state. In the bulk, however, no initial cracks could be detected in the SiC particles. The cracks are probably induced by the machining and polishing of the sample.

Fig 5.10b illustrates the damage observed in the material for a true plastic strain $\varepsilon_p = 5.10^{-3}$ (slightly larger than 2.10^{-3}, the conventional plastic offset used to define the material yield stress). At that stage, bright fringes, perpendicular to the stress direction are clearly visible in some SiC particles (detail B). For the specimen detector distance used, those fringes correspond to cracks open in mode I as shown in Fig 5.9a. Some broken SiC particles were also observed at the surface for the same strain level. No particle matrix decohesion could be detected at that stage of deformation with the available experimental resolution.

The number of cracked particles increased with plastic strain, both in the bulk and at the surface. This is shown for the bulk in Fig 5.10c and d. The white fringes, corresponding to cracks, became thicker (detail B on Fig 5.10c) and eventually appeared in black, when the strain increased. This indicates a steady growth of the crack opening in the SiC particles when the matrix was deforming plastically. For a given strain level, no obvious difference in the crack opening could be detected between the surface and the bulk of the sample. Some multiple cracking of the SiC particles was occasionally observed, both in the bulk and at the surface, but this is not the dominant cracking mechanism for the investigated deformation levels.

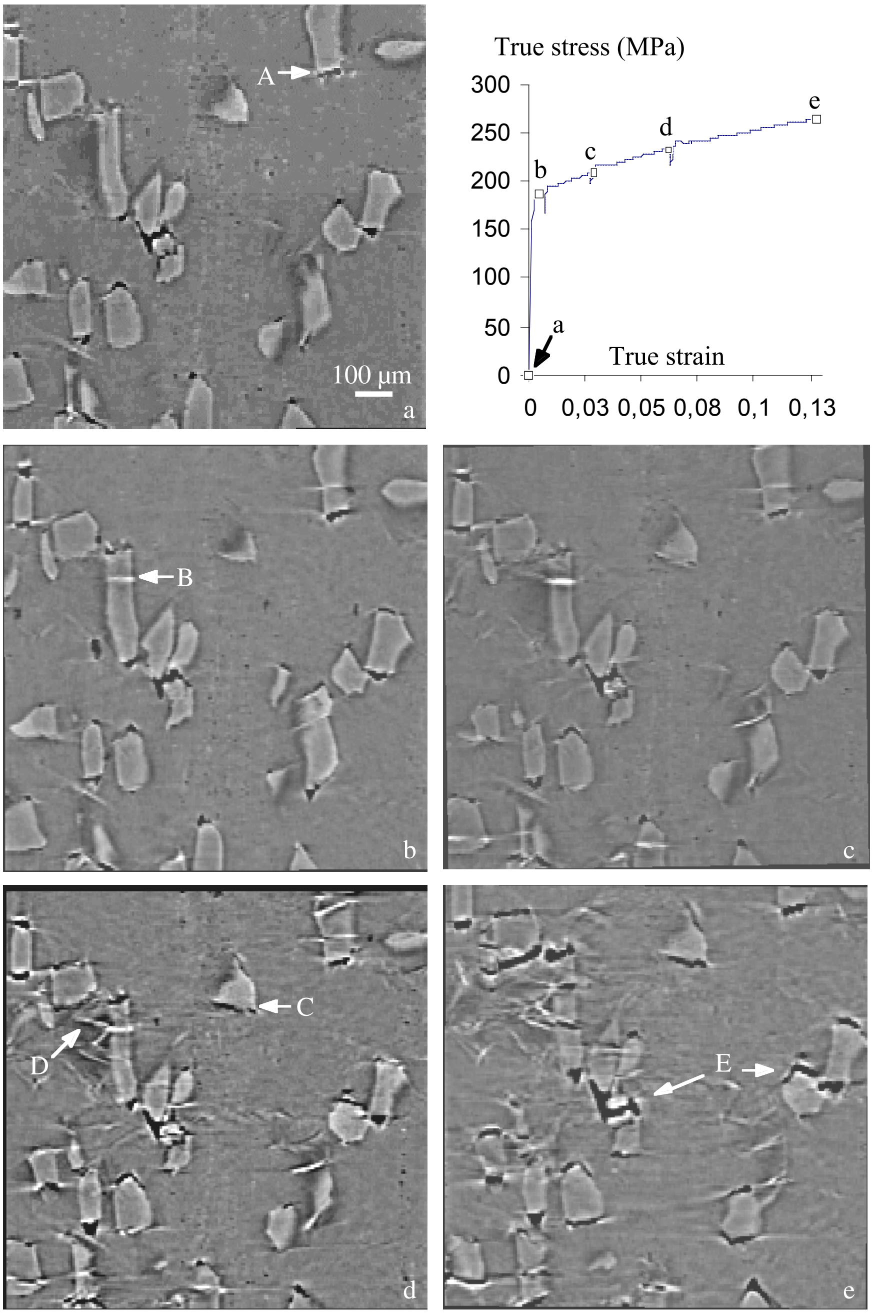

Fig 5.10 Reconstructed images of the same internal section of the extruded composite at five different stages of plastic deformation (a : initial state b : $\varepsilon_p = 5.10^{-3}$ c : $\varepsilon_p = 3.10^{-2}$ d : $\varepsilon_p = 6.10^{-2}$ e : $\varepsilon_p = 13.10^{-2}$) which are indicated on the tensile curve of the material. The strain was applied in the vertical direction. In the initial state, some matrix particle decohesions induced by the extrusion process are visible in the bulk (detail A). At the onset of plasticity, some cracks appear in the SiC particles (detail B). Those cracks appear as bright fringes which grow thicker when the cracks open. At the later stages of deformation, some particle matrix decohesions become visible in the bulk of the material (detail C). Eventually, the extrusion induced decohesions start to propagate under load (detail E).

For a plastic strain $\varepsilon_p = 6\ 10^{-2}$ the first interfacial decohesions are detected (detail C on Fig 5.10d) at the surface and in the bulk. At that stage, one can also notice a fuzzy contrast in the matrix on the reconstructed images (Fig 5.10d and e). This contrast is not observed in the sections corresponding to non deformed parts of the samples (far from the tensile gauge) and seems to be more pronounced near the SiC particles. Furthermore, in some cases (detail D), this contrast takes a V shape. The origin of this fuzzy contrast is unknown.

In the last stages of deformation, the extrusion-induced voids, present in the initial state, start to grow (detail E on Fig 5.10e) and the damage tends to be homogeneous in the material.

5.2.2.4 Discussion

In the investigation of the fibre reinforced composite, phase sensitive radiography and tomography revealed that monotonic tensile testing leads to multiple fracture of the fibre. This was already reported for the same kind of material, strained under similar conditions [Rom92]. The numerous cracks observed in the fibre, giving SiC fragments, are thought to be due to constructive interferences of shock waves corresponding to the sudden release of elastic energy in the fibre when it breaks [Rom98]. Besides, reconstructed images showed, when compared to SEM observations, that specimen preparation for post mortem observations can cover up some characteristic features of the rupture process.

The initial investigations of a particle reinforced composite (Fig 5.6 to Fig 5.9) demonstrated clearly the potential of phase sensitive imaging for materials science studies. The method was shown to offer several advantages:

- Fresnel diffraction contrast appearing in the vicinity of particle/matrix interfaces greatly enhances the detection of the microstructure. This is invaluable because the variations in attenuation contrast are too small and absorption radiography and tomography fail. The reconstructed (defocused) images are reliable, as shown by the comparison of SEM surface observation and the tomographic slice corresponding to the surface.

- Thanks to the interference fringes they produce, cracks with an opening down to 0.5 µm, i.e. one order of magnitude smaller than the voxel size, can be detected in the SiC particles. It is thus possible to observe the cracks at an early stage while keeping the 3D field of view large.

- The simplicity of the set-up, operating in air, and the large sample-detector distance easily allow to install a tensile testing machine.

Although the validity of the algorithm used for the tomographic reconstruction is debatable, it is a workable solution in this case. It uses a single recording distance and thus minimum data collection. The radius of the Fresnel zone was about 6 µm in these experiments, hence the images of the particles are formed in the edge-detection regime, whereas the cracks appear in the holographic regime. The contrast appearing at the Al/SiC edges , recorded in weak defocusing conditions, is essentially a bright and dark fringe. The contrast can in a first approach be connected to a Laplace operator acting on the phase modulation or the density distribution for respectively the radiographs and tomographs. This was discussed in § 4.4. The grey level profile across an Al/SiC edge (see Fig 5.9b) is similar to the second derivative of a step function. The step is supposed to be steep, but of course not infinitely steep. The sign of the min/max oscillation is in agreement with the higher electron density of SiC compared to aluminium. The position where the grey level crosses the average level is to a good approximation the position of the edge. The Fresnel diffraction contrast introduced by the cracks is more complex due to the narrow size of the feature compared to the Fresnel zone.

The second set of observations (Fig 5.10) are more important from a materials science point of view because they were made in-situ and on an oxide-free sample. They represent a systematic survey of the internal damage during a monotonic tensile test in a particle reinforced composite. The three-dimensional observations made at different strain levels reveal the chronology of the damage mechanisms. It is also possible to extract a lot of quantitative information on the particle geometry, the damage progression and their relationships. These observations can qualitatively and quantitatively be compared with surface damage characterisation in SEM during mechanical tests in order to validate or invalidate the latter. The experimental information is valuable for modelling damage development in composite materials. The analysis is summarised below; for a detailed discussion see reference [Buf99, Mai 99].

The quantitative analysis was performed manually on the reconstructed slices of the composite. No adapted algorithm could be found to do this automatically in a reliable way. This is due to the specificity of the diffraction contrast in the images. Several threshold methods are based on taking a specific derivative of the images in order to enhance the edges where sudden level changes occur. In the present case this is in a way already done by the defocusing itself. Automatic processing may therefore be possible in a later stage. The size of the particles was measured along three perpendicular directions. For each deformation stage the fraction of broken particles in the bulk and at the surfaces was determined. The size information was in agreement with a similar (automatic) analysis of surface observations by SEM. The volume of the particles at the surface is, as expected, on average about half the one of the bulk. The aspect ratio of the particles, i.e. the ratio of their size in the y-direction (parallel to strain and extrusion direction) and the z-direction (perpendicular to the considered surface), plays an important role in particle cracking. The particles at the surface have a larger y/z ratio. Almost 20 % of them have an aspect ratio larger than 4 (to be compared to 2 % for the particles located in the bulk).

The evolution of the number of broken particles as a function of the true plastic strain is shown on Fig 5.11. The broken particles present in the initial state at the surface were not included on the curve corresponding to the surface particles. It can be seen from this figure that the number of broken particles at the surface increases less rapidly with the plastic strain than the fraction of broken particles in the bulk. The ratio between the number of broken particles in the bulk and at the surface is about identical for the two strain levels higher than 3 % in Fig 5.11.

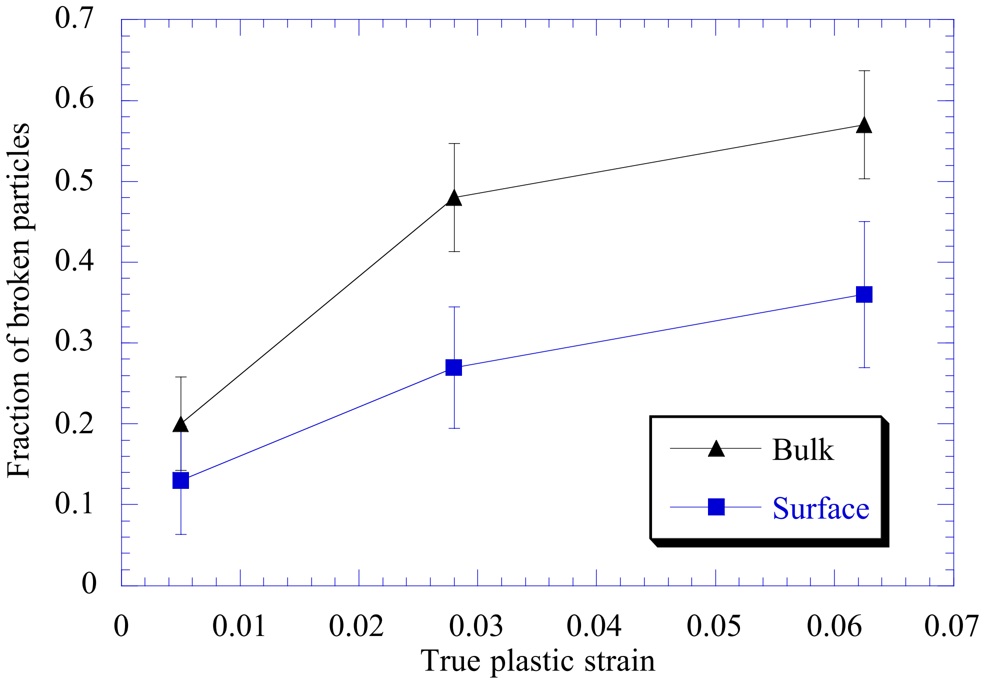

Fig 5.11 Fraction of broken particles as a function of the true plastic strain. The fraction of broken particles is larger in the bulk (triangles) than at the surface (squares) for all the investigated strain levels.

From a qualitative point of view, at least three damage mechanisms occur in the studied material, during tensile deformation at room temperature. When the plastic strain increases, the observed chronology of damage events can be described as follows :

Mode I cracking of the SiC particles

Particle matrix decohesions

Propagation of pre-existing extrusion-induced voids.

Those damage mechanisms are observed both at the surface and in the bulk of the material. The results show that, for the composite studied, particle cracking is the first damage event to occur and it remains the main damage mechanism up to an average true plastic strain of 6%. This is in agreement with the results of Maire et al [Mai95] and Lewis and Withers [Lew95] who have shown, on different composites, that interfacial decohesion occurs only at the later stage of the material deformation. Besides, the large size of the SiC particles used in this study should promote the reinforcement cracking as an important failure mechanism, in agreement with the results of several authors [Llo91, Bré91, Lew95].

The damage behaviour at the surface and in the volume differ however from a quantitative point of view, i.e. the damage growth rate is higher in the bulk than at the surface for this material. Surface observations therefore underestimate the cracking of SiC particles during straining. The opposite behaviour is, at a first glance, expected from the higher aspect ratio of the particles at the surface. A higher aspect ratio results, for a particle in the volume, in a higher maximum stress and a larger amount of stored elastic energy. This is apparently counterbalanced by three phenomena:

- When the particle is close to the surface stress relaxation towards the surface can occur. The stored elastic energy as a function of the distance of the particle from the surface therefore decreases monotonically with this distance. The normal stress decreases also on average but locally the stress may be larger at the surface. This results from calculations based on three-dimensional finite elements methods [Buf99].

- For fragile SiC particles the probability of failure depends also on the probability of finding a critical defect in the particle (cf. Weibull probability of failure [Wei51]). Therefore the chance for failure decreases when the volume is smaller as it is the case for particles at the surface [Buf99].

- Due to specimen preparation some damage may have been introduced in the particle-matrix interfaces reducing its bonding. The load transfer from the matrix to surface particles could be reduced with respect to the bulk material.

The quantitative data obtained on the local damage rate can be used to model the macroscopic behaviour of the composite. First calculations indicate that the tensile curve is better modelled when bulk damage data are considered rather than surface data [Mai99].

5.3 Investigation of quasicrystals using phase radiography and X-ray topography

5.3.1 Introduction

Quasicrystals are a new class of solids with a long range order that is not periodic. They exhibit symmetries forbidden in ordinary crystals. Soon after their discovery in 1984 [She84], structural defects similar to those present in crystals were observed by transmission electron microscopy [Dev89, Yan92, Yan94]. Defects corresponding to the local inversion of the quasicrystallographic sequence (phason defects) were evidenced by high resolution electron microscopy [Hir88]. It has been proposed theoretically [Soc86] that the strain field around quasicrystalline structural defects, such as 'dislocations', can be considered as the sum of two components. Each is referred to a 3-dimensional subspace [Jan92]: the physical space (phonon strain) and the perpendicular one (phason strain). Nevertheless the study of quasicrystal defects is still an important and controversial topic. The actual extent of the strain field in each subspace and the behaviour of the defects under mechanical and thermal treatments remain to be determined.

Recently, X-ray topography (Bragg diffraction imaging) revealed, in icosahedral grains of Al-Pd-Mn and Al-Cu-Fe, the presence of peculiar defects having a loop-shaped contrast [Gas95a, Gas95b, Rei97]. They were found to be smaller in Al-Pd-Mn grains as-grown by the Czochralski method than in annealed grains. The loop-shaped defects have, compared to crystal defects, an unusual behaviour under annealing. Their contrast changes reversibly when the temperature is raised to about 750 ˚C and soon lowered to room temperature. They increase in density and size, up to a mean size of a few hundreds microns, in grains annealed for a long time (a few tens of hours) at 750 ˚C [Gas95b] in vacuum. Furthermore such loops were never observed on a lower size scale when examining the same grains by transmission electron microscopy (TEM).

Apart from these defects, inhomogeneities, i.e. holes and precipitates, were also observed in these two stable quasicrystal phases. Dodecahedral holes were first reported by Audier et al. [Aud90]. They were observed, by TEM, to develop on the edge of an icosahedral Al-Cu-Fe grain during surface melting or sublimation. Later on, Beeli [Bee92] discovered, by scanning electron microscopy, the same kind of faceted holes on fractured surfaces of Al-Pd-Mn quasicrystal grains. All these holes were located on the sample surfaces, without any indication on their possible existence in the bulk. Many studies can be found on the formation of secondary phase precipitates in the icosahedral matrix during the solidification of both Al-Cu-Fe [Gra93] and Al-Pd-Mn [Aud93] alloys. Precipitate formation is indeed so frequent that it is difficult to grow quasicrystal grains as a pure icosahedral phase. On the other hand, little is known on the nucleation and growth of precipitates during annealing.

We reported observations of both structural defects and inhomogeneities in Al-Pd-Mn samples, either as-grown or further annealed [Man97]. The investigations made combined use of radiography and X-ray topography. The first technique makes it possible to image inhomogeneities such as precipitates in the bulk of quasicrystals. The latter is sensitive to strain fields. Combined use, possibly in the same image, provides clues on the relationships between the holes or precipitates and the complicated defects that surround them.

5.3.2 Specificity of the set-up and samples

The particular set-up used for the experiments is shown in Fig 5.12. The incident monochromatic beam is delivered by the vertical monochromator. Three types of images can easily be obtained: 1) absorption or phase sensitive radiographs, 2) monochromatic beam topographs and 3) combined images.

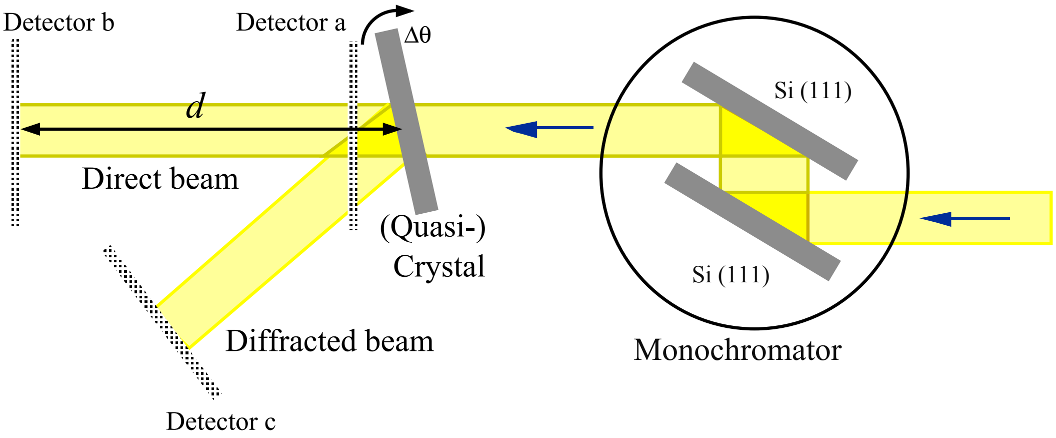

Fig 5.12 Experimental set-up for the investigation of quasicrystals by absorption/phase radiography and X-ray topography. The *detector a* position corresponds to the absorption radiograph, *detector b* to the propagation image (phase sensitive radiograph) and *detector c* to the Bragg diffraction image. If the quasicrystal is set for a strong Bragg reflection the propagation image is a combined image with phase sensitive and topographic contrast.

1) Radiographs

The *direct* beam is recorded while no strong Bragg reflection is excited in the quasicrystal. Absorption or phase sensitive images can be obtained by varying the specimen-detector distance (see § 2). The ordered character of the (quasi)crystal plays no role and only its average characteristics (density, linear attenuation coefficient) are relevant (see § 2.2.2).

2)_X-ray Topographs

Despite non-periodicity, quasicrystals produce sharp Bragg diffraction peaks, which can be indexed in a six-dimensional hyperspace. The present quality of quasicrystals is sufficiently good to use the Bragg *diffracted* beam as an image of the internal structure of the sample. Especially in its monochromatic configuration, X-ray topography [Tan76, Bar93b, Aut96] is sensitive to strains and other faults in the ordered atomic structure of the specimen that affect the Bragg diffracted wave. As is normally the case, for the present investigations we use only the variations in Bragg diffracted *intensity*. On the other hand in § 5.4 we will use the phase modulation of the

Bragg diffracted beam to visualise domains in twinned non-centrosymmetric crystals. Here the position sensitive detector is set in the diffracted beam close to the sample, at a distance such that the diffracted beam is completely separated from the direct one. Very recently the quality of quasicrystals improved to such a level that phase features similar to the ones observed in the radiographs are visible also in X-ray topographs when recorded in a defocused mode. When the incident beam is restricted laterally in one direction to about 20 µm, the resulting image is a section-topograph. It corresponds to a virtual cut of the sample by this narrow beam [Lan57, Lan80, Med97].

3) X-ray topography and phase radiography combined

When the (quasi) crystal is oriented for a strong Bragg reflection, the *direct* beam, parallel to the incoming one, carries topographic contrast superimposed on the radiographic one. The topographic contrast is related to the strain field of structural defects. In the present case of rather low absorption samples, the images of the strain field around defects show inverted contrast as compared to topographs in the diffracted beam [Bar93b], because more diffracted intensity means the direct beam is locally depleted.

The direct-beam image as well as the Bragg-diffracted beam image correspond geometrically, to a good approximation, to projections of the defects along the corresponding beams. Thus going over from reflection ***h*** to reflection ***-h*** produces a stereographic pair. Stereographic analysis of images has been widely used in X-ray topography [Lan80]. It can be applied both visually and through numerical analysis to yield the geometrical distribution of defects in the bulk of the sample. We applied this technique numerically to determine the volume distribution of features appearing in the phase sensitive images.

The investigated samples were centimeter-sized icosahedral single quasicrystals, Czochralski grown along a two-fold axis both by LTPCM in Grenoble [Bou95, Bou96] and at CECM Vitry (France), with a nominal composition (at. %) of $Al_{68.2}Pd_{22.8}Mn_9$ and $Al_{70.3}Pd_{21.4}Mn_{8.3}$ respectively. The experimental results of the following section were obtained with quasicrystals grown by LTPCM. Plate-shaped samples were cut perpendicular to the growth axis (thickness ≈ 600 µm). They feature high quasicrystalline quality as evidenced by the narrow diffraction peaks (≈ 300 µrad by using a 250 x 250 µm^2 pinhole) they produce. They were observed both in the as-grown state and after further annealing. The characteristics of the specimens and the details of the annealing treatments are collected in Table 5-1. The only sample preparation step used before the imaging experiments was mechanical polishing of both surfaces, performed with emery and diamond papers down to grade 0.5 µm, in order to eliminate surface oxidation due to the annealing treatment. Each sample was observed by visible light microscopy before the X-ray experiments in order to evaluate the surface state and to compare it with the bulk observations by radiography and X-ray topography.

	Composition	Thickness (μm)	Annealing time	Annealing temperature	↑ rate ↓ rate	Pressure crucibles
A	$Al_{68.6}Pd_{24.7}Mn_{6.7}$	645	as-grown			
A1	$Al_{69.5}Pd_{24.9}Mn_{5.6}$	645	96 h	750°C/h	↑ 600°C/h ↓ 100°C/h	10^{-8} Torr on SiO_2 boat
B	$Al_{68.8}Pd_{22}Mn_{9.2}$	520	2 × 24 h	750°C/h	↑ 600°C/h ↓ 600°C/h	10^{-7} Torr graphite crucible
C	$Al_{67.8}Pd_{23.8}Mn_{8.4}$	470	48 h 96 h	600°C/h 750°C/h	↑ 600°C/h ↑ 300°C/h ↓ 100°C/h	10^{-4} Torr Nb crucible

Table 5-1 Sample characteristics and annealing details.

5.3.3 Experimental results

5.3.3.1 As-grown samples

Examples of the previously reported loop shaped defects are shown in the topographs of Fig 5.13a and c. They were obtained with the as-grown sample A for the reflection $\boldsymbol{h} = \tau^3(0/\bar{2}\ 0/0\ 0/0)$ in Cahn et al.'s notation [Cah86], τ being the golden mean. Two kinds of contrasts can be distinguished in these Bragg diffraction images. The topograph on Fig 5.13a shows the first kind of contrast (D1), with two lobes (black/white) and image sizes varying from 10 up to 60 μm. The section topograph in Fig 5.13c shows, in addition to the two-lobe contrasts (D2), other features corresponding to the loop shaped defects (LSD).

Fig 5.13b is a phase sensitive radiograph of the same region as in Fig 5.13a. Hexagonal images with an internal line pattern, labeled H, stand out. They correspond to the projection of faceted objects. Comparison between Fig 5.13a and b establishes the correspondence between these features and the two-lobe contrasts visible on the topographs. The phase radiograph of Fig 5.14a, at higher magnification, shows that these features all have the same orientation reflecting the quasicrystal symmetry. Their geometry can be interpreted as a planar projection, along a twofold axis, of dodecahedral objects. Since the radiograph corresponds to the edge-detection regime for this specimen-detector distance ($D \approx d = 0.5$ m), the external borders (white/black lines) of these features are enhanced. The strong edge contrast associated to four of the six borders is due to the small angle between the beam direction and the facets delimiting the object, resulting in a large and abrupt phase jump. The two horizontal borders are less marked, the angle of the X-ray beam with respect to the faces of the dodecahedra being larger. The internal black lines can be understood as a Fresnel biprism-like effect on the faces. The features have various sizes but groups with similar sizes can be recognised in Fig 5.14a.

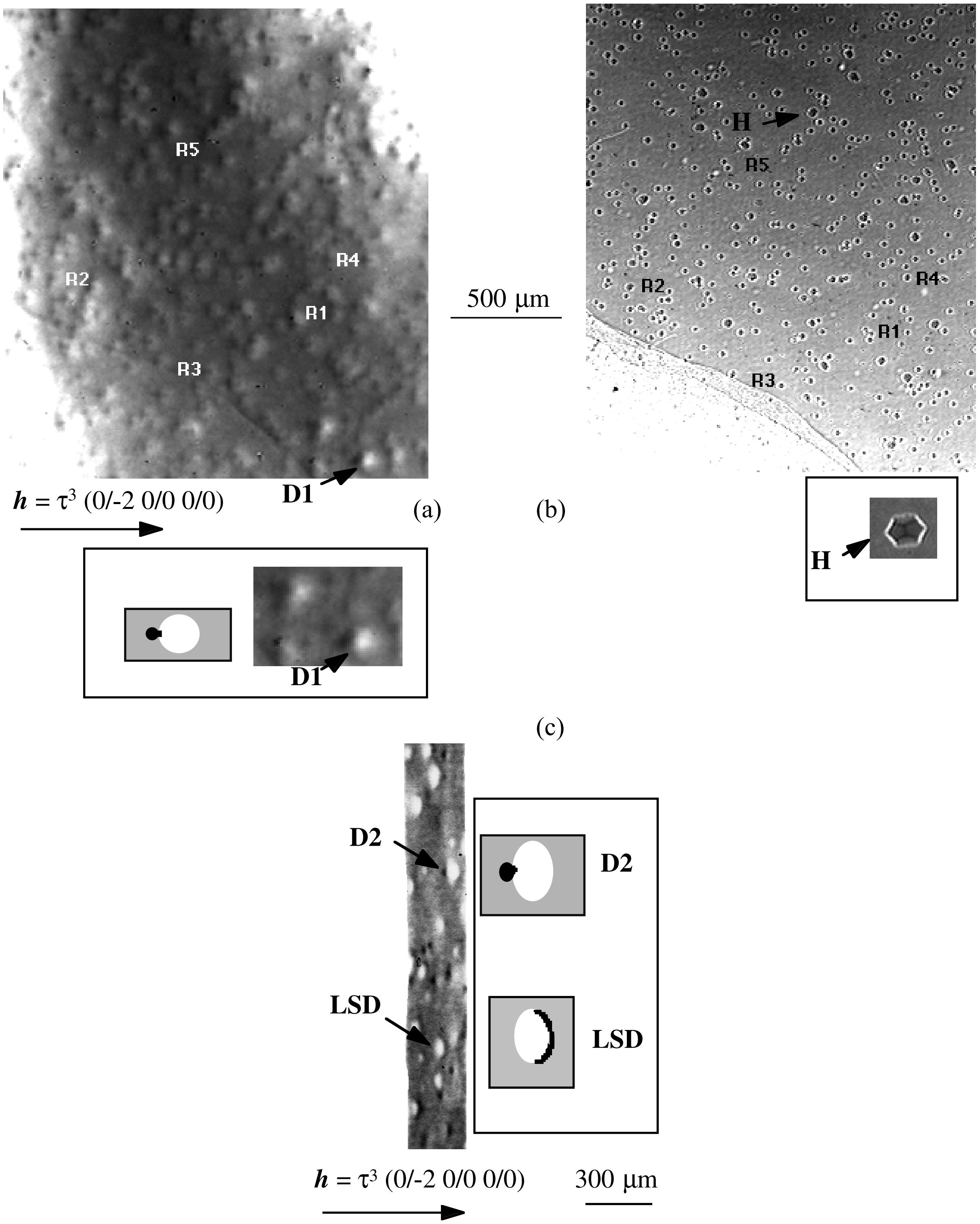

Fig 5.13 Images of the as-grown sample A, recorded at $\lambda = 0.35$ Å. (a) X-ray topograph ($d = 0.2$ m). (b) Phase sensitive radiograph of the same region as in (a) ($d = 0.2$ m). In (a) and (b) we indicate with Rj ($j = 1$ to 5) the same sample regions, to facilitate comparison; the labeled defects, D1 and H, correspond to a two-lobe defect and to a hole, respectively. (c) Section topograph ($d = 0.2$ m): two types of defects (D2 and LSD arrowed) are visible. In the insert of figures (a), (b) and (c) the magnified images of defects D1, D2 and H are presented.

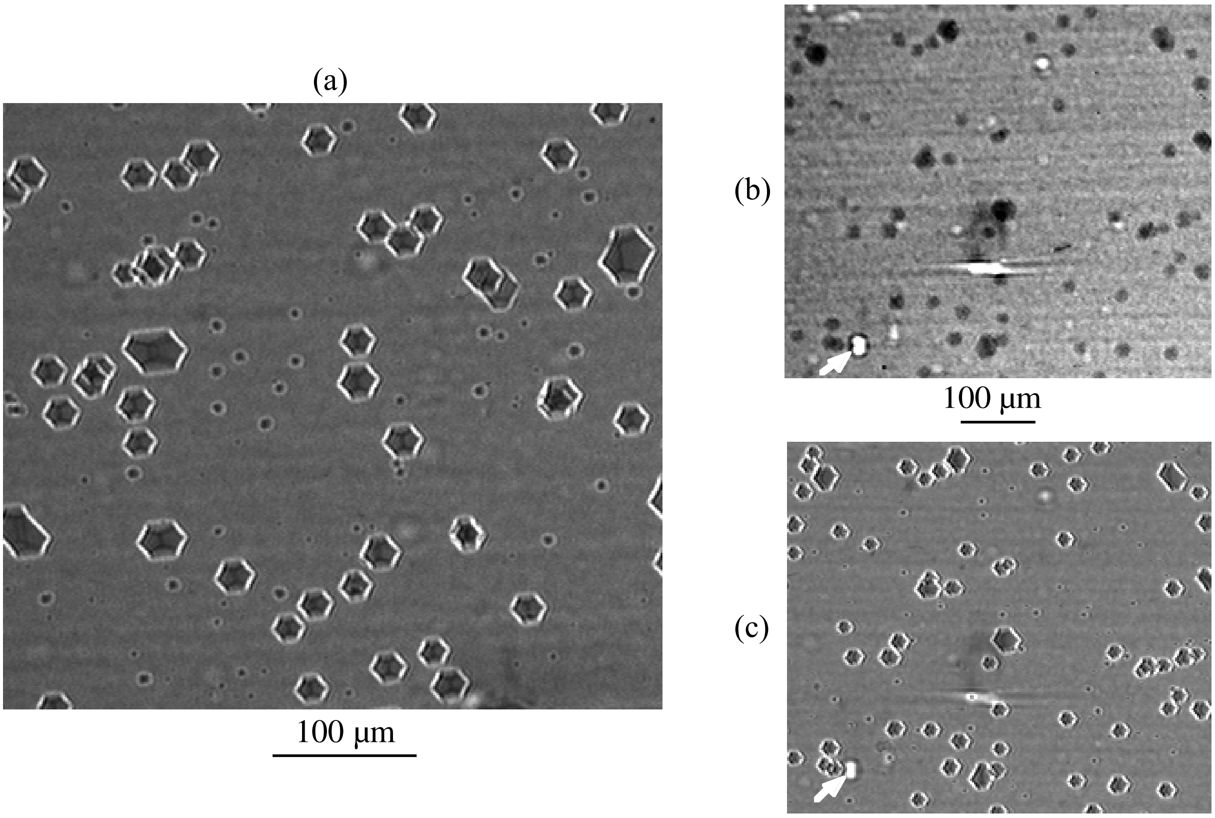

Fig 5.14 Radiographs of the as-grown sample A. (a) Phase sensitive radiograph at a higher magnification for the sample out of Bragg diffraction. (b) Absorption and (b) phase sensitive radiograph of the same sample region, recorded at $d = 0.01$ m and 0.5 m respectively; the arrows indicate contrast, due to a defect in the monochromator, that can serve as a fiducial point. In radiograph (b) the contrast was enhanced to make the absorption contrast visible.

The contrast inside the hexagonal images is darker than in the surrounding quasicrystal matrix. Since the images are reproduced according to the usual convention for X-ray images, this corresponds to more intensity in the transmitted beam, hence the objects have a smaller attenuation coefficient than the quasicrystal matrix. The stereographic-pair approach unambiguously confirmed the assignment of these features to dodecahedral objects. They are similar to the holes observed in the past by SEM at the surface of Al-Pd-Mn grains [Bee92, Bee93] and to those which have been seen on a very small scale by TEM in Al-Cu-Fe [Aud90]. The same kind of observation was made on the surface of our samples. The dodecahedral objects observed in the bulk by radiography are therefore identified as being *holes*. This assignment was quantitatively confirmed by calculation of the intensity variation.

The advantage of phase imaging is to reveal, in a non-destructive way, holes located inside the quasicrystal matrix. A comparison of Fig 5.14b and c confirms that absorption contrast is inadequate to localise the smaller ones (1-5 µm range) and to characterise their shape and orientation. The smallest visible holes are smaller than the resolving power of the high resolution film used as detector. Their presence can still be recognised by the Fresnel diffraction fringes they produce. At the wavelength used ($\lambda = 0.35$ Å) the linear absorption coefficient μ of the quasicristalline material is about 10 mm^{-1} and the expected intensity variation due to absorption of a feature with a thickness of 5 µm is about 0.04, whereas the introduced phase shift for this same feature is about 0.7 rad. This confirms that although the quasicristalline material is rather dense ($\rho \approx 5$ g/cm^3) the gain provided by phase sensitivity remains important.

The distribution of the holes in the volume was determined by using stereographic radiograph pairs. The depth z_d of a hole is obtained from the relation

$$z_\mathrm{d} = c_0 + \frac{x_\alpha - x_{-\alpha}}{2\sin\alpha} \tag{5.1}$$

where $x_{\pm\alpha}$ is the horizontal distance of the hole center from a fixed reference point (for instance a singularity on the image originating from a defect in the monochromator) on the images, measured for two angular ($\pm\ \alpha$) sample orientations. The constant c_0 depends on the distance between the sample surface and the rotation axis. Fig 5.15 shows the depth distribution of 61 holes randomly chosen on the stereographic images recorded with $\alpha = 30^\circ$. The holes appear to be rather homogeneously distributed in the bulk. This was later confirmed by tomographic investigation of the same sample [Gas99].

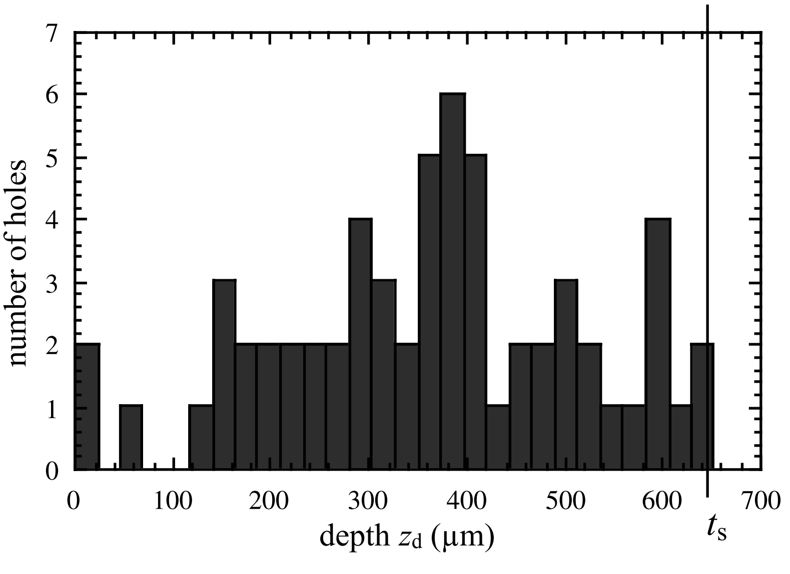

Fig 5.15 The depth (z_d) distribution of 61 holes, randomly chosen on a radiograph, in the volume of the as-grown sample A. 't_s' represents the sample thickness.

5.3.3.2 Annealed grains

Three Al-Pd-Mn grains, labeled A1, B and C, were annealed (see Table 5-1). Sample A1 was a part of sample A. An X-ray topograph and a phase sensitive radiograph, recorded after annealing, are shown respectively on Fig 5.16a and b. Because the sample was curved, only a part diffracts strongly in Fig 5.16a. Small loop shape defects, with sizes varying from 20 to 100 µm, are visible. Their contrast is weak.

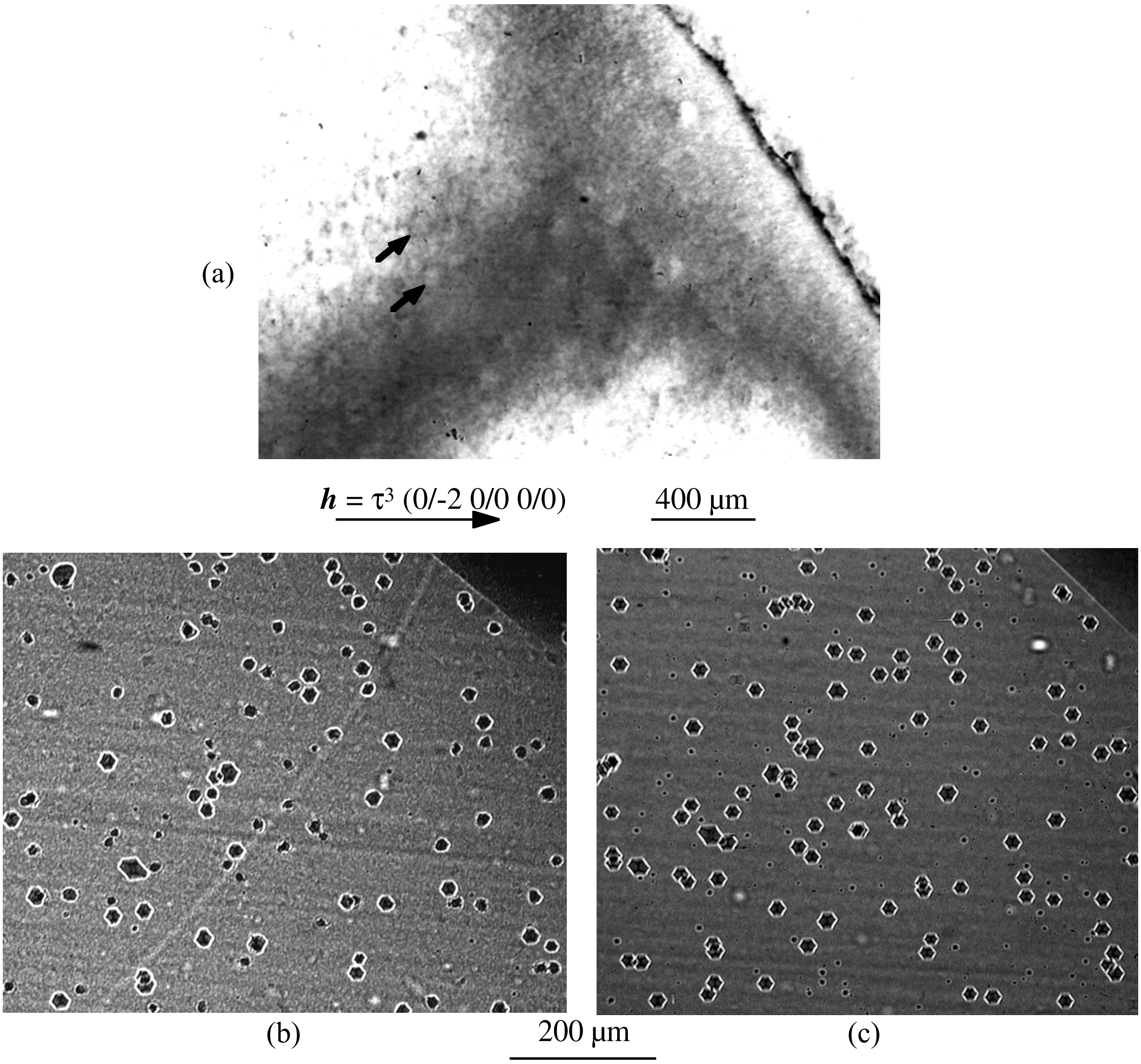

Fig 5.16 (a) X-ray topograph ($\lambda = 0.35$ Å) of sample A1 after the thermal treatment. Phase sensitive radiographs ($d = 0.5$ m) representing the same region before (c) and after (b) annealing, respectively.

The comparison of radiographs of the same region before (Fig 5.16c) and after (Fig 5.16b) annealing, shows that the shape, the size and, in some cases, the position of several holes changed after the thermal treatment. The histograms representing the size distribution of the holes, before and after the annealing process, are given on Fig 5.17. Two families of holes, with sizes $a \approx 5$ µm and $a \approx 20$ µm, prevail in the as-grown state, with a mean density of 500 holes / mm^3 for the first family ('small' holes) and of 250 holes / mm^3 for the second one ('big' holes). Only few holes with an intermediate or bigger size are present in the sample. Some holes with a smaller size can be recognised in Fig 5.14a, but their exact size can not be determined because of the limited spatial resolution and the defocusing. The holes occupy up to about 0.2 % of the volume. The size distribution of the holes after annealing shows a decrease in the total number of *observed* holes, and a more homogeneous distribution of sizes. The first effect may be related to the tendency of the holes to shrink. They are no longer observable when their size falls below the detection limit.

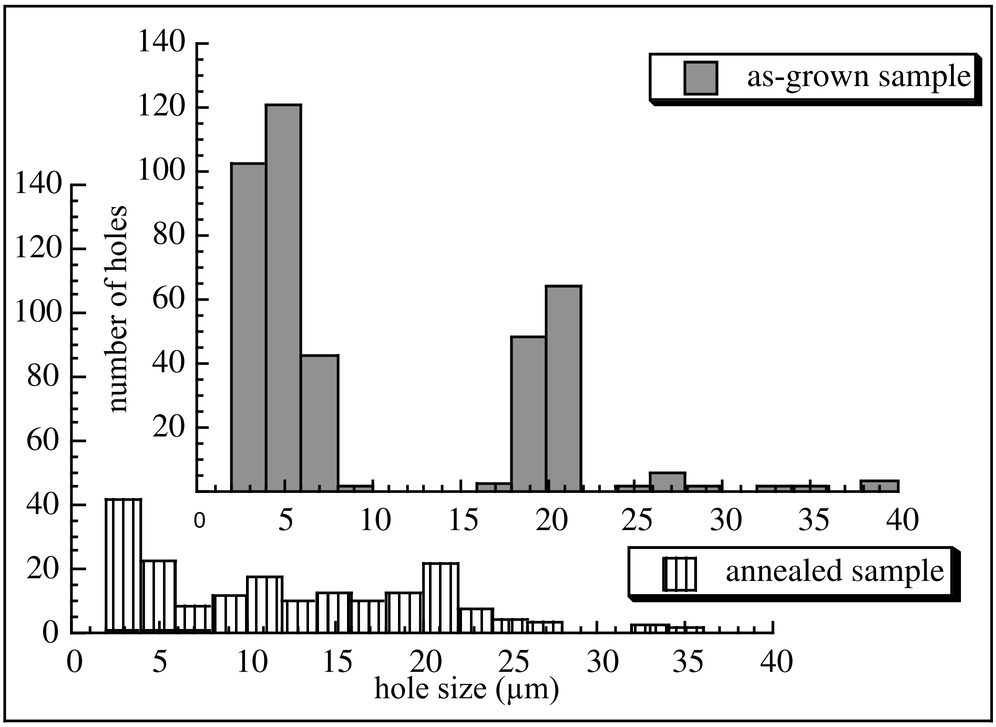

Fig 5.17 The hole size distribution for sample A1 before (full bars) and after (dashed bars) the annealing process.

Sample B is a single quasicrystal grain which featured, before annealing, the same type of topographic images as did sample A. We present only the results obtained after annealing. Fig 5.18a and b show respectively the projection and the section topographs recorded with the same wavelength and diffraction vector as for sample A. Fig 5.18a reveals entangled loop shaped defects, with size on the order of 100 μm, looking similar to those in Fig 5.13c and Fig 5.16a. Sometimes they are organised into necklace configurations. In the phase sensitive radiograph of Fig 5.18c many holes, with an irregular external shape and more complex internal faceting, are visible together with lamella-shaped features. The lamellar features have lower density than the quasicrystalline matrix and they are located mostly around holes. It was determined by SEM microanalysis that they are Pd-depleted precipitates, with chemical composition $Al_{70.63}Pd_{7.93}Mn_{21.44}$. Similar precipitates were already observed to nucleate and to grow, with a crystalline structure, in a sample with the same composition as sample B, during TEM in situ annealing experiments at 800 ˚C [Rei97, Rei98].The depth distribution of the holes, as well as their volume fraction, are very difficult to evaluate in this sample because of their high density (about 2.10^3 holes / mm^3) and irregular shape. It is indeed impossible to unambiguously recognize individual holes on stereographic pairs. A tomographic investigation can solve this problem but the field of view would be strongly reduced and the sample must be recut.

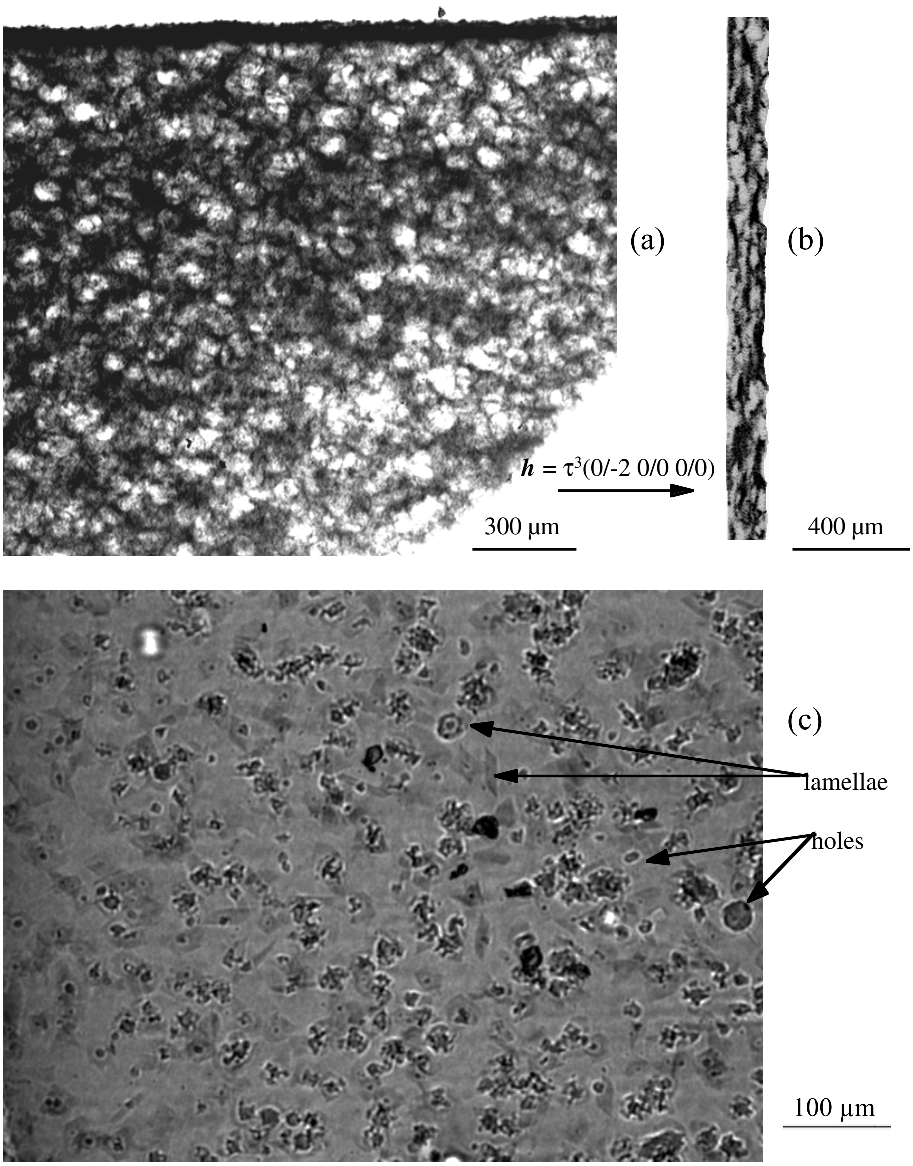

Fig 5.18 Projection topograph (a) and section topograph (b) of sample B ($\lambda = 0.35$ Å, $d = 0.2$ m). (c) Phase radiograph ($d = 0.5$ m) showing holes and lamellar precipitates (arrowed).

Sample C was only observed after a 96 hours annealing at 750 ˚C. The topograph of Fig 5.19 shows a dense network of large loop shaped defects (a few hundred micrometers in size), again organised, in several cases, into necklace configurations (Fig 5.19b).

The phase sensitive radiographs (Fig 5.20) display holes and precipitates distributed throughout the grain. Most of the holes are rather small ($a \approx 3$ - 7 µm), but some big holes ($a \approx 30$ - 40 µm) are visible on the phase radiographs. The holes are fewer than in sample B, i.e. 7 - 8.10^2 mm^{-3} and they take up about 0.2 % of the volume. Their shape is more regular than in sample B and internal faceting is distinguishable only in some cases. Big holes feature very irregular borders which are made up of several smaller holes (Fig 5.20b).

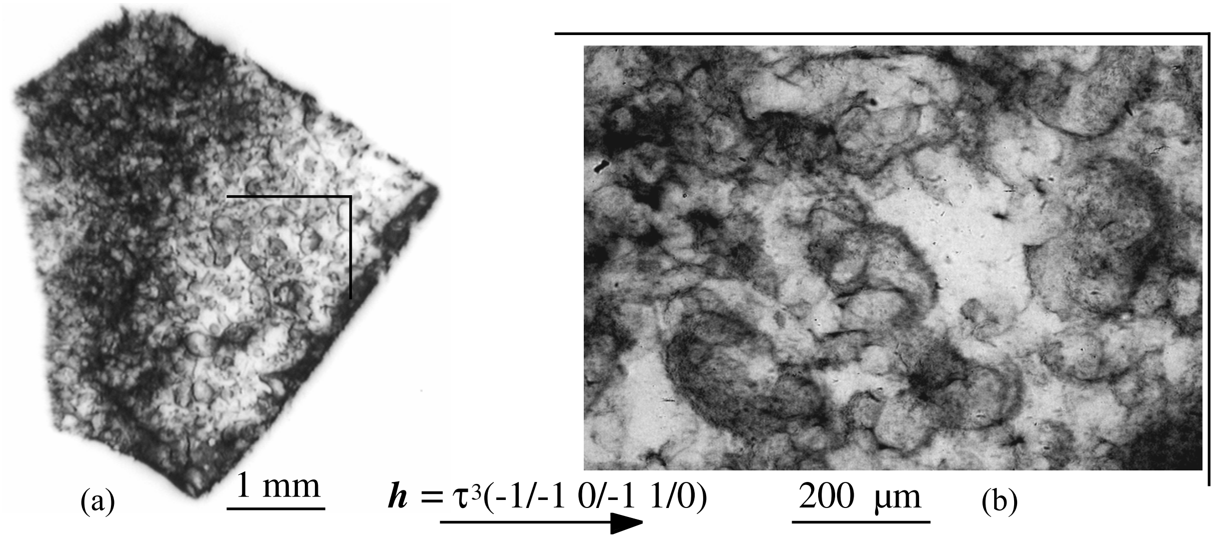

Fig 5.19 (a) X-ray topograph ($\lambda = 0.35$ Å; $d = 0.2$ m) of the annealed sample C showing a complicated network of big entangled loop shaped defects organised in several cases into necklace configurations (b)

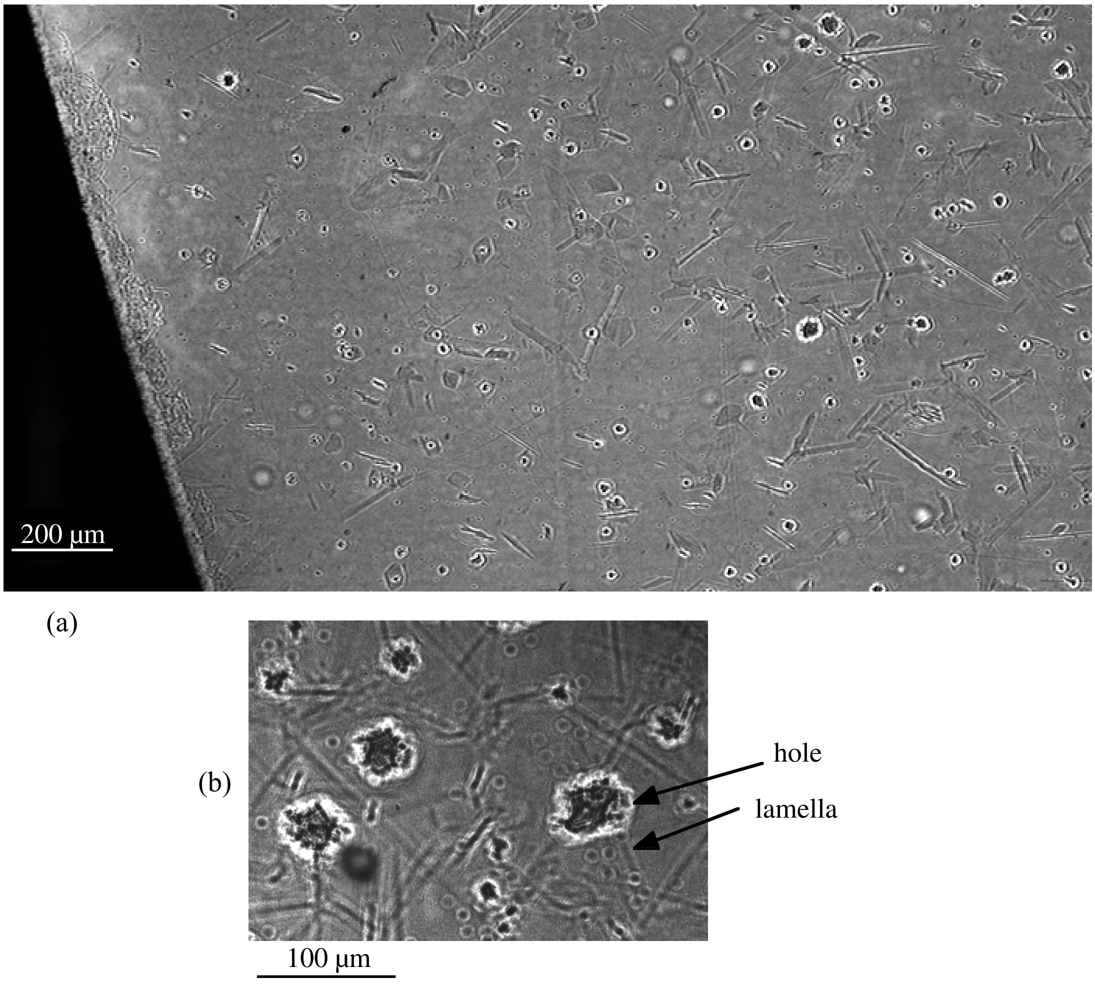

Fig 5.20 (a) Phase sensitive radiograph of sample C ($d = 0.5$ m) showing holes and precipitates distributed throughout the grain. (b) Detail showing at higher magnification precipitates and holes (arrowed); The border is constituted of several smaller holes.

Numerous lamellar precipitates, with various orientations, are also seen. They have a composition close to that of the precipitates in sample B ($Al_{74.2}Pd_{7.25}Mn_{18.55}$). Most of them display an elongated shape, and Fresnel diffraction fringes are visible at their edges. The elongated precipitates have a typical width of a few micrometers as measured on the images recorded at $D = 0.1$ m. Their defocused images are therefore no longer in the edge-detection regime for $D \approx 0.5$ m. These precipitates are practically invisible in the absorption images. By using equations (2.15) and (2.23) considering precipitates with a thickness of 5 μm and a density of about 3.9 g/cm^3, we find for $\lambda = 0.35$ Å that the phase shift $\Delta\varphi$ is 0.15 rad and the intensity modulation due to absorption is 0.02. This confirms that absorption radiography is indeed not suited for the observation of the precipitates.

TEM observations, performed after thinning pieces of sample C, also revealed lamellae analogous to the more elongated ones visible on the radiograph [Rei97, Rei98]. It was checked with stereographic images that the stick-like appearance of the elongated precipitates is only apparent. Their real shape is rather plate-like, but many lamellae are approximately perpendicular to the surface and parallel to the observation direction in Fig 5.20. For TEM experiments a possible explanation of the observed elongated shape could be the limited volume available in the thinned specimens.

The efficiency of the combination of phase sensitive radiography with X-ray topography is strikingly illustrated in Fig 5.21. It displays two direct-beam images recorded when the sample is set for a strong Bragg reflection. Fig 5.21a shows the same region as in Fig 5.19b, but here the loop shaped defects have a negative white contrast. The loop shaped defects, holes and precipitates are thus observed simultaneously. Fig 5.21b clearly indicates that big loop shaped defects (size of a few hundred micrometers) are often located around the precipitates, while smaller loop shaped defects (size < 100 μm) mainly surround the holes.

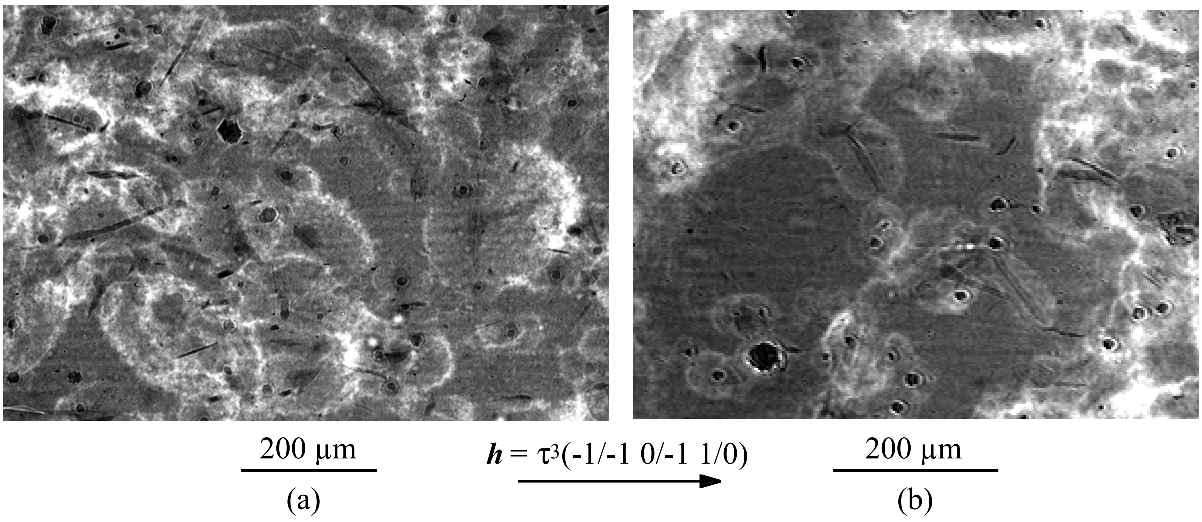

Fig 5.21 Combination of X-ray topography and phase sensitive radiography ($\lambda = 0.35$ Å; $d = 0.2$ m). (a) The same region of sample C as shown on Fig 5.19b; (b) a different region of sample C.

5.3.4 Discussion

It is clear that Al-Pd-Mn icosahedral quasicrystals, grown by the Czochralski technique, contain not only structural defects, but also inhomogeneities, viz. holes and precipitates. Structural defects and holes seem unavoidable in the as-grown state, while precipitates develop, in some cases, during the high temperature anneal. Numerous questions arise about these quasicrystalline features, particularly their origin and their relationships.

5.3.4.1 Holes

Dodecahedral holes were positively identified through careful analysis of the phase radiographic contrast from as-grown grains. Moreover these holes, which were previously observed at the surface of quasicrystalline grains [Aud90, Bee93], were unambiguously shown to be in fact distributed throughout the volume of the samples. Further a discrete distribution of the hole sizes is observed.

It is sure that their dodecahedral faceting reflects the icosahedral symmetry. On the phase sensitive radiographs of the annealed sample A1 it can be noticed that, after annealing, the periphery of most of the hole images tends to round. SEM observations of the external sample surfaces and the analysis of the radiographs at high magnification show that this is in fact due to a modification of the faceting. After annealing, the faceting becomes more complicated than in the regular dodecahedral holes observed in the as-grown samples. Several small new facets are visible, mainly at the edges and at the corners of the dodecahedra.

The exact origin of the holes is still a controversial topic. The information collected by radiography and tomography on the hole sizes and their spatial distribution is definitely relevant in this discussion. The results collected so far show that some apparently possible origins are highly unlikely.

Such is the case for the incorporation in quasicrystals, after dissolution in their melt, of the environmental gases that are sometimes used in the Czochralski growth technique. The last investigated quasicrystal grains were grown under a vacuum of 10^{-6} Torr and contained the same holes, with a similar bimodal distribution in the volume, which rules out this possibility. Another mechanism involves condensation of vacancies generated by oxidation. This possibility can be rejected mainly because of the poorly oxidizing environmental conditions of the growth techniques used. According to other authors [Bee97] holes could result from the condensation of thermal vacancies during the after-growth cooling of the grains. The diffusion mechanisms in quasicrystals are unknown but the formation and migration energies of thermal vacancies would have to be very different from those of crystals to explain the observed large size and volume fraction of the holes.

Only origins of the holes related to the growth process appear as meaningful on the basis of the radiographic observations. One extrinsic and two intrinsic possible causes were considered [Man98, Gas99]. The first intrinsic origin involves voids induced by growth frustration to maintain the long range quasicrystal orientational order. However there is a large discrepancy between the size of the observed holes and that of the voids which could be generated, unless they could grow or coalesce during after-growth cooling. The second intrinsic origin of holes results directly from the 'cluster model' of Janot et al. [Jan94, Jan97], explaining the quasicrystal structure as a self-similar inflation of a 51 atom cluster. It predicts well defined discrete size distributions and distances between the holes. Some of the observations (hole sizes) agree statistically with the predictions of the model whereas other do not (e.g. observed volume fractions). The extrinsic cause of the presence of holes is related to the bad wetting of external surfaces by liquids. This very special property of quasicrystals [Riv97], could explain the formation of holes at the growing interface, and their trapping inside the matrix, provided the bad wetting property is valid for the melt.

The validity of these hypotheses will be tested by a combined X-ray topography and phase radiography study of the quasicrystal solidification process in situ.

5.3.4.2 Lamellar precipitates

Lamellar precipitates, with lengths varying from 20 μm to 100 μm, were observed by phase radiography in samples B and C, after annealing at temperatures of about 750° C, mainly in the vicinity of holes. Similar lamellar precipitates were also identified by TEM, and selected area electron diffraction showed that these precipitates are crystalline, with an orthorhombic structure. A two-fold symmetry axis coincides with a five-fold axis of the icosahedral matrix [Rei98]. The icosahedral domain in the phase diagram is very narrow. A slight variation of the stoichiometry during the annealing can cause the precipitation of additional phases. The observed crystalline phase could not be identified as one of the phases predicted by the solidification diagram. This indicates that the equilibrium conditions were not reached during the annealing.

In the case of the annealed sample A1 no precipitates were detected. This could be explained by the better vacuum used during its annealing ($\approx 10^{-8}$ instead of $\approx 10^{-6}$ Torr). It can also be associated with the slight variations of chemical composition which is the other known difference between the studied samples (see Table 5-1).

5.3.4.3 Inhomogeneities and structural defects

Two kinds of contrasts were distinguished on X-ray topographs: one characterised by two lobes, and another corresponding to the loop shaped defects. By comparing the topographs with the phase radiographs of the same sample, a direct correspondence between the two-lobe contrasts and the holes was established. A similar correspondence could not be established for the small loop shaped defects, characteristic of the as-grown state. In the annealed grains, the loop shaped defects were larger and it was easier to realise that they surround both holes and lamellar precipitates. This becomes particularly evident through the combined images.

The two-lobes contrasts could be related to the strain field around the holes. The loop shaped defects on the other hand could be associated to defects resulting from the relaxation of the strain fields surrounding holes and precipitates. The determination of the displacement vectors corresponding to these defects remains difficult because of their large number and entangled configuration [Gas95a].

5.3.5 Conclusion

X-ray topography and phase sensitive radiography are powerful for the identification of defects in real quasicrystals. Phase radiography and tomography show clearly that holes and lamellar crystalline precipitates are located in the bulk and provide quantitative data (hole size, hole density, close pair distances). These observations enable to reject a number of possible origins of the holes and support mechanisms related to the growth process. A better understanding of the topographic contrast and the structural defects in quasicrystals is possible thanks to the information on inhomogeneities revealed by phase radiography. By combination of both X-ray imaging techniques, the structural defects were shown to be located around holes and lamellar precipitates. This suggests that they result from the relaxation of the elastic strain field surrounding holes and precipitates.

5.4 Observation of ferroelectric domains and phase retrieval

5.4.1 Introduction

The possibility to sense the phase of a coherent X-ray beam by simple propagation can be extended to Bragg diffracted beams exiting a crystal. The combination of Fresnel diffraction (propagation) and Bragg diffraction is particularly interesting when the sample behaves as a phase object only when set to Bragg diffract and when the diffracted beam has homogeneous intensity at the exit of the crystal. We used simultaneously Fresnel and Bragg diffraction to visualise ferroelectric domains within a periodically poled lithium niobate crystal. The wavefront of the Bragg-diffracted X-ray beam is 'split' by the phase difference between the structure factors of adjacent domains. This shift is measured through quantitative analysis of the image contrast as a function of propagation distance. It gives information about atom displacements at the microscopic level.

The studied material, $LiNbO_3$, is ferroelectric below ≈ 1200°C as schematically represented in Fig 5.22a [Abr94, Wei85]. Its crystal system is trigonal (space group R3c [Abr66]) and we will describe it with a hexagonal unit cell. The displacement of the Nb and Li atoms along the c_H-axis determine the spontaneous polarisation. The Nb atom is displaced from the halfway position between two oxygen layers say to a slightly higher position. The Li-atom is then found slightly above the oxygen layers. At room temperature the structure is therefore non-centrosymmetric and an inversion yields the structure schematically drawn in Fig 5.22c with opposite spontaneous polarisation. Above its Curie temperature (second-order transition) the structure is centro-symmetric (space group more probably $R\bar{3}c$ [Boy94, Abr66]) and paraelectric. The Nb atom is then localised exactly half-way between two oxygen layers on an inversion center (Fig 5.22b).

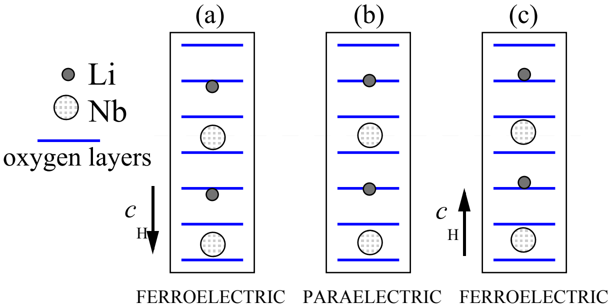

Fig 5.22 Schematic drawing of the atomic positions of niobium and lithium with respect to the oxygen layers in $LiNbO_3$ for the ferroelectric structure (a), the paraelectric one stable above ≈ 1200°C (b) and the inversed ferroelectric structure (c).

Lithium niobate displays strong second-order non-linear optical effects, with a particularly high value of $\chi^{(2)}_{333}$. This element of the second-order nonlinear susceptibility tensor describes a quadratic contribution of the electric field to the polarisation with all components of the fields along the c_H-axis [Bye77]. The high value of this tensor element (equal to twice the customary tensor element d_{33} in reduced notation) seems attractive for second-harmonic generation. A high efficiency implies the phase matching condition [Bye77]

$$\Delta k = k(2\omega_v) - 2k(\omega_v) = 0 \tag{5.2}$$

with ω_v the optical angular frequency and e.g. $k(\omega_v)$ the wavenumber at this angular frequency. This condition assures that the driving polarisation for second-harmonic generation is uniform along the device. If the phase velocity is not matched, the energy initially transferred from the incident wave to the second harmonic will return to the first harmonic, and increasing the length of the device is not effective. The phase matching condition is in general not fulfilled because the refractive index varies with the optical wavelength. A solution consists in changing the sign of the nonlinear optical coefficient periodically in order to avoid that the driving polarisation should get out of phase [Arm62]. A periodically inverted domain structure, as depicted in Fig 5.23, is therefore introduced in a $LiNbO_3$ single crystals. Enhanced efficiency is obtained when the domain period a is such that

$$\Delta k = k(2\omega_v) - 2k(\omega_v) - \frac{2\pi}{a} = 0 \tag{5.3}$$

Domain inversion can be obtained by applying a strong external electric field during a short time (≈ 100 µs) along the $-c_H$-axis. By using a patterned electrode [Yam93, Mye95, Shi96] on one face of the crystal, a periodic structure is produced . An important issue is the characterisation of the poling process. As the optical waves may propagate in the volume of the second harmonic generation device, it is important to assess the domain quality not only at the surface but also in the volume. It can for example be expected that the domain quality gets worse deeper in the crystal at a larger distance from the patterned electrode. Various methods revealing ferroelectric domains in $LiNbO_3$ were reported: chemical etching [Nas76], electron microscopy [Wic68, Hou95], pyroelectrically induced electron emission [Kug95] and X-ray Bragg-diffraction imaging [Wal70, Vre84, Hu96, Rej98a, Hu98, Rej98b].

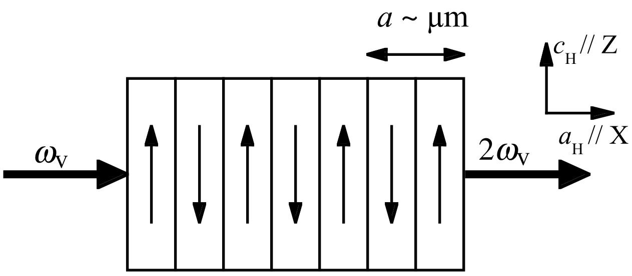

Fig 5.23 Principle of periodic inversion of the domain structure in order to achieve optical second-harmonic generation with enhanced efficiency.

5.4.2 Experiments

We use the usual axis choice schematically shown in Fig 5.23. The Z-axis of the orthonormal XYZ-system is parallel to the hexagonal c_H-axis, the X-axis is parallel to the a_H-axis which is chosen perpendicular to the mirror plane in the structure. The periodicity occurs in the X direction, hence the domain walls are perpendicular to this axis. The periodically poled samples were produced by bulk electric-field poling [Mye95] using a Z-cut wafer (surface perpendicular to the Z-axis) from a congruent $LiNbO_3$ crystal supplied by Crystal Technology. The congruent composition [Abr86] is not exactly stoechiometric but is approximately $Li_{0.95}Nb_{1.01}O_3$. We are grateful to M. Arbore, M. Fejer and G. Foulon from Stanford University, USA for poling and supplying the crystals. The domain reversal was performed across the whole 0.5 mm thickness of the crystals. We used crystals with a nominal domain period of 23 µm and 15 µm. The images were recorded on Kodak Industrex SR films with exposure times ranging from one second to a few minutes.

The simple set-up designed to perform white beam section topography is schematically represented in Fig 5.24a. Several reflecting planes fulfill the Bragg condition of diffraction for different wavelengths, and a Laue pattern is produced. Because the incident white beam is limited in height to about 15 µm, each spot is a section-topograph. This technique is usually used to reveal small distortions within nearly perfect crystals. However it allows, when using a coherent beam and a significant sample-detector distance, to observe phase shifts within the diffracted beam. The sample-detector distance *d* determines the defocusing distance *D* through equation (2.60).

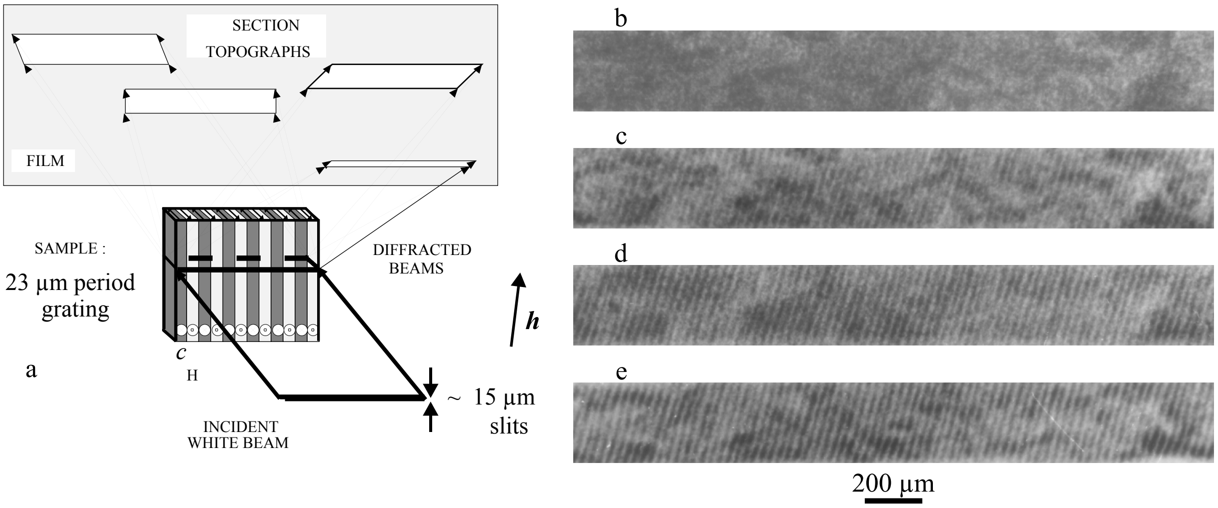

Fig 5.24 a) Set-up for white beam section topography: the defects present in a single crystal can be observed within the Laue spots. b)-e) Section topographs using the 274 reflection, $\lambda = 0.24$ Å, recorded at different defocusing distances D: b) $D = 0.11$ m, c) $D = 0.51$ m, d) $D = 1.11$ m, e) $D = 1.67$ m. The scattering plane is approximately vertical.

Fig 5.24b-e show a set of section topographs of the sample with 23 µm period obtained using the 274 reflection for different defocusing distances *D*. This procedure is used because only 'standard' topographic images [Bar93b] are observed when the detector is close to the crystal ($D = 0$). The slits were perpendicular to the domain walls, as shown on Fig 5.24a, and the diffraction plane was approximately vertical. The images represent a virtual slice of the crystal volume. Only very faint contrast of inverted domains is found in Fig 5.24b, recorded at $D = 0.11$ m. Stronger contrast appears over the whole section topograph of Fig 5.24c, corresponding to $D = 0.51$ m. This contrast consists of parallel lines periodically spaced, with a period equal to the period of poling (23 µm). The contrast increases with *D* (Fig 5.24d-e).

As it is a white beam experiment many other reflections were recorded in a similar way [Rej98b]. The geometrical resolution (determined by the source size through $d\, s/l$) is better when Bragg diffraction occurs in the horizontal plane and the domain walls are horizontal. We also recorded topographs using this horizontal diffraction plane geometry. The section topographs obtained at small distances ($D < 2$ m) display finer features: additional black and white lines can be observed between the main ones [Rej98b].

When the slits are removed and the symmetrical Bragg geometry is used, as shown in Fig 5.25a, a projection topograph, mainly sensitive to the surface of the crystal, is obtained [Tan76]. Fig 5.25b-h show the images of a sample with 14.8 µm period using the 006 reflection at $\lambda = 1$ Å with a defocus distance varying from 0.11 m to 2.65 m [Clo99]. The (quasi-)period corresponds again to the poling period. Especially in Fig 5.25b and c, obtained at $D = 0.11$ m and $D = 0.3$ m respectively, a fine interference-like pattern is clearly observed. The topograph of Fig 5.25e, recorded at $D = 1.09$ m, seems a reliable picture of the domain structure expected from the poling process. The contrast is faint (but present) in Fig 5.25g at $D = 2.25$ m whereas it is stronger again in Fig 5.25h corresponding to a larger distance. The periodicity in the image is strongly perturbed, especially at larger distance, due to topographic contrast which seems independent of the domain structure but connected to the crystalline quality of the sample.

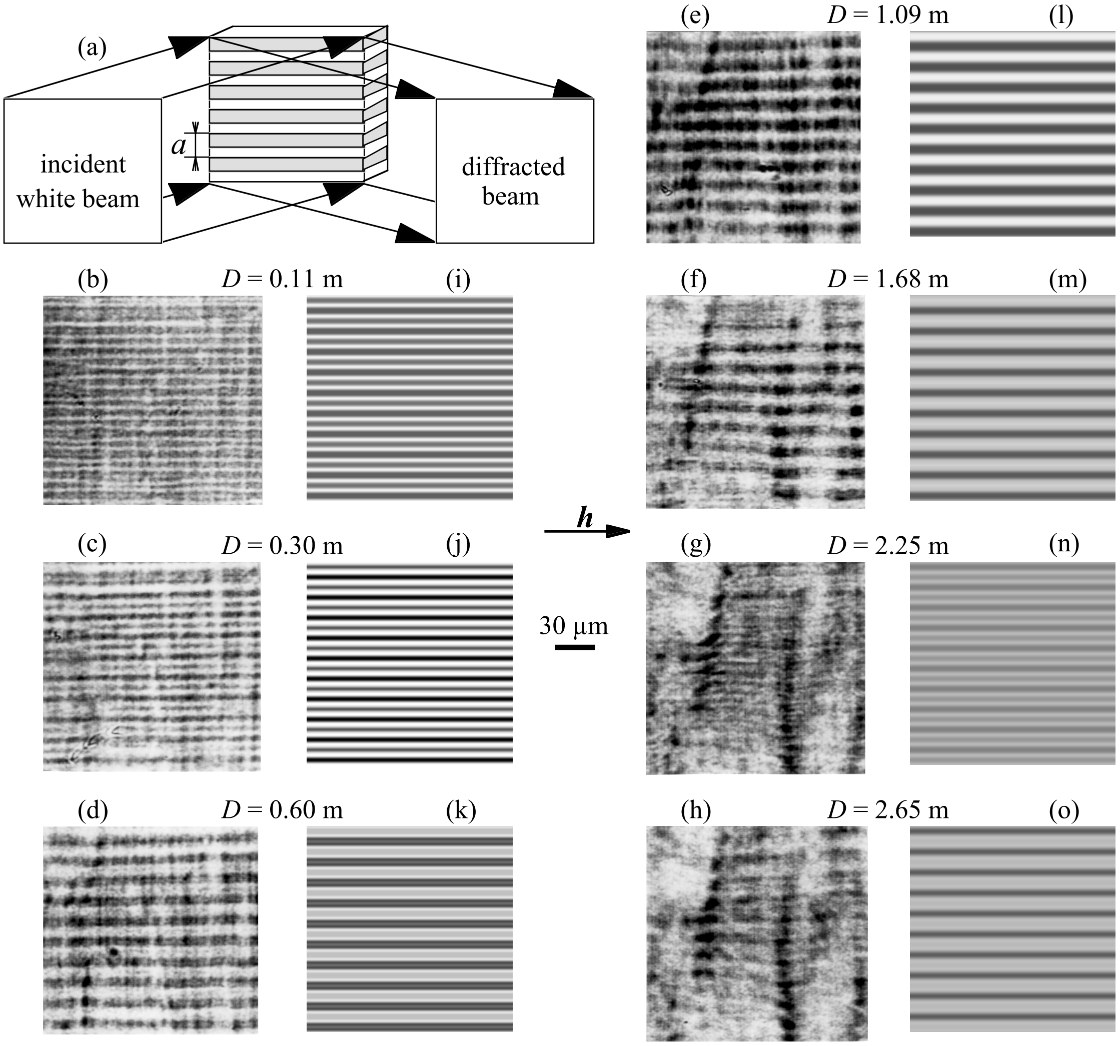

Fig 5.25 a) Scheme of the white beam experimental set-up using the 006 symmetric reflection at $\lambda = 1$ Å. The scattering plane and the domains are horizontal. b)-h) Experimental topographs for different defocusing distances D. i)-o) Simulated intensity distributions corresponding to the experimental distances. For the simulations a periodic rectangular phase profile is assumed with $\Delta\varphi = 140°$, $b = 0$, $\Delta A = 0.05$ (see text).

5.4.3 Discussion

It is obvious that the images vary strongly as a function of the defocusing distance. This type of behavior may arise from three possible origins:

i) different orientations of the reflecting planes ('misorientation' contrast) in neighbouring domains. This results in different propagation directions and a lateral displacement of the diffracted intensity distribution. It is normally assumed that the superposition at the detector level occurs *incoherently* [Tan76] (see ii). However this is not the main origin of the observed features, for at least three reasons: 1) the dependency of contrast on the propagation distance does not correspond to the behaviour (i.e., periodic alternation of black, grey and white lines) expected from misorientation contrast between adjacent domains as a function of the sample-detector distance; 2) the observed contrast strongly depends on the incident white beam spectrum, which can be modified by varying the gap of the wiggler source. The relative contribution of the reflection and its harmonics is altered, resulting in a dramatic change, or even the vanishing, of the observed contrast. This is in contradiction with the expected behaviour of misorientation contrast, which is not sensitive to the energy spectrum variation. 3) the diffraction plane is nearly parallel to the domain walls. The modification of the Bragg angle θ_B in the direction perpendicular to the domain walls is therefore given by the misorientations multiplied by $\sin\theta_B$ (≈ 0.1). One should observe a much larger effect when working with the diffraction plane perpendicular to the domain walls. This is exactly opposite to the observations.

ii) different orientations of the reflecting planes introducing a change in the propagation direction but a *coherent superposition* at the level of the detector. This contrast mechanism is unlikely too because reasons 1) and 3) mentioned above are still valid. Images similar to those of Fig 5.25 were reported by other authors who explain their observations by lattice distorsions introduced by the poling process [Hu98]. The fringe spacing (fine fringes appearing also on Fig 5.25b and c) would then be determined by the angle $\Delta\alpha$ between the wave vectors of the interfering waves. Their spacing $\lambda/\Delta\alpha$ (cf. Fresnel's biprism) would be independent of the propagation distance. In order to explain the observed increase of the fringe spacing with defocusing distance, the authors come to the untenable position where they have to change the value of the involved lattice distorsions with the defocusing distance. Finally, as the authors omitted the geometrical factor $\sin\theta_B$ (≈ 0.1), the measurements of the lattice distorsions they performed by high resolution X-ray diffraction indicate that the lattice distorsions (if present) are at least one order of magnitude too small to explain the observations. The misorientation can nevertheless play a role in the neighbourhood of the surface, or if an external parameter (electric field [Rej98a], temperature) is applied.

iii) different structure factors ('structure factor' contrast). Reflecting planes $\boldsymbol{h}$ (hkl) in domain I correspond to planes $-\boldsymbol{h}$ in the inverted structure of domain II. It is important to note that the relative difference of the moduli $|F_{\boldsymbol{h}}|$ and $|F_{-\boldsymbol{h}}|$ of the respective structure factors, calculated using the Fhkl software [Soy95], with dispersion corrections of course taken into account, is less than 1 % in the case of Fig 5.24. For the images obtained in reflection geometry the relative difference is slightly higher because of the lower energy (≈ 5 %). Therefore the change in structure factor modulus cannot explain the observed contrast. $F_{\boldsymbol{h}}$ and $F_{-\boldsymbol{h}}$ differ however substantially in their phases φ_I and φ_{II}. The waves diffracted by adjacent domains exhibit, when they leave the crystal, a phase shift $\Delta\varphi = |\varphi_I - \varphi_{II}|$. The value of this shift is identical in the case of dynamical or cinematical diffraction [Aut78]. For simple transmission, i.e. in the absence of Bragg diffraction this shift is zero. Interference between parts of the wavefront diffracted by different domains then occurs through free space propagation, well described as Fresnel diffraction. As in the case of phase sensitive radiography, this turns the phase modulation into an amplitude and a corresponding intensity modulation.

As the wave exiting the crystal is (approximately) periodic, the Fresnel diffraction pattern is ideally periodic both in the direction of the object periodicity (period a) and in the propagation direction (period $D_T = 2a^2/\lambda$). This corresponds to the Talbot effect described and demonstrated in § 4.2 for a periodically modulated wave transmitted by a phase object. No contrast is expected immediately behind the object. For the section topographs of Fig 5.24 the Talbot distance D_T is 44 m. The contrast increases therefore monotonically. For the projection topographs obtained in reflection geometry (Fig 5.25b-h) D_T is 4.38 m. The first image is already weakly defocused and a fine interference pattern appears. The weakest contrast is observed in the topograph of Fig 5.25g for $D = 2.25$ m. Faint contrast remains visible because the defocusing distance is not exactly equal to $D_T/2 = 2.19$ m. The image of Fig 5.25e ($D = 1.09$ m) corresponds to a defocus close to $D_T/4$ where the phase object and the intensity distribution in the image are simply related. Expression (4.11) shows that if the domain pattern introduces a symmetric rectangular phase profile the intensity distribution has an identical shape at this distance.

A quantitative approach giving access to the phase shift and the angular divergence of the wave exiting the crystal is shown on Fig 5.26. As in the case of a periodic object in transmission geometry (see § 4.2), we consider the Fourier coefficients $I^{(m)}(D)$ of the intensity profile recorded at defocusing distance D. They are measured on the topographs of Fig 5.24b-e by averaging the experimental intensity distribution in the direction parallel to the lines and calculating the discrete Fourier transform. On the other hand the Fourier coefficients can be calculated by simulation with expression (4.12). The periodic phase modulation used is shown in the inset of Fig 5.26. It is characterised by a phase-shift $\Delta\varphi$ and a linear transition of scaled width b between the two phase levels. The angular beam profile of the diffracted wave in the absence of a domain structure is assumed to have a gaussian profile with width s_α (cf. expression (4.15)). The effect of the partial coherence is thus considered in the calculations by multiplying the ideal Fourier coefficients by the degree of coherence given by expression (4.16). The coefficients $I^{(m)}_{\text{coh}}$ corresponding to illumination by an ideally coherent plane wave were numerically calculated within the Fresnel diffraction approximation using Fourier transformations (expression (2.90)).

Expressions (4.12) and (4.16) were used to fit our experimental data as a function of D for the first Fourier coefficient, the higher-order ones being too weak for interpretation. The estimated value, obtained by a non linear least squares fit, for the phase shift $\Delta\varphi$ is 80°. This value is consistent with the phase shift of 70° calculated on the basis of the accepted structure of lithium niobate [Abr86] with the Fhkl program. The main contribution to the structure factor is that from the heavier niobium atom. It is important to notice that the value of the phase shift depends on the relative position of the crystal structure of domain I with respect to domain II. If the lattices have relative positions such that the Z coordinate of the Nb atoms does not change when going from one domain to the next, the phase shift will be much smaller. To calculate the phase shifts we used the more acceptable model which assumes continuous oxygen layers across the domain wall. This corresponds to the picture of Fig 5.22 and the Nb atom changes its position along the c_{H} axis by 0.54 Å.

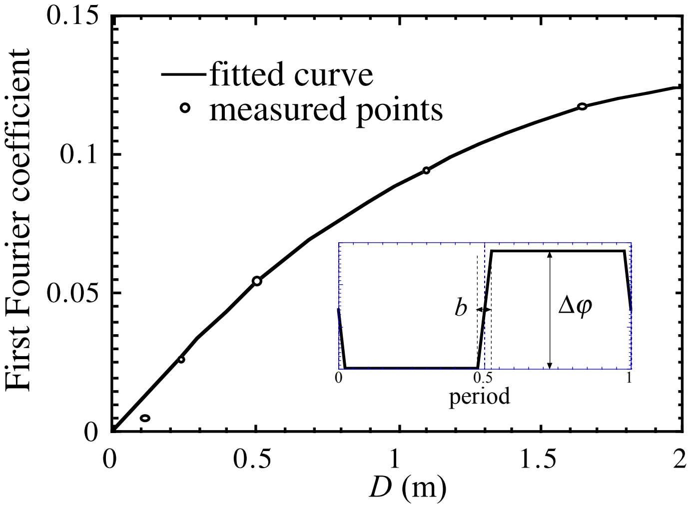

Fig 5.26 Modulus of the first Fourier coefficient as a function of defocusing distance for the 274 reflection at $\lambda = 0.24$ Å (Fig 5.24). The fitted curve corresponds to expressions (4.12) and (4.16) with the phase modulation shown in the inset. $\Delta\varphi = 80°$, $b = 0.05$, divergence $s_{\alpha} = 3.6$ µrad.

The width w of the transition between the two phase levels is small (5 % of the period). We attribute it to the diffraction geometry and the finite extension, about 15 µm, of the incident beam in its narrow direction. It seems unlikely that it corresponds to the thickness of the wall between adjacent domains, which is probably orders of magnitude smaller. The beam divergence resulting from the fit, 3.6 µrad, is larger than the angular source size (< 2 µrad). It includes contributions from the crystal quality of the sample and the small value of the Darwin width of the reflection used. The lattice distorsions introduce a supplementary divergence, the value of which provides statistical information on these distorsions. Schematically, if the typical size of a 'perfect' crystal portion is s_{pc}, the supplementary divergence is of the order of $\lambda / s_{\mathrm{pc}}$.

The simulated intensity distributions shown in Fig 5.25i-o are in good qualitative agreement with the experimental images of Fig 5.25b-h obtained in reflection geometry. They are based on the phase changes associated with the domain structure, and do not take into account the defects present in the real crystal. The fine interference pattern seen in Fig 5.25b-c appears also on the corresponding simulations. The agreement is better in some regions of the sample, as expected because the domain structure is not completely periodic. In a later stage, it should be possible to reconstruct the complex amplitude at the exit of the crystal and the corresponding domain distribution from the experimental images using a holographic reconstruction (see § 4.3). From the simulations we estimate the phase shift for reflection 006 to be 140° ± 5°, also in agreement with the value of 141° calculated from the structure of $\mathrm{LiNbO_3}$. The good simulations are obtained without any transition layer between the two phase levels ($b = 0$). When working with the symmetrical Bragg reflection and proper alignment, i.e. with the diffraction vector parallel to the domain walls, it is less likely that an apparent transition layer should appear due to geometric artefacts. In a perfect geometry the transition layer would correspond to a finite thickness of the domain wall where the crystal structure gradually changes from the ferroelectric through the paraelectric to the inverted ferroelectric structure. If such a domain wall exists its thickness apparently has no effect on the recorded Fresnel diffraction patterns (< 0.1 µm).

The simulations neglect the contribution of the higher harmonics, e.g. reflection $2\boldsymbol{h}$ corresponding to wavelength $\lambda/2$, and assume the diffraction vector is exactly parallel to the domain walls. This simplification of the diffraction geometry eliminates the possibility of multiple diffraction in different domains. Domain boundary contrast attributed to the phase difference between structure factors can build up *within* the crystal and it was formerly interpreted in analogy with the contrast of a stacking fault in the dynamical theory of X-ray diffraction [Tak78]. In the present case, a weak 'dynamical contrast' is observed in the section topographs only close to the sample on reflections with larger Darwin widths, and it is neglected.

The atomic displacement of the niobium ion, 0.54 Å along the c_H axis, is the main contribution to the phase shift between the structure factors of neighbouring domains. Reflections of the type hk0 are not sensitive to this displacement ($\boldsymbol{h}.\boldsymbol{r} = 0$ in expression (2.28)). However, a weak contrast is observed on most of these reflections. The thermal vibrations of the atoms change the modulus (cf. Debye-Waller factor) but also the phase of the structure factor. If only harmonic vibrations occur the temperature factor appearing in expression (2.28) of the structure factor is invariant for an inversion. On the other hand, anharmonic thermal vibrations can be inversion variant and introduce a supplementary shift [Daw67, Zuc82, Cop93]. Anharmonicity was reported for congruent $LiNbO_3$ [Abr86, Iyi92, Zot94] and such vibrations of the Nb atom are not in disagreement with the restrictions imposed by the symmetry of the Nb site.

5.4.4 Conclusion

The simultaneous use of Fresnel and Bragg diffraction allows to visualise, in a simple way, the distribution of inverted ferroelectric domains within the volume of periodically poled crystals produced for non-linear optics applications. Bragg diffraction introduces a phase shift between the waves diffracted in adjacent domains due to the phase difference between their structure factors. Fresnel diffraction and its special manifestation for periodic objects, the Talbot effect, determine the intensity variations after free space propagation. Through the measurement of the observed contrast as a function of propagation distance, the phase difference between the structure factors of reflections $\boldsymbol{h}$ and $-\boldsymbol{h}$ can be directly obtained. This approach is a new way to investigate any crystal feature which introduces a distortion of the phase of the Bragg diffracted wave. In particular it allows to determine precisely the atomic positions in twinned non-centrosymmetric crystals, and their variations as a function of an external parameter.

6 Conclusion

Third-generation synchrotron radiation sources are bringing into the X-ray field a revolution comparable to the advent of lasers in classical optics and the development of the field emission gun in electron microscopy. Established techniques such as X-ray crystallography and spectrometry greatly benefit from this and it is now possible to solve large biological structures with atomic resolution or map specimen composition with unprecedented precision. Inelastic and magnetic X-ray scattering are becoming useful techniques. A particular characteristic of X-ray beams produced by these sources is their relatively large degree of spatial coherence. This produces novel effects, in particular coherent scattering and imaging.
A century after the beginning of absorption radiography, a trivial form of phase radiography and tomography thus appeared. Based on simple propagation, it makes it possible to visualise internal structures in optically non transparent materials, with a resolution and sensitivity far superior to conventional X-ray imaging based on absorption. Our work is a contribution to the development of the technique of Fresnel imaging and to its use as a tool to investigate material problems in various areas.

In section 2 (Principles) the propagation method was compared with existing phase techniques and the theoretical framework of the image formation process was given. The comparison of three phase sensitive imaging techniques shows that, for hard X-rays, the defocusing method may be preferable when a simple, flexible set-up and optimum spatial resolution are required. An adapted theoretical framework based on a wave-optical approach was described. Fourier optics seems an effective method to treat the direct problem and makes it easy to simulate the defocused images when the object is known. It makes efficient use of Fourier transforms. Images obtained under weak defocusing conditions, in the edge-detection-regime, can often be interpreted directly: this opened the way to the use of Fresnel imaging as a direct imaging technique for hard X-rays. Further from the sample, the holographic nature of the images appears. It is useful for extracting quantitatively the phase with an adapted algorithm.

In section 3 (Implementation) the instrumentation used for phase sensitive imaging was described. The coherence properties of the beam can give rise to spurious images. In order to avoid them or a coherence degradation, the optical elements in the X-ray beam must fulfil stringent quality requirements. The problems encountered and the way they were solved were summarised. The set-up is well adapted to perform scans over the angular position of the sample for tomography and scans over the object-detector distance for in-line holography. The X-ray detector plays a major role because it presently limits the spatial resolution achievable in the recorded Fresnel diffraction patterns. We developed CCD-based detector systems with pixel sizes ranging from 0.5 μm to 10 μm (resolution ≈ 1.5 μm in the best case). A method rather robust to noise, based on the image of an edge, was used to determine the transfer function. Three methods to deconvolve the recorded images were compared. The method using reblurring and constraints turned out to be very efficient. The weak point of these detectors is their rather small sensitivity and detective quantum efficiency, due to the fact that the scintillator is kept thin to preserve good spatial resolution. Improvements can be expected by using structured, light guiding screens. The spatial resolution obtained approaches the limit of visible light optics. The possibility to overcome this limitation was demonstrated with a lensless set-up that magnifies by projection. Using the beam exiting an X-ray waveguide as the effective source, a spatial resolution in the holograms of 0.14 μm was demonstrated in one direction. Extension to two dimensions, i.e. the development of a real X-ray point source, is tempting but not straightforward. A different approach to further improving the spatial resolution consists in using another type of (on-line) detector. X-ray → electron conversion followed by an electron-zoom tube may be possible.

Section 4 described the methods to retrieve the quantitative information contained in the Fresnel diffraction patterns. The variation with propagation distance of the diffraction pattern was used both to study periodic objects and to handle the inverse problem, i.e. to extract the phase information. We performed on periodic objects a first investigation for hard X-rays of the 160 year old Talbot effect. The expected periodicity with defocusing distance is not perfect due to the partial coherence of the incident beam. A precise method to measure the degree of spatial coherence was deduced and implemented. Focus variation, as applied in transmission electron microscopy, consists in recording at different distances a series of images which are combined through a suitable algorithm to reconstruct the wave function. The algorithm, adapted to the X-ray case, was presented. Physically meaningful constraints valid for X-rays in the absence of strong Bragg diffraction were important for successful retrieval of the phase. They compensate for the low sensitivity of the defocusing method for smooth variations in the phase modulation. Phase maps were reconstructed from one-dimensional images of a simple test sample and two-dimensional images of a complicated polymer foam. The phase profile of the test sample was found to be qualitatively and quantitatively in agreement with the expected profile. The retrieved phase maps offer in a single image good sensitivity (weak phase jumps are detected) and optimum spatial resolution. This image can be straightforwardly interpreted as a projection of the electron density in the sample along the X-ray path. The success of this ‘holographic’ reconstruction opened the way to quantitative three-dimensional imaging. This was done in two steps by ‘holo-tomography’. For each angular position of the sample the phase map was reconstructed from four defocused images. This large number of projections constituted the correct input for the ensuing tomographic reconstruction. The three-dimensional distribution of the refractive index decrement of a polymer foam was determined in this way. This yielded interesting microstructural information. We gave a justification for an approximate tomographic approach using the algorithm for absorption tomography and a scan at one single distance. The reconstructed distribution is under weak defocusing conditions approximately the sum of two terms: the usual linear absorption coefficient and a contribution proportional to the three-dimensional Laplacian of the refractive index decrement. With two tomographic scans both contributions can be separated.

In section 5 applications of phase sensitive radiography and tomography were presented.
Damage mechanisms in composite materials were characterised with these techniques. This turned out to be effective for several reasons. The Fresnel fringes enhance the particle/matrix contrast and allowed to reveal the microstructure in materials containing phases with very similar X-ray attenuation. Cracks could easily be detected and localised in the volume of the strained composite, even when their opening was small compared to the spatial resolution, thanks to the diffraction pattern produced. Although the images are defocused, the agreement with the real sample remains excellent, as was shown by comparing the tomographic slices with surface observations by scanning electron microscopy. The latter offers a better spatial resolution but images only the surface. For bulk observations, destructive post mortem preparation of the sample is required, and this can cover up some characteristic features of the damage process. The simplicity of the set-up easily allowed to install a tensile testing machine. Three-dimensional in-situ observations of the initiation and development of damage inside a particle reinforced composite were performed. Qualitatively, the same damage mechanisms were observed at the surface and in the bulk of the sample, the rupture of the SiC particles being the dominant mechanism for the early stages of plastic deformation. Quantitatively, however, it was found that the damage growth rate is larger inside the sample. This result can be understood in terms of stored elastic energy and probability of fracture.
The combined use of X-ray topography and phase sensitive radiography allowed to identify defects in quasicrystals. Phase radiography and tomography clearly showed that holes and lamellar crystalline precipitates are located in the bulk and provide quantitative data (hole size, hole density, close pair distances). These observations allow to reject a number of possible origins of the holes and they support mechanisms related to the growth process. By combining both X-ray imaging techniques, the structural defects were shown to be located around holes and lamellar precipitates. This suggests that they result from the relaxation of the elastic strain field surrounding holes and precipitates.
By simultaneous use of Fresnel and Bragg diffraction, we could visualise the distribution of inverted ferroelectric domains within the volume of periodically poled lithium niobate crystals. Bragg diffraction introduces a phase shift between the waves diffracted in adjacent domains due to the phase difference of their structure factors. Fresnel diffraction determines the intensity variations after free space propagation. This allowed to solve, in a particular case, the famous phase problem of crystallography in a very direct way. The phase difference between the structure factors of adjacent domains was obtained. This approach is a new way to investigate any crystal feature which introduces a distortion of the phase of the Bragg diffracted wave. It allows to determine precisely the atomic positions in twinned non-centrosymmetric crystals, and their variations as a function of an external parameter.

References

[Abr66] S.C. Abrahams, H.J. Levinstein and J.M. Reddy, J. Phys. Chem. Solids **27**, 1019 (1966).

[Abr86] S.C. Abrahams and P. Marsh, Acta Cryst. **B42**, 61 (1986).

[Abr94] S.C. Abrahams, Acta Cryst. **A50**, 658 (1994).

[Aks92] S. Aksoy, P. Elleaume and H. Moulin, *Users' Manual for 'Xray'*, internal publication ESRF, (1992).

[And72] M. Ando and S. Hosoya, in *Proc. 6th Intern. Conf. on X-ray Optics and Microanalysis*, eds. G. Shinoda, K. Kohra and T. Ichinokawa (Univ. of Tokyo Press, Tokyo, 1972), p. 63.

[And77] H.C. Andrews and B.R. Hunt, *Digital Image Restoration*, (Prentice-Hall, Englewood Cliffs, 1977).

[Ari85] V.V. Aristov, A.I. Erko, and V.V. Martynov, Opt. Commun. **53**, 159-163 (1985); Opt. Spectrosc. **64**, 376-380 (1988); A.I. Erko, V.V. Aristov and B. Vidal, *Diffraction X-ray Optics* (IOP Publishing, Bristol, 1996).

[Ari87] V.V. Aristov, Y.A. Basov, S.V. Redkin, A.A. Snigirev and V.A. Yunkin, Nucl. Instr. Meth. A **261**, 72 (1987); A. Snigirev, Rev. Sci. Instrum. **66**, 1 (1995).

[Arm62] J.A. Armstrong, N. Bloemberger, J. Ducuing and P.S. Pershan, Phys. Rev. **127**, 1918 (1962).

[Arn79] U.W. Arndt and D.J. Gilmore, J. Appl. Crystallogr. **12**, 1 (1979).

[Arr92] V. Arrizón and J. Ojeda-Castañeda, J. Opt. Soc. Am. A **9**, 1801 (1992).

[Arr95] V. Arrizón and E. López-Olazagasti, J. Opt. Soc. Am. A **12**, 801 (1995).

[Aud90] M. Audier, P. Guyot and Y. Brechet, Phil. Mag. Lett. **61**, 55 (1990).

[Aud93] M. Audier, M. Durand-Charre and M. de Boissieu , Phil. Mag. B **68**, 607 (1993).

[Aut78] A. Authier in *Diffraction and Imaging Techniques in Material Science*, eds S. Amelinckx, R. Gevers and J. Van Landuyt (North Holland, Amsterdam, 1978) **II**, p. 715.

[Aut96] A. Authier, in *X-ray and Neutron Dynamical Diffraction: Theory and Applications*, Erice, Italy, eds A. Authier, S. Lagomarsino and B. K. Tanner (Plenum Press, New York, 1996), NATO ASI Series **B 357**, p. 1.

[Baa95] G.Y. Baaklini, R.T. Bhatt, A.J. Eckel, P. Engler, M.G. Castelli, and R.W. Rauser, Mater. Eval. **Sept.**, 1040 (1995).

[Bao92] G.Bao, Acta Metall. Mater. **40**, 10 (1992).

[Bar93a] J. Baruchel , A. Draperi and F. Zontone, J. Phys.D: Appl. Phys. **26**, 9 (1993).

[Bar93b] J. Baruchel, in *Neutron and Synchrotron Radiation for Condensed Matter Studies,* eds J. Baruchel, J.L. Hodeau, M.S. Lehmann, J.R. Regnard and C. Schlenker (Ed. de Physique and Springer -Verlag, Berlin , 1993), **I**, p. 399.

[Bar97] J. Baruchel, J.Y. Buffière, P. Cloetens, J.P. Guigay, G. Peix, F. Peyrin, M. Salomé-Pateyron, and M. Schlenker and P. Spanne, in *Coherent Electron-Beam X-Ray Sources: Techniques and Applications*, eds A.K. Freund, H.P. Freund and M.R. Howells, Proc. SPIE **3154,** San Diego 1997, p. 51.

[Bat64] B.W. Batterman and H. Cole, Rev. Mod. Phys. **36**, 681 (1964).

[Bat89] R.H.T. Bates and J.M. Rodenburg, Ultramicroscopy **31**, 303 (1989).

[Bec95] F. Beckmann, U. Bonse, F. Busch, O. Günnewig and T. Biermann, HASYLAB Annual Report **II**, 691 (1995).

[Bec97] F. Beckmann, U. Bonse, F. Busch, and O. Günnewig, J. Computer Assist. Tomography **21**, 539 (1997).

[Bec98] F. Beckman, *Entwicklung, Aufbau und Anwendung eines Verfahrens der Phasenkontrast-Mikrotomographie mit Röntgen-Synchrotronstrahlung,* Ph.D. thesis, (University of Dortmund, Germany, 1998).

[Bee92] C. Beeli, *Electron Quasicrystallography*, Ph. D. Thesis, (ETH Zurich, Switzerland, 1992).

[Bee93] C. Beeli and H.-U. Nissen, Phil. Mag. B **68**, 487 (1993).

[Bee97] C. Beeli , T. Gödecke and R. Lück, in *Proceedings of the 6th International Conference on Quasicrystals*, Tokyo, Japan, eds S. Takeuchi and T. Fijiwara (World Scientific, Singapore, 1997), p. 421.

[Big71] F. Biggs and R. Lighthill, Research Report ref. SC-RR-71 0507 (1971); ref. SC-RR-72 0685 (1972)

[Bla57] G. Black and E.H. Linfoot, Proc. Roy. Soc. A **239**, 522 (1957).

[Bon60] W.L. Bond, Acta Cryst. **13** 814 (1960).

[Bon65] U. Bonse and M. Hart, Appl. Phys. Lett. **7**, 99 (1965).

[Boo94] J.M. Boone and J.A. Seibert, Med. Phys. **21**, 1541 (1994).

[Bor80] M. Born and E. Wolf, *Principle of Optics*, 6th ed. (Pergamon Press, Oxford, New York, 1980).

[Bou95] M. Boudard, E. Bourgeat-Lami, M. de Boissieu, C. Janot, M. Durand-Charre, H. Klein, M. Audier and B. Hennion, Phil. Mag. Lett. **71**, 11 (1995).

[Bou96] M. Boudard, M. de Boissieu, J.-P. Simon, J.-F.Berar and B. Doisneau, Phil. Mag. Lett. **74**, 429 (1996).

[Boy94] H. Boysen and F. Altorfer, Acta Cryst. **B50**, 405 (1994).

[Bra95] S. Brauer, G.B. Stephenson, M. Sutton, S.G.J. Mochrie, S.B. Dierker, R.M. Fleming, R. Pindak, I.K. Robinson, G. Grübel, J. Als-Nielsen and D.L. Abernathy, Rev. Sci. Instrum. **66**, 1506 (1995).

[Bre55] E. Breitenberger, Prog. Nucl. Phys. **4**, 56 (1955).

[Bré91] Y. Bréchet, J.D. Embury, S.Tao, L. Luo, Acta Metall. Mater. **39**, 8 (1991).

[Bre93a] T.M. Breunig, M.C. Nichols, J.H. Kinney and D.L. Haupt, in *Proc. 17th Annual Conference on Composites and Advanced Ceramic Materials*, (American Ceramic Society, Cocoa Beach, January 1993), p. 500.

[Bre93b] T.M. Breunig, S.R. Stock, A. Guvenilir, J.C. Elliott, P. Anderson and G.R. Davis, Composites **24**, 209 (1993).

[Bri74] E. Brigham, *The Fast Fourier Transform* (Prentice-Hall,1974).

[Bro86] D. Broek, in *Elementary Engineering Fracture Mechanics* (Martinus Nijhoff Publishers, 1986), p. 79.

[Buf97] J.-Y. Buffière, E. Maire, C. Verdu, P. Cloetens, M. Pateyron, G. Peix, and J. Baruchel, Mat. Sc. Eng. **A234-236**, 633 (1997).

[Buf98] J.-Y. Buffière, E. Maire, P. Cloetens, G. Peix, M. Salomé and J. Baruchel, ESRF Newsletter **30**, 20 (1998).

[Buf99] J.-Y. Buffière, E. Maire, P. Cloetens, G. Lormand, and R. Fougères, Acta Materiala in press, (1999).

[Bus96] V.A. Bushuev, V.N. Ingal, and E.A. Belyaevskaya, Kristallografiya, **41**, 808 (1996).

[Bye77] R.L. Byer in *Nonlinear Optics,* eds. P.G. Harper and B.S. Wherrett (Academic Press, London, 1977), p. 51.

[Cah86] J. W. Cahn, D. Shetchman and D. Gratias, J. Mater. Res. **1**, 13 (1986).

[Car77] W.H. Carter and E. Wolf, J. Opt. Soc. Am. **67**, 785 (1977).

[Cha96] H.N. Chapman, Ultramicroscopy, **66**, 153 (1996).

[Cha98] D. Chapman, W. Thomlinson, Z. Zhong, R.E. Johnston, E. Pisano, D. Washburn, D. Sayers, and C. Segre, Synchrotron Radiation News, **11**, 4 (1998).

[Che] H. Chen and M. Kuriyama, unpublished manuscript (undated).

[Clo95] P. Cloetens, J. Baruchel, R. Barrett, M. Ohler, M. Schlenker and J.-P. Guigay, Poster presentation at the French Society of Physics, Marseille 9/1995.

[Clo96] P. Cloetens, R. Barrett, J. Baruchel, J.P. Guigay and M. Schlenker, J. Phys. D: Appl. Phys. **29**, 133 (1996).

[Clo97a] P. Cloetens, M. Pateyron-Salomé, J.-Y. Buffière, G.Peix, J. Baruchel, F. Peyrin and M. Schlenker, J.Appl. Phys. **81**, 9 (1997).

[Clo97b] P. Cloetens, J.P. Guigay, C. de Martino, J. Baruchel, and M. Schlenker, 1997 *Optics Letters* **22** 1059.

[Clo97c] P. Cloetens, J.P. Guigay, C. De Martino, M. Pateyron Salomé, M. Schlenker, and D. Van Dyck, Proc. SPIE **3154**, San Diego 1997, 72.

[Clo98a] P. Cloetens, J.I. Espeso and F. Sever, ESRF Newsletter **30**, 53 (1998).

[Clo98b] P. Cloetens, J. Baruchel, J.P. Guigay, W. Ludwig, L. Mancini, P. Pernot and M. Schlenker, in *Proceedings: Microscopy & Microanalysis 1998*, ed. G.W. Bailey (Springer-Verlag, New-York, 1998) **4**, p. 376.

[Clo99] P. Cloetens, W. Ludwig, J. Baruchel, J.-P. Guigay, P. Pernot-Rejmánková, M. Salomé-Pateyron, M. Schlenker, J.-Y. Buffière, E. Maire, and G. Peix, J. Phys. D: Appl. Phys. in press, (1999).

[Cly93] T.W. Clyne, P.J. Withers, in *An Introduction to Metal Matrix Composites,* (University Press, Cambridge, 1993).

[Coe92] W. Coene, G. Janssen, M. Op de Beeck and D. Van Dyck, Phys. Rev. Lett. **69**, 3743 (1992).

[Coï95] R. Coïsson, Applied Optics **34**, 904 (1995).

[Cop93] P. Coppens in *International Tables of Crystallography*, eds U. Shmueli (Kluwer Academic Publishers, Dordrecht 1993), p. 18.

[Cow57] J.M. Cowley and A.F. Moodie, Acta Crystallogr.**10**,609 (1957).

[Cow75] J.M. Cowley, *Diffraction Physics*, 2nd ed. (North-Holland Publ. Co., Amsterdam, Oxford, 1975), p. 59.

[Cro70] D.T. Cromer and D. Liberman, Journ. Chem. Phys. **53**, 1891 (1970).

[Dab91] I. Daberkow, K.-H. Herrmann, L. Liu and W.D. Rau, Ultramicr. **38**, 215 (1991).

[Dab96] I. Daberkow, K.-H. Herrmann, L. Liu, W.D. Rau and H. Tietz, Ultramicr. **64**, 35 (1996).

[Dai74] J.C. Dainty and R. Shaw, *Image Science* (Academic Press, London, 1974).

[Dav26] B. Davis and C.M. Slack, Phys. Rev. **27**, 18 (1926).

[Dav95] T.J. Davis, D. Gao, T.E. Gureyev, A.W. Stevenson and W. Wilkins, Nature **373**, 595 (1995); T.J. Davis, D. Gao, T.E. Gureyev, A.W. Stevenson and W. Wilkins, Phys. Rev. Lett. **74**, 3173 (1995); D. Gao, T.J. Davis, and W. Wilkins, Aust. J. Phys. **48**, 103 (1995); T.J. Davis and A.W. Stevenson, J. Opt. Soc. Am. A **13**, 1193 (1996).

[Daw67] B. Dawson, Proc. Roy. Soc. **A298**, 255 (1967).

[Dev89] J. Devaud-Rzepski, M. Cornier-Quiquandon and D. Gratias, in *Proceedings of the 3rd International Conference on Quasicrystals*, Vista Hermoza, Mexico, eds M. J. Yacaman, D. Romeu, V. Castano and A. Gomez (World Scientific, Singapore, 1989), p. 498.

[DiF98] S. Di Fonzo, W. Jark, G. Soullié, A. Cedola, S. Lagomarsino, P. Cloetens and C. Riekel, J. Synchrotron Rad. **5**, 376 (1998).

[Ell98] P. Elleaume, personal communication

[Epe85] Y. Epelboin, Mater. Sci. Eng. **73**, 1 (1985); Prog. Cryst. Growth Charact. **14**, 465 (1987).

[Esp98] J. Espeso, P. Cloetens, J. Baruchel, J. Härtwig, T. Mairs, J.C. Biasci, G. Marot, M. Salomé and M. Schlenker, J. Synchrotron Rad. **5**, 1243 (1998).

[Fen95] Y.P. Feng, S.K. Sinha, E.E. Fullerton, G. Grübel, D. Abernathy, D.P. Siddons and J.B. Hastings, Appl. Phys. Lett. **67**, 3647 (1995).

[Fez97] K. Fezzaa, F. Comin, S. Marchesini, R. Coïsson, and M. Belakhovsky, J. X-ray Sci. Technol. **7**, 12 (1997).

[Fla93]] P. Flandrin, *Temps-fréquence* (Hermès, Paris, 1993) p. 101.

[För80] E. Förster, K. Goetz and P. Zaumseil, Kristall und Technik **1**, 937 (1980).

[Fuj74] H. Fujiwara, Opt. Acta **21**, 861 (1974).

[Gab48] D. Gabor, Nature **161**, 777 (1948).

[Gas95a] J. Gastaldi, E. Reinier, C. Jourdan, G. Grange, A. Quivy and M. Boudard, Phil. Mag. Lett. **72**, 311 (1995).

[Gas95b] J. Gastaldi , E. Reinier , G. Grange , C. Jourdan and I. Smolsky, in *Proceedings of the 5th International Conference on Quasicrystals*, Avignon, France, eds C. Janot and R. Mosseri (Word Scientific, Singapore, 1995), p. 287.

[Gas99] J. Gastaldi, L. Mancini, E. Renier, P. Cloetens, W. Ludwig, C. Janot, J. Baruchel, J. Härtwig and M. Schlenker, J. Phys. D: Appl. Phys. in press, (1999).

[Goe79] K. Goetz and P. Zaumseil, 'Habilitationsschrift' and Ph. D. Thesis, Jena, 1979.

[Goo68] J.W. Goodman, *Introduction to Fourier Optics* (McGraw-Hill, San Francisco, 1968).

[Gra93] D. Gratias, Y. Calvayrac, J. Devaud-Rzepski, F. Faudot, M. Harmelin, A. Quivy and P. A. Bancel, Journal of Non Crystalline Solids **153-154**, 482 (1993).

[Gro80] J. Gronkowski, *Phys. Status Solidi a* **57**, 105 (1980).

[Grü94] G. Grübel, J. Als-Nielsen, D.L. Abernathy, G. Vignaud, S. Brauer, G.B. Stephenson, S.G.J. Mochrie, M. Sutton, I.K. Robinson, R.M. Fleming, R. Pindak, S.B. Dierker, and J.F. Legrand, ESRF Newsletter **20**, 14 (1994).

[Gui71] J.P. Guigay, Opt. Acta **18**, 677 (1971).

[Gui77] J.P. Guigay, Optik **49**, 121 (1977).

[Gui78] J.P. Guigay, Optics Communication **26**, 136 (1978).

[Gui94] A. Guinier, *X-Ray Diffraction In Crystals, Imperfect Crystals, and Amorphous Bodies* (Dover Publications Inc., New-York 1994), p. 2.

[Gur95] T.E. Gureyev, A. Roberts and K.A. Nugent, J. Opt. Soc. Am. A **12**, 1932 (1996); **12**, 1942 (1995); T.E. Gureyev and K.A. Nugent, J. Opt. Soc. Am. A **13**, 1670 (1996); T.E. Gureyev and S.W. Wilkins, J. Opt. Soc. Am. A **15**, 579 (1998).

[Guv97] A.Guvenilir, T.M. Breunig, J.H. Kinney and S.R. Stock, Acta Mater. **45**, 5 (1997).

[Hai97] M. Haider and S. Uhlemann, *Proc. 55th Ann. Meeting EMSA*, Cleveland, Ohio, 1997, p. 1179.

[Ham95] H. Hamam and J.L. De Bougrenet de la Tocnaye, J. Opt. Soc. Am. A **12**, 1920 (1995).

[Han72] K.J. Hanszen, Optik **36**, 41 (1972).

[Har75] M. Hart, Proc. R. Soc. Lond. **A346**, 1 (1975).

[Har94] Ya.M. Hartman and A. Snigirev, in *X-ray Microscopy IV* (Bogorodskii Pechatnik Publishing Company, Moscow 1994), p. 429.

[Haw74] P.W. Hawkes, Optik **41**, 64 (1974).

[Hec98] E. Hecht, *Optics*, 3th ed. (Addison-Wesley, 1998).

[Hen93] B.L. Henke, E.M. Gullikson and J.C. Davis, Atomic Data and Nuclear Data **54-2**, (1993).

[Her80] G.T. Herman, *Image reconstruction from projections* (Academic Press, New York, 1980).

[Her95] C. Hervé and J. Cerrai, VCCD3 specification, version 0.4, CS/EL/95/0x, internal communication.

[Hig97] O. Hignette, internal communication.

[Hir88] K. Hiraga, B. P. Zhang, M. Hirabayashi, A. Inoue and T. Masumoto, Jap. J. Appl. Phys. **L951**, 27 (1988).

[Hir95] T. Hirano, K. Usami, Y. Tanaka, and C. Masuda, J. Mater. Res. **10**, 381 (1995).

[Hop55] H.H. Hopkins, Proc. Roy. Soc. A **231**, 91 (1955).

[Hou95] M. Houe and P. D. Townsend, Appl. Phys. Lett. **66**, 2667 (1995).

[Hu96] Z. W. Hu, P. A. Thomas, and J. Webjörn, J. Appl. Cryst. **29**, 279 (1996).

[Hu98] Z. W. Hu *et al.*, Nature **392**, 690 (1998).

[Hun77] B.R. Hunt, IEEE Trans. Computers C **26**, 219 (1977).

[Hun91] W.H. Hunt, J.R. Brockenborough and P.E.Magnusen, Scripta Metall. Mater. **25**, 15 (1991).

[Ing95] V.N. Ingal and E.A. Beliaevskaya, J. Phys. D: Appl. Phys. **28**, 2314 (1995).

[Ing96] V.N. Ingal and E.A. Beliaevskaya, Physica Medica **12**, 75 (1996).

[Ish80] Ishizuka, Ultramicr. **5**, 55 (1980).

[Iyi92] N. Iyi, K. Kitamura, F. Izumi, J.K. Yamamoto, T. Hayashi, H. Asano and S. Kimura, Journal of Solid State Chemistry **101**, 340 (1992).

[Jac88] C. Jacobsen, J. Kirz, M. Howells, K. McQuaid, S. Rothman, R. Feder and D. Sayre, in *X-ray Microscopy II*, eds. D.Sayre, M. Howells, J. Kirz and H. Rarback (Springer-Verlag, Berlin, 1988), p. 253.

[Jan92] *Quasicrystal - A primer*, C. Janot (Oxford Science Publication, 1992).

[Jan94] C. Janot and M. de Boissieu, Phys. Rev. Lett. **72**, 1674 (1994).

[Jan97] C. Janot, J. Phys.: Condens. Matter **9**, 1493 (1997).

[Jans97] *Deconvolution of images and spectra* 2nd ed., ed. P.A. Jansson (Academic Press, San Diego, 1997).

[Jar96] W. Jark, S. Di Fonzo, S. Lagomarsino, A. Cedola, E. Di Fabrizio, A. Brahm and C. Riekel, J. Appl. Phys. **80**, 4831 (1996).

[Joy88] D. Joyeux, S. Lowenthal, F. Polack and A. Bernstein, in *X-ray Microscopy II*, eds. D.Sayre, M. Howells, J. Kirz and H. Rarback (Springer-Verlag, Berlin, 1988), p. 246.

[Kam65] Y. Kamiya and A.R. Lang, J. Appl. Phys. **36**, 579 (1965).

[Kai80] T. Kailath, *LinearSystems* (John Wiley, New-York, 1980).

[Kim86] K.-J. Kim, Nucl. Inst. Meth. A **246**, 71 (1986).

[Kin90] J.H. Kinney, S.R. Stock, M.C. Nichols, U. Bonse, T.M. Breunig, R.A. Saroyan, R. Nusshardt, Q.C. Johnson, F. Busch and S.D. Antolovich, J. Mater. Res. **5**, 1123 (1990).

[Kin93] J.H. Kinney, D.L. Haupt, T.M. Breunig, M.C. Nichols, T.L. Starr and S.R. Stock, in *Proc. 17th Annual Conference on Composites and Advanced Ceramic Materials*, (American Ceramic Society, Cocoa Beach, January 1993), p. 1028.

[Kir84] E.J. Kirkland, Ultramicroscopy **15**, 151 (1984).

[Kis96] M.T. Kiser, F.W. Zok and D.S. Wilkinson, Acta Metall. Mater. **44**, 9 (1996).

[Kno65] G. Knop and W. Paul, in *Alpha-, Beta- and Gamma-ray Spectroscopy I*, ed. K. Siegbahn (North-Holland Publishing Company, Amsterdam, 1965), p. 1.

[Koc98] A. Koch, C. Raven, P. Spanne and A. Snigirev, J. Opt. Soc. Am. A **15**, 1940 (1998).

[Kug95] V. D. Kugel, G. Roseman and D. Shur, J. Phys. D: Appl. Phys. **28**, 2360 (1995).

[Lab96] J.C. Labiche, J.Segura-Puchades, D. Van Brussel, J.P. Moy, ESRF Newsletter **25**, 41 (1996).

[Lag96] S. Lagomarsino, W. Jark, S. Di Fonzo, A. Cedola, B. Mueller, P. Engstrom and C. Riekel, J. Appl. Phys. **79**, 4471 (1996).

[Lag97] S. Lagomarsino, A. Cedola, P. Cloetens, S. Di Fonzo, W. Jark, G. Soullié and C. Riekel, Appl. Phys. Lett. **71**, 2557 (1997).

[Lai95] B. Lai, W. Yun, Y. Xiao, L. Yang, Z. Cai, A. Krasnoperova, F. Cerrina, E. Di Fabrizio, L. Grella and M. Gentili Rev. Sci. Instrum. **66,** 2287 (1995).

[Lan57] A. R. Lang , Acta Metall. **5**, 358 (1957).

[Lan78] A.R. Lang, in *Diffraction and Imaging Techniques in Material Science*, 2nd ed., eds. S. Amelinckx, R. Gevers and J. Van Landuyt (North-Holland Publ. Co., Amsterdam, 1978), p. 623.

[Lan80] A. R. Lang , in *Characterization of Crystal Growth Defects by X-ray Methods*, eds B. K. Tanner and D. K. Bowen (Plenum Press, New York, 1980), p. 512.

[Lei62] E.N. Leith and J. Upatnieks, J. Opt. Soc. Am. **52**, 1123 (1962).

[Len98] B. Lengeler, private communication.

[Lew95] C.A. Lewis and P.J. Withers, Acta Metall. Mater. **43**, 10 (1995).

[Liu87] G. Liu and P.D. Scott, J. Opt. Soc. Am. A **4**, 159 (1987).

[Liu89] L. Liu, Appl. Opt. **28**, 4668 (1989).

[Liu93] X. Liu and C. Bathias, Comp. Sc.Tech. **46**, 245 (1993).

[Llo91] D.J. Lloyd, Acta Metall. Mater. **39**, 1 (1991).

[Lon90] B. London, R.N. Yancey and J.A. Smith, Mater. Eval. **May**, 604 (1990).

[Lud98] W. Ludwig, B. Nadrowsky and P. Cloetens, internal communication.

[Mai95] E. Maire, C. Verdu, G. Lormand, and R. Fougères, Mat. Sc. Eng. **A196,** 135 (1995).

[Mai99] E. Maire et al., manuscript in preparation.

[Mal68] C. Malgrange, E. Velu and A. Authier, J. Appl. Cryst. **1**, 181 (1968).

[Man98] L. Mancini, E. Reinier, P. Cloetens, J. Gastaldi, J. Härtwig, M. Schlenker and J. Baruchel, Phyl. Mag. A **78**, 1175 (1998).

[Mat98] I. Matsouli, V.V. Kvardakov, J.I. Espeso, L. Chabert and J. Baruchel, J. Phys. D: Appl. Phys. **31**, 1478 (1998).

[McC92] B.C. McCallum and J.M. Rodenburg, Ultramicroscopy **45**, 371 (1992).

[Med97] C. Medrano, P. Rejmánková, M. Ohler and I. Matsouli, Il Nuovo Cimento D **19**, 195 (1997).

[Mei86] E.S. Meinel, J. Opt. Soc. Am. A **3**, 787 (1986).

[Mic88a] G. Michot, in *Crystal Properties and Preparation,* (Trans. Tech. Publications, Switzerland, 1988) **17-18**, p. 55.

[Mic88b] G. Michot, and A. George, Scripta Met. **22**, 1043 (1988).

[Moc95] A. Mocellin, Y. Bréchet, and R. Fougères, Acta Metall. Mater. **43**, 1135 (1995).

[Mom95] A. Momose, Nucl. Inst. Meth. A **352**, 622 (1995).

[Mom96] A. Momose, T. Takeda, Y. Itai and K. Hirano, Nature Medicine **2**, 473 (1996).

[Mou97] D. Mouze, in *Handbook of Microscopy, Methods I*, eds S. Amelinckx, D. Van Dyck, J. Van Landuyt and G. Van Tendeloo (VCH Verlagsgesellschaft mbH, Weinheim, 1997), p. 131.

[Müc97] F. Mücklich in *Handbook for Microscopy*, eds. S. Amelinckx, D. Van Dyck, J. Van Landuyt and G. Van Tendeloo, vol. I (Methods), (VCH, Weinheim,1997), p.7.

[Mum91] P.M. Mummery, B. Derby, D. Buttle and C.B. Scruby, in *Proc. Euromat 91,* eds T.W. Clyne and P.W. Withers (Cambridge, 1991), **2**, p. 863.

[Mum93] P.M. Mummery, P. Anderson, G.R. Davis, B. Derby and J.C. Elliott, Scripta Metall. Mater. **29**, 1457.(1993).

[Mum94] P.M. Mummery and B. Derby, Jal. Mat. Sc. **29**, 5615 (1994).

[Mye95] L. E. Myers et al., J. Opt. Soc. Am. **B12**, 2102 (1995).

[Nas76] K. Nassau, H. J. Levinstein, and G. M Loiacono, Appl. Phys. Lett. **6**, 228 (1965).

[Nug96] K.A. Nugent, T.E. Gureyev, D.F. Cookson, D. Paganin and Z. Barnea, Phys. Rev. Lett. **77**, 2961 (1996).

[Opd94] M. Op de Beeck, *Direct Structure Reconstruction in High Resolution Transmission Electron Microscopy,* Ph.D thesis (Universiteit Antwerpen, Belgium,1994), p. III.1-38.

[Opd96] M. Op de Beeck, D. Van Dyck and W. Coene, Ultramicroscopy **64**, 167 (1996).

[Pap74] A. Papoulis, J. Opt. Soc. Am. **64**, 779 (1974).

[Par54] L.G. Parrat, Phys. Rev. **95**, 359 (1954).

[Pat89] K. Patorski, in *Progress in Optics XXVII*, ed. E. Wolf (Elsevier Science Publishers B.V, 1989), p. 3.

[Pat98] M. Pateyron, *Acquisition et quantification d'images du réseau trabéculaire osseux en microtomographie tridimensionnelle utilisant le rayonnement synchrotron*, PhD thesis, (INSA Lyon, France, 1998).

[Pei98] G. Peix, P. Cloetens, M. Pateyron-Salomé, J.Y. Buffière, J. Baruchel, F. Peyrin, and M. Schlenker Proc. SPIE San Diego 97 **3149** (1997) 149-157. J. Baruchel, J.Y. Buffière, P. Cloetens, J.P. Guigay, G. Peix, F. Peyrin, M. Salomé-Pateyron, and M. Schlenker and P. Spanne, in *Developments in X-Ray Tomography*, ed U. Bonse, Proc. SPIE **3149,** San Diego 1997, p. 149.

[Pin84] Z.G. Pinsker, *Dynamical Scattering of X-rays in Crystals* (Springer, Heidelberg, 1984).

[Pod89] K.M. Podurets, V.A. Somenkov, R.R. Chistyakov and S.Sh. Shilstein, Physica B **156-157**, 691 (1989).

[Pog97] A. Pogany, D. Gao, and S.W. Wilkins, Rev. Sci. Instrum. **68**, 2774 (1997).

[Rad17] J. Radon, Ber. Verh. Sächs. Akad. Wiss. Leipzig, Math-Nat. **69**, 262 (1917).

[Rao93] D. Raoux, in *Neutron and Synchrotron Radiation for Condensed Matter Studies,* eds J. Baruchel, J.L. Hodeau, M.S. Lehmann, J.R. Regnard and C. Schlenker (Ed. de Physique and Springer -Verlag, 1993), **I**, p. 37.

[Rav96] C. Raven, A. Snigirev, I. Snigireva, P. Spanne, A. Souvorov and V. Kohn, Appl. Phys. Lett. **69**, 1826 (1996).

[Ray1881] Lord Rayleigh, Lond. Dubl. Edinb. Phil. Mag. **11**, 196 (1881).

[Rei97] E. Reinier, J. Gastaldi, L. Mancini, J. Härtwig, J. Baruchel and N. Baluc, in *Proceedings of the 6th International Conference on Quasicrystals*, Tokyo, Japan, eds S. Takeuchi and T. Fijiwara (World Scientific, Singapore 1997), p. 417.

[Rei98] E. Reinier, L. Mancini, J. Gastaldi, N. Baluc, J. Härtwig and J. Baruchel, Physica B in press, (1998).

[Rej98a] P. Rejmánková *et al.*, J. Appl. Cryst. **31**, 106 (1998).

[Rej98b] P. Rejmánková-Pernot, P.Cloetens, J.Baruchel, J.-P.Guigay, and P.Moretti, Phys. Rev. Lett. **81**, 3435 (1998).

[Ric72] W.H. Richardson, J. Opt. Soc. Am. **62**, 55 (1972).

[Riv97] N. Rivier, in *New Horizons in Quasicrystals*, eds A. I. Goldman, D. J. Sordelet, P. A. Thiel and J. M. Dubois (World Scientific, 1997), p. 188.

[Rom92] I. Roman and R. Aharonov, Acta Metall. Mater. **40**, 477 (1992).

[Ryt89] S.M. Rytov, Yu.A. Kravtsov and V.I. Tatarskii, *Principles of Statistical Radiophysics*, (Springer-Verlag, Berlin, 1989), **3 & 4**.

[Say95] D. Sayre and H.N. Chapman, Acta Cryst. A**51**, 237 (1995).

[Sch73] P. Schiske, in *Image Processing and Computer-aided Design in Electron Optics*, ed. P.W. Hawkes (Academic Press, London, 1973), p. 82.

[Sch80] M. Schlenker, W. Bauspiess, W. Graeff, U. Bonse and H. Rauch, J. Magn. Magn. Mat. **15-18**, 1507 (1980).

[Sch87] L.H. Schwartz and J.B. Cohen, *Diffraction from Materials*, 2nd ed. (Springer-Verlag, Berlin, 1987) p. 446.

[Sch93] M. Schlenker, in *Neutron and Synchrotron Radiation for Condensed Matter Studies,* eds J. Baruchel, J.L. Hodeau, M.S. Lehmann, J.R. Regnard and C. Schlenker (Ed. de Physique and Springer -Verlag, Berlin , 1993), **I**, p. 147.

[Sch95] G. Schmahl, D. Rudolph, P. Guttmann, G. Schneider, J. Thieme and B. Niemann, Rev. Sci. Instrum. **66**, 1282 (1995).

[Sch96] I. Schelokov, O. Hignette, C. Raven, I. Snigireva, A. Snigirev and A. Souvorov, Proc. SPIE **2805**, 282 (1996).

[She84] K. Shechtman, I. Blech, D. Gratias and J.W. Cahn, Phys. Rev. Lett. **53**, 1951 (1984).

[Shi96] Shi-ning Zhu et al., J. Phys. D: Appl. Phys. **28**, 76 (1996).

[Sin88] S.K. Sinha, E.B. Sirota, and S. Garoff, Phys. Rev. B **38**, 2297 (1988).

[Sni95] A. Snigirev, I. Snigireva, V. Kohn, S. Kuznetsov and I. Schelokov, Rev. Sci. Instrum. **66**, 5486 (1995).

[Sni96a] A. Snigirev, I. Snigireva, V. Kohn, and S. Kuznetsov, Nucl. Instrum. Methods **A370**, 634 (1996).

[Sni96b] A. Snigirev, V. Kohn, I. Snigireva and B. Lengeler, Nature **384**, 49 (1996).

[Sni97] A. Snigirev, I. Snigireva, P. Bösecke, S. Lequien and I. Schelokov, Opt. Commun. **135**, 378 (1997).

[Sny83] A.W. Snyder and J.D. Love, *Optical Waveguide Theory* (Chapman & Hall, London, 1983).

[Soc86] J.E.S. Socolar, T.C. Lubensky and P.J. Steinhardt, Phys. Rev. B **34**, 3345 (1986).

[Som91] V.A. Somenkov, A.K. Tkalich and S.Sh. Shil'shtein, Zh. Tekh. Fiz. **61**, 197 (1991).

[Soy95] A. Soyer, J. Appl. Cryst. **28**, 244 (1995).

[Spe95] J.C.H. Spence, X. Zhang and W. Qian, in *Electron Holography*, eds. A. Tonomura, L.F. Allard, G. Pozzi, D.C. Joy and Y.A. Ono (Elsevier Science, Amsterdam, 1995), p. 267.

[Spi94] E. Spiller, *Soft X-ray optics* (SPIE Optical Engineering Press, Washington, 1994), p. 2.

[Sut91] M. Sutton, S.G.J. Mochrie, T. Greytak, S.E. Nagler, L.E. Berman, G.A. Held and G.B. Stephenson, Nature **352**, 608 (1991).

[Swa73] R.K. Swank, Appl. Opt. **12**, 1865 (1973).

[Tak78] K. Takahashi and M. Takagi, J. Phys. Soc. Japan **44**, 1266 (1978).

[Tak98] Y. Takayama, T. Hatano, T. Miyahara, and W. Okamoto, J. Synchrotron Rad. **5**, 1187 (1998).

[Tal1836] H.F. Talbot, Phil.Mag., 3rd Series **9**, 401 (1836).

[Tan76] B. K. Tanner, *X-ray Diffraction Topography* (Oxford, Pergamon Press, 1976), p. 1.

[Tea82] M.R. Teage, J. Opt. Soc. Am. **72**, 1199 (1982).

[Van87] D. Van Dyck and W. Coene, Optik **77**, 125 (1987).

[Van97] D. Van Dyck, in *Handbook of Microscopy, Methods I*, eds. by S. Amelinckx, D. Van Dyck, J. Van Landuyt and G. Van Tendeloo (VCH Verlagsgesellschaft mbH, Weinheim, 1997), p. 404.

[Vre84] T. Vreeland, Jr. and V. S. Speriosu, in *Application of X-ray Topographic Methods to Materials Science*, eds S. Weissmann, F. Balibar and J.-F. Petroff (Plenum Press, New York and London, 1984), p. 501.

[Wad74] R.W. Wade, Optik **40**, 201 (1974).

[Wal70] C. A. Wallace, J. Appl. Cryst. **3**, 546 (1970).

[Wei51] W.Weibull, J. Appl. Mech. **18**, 293 (1951).

[Wei85] R.S. Weis and T.K. Gaylord, Appl. Phys. **A37**, 191 (1985).

[Whi15] E.T. Whittaker, Proc. Roy. Soc. Edinburgh **35**, 181 (1915).

[Wic68] B. J. Wicks and M. H. Lewis, Phys. Stat. Sol. **26**, 571 (1968).

[Wil96] S.W. Wilkins, T.E. Gureyev, D. Gao, A. Pogany and A.W. Stevenson, Nature **384**, 335 (1996).

[Wol78] E. Wolf, J. Opt. Soc. Am. **68**, 6 (1978).

[Yam93] M. Yamada, N. Nada, M. Saitoh and K. Watanabe, Appl. Phys. Lett. **62**, 435 (1993).

[Yan92] Y. Yan and Z. Wang , Phil. Mag. Lett. **66**, 253 (1992) .

[Yan94] X. Yang , Z. Wang and R. Wang , Phil. Mag. Lett. **69**, 15 (1994) .

[Yar91] A. Yariv, *Optical Electronics*, (Saunders College Publishing, Philadelphia, 1991).

[Zer35] F. Zernike, Z. Tech. Phys. **16**, 454 (1935).

[Zon96] F. Zontone, L. Mancini, R. Barrett, J. Baruchel, J. Härtwig and Y. Epelboin, J. Synchrotron Rad. **3**, 173 (1996).

[Zot94] N. Zotov, H. Boysen, H. Frey, T. Metzger and E. Born, J. Phys. Chem. Solids **55**, 145 (1994).

[Zuc82] U.H. Zucker and H. Schulz, Acta Cryst. **A38**, 563 (1982).